Analysis of Material Deformation and Wrinkling Failure in Conventional Metal Spinning Process

WANG, LIN

Analysis of Material Deformation and Wrinkling Failure in Conventional Metal Spinning Process

Lin Wang

Doctor of Philosophy

School of Engineering and Computing Sciences

Durham University

2012

Analysis of Material Deformation and Wrinkling Failure in Conventional Metal Spinning Process

Lin Wang

Abstract

Sheet metal spinning is one of the metal forming processes, where a flat metal blank is rotated at a high speed and formed into an axisymmetric part by a roller which gradually forces the blank onto a mandrel, bearing the final shape of the spun part. Over the last few decades, sheet metal spinning has developed significantly and spun products have been widely used in various industries. Although the spinning process has already been known for centuries, the process design still highly relies on experienced spinners using trial-and-error. Challenges remain to achieve high product dimensional accuracy and prevent material failures. This PhD project aims to gain insight into the material deformation and wrinkling failure mechanics in the conventional spinning process by employing experimental and numerical methods. In this study, a tool compensation technique has been proposed and used to develop CNC multiple roller path (passes). 3-D elastic-plastic Finite Element (FE) models have been developed to analyse the material deformation and wrinkling failure of the spinning process. By combining these two techniques in the process design, the time and materials wasted by using the trial-and-error could be decreased significantly. In addition, it may provide a practical approach of standardised operation for the spinning industry and thus improve the product quality, process repeatability and production efficiency. Furthermore, effects of process parameters, e.g. roller path profiles, feed rate and spindle speed, on the variations of tool forces, stresses, strains, wall thickness and wrinkling failures have also been investigated. Using a concave roller path produces high tool forces, stresses and reduction of wall thickness. Conversely, low tool forces, stresses and wall thinning have been obtained in the FE model which uses the convex roller path. High feed ratios help to maintain original blank thickness but also lead to material failures and rough surface finish. Thus it is necessary to find a “trade off” feed ratio for a spinning process design.

Declaration

I hereby declare that this thesis is my own work, which is based on research carried out in the School of Engineering and Computing Sciences, Durham University, UK. No portion of the work in the thesis has been submitted in support of an application for another degree or qualification of any other university or institute of learning.

Acknowledgements

My deepest gratitude goes first and foremost to my supervisor, Dr. Hui Long, for her constant encouragement and guidance through all the stages of my PhD research and thesis writing. Her tremendous effort and tireless support made this work possible and was critical to the successful completion of this thesis.

Secondly, I would like to acknowledge the consistent support and valuable advice from Mr. David Ashley, Mr. Martyn Roberts, Mr. Peter White, Mr. Fred Hoye, Mr. Paul Johnson, and Mr. Kris Carter of Metal Spinners Group Ltd, where I worked as a KTP associate for two years.

I appreciate the contribution to this research by former students of Durham University, Mr. Seth Hamilton, Mr. Stephen Pell, and Mr. Paul Jagger for their suggestion and assistance on FE modelling and the experimental design of metal spinning.

My sincere thanks also go to Miss. Rachel Ashworth for sharing literatures and discussing theoretical analysis of the metal spinning process. I gratefully acknowledge Dr. Xiaoying Zhuang and Mr. Xing Tan for their precious advice on the thesis writing.

Finally, I should like to express my heartfelt gratitude to my beloved parents. This thesis is by all means devoted to them because they have assisted, supported and cared for me all of my life.

The first two years of this PhD study were financially supported by UK Technology Strategy Board and Metal Spinners Group Ltd, Project No. 6590. The final year of study was sponsored by School of Engineering and Computing Sciences, Durham University.

Publications

Aspects of the work presented in this thesis have been published in the following journal papers and conference proceedings:

1. Wang, L., Long, H., 2011. Investigation of material deformation in multi-pass conventional metal spinning. Materials & Design, 32, 2891-2899.

2. Wang, L., Long, H., Ashley, D., Roberts, M., White, P., 2011. Effects of roller feed ratio on wrinkling failure in conventional spinning of a cylindrical cup. Proceedings of IMechE: Part B: Journal of Engineering Manufacture, 225, 1991-2006.

3. Wang, L., Long, H., 2011. A study of effects of roller path profiles on tool forces and part wall thickness variation in conventional metal spinning, Journal of Materials Processing Technology, 211, 2140-2151.

4. Wang, L., Long, H., Ashley, D., Roberts, M., White, P., 2010. Analysis of single-pass conventional spinning by Taguchi and Finite Element methods, Steel Research International, 81, 974-977.

5. Wang, L., Long, H., 2010. Stress analysis of multi-pass conventional spinning, Proc. of 8th International Conference on Manufacturing Research, Durham, UK.

6. Wang, L., Long, H., 2011. Investigation of Effects of Roller Path Profiles on Wrinkling in Conventional Spinning, Proc. of 10th International Conference on Technology of Plasticity, Aachen, Germany.

7. Long, H., Wang, L., Jagger, P., 2011. Roller Force Analysis in Multi-pass Conventional Spinning by Finite Element Simulation and Experimental Measurement, Proc. of 10th International Conference on Technology of Plasticity, Aachen, Germany.

Table of Contents

List of Figures

List of Tables

List of Abbreviations

2-D	Two Dimension
3-D	Three Dimension
ANOM	Analysis of Means
CAM	Computer Aided Manufacturing
CNC	Computer Numerical Control
CPU	Central Processing Unit
DoE	Design of Experiment
DOF	Degree of Freedom
FE	Finite Element
FEM	Finite Element Method
OFAT	One-Factor-At-a-Time
PNC	Playback Numerical Control
RAM	Random-Access Memory
RSM	Response Surface Methodology
S/N	Signal to Noise ratio

Nomenclature

a	Length of a half-wave wrinkle in the tangential direction of flange
b	Width of wrinkled plate in the radial direction of flange
B	Strain matrix
c^d	Wave speed of the material
D	Flexural rigidity of plate
D	Matrix of material constants
D_0	Original diameter of the blank
D_1	Final diameter of the blank
$d\varepsilon$	Element strain increments
E	Young's Modulus
E_0	Reduced Modulus
E_b	Energy due to the bending in the wrinkled flange
E_l	Energy due to the lateral concentrated loading from the roller
E_p	Slope of the stress strain curve at a particular value of strain in the plastic region
E_r	Energy due to the radial elongation of the flange under tensile radial stresses
E_t	Energy due to the circumferential shortening of the flange under compressive tangential stresses
f_b	Body force
f_s	Surface force
F	External applied force vector / Feed rate
F_a	Axial tool force
F_r	Radial tool force
F_t	Tangential tool force
G	Shear modulus
h	Plastic hardening modulus
I	Internal element force vector

J	Jacobian matrix
K	Stiffness matrix
L	Matrix of partial differential operator
L^e	Characteristic element length
M	Mass matrix / Material type
n	The number of the time increment / Sample number of the experiment
n_d	Number of nodes forming the element
n_f	Number of Degree of Freedom
N	Number of the nodes along the edge of workpiece
N	Shape function
$\dot{p}$	Effective plastic strain rate
P	Lateral concentrated load
r	Radial direction in a cylindrical coordinate system of the mandrel / Roller nose radius
R	The radius of the round part of the mandrel
S	Spindle speed
S_f	Domain of area
T	Time of the analysed process / Kinetic energy
T	Transformation matrix
t	Tangential direction in a cylindrical coordinate system of the mandrel / Wall thickness
t_0	Original thickness of the blank
t_1	Final thickness of the blank
u	Vector of displacement
U_i	Radial coordinate of element node *i* along the edge of workpiece
U	Displacement vector
V	Domain of volume
v	Poisson's ratio
w	Buckled deflection surface
W_f	Work done by external force

X	x-coordinate of the global coordinate system
x	Coordinate in transverse direction of local coordinate system
Y	y-coordinate of the global coordinate system
y_i	Outputs of different samples
z	Coordinate in longitudinal direction of local coordinate system / Axial direction in a cylindrical coordinate system of the mandrel
α	Inclined angle of the mandrel in shear forming
Δt	Time increment
θ	Angle between local coordinate system and the global coordinate system
λ	Lamé's constant
μ	Lamé's constant
ρ	Mass density of material
σ	Stress
σ_1	Principal stress
σ_2	Principal stress
σ_r	Radial stress
σ_t	Tangential stress
σ_y	Yielding stress
σ_e	Effective stress
ε	Strain
ε^e	Elastic strain
ε^p	Plastic strain
$\dot{u}$	Vector of velocity
$\ddot{u}$	Vector of acceleration
$\bar{y}$	Mean outputs of different samples
γ	Maximum deflection of the buckling surface
$\overline{U}$	Mean value of radial coordinate of element nodes on the workpiece edge
$\prod$	Strain energy
ξ	Natural coordinate of an element

η	Natural coordinate of an element
ξ	Natural coordinate of an element
τ	Shear stress
χ	Curvature of a plate

Terminology in Spinning

There are currently no universally agreed terminologies of the metal spinning process. Different researchers and engineers may use different terms referring to the same technique. The spinning terms used in this thesis, corresponding alternatives and explanations are shown below.

Terms	Alternative	Explanation
Mandrel	Former, chunk	Rigid tool which bears the final profile of the desired spun product.
Backplate	Tailstock	Circular disk which clamps the blank onto the mandrel
Roller nose radius	Roller round-off radius	Blending radius between the two flat surfaces on the outer surface of the roller (Music et al., 2010).
Roller path	Tool path	The trace of roller movement, e.g. linear, convex, concave, etc.
Forward path	Rim-directed movement	Roller feeds towards the edge of the blank
Backward path	Centre-directed movement	Roller feeds towards the centre of the blank
Feed rate	Feed	Feeding speed of the roller (unit: *mm/min*)
Spindle speed	Mandrel speed, rotational speed	Rotational speed of the mandrel (unit: *rpm*)
Feed ratio	Feed per revolution, feed	Ratio of feed rate to spindle speed (unit: *mm/rev*)
Conventional spinning	Multiple-pass spinning, manual spinning	Spinning process which deliberately reduces the diameter of the workpiece but without changing the wall thickness by using multiple roller passes
Shear forming	Shear spinning, power spinning	Spinning process which maintains the diameter of the workpiece and deliberately decreases the wall thickness by a single roller pass
Spinnability	Formability	The ability of a sheet metal to undergo deformation by spinning without wrinkling or cracking failures

1. Introduction

1.1 Background

Sheet metal spinning is one of the metal forming processes, where a flat metal blank is formed into an axisymmetric part by a roller which gradually forces the blank onto a mandrel, bearing the final shape of the spun part. As shown in Figure 1.1, during the spinning process, the blank is clamped between the mandrel and backplate; these three components rotate synchronously at a specified spindle speed. Materials used in the spinning process include non-alloyed carbon steels, heat-resistant and stainless steels, non-ferrous heavy metals and light alloys (Runge, 1994). The process is capable of forming a workpiece with a thickness of 0.5 *mm* to 30 *mm* and diameter of 10 *mm* - 5 *m*.

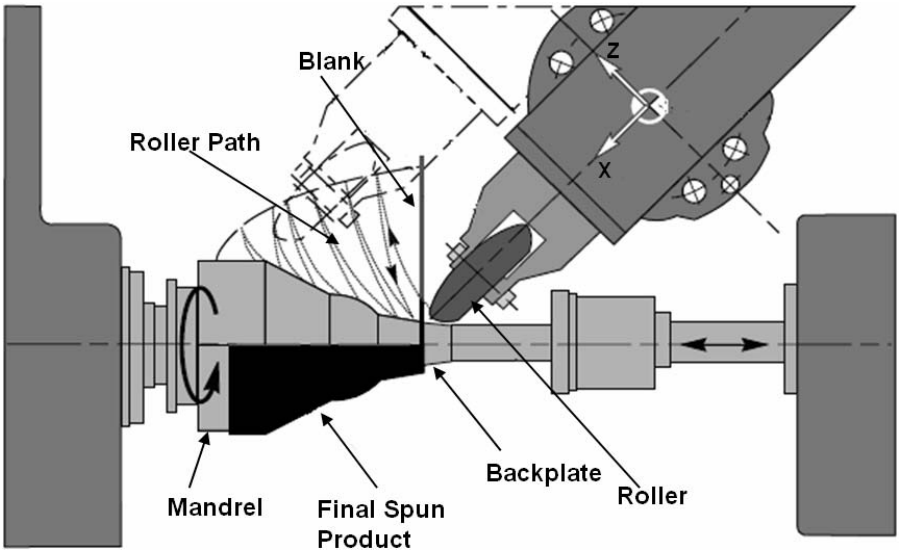

Figure 1.1 Setup of metal spinning process, adapted from Runge (1994)

Due to its incremental forming feature, metal spinning has some unique advantages over other sheet metal forming processes. These include process flexibility, non-dedicated tooling, low forming load, good surface finish and improved mechanical properties of the spun part (Wick et al., 1984). Hence, the sheet metal spinning process has been frequently used to produce components for the automotive, aerospace, medical, construction and defence industries, as shown in Figure 1.2.

Figure 1.2 Applications of spun parts (http://www.metal-spinners.co.uk)

There are two types of sheet metal spinning: in conventional spinning, as shown in Figure 1.3(a), a blank is formed into the desired shape by multiple roller passes to maintain the original wall thickness (t_0); however, the diameter of the spun part (D_1) has been reduced from the original diameter (D_0). Conversely, during shear forming, the roller deforms the blank by one single pass as shown in Figure 1.3(b). The diameter of the spun part (D_1) remains unchanged but the wall thickness of the spun part is reduced deliberately. The final thickness of the spun part, t_1, can be determined by the sine law:

$$t_1 = t_0 \cdot \sin\alpha \tag{1}$$

where t_0 is the original thickness of the blank, α is the inclined angle of the mandrel.

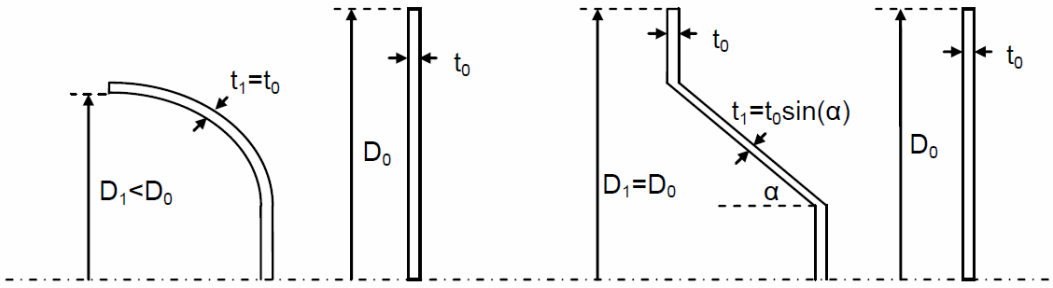

(a) Conventional spinning: spun part (left), blank (right)

(b) Shear forming: spun part (left), blank (right)

Figure 1.3 Conventional spinning and shear forming, adapted from Music et al. (2010)

During the conventional spinning process, a local plastic deformation zone is generated at the roller contact area. The stress patterns of this zone depend on the roller feeding direction (Runge, 1994). In the forward pass (the roller feeds towards the edge of the blank), tensile radial stresses and compressive tangential stresses are induced, as shown in Figure 1.4(a). The tensile radial stresses lead to a material flow towards the edge of the blank causing thinning of the blank, which is balanced by the thickening effects of the compressive tangential stresses, maintaining an almost constant thickness. In the backward pass (the roller feeds towards the mandrel), however, the material builds up in front of the roller, generating compressive radial stresses and compressive tangential stresses, as shown in Figure 1.4(b).

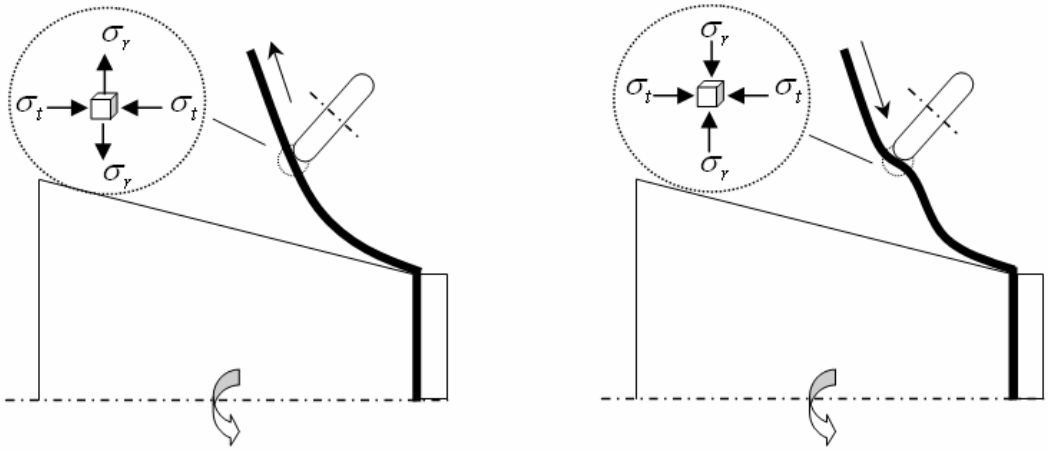

(a) Forward pass (b) Backward pass

Figure 1.4 Stress distributions of roller working zone during conventional spinning

There are three types of common material failures in the sheet metal spinning process (Wong et al., 2003): wrinkling, circumferential cracking and radial cracking, as shown in Figure 1.5. Wrinkling is caused by buckling effects of the unsupported flange of the metal sheet during spinning. Once the compressive tangential stress in the workpiece exceeds a buckling stability limit, wrinkling will occur. Therefore, multiple roller passes are generally required in order to keep the compressive tangential stress below the buckling limit. In the sheet metal spinning process, excessive stresses in either radial or tangential direction of the spun part are undesirable. High tensile radial stresses lead to the circumferential cracking failure, mainly in the area close to the mandrel, as

illustrated in Figure 1.5(b). The radial cracking shown in Figure 1.5(c) is normally caused by the bending effects over existing severe wrinkles.

(a) Wrinkling (b) Circumferential cracking (c) Radial cracking

Figure 1.5 Typical material failure modes in metal spinning (Wong et al., 2003)

Up to now, research on the sheet metal spinning process has been carried out by using three techniques, i.e. theoretical study, experimental investigation and FE simulation. Each technique has its own advantages and disadvantages. For instance, theoretical study is the least expensive method used when analysing the metal spinning process and it has the potential to assist process design and predict material failures. However, due to the complex nature of metal spinning, theoretical study has to be developed on certain simplified assumptions. It is therefore almost impossible to obtain detailed and reliable results, such as stress and strain, by applying the theoretical analysis alone. On the other hand, accurate tool forces, strains and material failures can be obtained via experimental investigation. Nevertheless, carrying out experiments with various parameters at different levels costs a significant amount of time and material; thoroughly analysing their effects on material deformation is extremely difficult. FE simulation has the potential to provide in-depth understanding of the material deformation and failure mechanics, and can therefore develop guidance in determining process parameters and improve product quality. However, FE simulation of the spinning process involves three areas of non-linearity: material non-linearity, geometry non-linearity and boundary non-linearity. It generally takes extremely long computational time due to the nature of incremental forming and complex contact conditions.

The shear forming process has been investigated intensely by many researchers who have been using both experimental and numerical approaches since 1960. On the other hand, limited publications on conventional spinning mainly focus on one-pass deep drawing conventional spinning and simple multi-pass conventional spinning (less than three passes, linear path profile). The process design of conventional spinning thus still remains a challenging task and material failures significantly affect production efficiency and product quality. In the present industrial practice, the trial-and-error approach is commonly used in the process design (Hagan and Jeswiet, 2003). With the aid of Playback Numerical Control (PNC) of the spinning machine, all the processing commands developed by experienced spinners are recorded and used in the subsequent spinning productions (Pollitt, 1982). Nevertheless, the process design inevitably results in significant variations and discrepancies in product quality and geometrical dimensions (Hamilton and Long, 2008). Furthermore, the procedure of the PNC process development and validation unduly wastes a considerable amount of time and materials. It is therefore essential to study the material deformation and failure mechanics in the multi-pass conventional spinning process and to analyse the effects of process parameters on the quality of spun products.

1.2 Scope of Research

The aim of this research is to gain in-depth understanding of material deformation and wrinkling failures, and thus to provide guidance on process design for the conventional spinning process. A schematic diagram of the system in the conventional spinning process is shown in Figure 1.6, where the underlined texts indicate the parameters and outputs that have been investigated by this study.

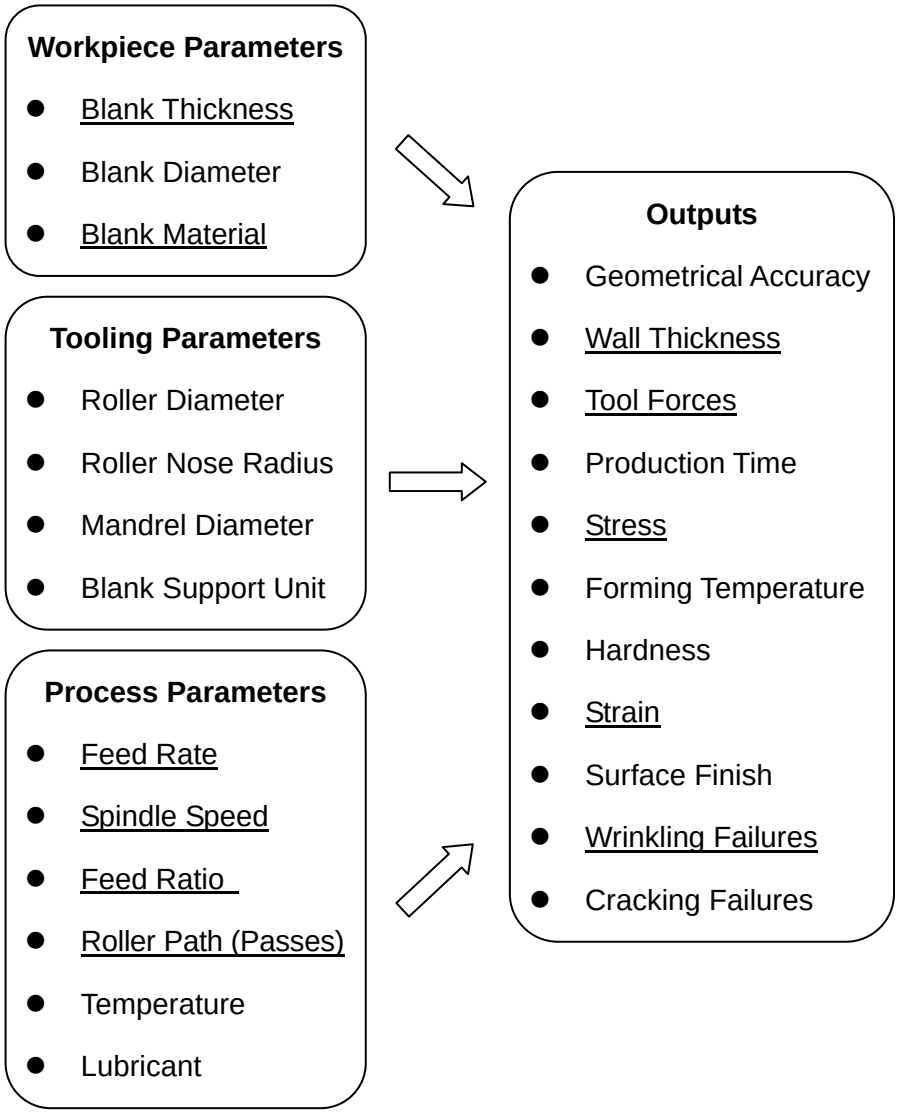

Figure 1.6 System of conventional spinning process, adapted from Runge (1994)

In this project contributions have been made on six areas of research work on the conventional spinning process:

1) Finite Element Simulation

3-D elastic-plastic models of metal spinning have been developed using commercial FE software Abaqus. The explicit FE solution method has been chosen to simulate the spinning process, because it is more robust and efficient to model 3-D problems that involve highly nonlinearities. The computing performance of different types of elements and different scaling methods has been evaluated respectively.

2) Experimental Investigation

CNC programming has been used to develop roller path (passes) in this study by using spinning Computer Aided Manufacturing (CAM) software - OPUS. To make the workpiece successfully conform to the non-linear profile of the mandrel, the tool compensation techniques have been proposed and employed in the multiple roller passes design. In addition, the Taguchi method has been used to design an experiment and to analyse the dimensional variation of spun samples. Experimental investigation has also been conducted to study the wrinkling failures.

3) Theoretical Analysis of Wrinkling

Energy methods and two-directional plate buckling theory have been used to predict the critical condition of wrinkling failure in conventional spinning. To predict wrinkling failures, a theoretical model involving the radial stress, tangential stress, flange dimension and material property has been developed.

4) Material Deformation

Based on the FE simulation, the variations of tool forces, stresses, strains and wall thickness have been investigated numerically. Axial force dominates at the beginning of the conventional spinning; radial force increases gradually over the process; tangential force is the smallest and remains almost constant. Stress analysis shows that high tensile and compressive radial stresses take place behind and in front of the roller contact. Two pairs of oppositely directed radial bending effects have been observed in the workpiece. The dominated in-plane tensile radial strains of the workpiece are believed to be the main reason behind the wall thinning.

5) Wrinkling Failures

In order to understand the wrinkling failure mechanics, FE analysis results of tool forces and stresses of a wrinkle-free model and a wrinkling model have been compared. It is believed that sudden changes and fluctuations in the tool forces could be used to determine the approximate moment that wrinkling occurs. If compressive tangential

stresses at the flange area near the local forming zone do not fully “recover” to tensile tangential stresses after leaving roller contact, wrinkling failure will take place.

6) Effects of Parameters

Using a concave roller path produces high tool forces, stresses and reduction of wall thickness. Conversely, low tool forces, stresses and wall thinning have been obtained in the FE model which uses the convex roller path. Moreover, results of an experiment show that the type of material has the most significant effects on the dimensional variations of spun parts, followed by the effects from feed rate and spindle speed. It has been shown that high feed ratios help to maintain original blank thickness. However, high feed ratios also lead to material failures and rough surface finish.

1.3 Structure of Thesis

This thesis consists of seven main chapters, the contents of which are detailed as below:

Chapter 2 gives a systematic review on the published literature of research on the sheet metal spinning. Three main investigation techniques used in the research of the sheet metal spinning process are reviewed, i.e. theoretical study, experimental investigation and FE analysis. Additionally, research on the material deformation and wrinkling failure mechanics is presented. Effects of four key process parameters, namely, feed ratio, roller path (passes), roller profile, and clearance between roller and mandrel, on the quality of the spun parts are also discussed.

The fundamental theory of Finite Element Method has been discussed in Chapter 3, such as Hamilton’s Principle and basic analysis procedure of FEM. Moreover, the formulations of four different types of finite elements, i.e. 3-D solid element, 2-D plane stress/strain element, plate element and shell element, are presented. Two commonly used non-linear FE solution methods, implicit method and explicit method, are compared. Additionally, the elastic-plastic material constitutive model and contact

algorithms of FE simulation have been briefly outlined.

Chapter 4 presents an investigation of the effects of roller path profiles on material deformation. Four roller path profiles are designed and developed to carry out experimental investigation and FE simulations. The techniques of developing 3-D FE models of metal spinning are explained in detail. These FE models are verified by conducting a mesh convergence study, assessing scaling methods and comparing dimensional results.

In Chapter 5, material deformation in a multi-pass conventional spinning process is investigated experimentally and numerically. The tool compensation technique is studied and used in the CNC multiple roller passes design. The Taguchi method is applied to design the experiment and to analyse the effects of process parameters on the dimensional variations of spun parts. In addition, FE simulation is conducted to investigate the variations of tool forces, stresses, wall thickness, and strains in this multi-pass conventional spinning process.

Theoretical analysis, experimental investigation and FE simulation of the wrinkling failures in conventional spinning are carried out in Chapter 6. The theory of two-direction plate buckling and the energy method are employed to determine the critical condition of wrinkling in the conventional spinning. The severity of wrinkles is quantified and a forming limit study is carried out by conducting FE simulations. Furthermore, the computational performance of the solid and shell elements in simulating the spinning process is examined. Stresses and tool forces are also investigated in order to gain insight into the wrinkling failure mechanics.

Chapter 7 summarises key conclusions of this study on material deformation and wrinkling failures in conventional spinning. Future research trends of sheet metal spinning processes are also outlined.

2. Literature Review

This chapter consists of three main sections which review the published literature of studies on sheet metal spinning. In Section 2.1, three main investigation techniques in the research of metal spinning, i.e. theoretical study, experimental investigation and FE analysis are presented. Section 2.2 outlines research on the material deformation and wrinkling failure mechanics in the sheet metal spinning process. Section 2.3 discusses the effects of four key process parameters on the material deformation and failure of the sheet metal spinning process. The end of this chapter gives a brief summary and discusses the knowledge gap identified.

2.1 Investigation Techniques

In this section, the methodology of theoretical analysis and experimental investigation on the tool forces, strains and material failures of the spinning process are reviewed. Moreover, the key factors in the FE simulation, such as FE solution methods, material constitutive model, element selection, meshing strategy and contact treatment, are discussed in detail.

2.1.1 Theoretical Study

Compared with the limited theoretical studies on the strain and wrinkling failure, most of the research work focuses on the theoretical analysis of tool forces, where eight analytical force models are identified in this literature review. However, all of these analytical force models are developed for the shear forming but not for conventional spinning.

2.1.1.1 Analysis of Tool Forces

In those eight published papers, the deformation energy method has been used to predict the tool forces, i.e. the work done by the external force is assumed to be equal to

the deformation energy of the workpiece. Most of the analytical models developed in 1960s only took the tangential force component into account (Avitzur and Yang, 1960, Kalpakcioglu, 1961a, Sortais et al., 1963). This is because the tangential force consumes most of the power in the spinning, and it is thus significantly important for the design of spinning machines. Researchers (Avitzur and Yang, 1960, Kim et al., 2003, Kobayashi et al., 1961) calculated the tool force based on the assumption that the deformation mode in spinning is a combination of bending and shearing. Moreover, by assuming uniform roller contact pressure, Kobayashi et al. (1961) estimated the radial and axial forces from the projected contact areas. A similar approach has also been employed by Chen et al. (2005a), Kim et al. (2006) and Zhang et al. (2010).

2.1.1.2 Prediction of Strains

By assuming hoop strain to be zero in shear forming and neglecting the thickness strain in conventional spinning on a spherical mandrel, Quigley and Monaghan (2000) proposed a theoretical analytical method to predict the strains using the constancy of volume. The verifying experiment indicated that the theoretical strain results only agreed well in the middle section of workpiece along its radial direction. Beni et al. (2011) also applied this method and compared the theoretical results with their experimental results. The authors reported that the theoretical strain models could not predict the strain values accurately due to unrealistic assumption of zero hoop strain in shear forming and zero thickness strain in conventional spinning.

2.1.1.3 Investigation of Wrinkling Failures

In general there are two methods to analyse the wrinkling failures of engineering problems (Senior, 1956): (1) Equilibrium method, where the differential equations for the system in equilibrium are set up and solved to obtain the critical condition of wrinkling, such as Euler's solution for the buckling of a longitudinally loaded column (Gere, 2001). (2) Energy method, where a deflected form of the part is assumed and the potential energy related to this small deflection is evaluated. When the total energy which tends

to restore the equilibrium is higher than the energy due to forces displacing it, the system remains stable (Senior, 1956). The critical condition of wrinkling is given by equating the two energy values. Until now, very limited theoretical analyses have been reported on the wrinkling failure of metal spinning processes. Reitmann and Kantz (2001) used the equilibrium method to analyse various conditions of buckling. They reported that wrinkling in spinning processes could result from static buckling or dynamic buckling or both ways. By modifying the instability theory of the deep-drawing process (Senior, 1956) and using the energy method, Kobayashi (1963) proposed a theoretical model to determine the critical condition of the flange wrinkling in conventional spinning on a conical mandrel, with spinning ratio and cone angle as variables. Nevertheless, this theoretical model was based on an assumption of neglecting the radial stresses, i.e. one directional beam buckling theory (Chu and Xu, 2001). Therefore, Senior (1956)'s theoretical work may not be accurate in determining the critical condition of wrinkling failure in metal spinning.

2.1.2 Experimental Investigation

Experimental investigation has been applied to analyse the material deformation and failure in the sheet metal spinning process since the 1950s. In this literature review, 39 papers of experimental investigation in sheet metal spinning are included. The methodologies of measuring tool forces, investigating strains and material deformation, and analysing material failures are presented in this section. The statistical experimental design methods that have been used in spinning research are also discussed.

2.1.2.1 Measurement of Tool Forces

Experimental investigations into tool forces have been carried out on both shear forming and conventional spinning. Tool force in the spinning process is normally resolved into three orthogonal components, e.g. axial force - F_a, radial force - F_r and tangential force - F_t. However, the definition of force components in the shear forming study is generally different from that in the conventional spinning study. As shown in Figure 2.1(a), in the

analysis of shear forming, the axial force is normally defined as the force in line with the roller path in shear forming, also termed the feeding force. Radial force is defined as the force normal to the surface of the mandrel. By contrast, as shown in Figure 2.1(b), in the analysis of conventional spinning, the axial force is defined as the force in line with the mandrel's axis and the radial force is defined as the force parallel to the mandrel's radial direction. The definitions of tangential force in both shear forming and conventional spinning are the same, i.e. perpendicular to the axial and radial forces.

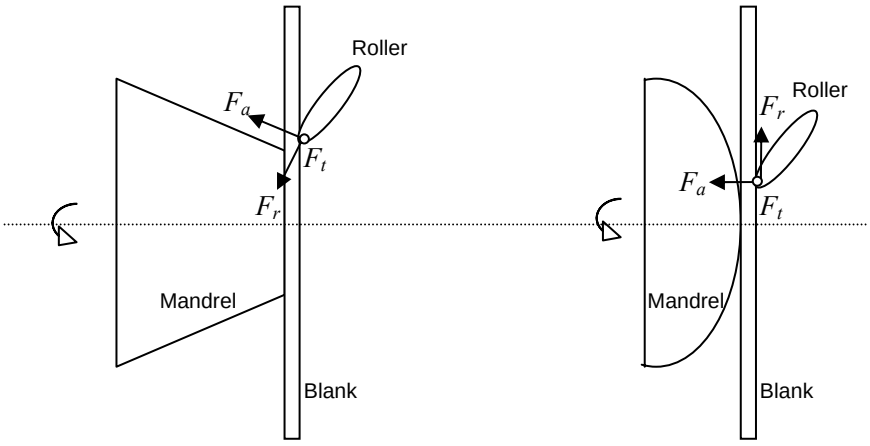

(a) Shear forming (b) Conventional spinning

Figure 2.1 Definitions of tool force components

Piezoelectric force transducers and strain gage sensors are two types of sensor which are commonly used to measure the force (Wilson, 2005). El-Khabeery et al. (1991) and Wang et al. (1989) measured the tool forces by using strain gauges mounted on the shafts supporting the roller. Nevertheless, since the spinning process is a dynamic process, the measurement by using strain gauges may be not able to capture the high frequency of tool force variations (Long et al., 2011). For this reason, many researchers have applied the piezoelectric force transducer to measure the dynamic force histories in the spinning process (Arai, 2006, Chen et al., 2001, Jagger, 2010). Figure 2.2 shows a typical force measurement system in the spinning study. During the spinning process, electrical signals measured from the force transducer are amplified, converted and then recorded by a computer with a data acquisition card and software.

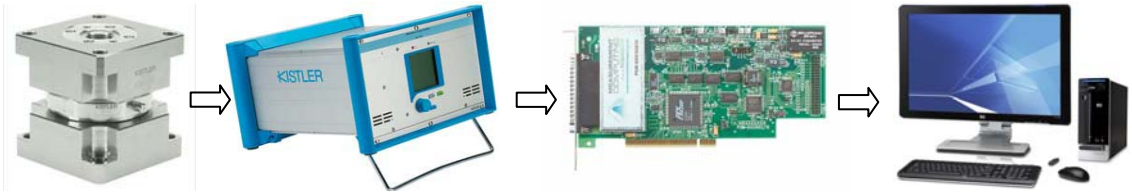

Figure 2.2 Force measurement system, adapted from Jagger (2010)

2.1.2.2 Investigation of Strains and Material Deformation

By using the grid marking method, strain analyses have been carried out on the conventional spinning process (Beni et al., 2011, Quigley and Monaghan, 2000, Razavi et al., 2005) and shear forming process (Shimizu, 2010). A pattern of circles is etched on the blank before forming (Joshi, 2002), as shown in Figure 2.3(a). After deformation the circles are transferred into ellipses with different sizes, which can be measured by optical projectors to obtain accurate strain results. To study the material deformation during the shear forming process, the plugged holes method has been employed by Avitzur et al. (1959). As shown in Figure 2.3(b), holes are drilled and plugged with metal material. After the spinning experiment, the workpeice is cut until the holes are revealed and used to study the material deformation. In addition, Kalpakcioglu (1961a) applied the grid line method to analyse the material deformation during the shear forming process. As illustrated in Figure 2.3(c), a blank is cut in the middle and the grid lines are inscribed on the interface surfaces. The two parts are soldered together to be used in the experiment, after which the two parts are separated by melting the solder. Then the interface surfaces are cleaned and polished to study the material deformation. The application of gird line method has also been extended to the study of deformation mechanics in incremental forming (Jackson and Allwood, 2009).

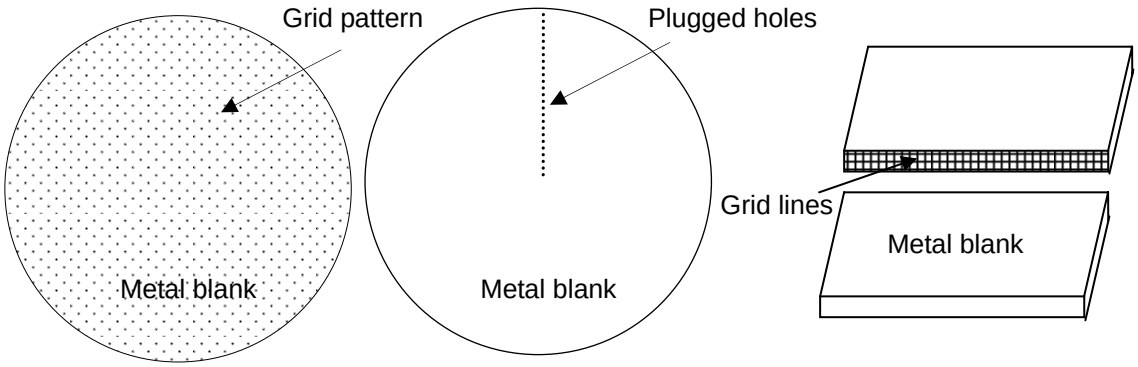

(a) Grid marking method (b) Plugged holes method (c) Grid line method

Figure 2.3 Methods for studying strains and material deformation

2.1.2.3 Study of Material Failures

Both wrinkling and cracking failures in the sheet metal spinning process have been studied through experiments. However, most of the experimental investigations on material failures focus on shear forming rather than conventional spinning. The early failure studies in shear forming have been carried out by investigating the spinnability (Kalpakcioglu, 1961b). Kegg (1961) defined it as the ability of metal to undergo shear forming deformation without fracture. In order to predict the fracture in shear forming, Kegg (1961) carried out a series of spinnability tests of various materials on a half ellipsoidal mandrel. Moreover, the author proposed a method to predict the spinnability of a given material, by correlating the maximum thickness reduction of the blank in the spinning with the reduction of area at fracture of the test sample in the tensile test. Hayama and Tago (1968) claimed that Kegg (1961)'s experimental results based on the half ellipsoidal mandrel may not be valid in the case with the conical mandrel. Hayama and Tago (1968) also expanded the term of spinnability as the ability of a sheet metal to undergo deformation by spinning without the wrinkles in the flange and no fractures on the wall. Furthermore, they divided the cracks into three types and analysed the cause of each type of crack. Most recently, Kawai et al. (2007) carried out spinnability studies of "die-less" shear forming on both conical and hemispherical parts by using a cylindrical mandrel for general purposes.

In order to study the deformation modes and wrinkling failure, Hayama et al. (1966)

measured the radial and circumferential strains as well as the periodic variations of curvatures on the flange, by attaching strain gauges on both sides of the flange before spinning. In a later study, Hayama (1981) used the sudden change of the vibration of the axial force (feeding force) to determine the exact moment when the wrinkling occurs in the shear forming. By applying a laser range sensor to monitor the height of the flange of the rotating workpiece, Arai (2003) experimentally measured the development of the wrinkles at different stages of forming. Based on a one-pass deep drawing conventional spinning experiment, Xia et al. (2005) carried out spinnability studies on blanks made by aluminium and mild steel. Kleiner et al. (2002) experimentally monitored the development of wrinkling failures in the first pass of a conventional spinning process. The authors divided the propagation of wrinkles into five stages: onset of wrinkling, expansion of wrinkling, first complete circle, increasing amplitude, and collapse of wrinkles, as shown in Figure 2.4.

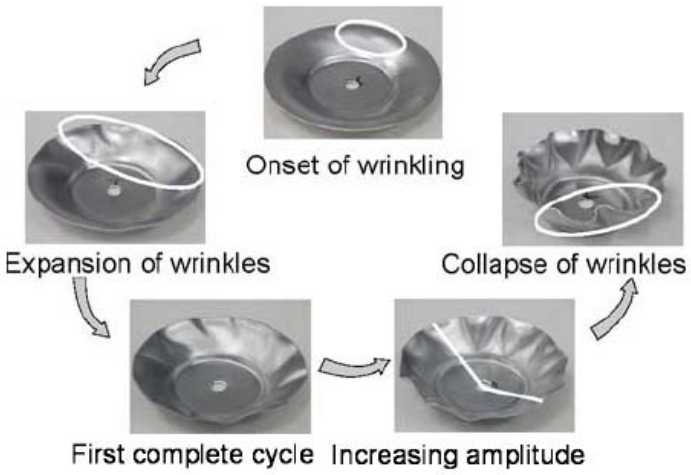

Figure 2.4 Propagation of wrinkles in spinning (Kleiner et al., 2002)

2.1.2.4 Design of Experiments

Early experimental studies (Hayama et al., 1965, Wang et al., 1989) focused on the effects of each process parameter (factor) on the spinning process, by varying a single factor while keeping other factors constant, i.e. the One-Factor-at-a-Time (OFAT) method. The major disadvantage of OFAT method is that the interactions between

different factors cannot be evaluated (Montgomery, 2009). For this reason, Design of Experiment (DoE) methods, in which several factors are varied simultaneously, have been employed to analyse the effects of process parameters on the dimensional variations of spun parts (Auer et al., 2004, Henkenjohann et al., 2005, Kleiner et al., 2005). Response surface methodology (RSM) has also been applied in the experimental investigations of tool forces and surface finish (Chen et al., 2001, Chen et al., 2005b, Jagger, 2010) in the sheet metal spinning process. RSM is a collection of mathematical and statistical techniques for establishing relations among various process parameters and optimising the response (Montgomery, 2009). It uses regression analysis to fit an equation to correlate the response with the process parameters.

2.1.3 Finite Element Analysis

Since the 1990s, FE analysis of sheet metal spinning process has seen significant development. In this section, 31 papers on FE analysis of spinning have been reviewed. Due to the nature of incremental forming, in the early studies, to reduce the computing time, certain simplifications had to be made. For instance, 2-D FE models (Alberti et al., 1989, Liu et al., 2002) or simplified 3-D FE models with axisymmetric modeling were used where the roller was approximated as a virtual ringed tool with variable diameters (Mori and Nonaka, 2005). More recently, with the development of computing hardware, 3-D FE models have been commonly applied to study the material deformation and failure mechanics in the spinning process. In this section, five key factors of the FE simulation are discussed, i.e. the FE solution method, material constitutive model, element selection, meshing strategy, and contact treatment.

2.1.3.1 Finite Element Solution Methods

Finite Element solution methods are generally resolved into the implicit method and the explicit method (Harewood and McHugh, 2007). The implicit FE analysis method iterates to find the approximate static equilibrium at the end of each load increment. It

controls the increment by a convergence criterion throughout the simulation. Because of the complex contact conditions and high non-linearity in the metal forming problems, a large number of iterations have to be carried out before finding the equilibrium; the global stiffness matrix thus has to be assembled and inverted many times during the analysis. Therefore, the computation is extremely expensive and memory requirements are also very high (Tekkaya, 2000). Additionally, the implicit method is unable to carry on the analysis if shape defects, e.g. wrinkling, occur in the sheet metal simulation (Alberti and Fratini, 2004). It is difficult to predict how long it will take to solve the problem or even if convergence can be achieved (Harewood and McHugh, 2007). Thus the implicit method is preferable to analyse some small 2-D problems and 3-D problems under simple loading conditions, for instance, modelling the springback after spinning (Bai et al., 2008, Zhan et al., 2008). On the other hand, the explicit FE analysis method determines a solution by advancing the kinematic state from one time increment to the next, without iteration. The explicit solution method uses a diagonal mass matrix to solve for the accelerations and there are no convergence checks. Therefore it is more robust and efficient for complicated problems, such as dynamic events, nonlinear behaviors, and complex contact conditions. Hence the explicit FE analysis method has been chosen by most researchers to analyse the metal spinning process.

2.1.3.2 Material Constitutive Model

The most commonly used yield criterion in engineering application, particularly for computational analysis, is von Mises criterion (Dunne and Petrinic, 2005). Figure 2.5 (a) shows the von Mises yield surface of isotropic hardening in 2-D space of principal stresses (σ_1, σ_2). In the isotropic material hardening, if the load is reversed at the load point (1), the material behaves elastically until reaching the load point (2), which is still on the yield surface. Any stress increase beyond this point will lead to plastic deformation. Clearly, the isotropic hardening leads to a very large elastic region in the reversed loading process. However, in reality, a much smaller elastic region is expected in the reversed loading process. This phenomenon is called the Bauschinger effect (also known as work softening), i.e. when a metal material is subjected to tension into

the plastic range, after the load is released and compression is applied, the yield stress in the compression is lower than that in the tension (Kalpakjian and Schmid, 2001). Kinematic hardening model takes the Bauschinger effect into account, where the yield surface translates in the stress space rather than expanding, as shown in Figure 2.5(b). During the spinning process, the roller induces constant tensile and compressive loadings on the workpiece. Hence, Klimmek et al. (2002) and Pell (2009) suggested that the Bauschinger effect should not be neglected in the FE simulation of spinning. However, due to the lack of specific material test data, none of those researchers have considered the Bauschinger effect.

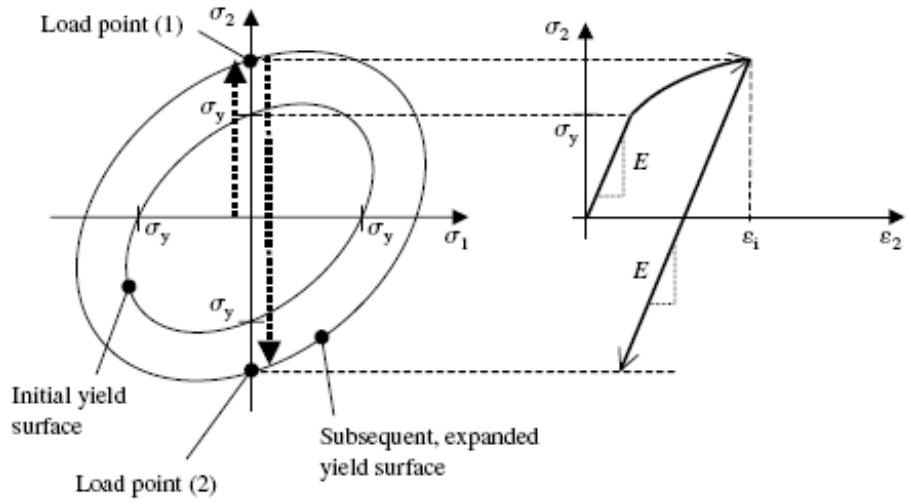

(a) Isotropic hardening

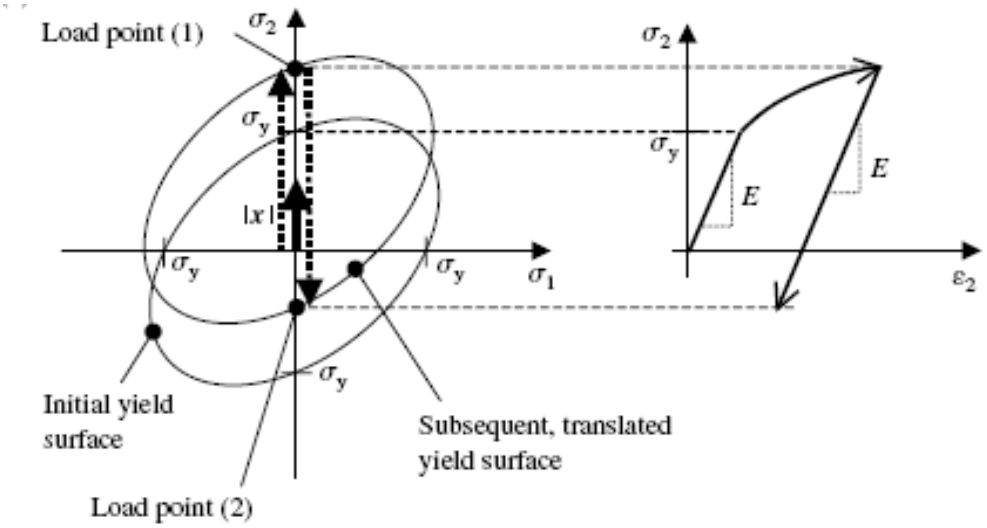

(b) Kinematic hardening

Figure 2.5 Material hardening models (Dunne and Petrinic, 2005)

2.1.3.3 Element Selection

The accuracy of any FE simulation is highly dependent on the type of element used in the simulation. Solid elements and shell elements are two types of the most commonly used elements in metal spinning simulation. Quigley and Monaghan (2002a) suggested that 8 noded hexahedral solid elements should be used, because a blank modelled by 2-D shell elements may not be able to handle the contact with the roller and mandrel at the same time. To solve this problem, Zhao et al. (2007) applied an offset of one-half of the blank thickness from the middle plane to both sides of the 2-D shell element. By comparing FE results obtained from solid and shell elements, Hamilton and Long (2008) concluded that wrinkling failure may be exaggerated if using shell elements. Most recently, Long et al. (2011) reported that the use of continuum shell elements produced axial force and thickness results which were in good agreement with the experiment. The FE models using solid elements produced considerably different tool force results in comparison with the experimentally measured axial and radial force values.

During the metal spinning process, the material undergoes a complicated loading process that includes bending effects (Sebastiani et al., 2007), which may cause the “hourglassing” problem as a result of using reduced integration linear solid elements. As shown in Figure 2.6, the bending of a reduced integration linear solid element presents a zero-energy deformation mode, as no strain energy is generated by the element distortion (Abaqus analysis user’s manual, 2008). Moreover, this “hourglassing” problem can propagate through the elements and produce meaningless numerical results. On the other hand, unlike the reduced integration linear solid element, which only uses one integration point along the thickness direction, multiple integration points are used through the thickness of a reduced integration linear shell element. Stresses and strains at each integration point of the shell element are calculated independently. This may be the reason why reduced integration linear shell elements can produce more accurate results of wrinkling (Wang et al., 2011) and tool forces (Long et al., 2011) than reduced integration linear solid elements.

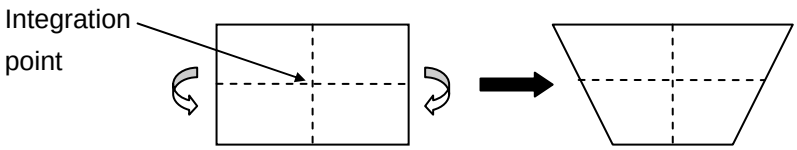

Figure 2.6 Deformation of a reduced integration linear solid element subjected to bending

2.1.3.4 Meshing Strategy

Various researchers have employed different meshing strategies, which affect the accuracy and efficiency of FE simulation in spinning. Four commonly used meshing strategies, as shown in Figure 2.7, are discussed in this section. The structured meshing technique (Mesh A) and the free meshing technique (Mesh C) solve the problem where triangular prism elements have to be used in the centre of the circular blank. However, the irregular mesh in Mesh A and C may result in local stress peaks due to an inhomogeneous mass distribution in the rotating blank (Sebastiani et al., 2006). In order to achieve a regular mesh, the central area of the blank which is clamped and does not undergo deformation, is neglected in Mesh B and Mesh D. Numerous researchers have used the sweep meshing technique shown in Mesh B (e.g. Quigley and Monaghan, 1999, Zhan et al., 2007). Correlations have been achieved between FE analysis and experimental results by using Mesh B (Awiszus and Härtel, 2011, Wang et al., 2011). However, Sebastiani et al. (2006) suggested that the small element size around the inner region may limit the increment size of the FE explicit solution method and thus decrease the computing efficiency. They proposed a meshing strategy - Mesh D which provides a solution to this problem by using more element seeds along the outer circle of the blank, while using less seeds along the inside circle. Nevertheless, triangular prism elements have to be applied to connect the inner region and outer region of the blank. Because of its constant bending and membrane strain approximations, high mesh density of triangular prism elements is generally required to accurately capture the bending deformation and the solution involves high strain gradients (Abaqus analysis user's manual, 2008).

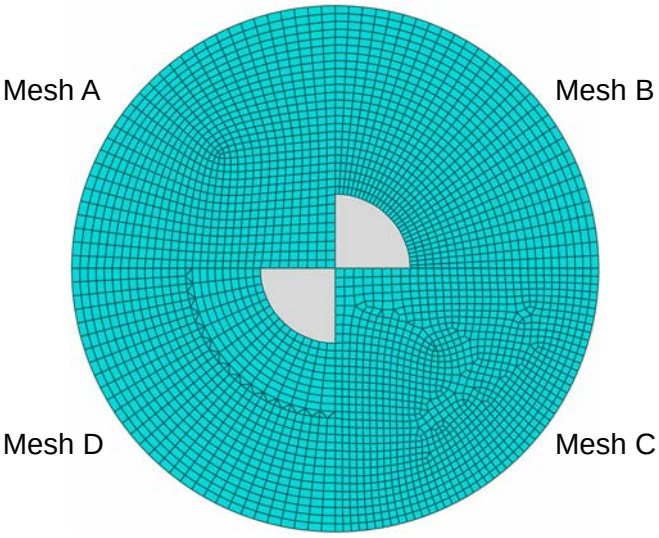

Figure 2.7 Mesh strategy, adapted from Sebastiani et al. (2006)

2.1.3.5 Contact Treatment

During the spinning process, the contact between the roller and blank is dynamic and complex. The penalty contact method has been applied to model the contact in the normal direction between the tool and blank surfaces. It has been shown to provide good results in the FE simulations of metal spinning (Bai et al., 2008, Liu, 2007, Zhao et al., 2007). Contact forces, which are calculated as the penetration distance multiplies the penalty stiffness, are applied to the slave nodes to oppose the penetration (Abaqus analysis user's manual, 2008). At the same time, reaction forces act opposite on the master surface at the penetration point.

The contact between roller and blank represents both the sliding and the rolling frictional behaviour (Bai et al., 2008). In the early spinning simulation studies, the rotation of the roller is simplified by neglecting the friction between the roller and the blank (Quigley and Monaghan, 2002a, Sebastiani et al., 2006, Zhao et al., 2007). However, this simplification cannot represent the actual spinning process, where the friction force makes the roller rotate along its axis. Consequently, many researchers such as Liu (2007), Wang and Long (2011c), and Zhan et al. (2008) assumed a small Coulomb frictional coefficient (0.01-0.05) between the roller and the blank.

2.2 Material Deformation and Wrinkling Failure

In this section, published literature regarding the tool forces, stresses and strains, and wrinkling failures in both shear forming process and conventional spinning process are reviewed. Analysing tool forces in the sheet metal spinning process is important to select process parameters, design spinning machines, and improve the quality of spun products (Wang et al., 1989). Moreover, investigating stresses, strains and material failures is essential to understand the deformation and failure mechanics and thus optimise the process design.

2.2.1 Tool forces

Until now, tool forces in shear forming, one-pass deep drawing conventional spinning, and multi-pass conventional spinning processes have been investigated intensively. Among the three force components generated in shear forming, as defined in Figure 2.1(a), the radial force is the highest, because the roller squeezes the material onto the mandrel during the whole process. The axial force ranks the second and the tangential force is the smallest (Arai, 2003, Hayama et al., 1965, Zhan et al., 2007). As reported in an experimental investigation of shear forming (Lee and Noble, 1982), both axial force and radial force decrease when increasing the angle between the roller axis and mandrel axis from 0° to approximately 60° with a slight increase thereafter. The tool forces would also decrease if a thinner blank were used (Chen et al., 2001, Hayama et al., 1965).

According to the experimental investigations of one-pass deep drawing conventional spinning (Hayama and Murota, 1963, Jurkovic et al., 2006, Xia et al., 2005), the peak values of the axial force are obtained at the middle stage of spinning. On the other hand, the maximum values of the radial force occur at the end of the process. The tangential force is again the smallest force among these three force components and it remains almost constant during the one-pass deep drawing spinning process.

Tool forces of the multi-pass conventional spinning process have been experimentally

investigated (Jagger, 2010, Wang et al., 1989) and analysed by FE simulation (Essa and Hartley, 2009, Liu, 2007, Pell, 2009). It has been reported that in the conventional spinning process, among three force components as defined in Figure 2.1(b), the axial force is the largest, while the tangential force is the lowest. In a 3-pass conventional spinning experiment, Wang et al. (1989) reported that when the thickness of the blank increases, tool forces increase accordingly. Wang et al. (1989) also gave an approximately proportional relationship among the peak values of the force components, where

$$F_a : F_r : F_t = 20 : 10 : 1 \quad (2)$$

The maximum force ratios obtained in an experiment (Jagger, 2010) and FE simulation (Wang and Long, 2011b) of 3-pass conventional spinning processes show a similar trend, as illustrated in equation (3) and (4), respectively.

$$F_a : F_r : F_t = 17 : 5 : 1 \quad (3)$$

$$F_a : F_r : F_t = 35 : 17 : 1 \quad (4)$$

Recently, Wang and Long (2011a) numerically compared the force histories when the workpieces were made of three material types in a multi-pass conventional spinning process. The authors reported that a FE model using stainless steel produced the highest tool forces, followed by a model using mild steel, while the lowest tool forces were obtained in a model using aluminium. Wang and Long (2011a) also compared the maximum tool forces of a wrinkle-free model and a wrinkling model; the tool forces in the wrinkle-free models were approximately one third of the corresponding forces in the wrinkling models.

2.2.2 Stresses

Klimmek et al. (2002) suggested that investigating the stress distribution of the workpiece, especially within the local forming zone, is essential to understand the cause of the wrinkling failure. The authors investigated the stress variations of two distinct elements during a forward roller pass. The first element is close to the centre of the blank, while the second element is located at the rim of the blank. They reported that

once the first element gets into the local forming zone, the tensile radial stress steadily increases to a maximum value. By contrast, as the roller gets to the edge of the blank, the compressive tangential stress of the second element increases dramatically. Sebastiani et al. (2007) developed a spinning model which uses three linear roller passes, including both forward passes and backward passes. The authors report that local radial bending effects exist in the workpiece during a forward pass, where the inner surface (mandrel facing) of the workpiece is subjected to compressive radial stresses while its outer surface (roller facing) is under tensile radial stresses, as also observed by Pell (2009) and Wang and Long (2010). Moreover, after a backward roller pass, a toothed stress pattern in the flange region has been observed by Sebastiani et al. (2007), who believe that it may be the pre-state of the wrinkling failure. A similar toothed stress pattern has also been noticed during a non-linear backward pass by Wang and Long (2011b). However, no correlations have been found between the toothed stress pattern and wrinkling failure.

2.2.3 Strains

Theoretically, in the conventional spinning process, the compressive hoop strain should balance the tensile radial strain. The thickness strain thus remains zero. However, in an experimental investigation of a one-pass deep drawing conventional spinning process (Hayama and Murota, 1963), tensile radial and hoop strains resulting in compressive thickness strains, have been observed at the bottom of a spun part. However, in the opening of a spun part, the unbalanced compressive hoop strains and tensile radial strains lead to a certain amount of tensile thickness strains. Thinning at the bottom and thickening in the opening of the spun parts in one-pass deep drawing conventional spinning have also been reported by Hamilton and Long (2008) and Xia et al. (2005).

The experimental results of the multi-pass conventional spinning on the spherical mandrel (Beni et al., 2011, Quigley and Monaghan, 2000, Razavi et al., 2005) show that the tensile radial strain and compressive hoop strain do not mirror each other, thus indicating that a certain amount of thickness strain exists in the workpiece, as confirmed

in the FE simulations by Wang and Long (2011b). In addition, Quigley and Monaghan (2000) reported that there was a certain degree of shear forming involved in the first roller pass of conventional spinning.

In the shear forming process, considerably high tensile radial strain and compressive thickness strain have been observed by Shimizu (2010), who experimentally investigated the strain distributions along the radial direction of the workpiece. By contrast, tangential strain keeps almost constant, only a slightly increase is observed in the opening of the spun part. Bending strains have been measured by strain gauges that mounted on both sides of the workpiece (Hayama et al., 1966), where bending and unbending are performed repeatedly in the local forming zone of the shear forming.

2.2.4 Wrinkling Failure

It is believed that in sheet metal spinning wrinkling takes place when the tangential compressive stress in the flange exceeds the buckling stability limit (Kleiner et al., 2002, Klimmek et al., 2002, Runge, 1994). However, it is still unknown how to determine the buckling limit which could be used to predict and prevent wrinkling failure. Kleiner et al. (2002) suggested that the wrinkling in the spinning process is not only caused by static buckling, but also influenced or even triggered by the dynamic effects from the feeding of roller and rotation of the workpiece.

The experimental results of Kleiner et al. (2002) indicate that the diameter and thickness have the most significant effects on wrinkling failure, followed by the feed rate, the spindle speed, the roller path and the material of the workpiece. Hayama et al. (1966) also reported that the feed ratio, blank thickness and blank diameter are very important contributing factors to wrinkling failure. Hayama (1981) suggested that the feed ratio is the most important parameter affecting spinnability. In general, wrinkles tend to occur when increasing the feed ratio and blank diameter or decreasing the blank thickness (Hayama et al., 1966, Kleiner et al., 2002, Xia et al., 2005).

Satoh and Yanagimoto (1982) reported that wrinkling resistance would be enhanced if a material with higher yielding stress was used, as they believe wrinkling occurs due to elastic buckling. Wang and Long (2011a) proposed that there may be a limit to the roller feed depth, beyond which wrinkling failures may take place. Furthermore, both Kawai and Hayama (1987) and Wang et al. (2011) reported that wrinkles may be smoothed out in subsequent passes of conventional spinning processes. Although several investigations have been conducted on the wrinkling failure of metal spinning, further investigation is still required to gain an in-depth understanding of wrinkling failure mechanics, the effects of process parameters, and to predict and prevent wrinkling failures.

2.3 Key Process Parameters

The process parameters play a decisive role in the design and optimisation of sheet metal spinning process. The effects of four key process parameters, i.e. feed ratio, roller path (passes), roller profile, and clearance between roller and mandrel, on the material deformation and failures of the spun parts are discussed in this section.

2.3.1 Feed Ratio

Feed ratio is defined as the ratio of the roller feed rate to the spindle speed. As long as the feed ratio remains constant, by changing the feed rate and the spindle speed proportionally, there would be no significant effects on the tool forces (Hayama et al., 1965, Jagger, 2010, Lee and Noble, 1982, Wang et al., 2011, Wang et al., 1989, Xia et al., 2005), wall thickness (Xia et al., 2005, Zhan et al., 2008), wrinkling failures (Hayama et al., 1966, Wang et al., 2011), cracking failures (Hayama and Tago, 1968) and surface finish (Ma et al., 2010) of the spun part.

Nevertheless, it has been reported that variation of feed ratio has considerable effects on the tool force, wall thickness, spinnability, surface finish and springback of the metal spinning process. When a higher feed ratio is applied, tool forces will increase

accordingly (El-Khabeery et al., 1991, Essa and Hartley, 2009, Hayama et al., 1965, Jagger, 2010, Liu, 2007, Ozer and Arai, 2009, Pell, 2009, Perez et al., 1984, Xia et al., 2005, Zhan et al., 2007). In addition, material failures tend to take place if a high feed ratio is used (Hayama, 1981, Hayama et al., 1966, Kawai et al., 2007, Ozer and Arai, 2009, Wang et al., 2011, Xia et al., 2005, Zhan et al., 2007).

On the other hand, Wong et al. (2003) suggested that a low feed ratio would result in excessive material flow in the outward direction, which unduly thins the blank, as Pell (2009), Wang et al. (2011) and Zhan et al. (2007) also reported. However, a lower feed ratio would result in a better surface finish of the spun part (Chen et al., 2001, El-Khabeery et al., 1991, Kleiner et al., 2005, Ma et al., 2010, Slater, 1979a, Wang et al., 2011, Slater, 1979a). Both El-Khabeery et al. (1991) and Essa and Hartley (2010) reported that springback would increase when a higher feed ratio is used.

2.3.2 Roller Path and Passes

By using multiple roller passes in conventional spinning, the tensile radial and compressive tangential stresses are induced gradually; hence material failures can be prevented (Runge, 1994, Sebastiani et al., 2007). Up to now, most investigations of roller path and passes in conventional spinning have focused on single pass or multi-pass with no more than 3 passes (mainly linear path). Consequently, there is still a huge knowledge gap between academic research and industrial production, where a considerable amount of roller passes have to be used to successfully produce complicated spinning parts (Filip and Neago, 2010). Three types of the roller path shown in Figure 2.8, straight line, concave curve and convex curve, have been experimentally studied by Kang et al. (1999) and Hayama et al. (1970). The difference between these two experiments was that only the single pass was studied by Kang et al.; whereas multiple passes were investigated by Hayama et al. Kang et al. (1999) concluded that the first pass in the conventional spinning plays a decisive role in the final blank thickness. After comparing four different types of roller path designs, Hayama et al. (1970) proposed that the involute curve path, which is a special type of concave

curve, gives the highest spinning ratio without material failures. This was supported by Liu et al. (2002), who numerically analysed the distributions of stresses and strains obtained from three different roller paths, i.e. straight line, involute curve and quadratic curve. Their FE analysis results illustrate that the stresses and strains obtained under the involute roller path are the smallest. Furthermore, Kawai and Hayama (1987) applied an involute curve in each pass in their experiments and studied the first pass and the remaining passes separately. They suggested that the angle of the first pass plays a dominant role in the generation of wrinkles and cracks.

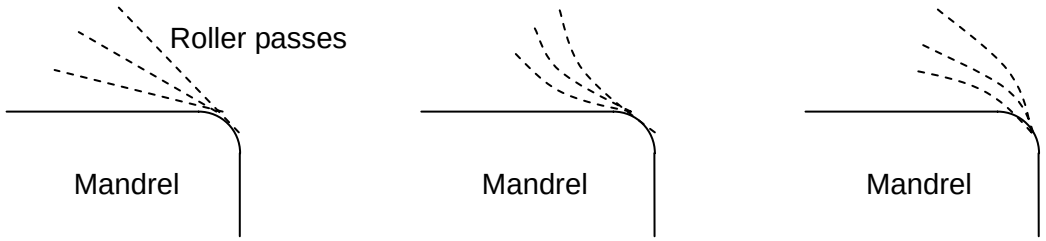

(a) Linear path (b) Concave path (c) Convex path

Figure 2.8 Various roller path profiles

2.3.3 Roller Profile

Figure 2.9 shows examples of various shapes of spinning roller (Avitzur et al., 1959). Roller diameter and nose radius are two key parameters that have been investigated by a few researchers. According to the literature review by Wong et al. (2003), the roller diameter has little effect on the final product quality, but a small roller nose radius would result in poor thickness uniformity. This is supported by El-Khabeery et al. (1991), who reported that an increase in roller nose radius would lead to a smaller reduction of wall thickness. Younger (1979) claimed that increasing the roller nose radius resulted in a decline of the axial force and had almost no effects on the variations of tangential force in a shear forming experiment. Both Essa and Hartley (2010) and El-Khabeery et al. (1991) pointed out that as the roller nose radius decreased, tool forces would go down accordingly in one-pass deep drawing conventional spinning. In a multi-pass conventional spinning experiment, Wang et al. (1989) also reported that all of the three

tool force components decrease when applying a smaller roller nose radius. According to an experimental wrinkling study in the shear forming, Hayama et al (1966) reported that the roller nose radius had little effects on the wrinkling failures in the shear forming process. Chen et al. (2001), El-Khabeery et al. (1991) and Kleiner et al. (2005) pointed out that increasing the roller nose radius would improve the surface finish of the spun part. Chen et al. (2001) suggested that a larger roller nose radius resulted in a larger contact area between roller and blank, thus producing a smoother material deformation.

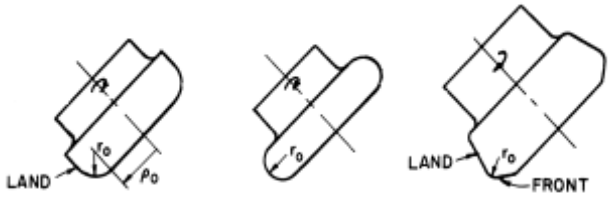

Figure 2.9 Various shapes of roller (Avitzur et al., 1959)

2.3.4 Clearance between Roller and Mandrel

In the single pass conventional spinning and shear forming process, the parts are spun within one pass, where the roller forms the workpiece onto the mandrel with a specified clearance. Therefore, the clearance between roller and mandrel is one of the key parameters in those processes. In the one-pass deep drawing conventional spinning process, radial and axial tool forces increase when the clearance decreases (Xia et al., 2005). This is because a smaller clearance would result in more thinning of the workpiece; thus the severe material deformation leads to high tool forces. According to Essa and Hartley (2010), if the clearance is smaller than the initial wall thickness, material builds up in front of the roller and causes wrinkles. Conversely, if the clearance is larger than the initial wall thickness, material escapes beneath the roller, resulting in dimensional inaccuracy.

As shown in Figure 2.10, in the shear forming process, the flange keeps straight when the clearance is equal to the theoretical value defined by the sine law ($t_0 \cdot \sin\alpha$)

(Hayama et al., 1965). This may be because that when the sine law is closely followed, stresses are confined within the zone under the roller and thus the flange remains virtually stress-free. However, when the clearance is smaller than the theoretical value ($t_1 < t_0 \cdot \sin\alpha$, over-spinning), the material builds up in front of the roller; the flange is bent forward and away from the roller. Conversely, when the clearance is larger than the theoretical value ($t_1 > t_0 \cdot \sin\alpha$, under-spinning), the material in the flange will be pulled inward, bending the flange towards the roller and potentially causing wrinkles. These findings are also reported by Lu et al. (2006), Slater (1979b) and Zhan et al. (2007).

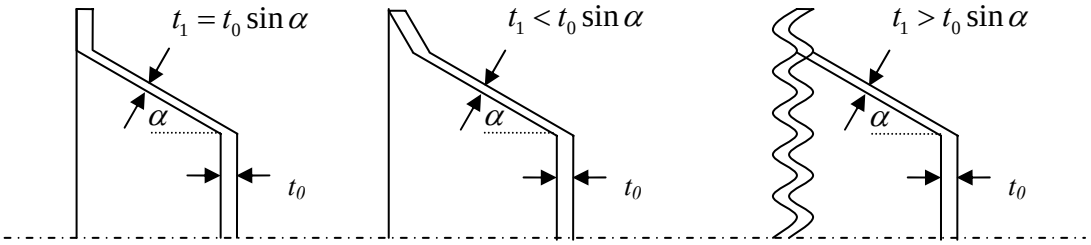

(a) True shear forming (b) Over-spinning (c) Under-spinning

Figure 2.10 Deviation from sine law in shear forming, adapted from Music et al. (2010)

2.4 Summary

In this chapter, published research regarding the investigation techniques, material deformation, wrinkling failure, and key process parameters of the sheet metal spinning process have been reviewed. Two major knowledge gaps have been identified: (1) Most research focus on shear forming rather than conventional spinning. Additionally, current studies in conventional spinning are limited to single-pass spinning or multi-pass spinning with linear path. Thus it is essential to investigate material deformation mechanics of multi-pass conventional spinning with non-linear path design. (2) The cause of wrinkling failures in the sheet metal spinning process is only partially understood. Moreover, it is also worth investigating how to determine the critical condition of wrinkling failure in order to predict and prevent it from occurring.

3. Fundamentals of Finite Element Method

The Finite Element Method (FEM) is a numerical method seeking an approximated solution of a complex engineering problem which is difficult to obtain analytically. It is realised by dividing the complicated analysis body into a finite number of elements. The behaviour of each element, which is in regular shape, may be predicted by certain mathematical equations. The summation of the individual element behaviours produces the expected behaviour of the whole analysis body. FEM was originally developed for solving complex elasticity and structural analysis problems in civil and aeronautical engineering in 1940s. By the early 70s, applications of FEM were limited in aeronautics, automotive, defence and nuclear industries, executed on expensive mainframe computers. Over the past decades, due to the rapid developing of computing capability, FEM has been widely used for analysing the problems involving solid mechanics, fluid mechanics, heat transfer, vibrations, electrical and magnetic fields, etc. The most common applications of FEM in industry are to design new products and processes, optimise existing products and processes so as to improve their performance. In this chapter, the fundamentals of Finite Element method, such as, Hamilton's Principle, the basic analysis procedure of FEM, and four types of finite elements are discussed in detail. Furthermore, the non-linear solution method, material constitutive model and contact algorithm are briefly outlined.

3.1 Hamilton's Principle

To obtain a solution of any solid mechanics FE problems, it is essential to satisfy the requirements of equilibrium, compatibility, constitutive equations and boundary conditions. However, obtaining the exact solution (known as strong form) of the equilibrium is usually extremely difficult for practical engineering problems. Instead, a weak form of equilibrium for the body as a whole is imposed even though it does not ensure pointwise equilibrium (Dunne and Petrinic, 2005). Hamilton's Principal, resulting from the Conservation of Energy, is one of the most commonly used weak form of

equilibrium in FEM. It states that the variation of the kinetic and strain energy plus the variation of the work done by external forces acting during any time interval from t_1 to t_2 must be zero. Mathematically, Hamilton's Principle states (Liu and Quek, 2003):

$$\delta \int_{t_1}^{t_2} L dt = 0 \tag{5}$$

The Lagrangian functional, L, is defined as

$$L = T - \Pi + W_f \tag{6}$$

where T is the kinetic energy, Π is the strain energy and W_f is the work done by external forces. These components of the Lagrangian functional can be expressed as follows

$$T = \frac{1}{2} \int \rho \dot{\mathrm{U}}^T \dot{\mathrm{U}} \mathrm{d}V \tag{7}$$

where ρ is the density and $\dot{\mathrm{U}}$ is the velocity.

$$\Pi = \frac{1}{2} \int \varepsilon^T \sigma \mathrm{d}V = \frac{1}{2} \int \varepsilon^T \mathrm{D} \varepsilon \mathrm{d}V \tag{8}$$

where ε and σ represent the strain and stress vectors, respectively; D the is matrix of material constants and will be discussed in Section 3.3.

$$W_f = \int \mathrm{U}^T \mathrm{f}_b \mathrm{d}V + \int \mathrm{U}^T \mathrm{f}_s \mathrm{d}S_f \tag{9}$$

where U is the displacement vector, the body force vector is expressed as $\mathrm{f_b}$ and surface force vector is defined as $\mathrm{f_s}$. S_f and V represent the domains of area and volume, respectively.

3.2 Basic Analysis Procedure of FEM

The solution process of general continuum problems normally follows a step-by-step procedure. In this section, the basic procedure of FEM is briefly summarised.

3.2.1 Domain Discretisation

The analysed body is represented as an assembly of subdivisions known as finite elements. This procedure is called meshing, which is usually carried out by using so called pre-processors. It is especially useful for meshing complicated geometries, such

as the example shown in Figure 3.1, where a cargo train body is meshed with thousands of finite elements. The elements are considered to be interconnected at specified joints called nodes. The selection of the type, number and size of finite elements are decided based on the characteristic of the analysed problem.

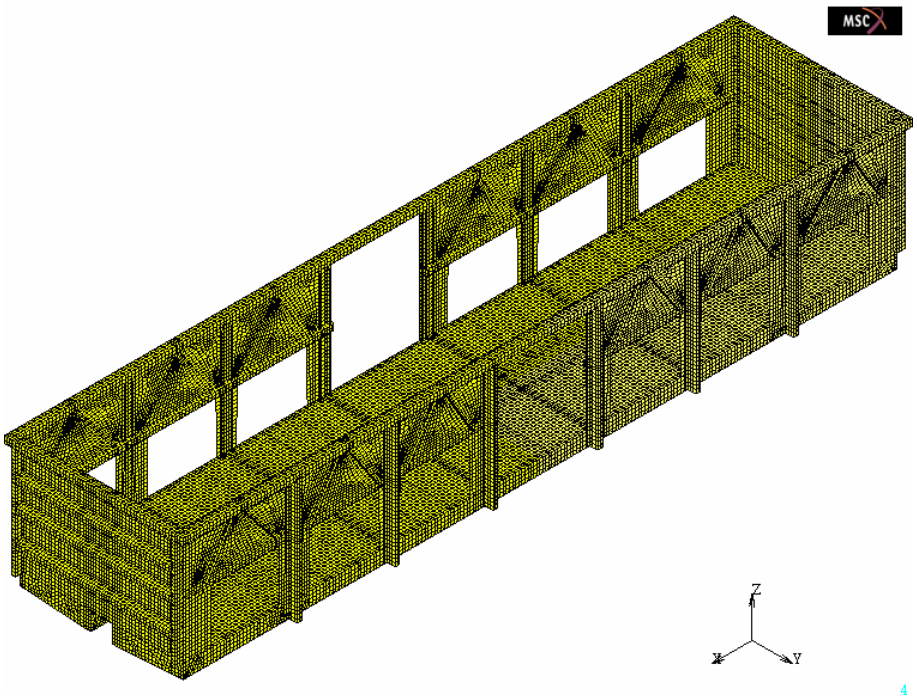

Figure 3.1 Finite Element Meshing (Wang, 2005)

3.2.2 Displacement Interpolation

Because the displacement solution in a complex structure under specified loading conditions cannot be predicted exactly, in FEM the displacement within an element is simply assumed by polynomial interpolation using the displacements at its nodes (Liu and Quek, 2003):

$$\mathrm{U}(x,y,z)=\sum_{i=1}^{n_d}\mathrm{N}_i(x,y,z)\mathrm{d}_i=\mathrm{N}(x,y,z)\mathrm{d}_e \tag{10}$$

where n_d is the number of nodes forming the element; d_i is the nodal displacement at the i th node and can be expressed in a general form of

$$\mathrm{d}_i = \begin{Bmatrix} d_1 \\ d_2 \\ \vdots \\ d_{n_f} \end{Bmatrix} \tag{11}$$

where n_f is the number of Degree Of Freedom (DOF) at a node.

The vector d_e in equation (10) represents the displacement vector of the entire element and it has the form of

$$\mathrm{d}_\mathrm{e} = \begin{Bmatrix} \mathrm{d}_1 \\ \mathrm{d}_2 \\ \vdots \\ \mathrm{d}_{n_d} \end{Bmatrix} \tag{12}$$

Thus the total DOF of the entire element is $n_d \times n_f$.

In equation (10), N is the matrix defining shape functions for the nodes in an element. It is predefined to assume the variations of displacement with respect to the coordinates of the element.

$$\mathrm{N}(x,y,z) = [\mathrm{N}_1(x,y,z) \quad \mathrm{N}_2(x,y,z) \quad \ldots \quad \mathrm{N}_{n_d}(x,y,z)] \tag{13}$$

where N_i is a sub-matrix of the shape functions for displacement components, which is arranged as

$$\mathrm{N}_i = \begin{bmatrix} N_{i1} & 0 & 0 & 0 \\ 0 & N_{i2} & 0 & 0 \\ 0 & 0 & \ddots & 0 \\ 0 & 0 & 0 & N_{in_f} \end{bmatrix} \tag{14}$$

where N_{ik} is the shape function for the kth displacement component (DOF) at the i th node.

3.2.3 Construction of Shape Function

For an element with n_d nodes at space coordinates x_i (i = 1, 2,....,n_d), where x^T = {x} for one-dimensional problems, x^T = {x, y} for 2-D problems, and x^T = {x, y, z} for 3-D problems, its displacement component u is approximated as (Liu and Quek, 2003)

$$u(\mathrm{x}) = \sum_{i=1}^{n_d} p_i(\mathrm{x})\alpha_i = \mathrm{p}^T(\mathrm{x})\alpha \tag{15}$$

in which $p_i(\mathrm{x})$ is the basic function of monomials and α is the coefficient for the monomial $p_i(\mathrm{x})$. Vector α is defined as

$$\alpha^T = \{\alpha_1, \alpha_2, \alpha_3, \ldots, \alpha_{n_d}\} \tag{16}$$

A basic of complete order of $p_i(\mathrm{x})$ in the one-dimensional problem can be written as

$$\mathrm{p}^T(x) = \{1, x, x^2, x^3, x^4, \ldots, x^p\} \tag{17}$$

$p_i(\mathrm{x})$ in the 2-D problem has the form

$$\mathrm{p}^T(\mathrm{x}) = \mathrm{p}^T(x, y) = \{1, x, y, xy, x^2, y^2, \ldots, x^p, y^p\} \tag{18}$$

and that in the 3-D problem is expressed as

$$\mathrm{p}^T(\mathrm{x}) = \mathrm{p}^T(x, y, z) = \{1, x, y, z, xy, yz, zx, x^2, y^2, z^2 \ldots, x^p, y^p, z^p\} \tag{19}$$

The n_d terms of $p_i(\mathrm{x})$ used in the basic should be selected from the constant term to higher orders symmetrically from the Pascal triangle (2-D problem) shown in Figure 3.2 or from the Pascal pyramid (3-D problem) shown in Figure 3.3. Moreover, the total number of terms involved in $p_i(\mathrm{x})$ should be equal to the number of nodal DOFs of an element (Rao, 2005).

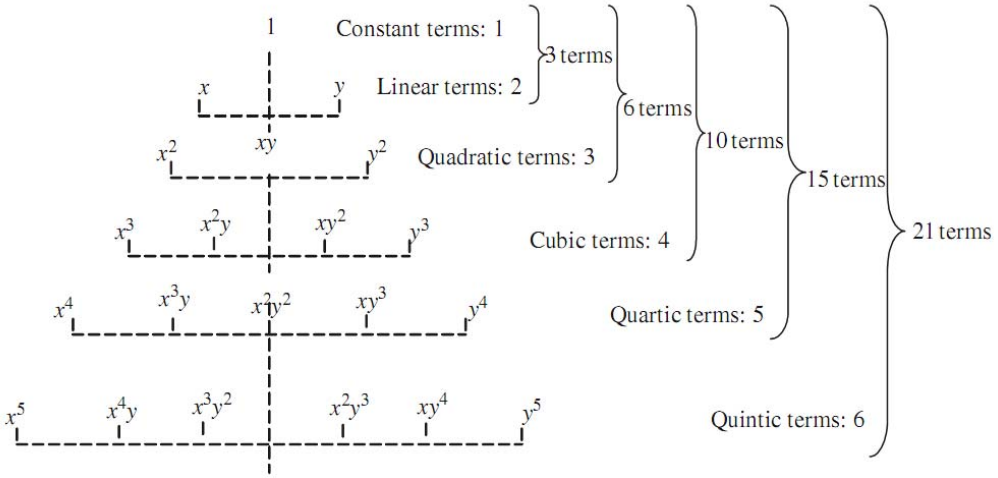

Figure 3.2 Pascal triangle of monomials (Liu and Quek, 2003)

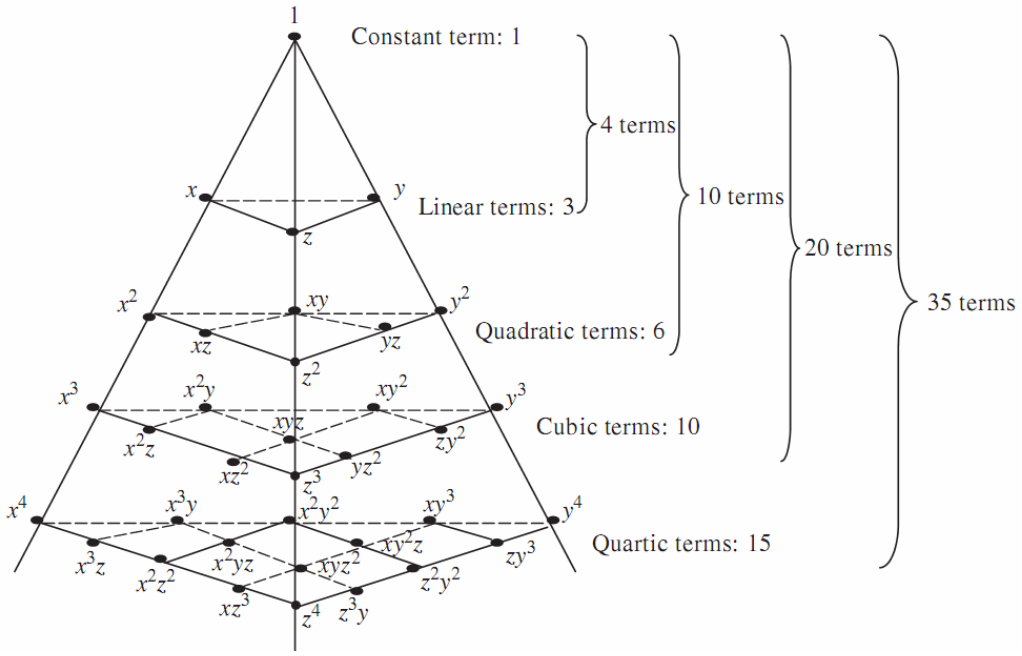

Figure 3.3 Pascal pyramid of monomials (Liu and Quek, 2003)

The coefficient vector α can be determined by

$$\alpha = \mathrm{P}^{-1}\mathrm{d}_e \tag{20}$$

where $\mathrm{d_e}$ is the displacement vector at all the n_d nodes in the element, as given in equation (12). Matrix P can be written as

$$\mathrm{P} = \begin{bmatrix} \mathrm{p}^T(\mathrm{x}_1) \\ \mathrm{p}^T(\mathrm{x}_2) \\ \vdots \\ \mathrm{p}^T(\mathrm{x}_{n_d}) \end{bmatrix} \tag{21}$$

Substituting equation (20) into equation (15),

$$u(\mathrm{x}) = \mathrm{N}(\mathrm{x})\mathrm{d}_e \tag{22}$$

Thus the matrix of shape function $\mathrm{N}(\mathrm{x})$ can be calculated as

$$\mathrm{N}(\mathrm{x}) = \mathrm{p}^T(\mathrm{x})\mathrm{P}^{-1} = \left[\underbrace{\mathrm{p}^T(\mathrm{x})\mathrm{P}_1^{-1}}_{N_1(\mathrm{x})} \quad \underbrace{\mathrm{p}^T(\mathrm{x})\mathrm{P}_2^{-1}}_{N_2(\mathrm{x})} \quad \cdots \quad \underbrace{\mathrm{p}^T(\mathrm{x})\mathrm{P}_\mathrm{n}^{-1}}_{N_n(\mathrm{x})} \right] \tag{23}$$

where $\mathrm{P_i^{-1}}$ is the ith column of matrix P^{-1}.

3.2.4 Formation of Local FE Equations

Once the shape functions are constructed, the strain vector can be calculated as

$$\varepsilon = \mathrm{B}\mathrm{d}_{\mathrm{e}} \tag{24}$$

where B is the strain matrix and defined by

$$\mathrm{B} = \mathrm{L}\mathrm{N} \tag{25}$$

in which L is a matrix of partial differential operator.

Substituting equation (24) into the strain energy term in (8)

$$\Pi = \frac{1}{2}\int \varepsilon^T \mathrm{D}\varepsilon \mathrm{d}V = \frac{1}{2}\int \mathrm{d}_e{}^T \mathrm{B}^T \mathrm{D}\mathrm{B}\mathrm{d}_e \mathrm{d}V = \frac{1}{2}\mathrm{d}_e{}^T \left(\int \mathrm{B}^T \mathrm{D}\mathrm{B}\mathrm{d}V\right)\mathrm{d}_e \tag{26}$$

By denoting

$$\mathrm{k}_{\mathrm{e}} = \int \mathrm{B}^T \mathrm{D}\mathrm{B}\mathrm{d}V \tag{27}$$

which is called the element stiffness matrix, equation (26) can be rewritten as

$$\Pi = \frac{1}{2}\mathrm{d}_e{}^T \mathrm{k}_e \mathrm{d}_e \tag{28}$$

Similarly, by substituting equation (10) into the kinetic energy term in (7)

$$T = \frac{1}{2}\int \rho \dot{\mathrm{U}}^T \dot{\mathrm{U}}\mathrm{d}V = \frac{1}{2}\int \rho \dot{\mathrm{d}}_e{}^T \mathrm{N}^T \mathrm{N}\dot{\mathrm{d}}_e \mathrm{d}V = \frac{1}{2}\dot{\mathrm{d}}_e{}^T \left(\int \rho \mathrm{N}^T \mathrm{N}\mathrm{d}V\right)\dot{\mathrm{d}}_e \tag{29}$$

By denoting

$$\mathrm{m}_{\mathrm{e}} = \int \rho \mathrm{N}^T \mathrm{N}\mathrm{d}V \tag{30}$$

which is known as mass matrix and the kinetic energy can be rewritten as

$$T = \frac{1}{2}\dot{\mathrm{d}}_e{}^T \mathrm{m}_e \dot{\mathrm{d}}_e \tag{31}$$

Finally, by substituting equation (10) into equation (9), the work done by external forces can be expressed as

$$W_f = \int \mathrm{U}^T \mathrm{f}_b \mathrm{d}V + \int \mathrm{U}^T \mathrm{f}_s \mathrm{d}S_f = \mathrm{d}_e{}^T \left(\int \mathrm{N}^T \mathrm{f}_b \mathrm{d}V\right) + \mathrm{d}_e{}^T \left(\int \mathrm{N}^T \mathrm{f}_s \mathrm{d}S_f\right) \tag{32}$$

By denoting

$$\mathrm{F}_b = \int \mathrm{N}^T \mathrm{f}_b \mathrm{d}V \tag{33}$$

$$\mathrm{F}_s = \int \mathrm{N}^T \mathrm{f}_s \mathrm{d}S_f \tag{34}$$

Then equation (32) can be rewritten as

$$W_f = \mathrm{d}_e{}^T \mathrm{F}_b + \mathrm{d}_e{}^T \mathrm{F}_s = \mathrm{d}_e{}^T \mathrm{f}_e \tag{35}$$

F_b and F_s are the forces acting on nodes of the elements. In terms of the work done by these nodal forces, it is equivalent to the body forces and surface forces on the elements. Hence, those nodal forces can be added up to form the total nodal force

$$\mathrm{f}_e = \mathrm{F}_b + \mathrm{F}_s \tag{36}$$

Substituting equations (28), (31) and (35) into (6)

$$L = \frac{1}{2}\dot{\mathrm{d}}_e{}^T \mathrm{m}_e \dot{\mathrm{d}}_e - \frac{1}{2}\mathrm{d}_e{}^T \mathrm{k}_e \mathrm{d}_e + \mathrm{d}_e{}^T \mathrm{f}_e \tag{37}$$

Applying Hamilton's Principle (5)

$$\delta \int_{t_1}^{t_2} \left(\frac{1}{2}\dot{\mathrm{d}}_e{}^T \mathrm{m}_e \dot{\mathrm{d}}_e - \frac{1}{2}\mathrm{d}_e{}^T \mathrm{k}_e \mathrm{d}_e + \mathrm{d}_e{}^T \mathrm{f}_e \right) \mathrm{d}t = 0 \tag{38}$$

Since the variation and integration operators are interchangeable

$$\int_{t_1}^{t_2} \left(\delta\dot{\mathrm{d}}_e{}^T \mathrm{m}_e \dot{\mathrm{d}}_e - \delta\mathrm{d}_e{}^T \mathrm{k}_e \mathrm{d}_e + \delta\mathrm{d}_e{}^T \mathrm{f}_e \right) \mathrm{d}t = 0 \tag{39}$$

The deriving from (38) to (39) can be found in Liu and Quek (2003). In equation (39), the variation and differentiation with time are also interchangeable

$$\delta\dot{\mathrm{d}}_e{}^T = \delta\left(\frac{\mathrm{d}\mathrm{d}_e{}^T}{\mathrm{d}t} \right) = \frac{\mathrm{d}}{\mathrm{d}t}\left(\delta\mathrm{d}_e{}^T \right) \tag{40}$$

Substituting equation (40) into (39) and integrating the first term

$$\int_{t_1}^{t_2} \delta\dot{\mathrm{d}}_e{}^T \mathrm{m}_e \dot{\mathrm{d}}_e \mathrm{d}t = \underbrace{\delta\mathrm{d}_e{}^T \mathrm{m}_e \dot{\mathrm{d}}_e \Big|_{t_1}^{t_2}}_{=0} - \int_{t_1}^{t_2} \delta\mathrm{d}_e{}^T \mathrm{m}_e \ddot{\mathrm{d}}_e \mathrm{d}t = -\int_{t_1}^{t_2} \delta\mathrm{d}_e{}^T \mathrm{m}_e \ddot{\mathrm{d}}_e \mathrm{d}t \tag{41}$$

Because the initial condition at t_1 and the final condition at t_2 have to be satisfied for any d_e, and no variation at t_1 and t_2 is allowed (Liu and Quek, 2003), $\delta\mathrm{d}_e = 0$, the first term on the right side of equation (41) vanishes.

Substituting equation (41) into (39) leads to

$$\int_{t_1}^{t_2} \delta\mathrm{d}_e{}^T \left(-\mathrm{m}_e \ddot{\mathrm{d}}_e - \mathrm{k}_e \mathrm{d}_e + \mathrm{f}_e \right) \mathrm{d}t = 0 \tag{42}$$

In order to have the integration in equation (42) as zero for an arbitrary integrand, the integrand itself has to be zero

$$\delta \mathrm{d}_e^{\,T}\left(-\mathrm{m}_e\ddot{\mathrm{d}}_e - \mathrm{k}_e\mathrm{d}_e + \mathrm{f}_e\right) = 0 \tag{43}$$

Because of the arbitrary nature of the variation of the displacements, to satisfy equation (43), we have

$$\mathrm{k}_e\mathrm{d}_e + \mathrm{m}_e\ddot{\mathrm{d}}_e = \mathrm{f}_e \tag{44}$$

3.2.5 Assembly of Global FE Equations

The element equation in (44) is formulated based on the local coordinate system of the element. To assemble all the element equations to form the global system equations, a coordinate transformation has to be carried out. By using the coordinate transformation, the displacement vector d_e can be transferred into a displacement vector U_e oriented in the global coordinate system.

$$\mathrm{d}_e = \mathrm{T}\mathrm{U}_e \tag{45}$$

where T is the transformation matrix. It can also be applied to transfer the force vector f_e in local coordinate system to force vector in global coordinate system.

$$\mathrm{f}_e = \mathrm{T}\mathrm{F}_e \tag{46}$$

Substituting equations (45) and (46) into (44), we have

$$\mathrm{K}_e\mathrm{U}_e + \mathrm{M}_e\ddot{\mathrm{U}}_e = \mathrm{F}_e \tag{47}$$

where

$$\mathrm{K}_e = \mathrm{T}^T\mathrm{k}_e\mathrm{T} \tag{48}$$

$$\mathrm{M}_e = \mathrm{T}^T\mathrm{m}_e\mathrm{T} \tag{49}$$

$$\mathrm{F}_e = \mathrm{T}^T\mathrm{f}_e \tag{50}$$

In the end, the FE equations of individual elements are assembled to form the global FE system equation:

$$\mathrm{KU} + \mathrm{M}\ddot{\mathrm{U}} = \mathrm{F} \tag{51}$$

where K and M are the global stiffness and mass matrix respectively, U is a vector of all the displacements at all nodes, and F is a vector of all external nodal forces.

3.3 Different Types of Finite Elements

Since 3-D solid and 2-D structural elements are the most commonly used elements in the FE analysis of metal forming process, the formulations of a 3-D solid element, a shell element, as well as a 2-D plane stress/strain element and a plate element which are used to generate the formulations of the shell element are discussed in this section.

3.3.1 3-D Solid Element

The 3-D solid element is the most general of all solid finite elements, as all its field variables are dependent of x, y and z. A 3-D solid element can be a tetrahedron or hexahedron in shape, where each node has three translational DOFs. Here, the 8 noded hexahedron element is taken as an example to explain the formulations of shape function, strain matrix, stiffness matrix and mass matrix in the 3-D solid element.

As shown in Figure 3.4, a hexahedron element has eight nodes, numbered 1, 2, 3, 4 and 5, 6, 7, 8 in a counter-clockwise manner. Since each node has three DOFs, there are total 24 DOFs in a hexahedron element. By using a natural coordinate system (ξ, η, ζ) with its origin at the centre of the element, it is easier to construct the shape functions and to evaluate the matrix integration than using the physical coordinate system (x, y, z). Assuming that the dimensions of the hexahedron element is $2a \times 2b \times 2c$, the relationship between local natural coordinate system and physical coordinate system is given by

$$\xi = x/a, \quad \eta = y/b, \quad \zeta = z/c \tag{52}$$

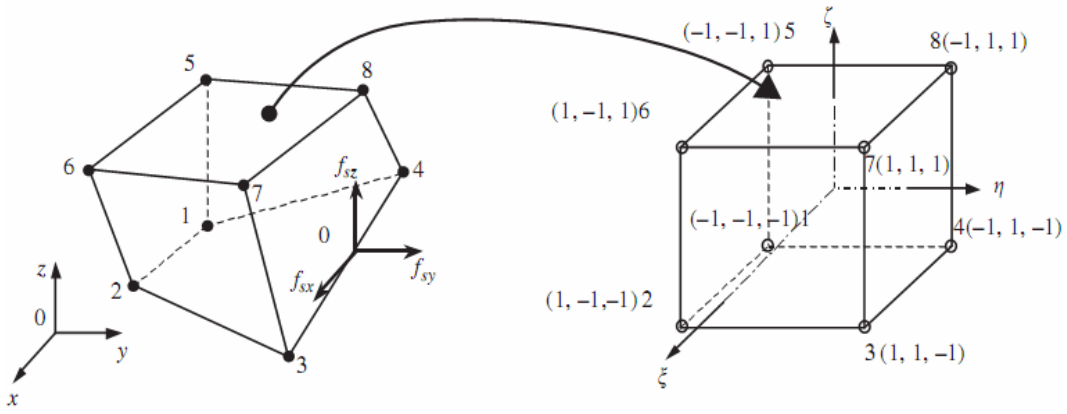

Figure 3.4 Hexahedron element and coordinate system (Liu and Quek, 2003)

The shape function of a hexahedron element is used to interpolate the coordinate from the nodal coordinates:

$$x = \sum_{i=1}^{8} N_i(\xi,\eta,\zeta)x_i \tag{53}$$

$$y = \sum_{i=1}^{8} N_i(\xi,\eta,\zeta)y_i \tag{54}$$

$$z = \sum_{i=1}^{8} N_i(\xi,\eta,\zeta)z_i \tag{55}$$

The shape functions are given as

$$N_i = \frac{1}{8}(1+\xi\xi_i)(1+\eta\eta_i)(1+\zeta\zeta_i) \tag{56}$$

where (ξ_i, η_i, ζ_i) denotes the natural coordinate of node i.

In a hexahedron element, the displacement vector U, which is a function of the coordinate x, y and z, is interpolated using the shape function

$$\mathrm{U} = \mathrm{N}\mathrm{d}_e \tag{57}$$

where the nodal displacement vector d_e is given by

$$\mathrm{d}_e = \begin{Bmatrix} \mathrm{d}_{e1} \\ \mathrm{d}_{e2} \\ \mathrm{d}_{e3} \\ \mathrm{d}_{e4} \\ \mathrm{d}_{e5} \\ \mathrm{d}_{e6} \\ \mathrm{d}_{e7} \\ \mathrm{d}_{e8} \end{Bmatrix} \tag{58}$$

In which d_{ei} is the displacement of the node i, where u, v, and w are its displacement components in x, y and z direction.

$$\mathrm{d}_{ei} = \begin{Bmatrix} u_i \\ v_i \\ w_i \end{Bmatrix} \quad (i = 1,2,...8) \tag{59}$$

The matrix of shape function is given as

$$\mathrm{N} = \begin{bmatrix} \mathrm{N}_1 & \mathrm{N}_2 & \mathrm{N}_3 & \mathrm{N}_4 & \mathrm{N}_5 & \mathrm{N}_6 & \mathrm{N}_7 & \mathrm{N}_8 \end{bmatrix} \tag{60}$$

where each sub-matrix is given by

$$\mathrm{N}_i = \begin{bmatrix} N_i & 0 & 0 \\ 0 & N_i & 0 \\ 0 & 0 & N_i \end{bmatrix} \tag{61}$$

The strain matrix can be written as

$$\mathrm{B} = \begin{bmatrix} \mathrm{B}_1 & \mathrm{B}_2 & \mathrm{B}_3 & \mathrm{B}_4 & \mathrm{B}_5 & \mathrm{B}_6 & \mathrm{B}_7 & \mathrm{B}_8 \end{bmatrix} \tag{62}$$

where

$$\mathrm{B}_i = \mathrm{L}\mathrm{N}_i = \begin{bmatrix} \partial N_i/\partial x & 0 & 0 \\ 0 & \partial N_i/\partial y & 0 \\ 0 & 0 & \partial N_i/\partial z \\ 0 & \partial N_i/\partial z & \partial N_i/\partial y \\ \partial N_i/\partial z & 0 & \partial N_i/\partial x \\ \partial N_i/\partial y & \partial N_i/\partial x & 0 \end{bmatrix} \tag{63}$$

Because the shape functions are defined in the natural coordinates (ξ, η, ζ), to obtain the derivatives with respective to x, y and z in the stain matrix, equation (64) needs to be used:

$$\begin{aligned}\frac{\partial \mathrm{N}_i}{\partial \xi} &= \frac{\partial N_i}{\partial x}\frac{\partial x}{\partial \xi} + \frac{\partial N_i}{\partial y}\frac{\partial y}{\partial \xi} + \frac{\partial N_i}{\partial z}\frac{\partial z}{\partial \xi} \\ \frac{\partial \mathrm{N}_i}{\partial \eta} &= \frac{\partial N_i}{\partial x}\frac{\partial x}{\partial \eta} + \frac{\partial N_i}{\partial y}\frac{\partial y}{\partial \eta} + \frac{\partial N_i}{\partial z}\frac{\partial z}{\partial \eta} \\ \frac{\partial \mathrm{N}_i}{\partial \zeta} &= \frac{\partial N_i}{\partial x}\frac{\partial x}{\partial \zeta} + \frac{\partial N_i}{\partial y}\frac{\partial y}{\partial \zeta} + \frac{\partial N_i}{\partial z}\frac{\partial z}{\partial \zeta}\end{aligned} \tag{64}$$

which can be expressed in the matrix form

$$\begin{Bmatrix} \partial N_i/\partial \xi \\ \partial N_i/\partial \eta \\ \partial N_i/\partial \zeta \end{Bmatrix} = \mathrm{J} \begin{Bmatrix} \partial N_i/\partial x \\ \partial N_i/\partial y \\ \partial N_i/\partial z \end{Bmatrix} \tag{65}$$

J is called Jacobian matrix

$$\mathrm{J} = \begin{bmatrix} \dfrac{\partial x}{\partial \xi} & \dfrac{\partial y}{\partial \xi} & \dfrac{\partial z}{\partial \xi} \\ \dfrac{\partial x}{\partial \eta} & \dfrac{\partial y}{\partial \eta} & \dfrac{\partial z}{\partial \eta} \\ \dfrac{\partial x}{\partial \zeta} & \dfrac{\partial y}{\partial \zeta} & \dfrac{\partial z}{\partial \zeta} \end{bmatrix} \tag{66}$$

By inverting equation (65), we obtain

$$\begin{Bmatrix} \partial N_i/\partial x \\ \partial N_i/\partial y \\ \partial N_i/\partial z \end{Bmatrix} = \mathrm{J}^{-1} \begin{Bmatrix} \partial N_i/\partial \xi \\ \partial N_i/\partial \eta \\ \partial N_i/\partial \zeta \end{Bmatrix} \tag{67}$$

from which the strain matrix B is evaluated.

Substituting the strain matrix B into equation (27), the stiffness matrix can be obtained

$$\mathrm{k}_\mathrm{e} = \int \mathrm{B}^T \mathrm{D}\mathrm{B}\mathrm{d}V = \int_{-1}^{+1}\int_{-1}^{+1}\int_{-1}^{+1} \mathrm{B}^T \mathrm{D}\mathrm{B}\det[\mathrm{J}]\mathrm{d}\xi\mathrm{d}\eta\mathrm{d}\zeta \tag{68}$$

where the matrix of material constants, D is given by

$$\mathrm{D} = \frac{E}{(1+v)(1-2v)} \begin{bmatrix} 1-v & v & v & 0 & 0 & 0 \\ v & 1-v & v & 0 & 0 & 0 \\ v & v & 1-v & 0 & 0 & 0 \\ 0 & 0 & 0 & \dfrac{1-2v}{2} & 0 & 0 \\ 0 & 0 & 0 & 0 & \dfrac{1-2v}{2} & 0 \\ 0 & 0 & 0 & 0 & 0 & \dfrac{1-2v}{2} \end{bmatrix} \tag{69}$$

in which E is the Young's Modulus and v is the Poisson's ratio

The determinate of the Jacobian matrix $\det[\mathrm{J}]$ in equation (68) is given by

$$\det[\mathrm{J}] = abc \tag{70}$$

The mass matrix can be obtained by substituting the shape function matrix equation (60) into (30)

$$\mathrm{m}_{\mathrm{e}} = \int \rho \mathrm{N}^T \mathrm{N} \mathrm{d}V = \int_{-1}^{+1}\int_{-1}^{+1}\int_{-1}^{+1} \rho \mathrm{N}^T \mathrm{N} \det[\mathrm{J}] \mathrm{d}\xi \mathrm{d}\eta \mathrm{d}\zeta \tag{71}$$

3.3.2 2-D Plane Stress/Strain Element

The 2-D plane stress/strain element is used to analyse structural problems where the loading and hence the deformation takes place within the plane. As shown in Figure 3.5, a rectangular 2-D plane stress/strain element has four nodes, numbered 1, 2, 3, 4 in a counter-clockwise manner. Each node has two DOFs, thus there are total eight DOFs in a rectangular 2-D plane stress/strain element. Again the formulation of the 2-D plane stress/strain element is based on a local natural coordinate system with its origin at the centre of the element. Figure 3.5 shows the mapping between the local natural coordinate system (ξ, η) and physical coordinate system (x, y) for the rectangular element, the dimension of which is defined as $2a \times 2b \times h$.

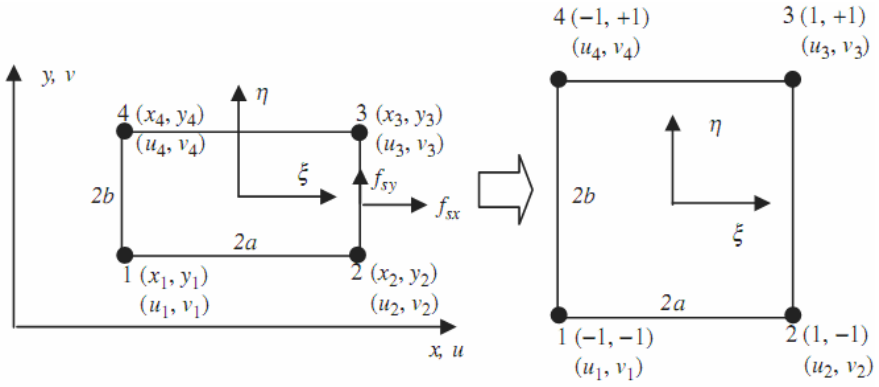

Figure 3.5 Rectangular 2-D plane stress/strain element (Liu and Quek, 2003)

The displacement vector U is assumed to have the form

$$\mathrm{U}(x, y) = \mathrm{N}(x, y)\mathrm{d}_e \tag{72}$$

where the nodal displacement vector d_e is given as

$$\mathrm{d}_e = \begin{Bmatrix} u_1 \\ v_1 \\ u_2 \\ v_2 \\ u_3 \\ v_3 \\ u_4 \\ v_4 \end{Bmatrix} \tag{73}$$

The matrix of a shape function has the form of

$$\mathrm{N} = \begin{bmatrix} N_1 & 0 & N_2 & 0 & N_3 & 0 & N_4 & 0 \\ 0 & N_1 & 0 & N_2 & 0 & N_3 & 0 & N_4 \end{bmatrix} \tag{74}$$

The shape function is given as

$$N_j = \frac{1}{4}(1+\xi\xi_j)(1+\eta\eta_j) \tag{75}$$

The strain matrix

$$\mathrm{B} = \mathrm{LN} = \begin{bmatrix} \partial/\partial x & 0 \\ 0 & \partial/\partial y \\ \partial/\partial y & \partial/\partial x \end{bmatrix} \mathrm{N} \tag{76}$$

Having obtained the shape function and the strain matrix, the stiffness matrix can be calculated as

$$\mathrm{k}_\mathrm{e} = \int \mathrm{B}^T \mathrm{DB} \mathrm{d}V = \int_{-1}^{+1}\int_{-1}^{+1} abh \mathrm{B}^T \mathrm{DB} \mathrm{d}\xi \mathrm{d}\eta \tag{77}$$

where the matrix of material constants, D is given by

$$\mathrm{D} = \frac{E}{1-v^2}\begin{bmatrix} 1 & v & 0 \\ v & 1 & 0 \\ 0 & 0 & (1-v)/2 \end{bmatrix} \text{ (for plane stress)} \tag{78}$$

$$\mathrm{D} = \frac{E(1-v)}{(1+v)(1-2v)}\begin{bmatrix} 1 & v/(1-v) & 0 \\ v/(1-v) & 1 & 0 \\ 0 & 0 & (1-2v)/(2(1-v)) \end{bmatrix} \text{ (for plane strain)} \tag{79}$$

The element mass matrix can be obtained by

$$\mathrm{m}_\mathrm{e} = \int \rho \mathrm{N}^T \mathrm{N} \mathrm{d}V = \int_{-1}^{+1}\int_{-1}^{+1} abh\rho \mathrm{N}^T \mathrm{N} \mathrm{d}\xi \mathrm{d}\eta \tag{80}$$

3.3.3 Plate Element

A plate element is geometrically similar to a 2-D plane stress/strain element, as shown in Figure 3.5. However the plate element only carries transversal loads and the bending deformation in the plate. The deformation resulted from the transverse loading on a plate is represented by the deflection and rotation of the normal of the middle plane of the plate, which are functions of x and y but independent of z. Considering a 4 noded plate element in the x-y plane, each node has three DOFs, i.e. the deflection w in z ***axis***, the rotation of the normal of the middle plane about x axis θ_x the rotation of the normal of the middle plane about y axis θ_y. Hence the total DOFs of a 4 noded plate element is 12.

For a 4 noded plate element, the deflections and rotations can be written as

$$\begin{Bmatrix} w \\ \theta_x \\ \theta_y \end{Bmatrix} = \mathrm{N}\mathrm{d}_e \tag{81}$$

The shape functions of 4 noded plate element are the same as that of 4 noded 2-D plane stress/strain element, as given in equation (75).

Based on the Reissner-Mindlin plate theory, which does not require the cross-section to be perpendicular to the axial axes after deformation (Liu and Quek, 2003), the two displacement components parallel to the underformed middle surface at a distance z from the centroidal axis can be expressed by

$$u(x, y, z) = z\theta_y(x, y) \tag{82}$$

$$v(x, y, z) = -z\theta_x(x, y) \tag{83}$$

The in-plane strain is given as

$$\varepsilon = -z\chi \tag{84}$$

where χ is the curvature, given as

$$\chi = \mathrm{L}\theta = \begin{Bmatrix} -\partial\theta_y/\partial x \\ \partial\theta_x/\partial y \\ \partial\theta_x/\partial x - \partial\theta_y/\partial y \end{Bmatrix} \tag{85}$$

The off-plane shear strain is given as

$$\gamma = \begin{Bmatrix} \xi_{xz} \\ \xi_{yz} \end{Bmatrix} = \begin{Bmatrix} \theta_y + \dfrac{\partial w}{\partial x} \\ -\theta_x + \dfrac{\partial w}{\partial y} \end{Bmatrix} \tag{86}$$

Hamilton's Principle is used to derive the equation of motion. The strain energy of a 4 noded plate element can be obtained as

$$\Pi = \frac{1}{2}\int_A \int_0^h \varepsilon^T \sigma \mathrm{d}z\mathrm{d}A + \frac{1}{2}\int_A \int_0^h \tau^T \gamma \mathrm{d}z\mathrm{d}A \tag{87}$$

where τ is the average shear stresses related to the shear strain in the form

$$\tau = \begin{Bmatrix} \tau_{xz} \\ \tau_{yz} \end{Bmatrix} = \kappa \begin{bmatrix} G & 0 \\ 0 & G \end{bmatrix} \gamma = \kappa \mathrm{D}_s \gamma \tag{88}$$

in which G is the shear modulus, and κ is a constant that is usually taken to be $\pi^2/12$ (Liu and Quek, 2003). Substituting equation (84) and (88) into (87), the strain energy becomes

$$\Pi = \frac{1}{2}\int_A \frac{h^3}{12} \chi^T \mathrm{D} \chi \mathrm{d}A + \frac{1}{2}\int_A \kappa h \gamma^T \mathrm{D}_s \gamma \mathrm{d}A \tag{89}$$

The kinetic energy of the plate element is given by

$$T = \frac{1}{2}\int \rho\left(\dot{u}^2 + \dot{v}^2 + \dot{w}^2\right)\mathrm{d}V \tag{90}$$

which is a summation of the contributions of three velocity components in the x, y and z directions. Substituting equation (82) and (83) into (90), the kinetic energy can be obtained (Liu and Quek, 2003)

$$T = \frac{1}{2}\int \rho(h\dot{w}^2 + \frac{h^3}{12}\dot{\theta}_x{}^2 + \frac{h^3}{12}\dot{\theta}_y{}^2)\mathrm{d}A = \frac{1}{2}\int (\mathrm{d}^T \mathrm{I} \mathrm{d})\mathrm{d}A \tag{91}$$

where

$$\mathrm{I} = \begin{bmatrix} \rho h & 0 & 0 \\ 0 & \rho h^3/12 & 0 \\ 0 & 0 & \rho h^3/12 \end{bmatrix} \tag{92}$$

To obtain the shape function, substituting equation (81) into (87) will lead to

$$\mathrm{k}_e = \int_A \frac{h^3}{12}\left[\mathrm{B}^{\mathrm{I}}\right]^T \mathrm{D}\mathrm{B}^{\mathrm{I}}\mathrm{d}A + \int_A \kappa h \left[\mathrm{B}^{\mathrm{O}}\right]^T \mathrm{D}_s \mathrm{B}^{\mathrm{O}}\mathrm{d}A \tag{93}$$

where

$$\mathrm{B}_{\mathrm{j}}^{\mathrm{I}}=\begin{bmatrix}0 & 0 & -\partial N_j/\partial x\\ 0 & \partial N_j/\partial y & 0\\ 0 & \partial N_j/\partial x & -\partial N_j/\partial y\end{bmatrix} \tag{94}$$

$$\mathrm{B}_{\mathrm{j}}^{\mathrm{O}}=\begin{bmatrix}\partial N_j/\partial x & 0 & N_j\\ \partial N_j/\partial y & -N_j & 0\end{bmatrix} \tag{95}$$

The mass matrix can be derived from the kinetic energy, i.e. equation (91)

$$\mathrm{m}_e=\int_A \mathrm{N}^{\mathrm{T}}\mathrm{IN}\mathrm{d}A \tag{96}$$

3.3.4 Shell Element

A shell element is able to carry loads in all direction, i.e. bending and twisting, as well as in-plane deformation. The simplest but widely used shell element can be formulated by combining the 2-D plane stress/strain element and the plate element, where the 2-D plane stress/strain element handles the membrane or in-plane effects, while the plate element deals with the bending or off-plane effects. In this section, the derivation of a 4 noded rectangular shell element is presented. There are 6 DOFs at a node of a shell element, i.e. three translational displacements and three rotational deformations. Figure 3.6 shows a rectangular shell element and the DOFs at each node.

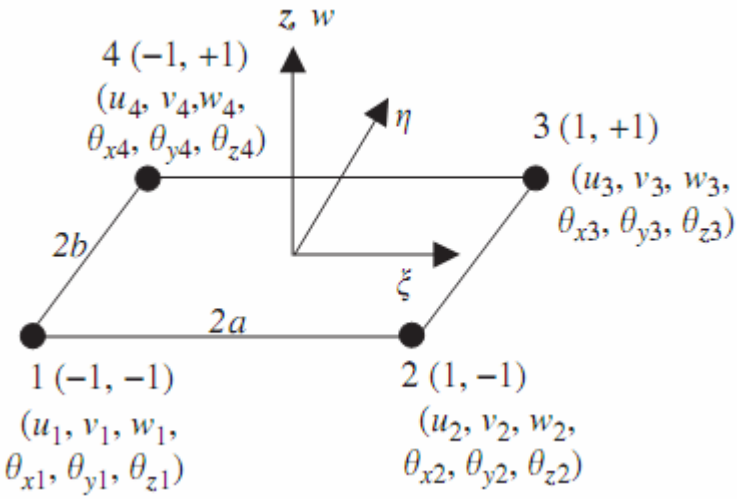

Figure 3.6 Rectangular shell element (Liu and Quek, 2003)

The nodal displacement vector of a rectangular shell element can be written as

$$\mathrm{d}_e = \begin{Bmatrix} \mathrm{d}_{e1} \\ \mathrm{d}_{e2} \\ \mathrm{d}_{e3} \\ \mathrm{d}_{e4} \end{Bmatrix} \tag{97}$$

where d_{ei} are the displacement vector at node i

$$\mathrm{d}_{ei} = \begin{Bmatrix} u_i \\ v_i \\ w_i \\ \theta_{xi} \\ \theta_{yi} \\ \theta_{zi} \end{Bmatrix} \tag{98}$$

The stiffness matrix of a 2-D solid rectangular element is used to deal with the membrane effects of a rectangular shell element

$$\mathrm{k}_{\mathrm{e}}^{\mathrm{m}} = \begin{bmatrix} \mathrm{k}_{11}^{\mathrm{m}} & \mathrm{k}_{12}^{\mathrm{m}} & \mathrm{k}_{13}^{\mathrm{m}} & \mathrm{k}_{14}^{\mathrm{m}} \\ \mathrm{k}_{21}^{\mathrm{m}} & \mathrm{k}_{22}^{\mathrm{m}} & \mathrm{k}_{23}^{\mathrm{m}} & \mathrm{k}_{24}^{\mathrm{m}} \\ \mathrm{k}_{31}^{\mathrm{m}} & \mathrm{k}_{32}^{\mathrm{m}} & \mathrm{k}_{33}^{\mathrm{m}} & \mathrm{k}_{34}^{\mathrm{m}} \\ \mathrm{k}_{41}^{\mathrm{m}} & \mathrm{k}_{42}^{\mathrm{m}} & \mathrm{k}_{43}^{\mathrm{m}} & \mathrm{k}_{44}^{\mathrm{m}} \end{bmatrix} \tag{99}$$

where the superscript m represents the membrane matrix. Each sub-matrix has a dimension of 2×2, as it corresponds to the two DOFs u and v at each node.

The stiffness matrix of a rectangular plate element is used to take account the bending effects in a rectangular shell element

$$\mathrm{k}_{\mathrm{e}}^{\mathrm{b}} = \begin{bmatrix} \mathrm{k}_{11}^{\mathrm{b}} & \mathrm{k}_{12}^{\mathrm{b}} & \mathrm{k}_{13}^{\mathrm{b}} & \mathrm{k}_{14}^{\mathrm{b}} \\ \mathrm{k}_{21}^{\mathrm{b}} & \mathrm{k}_{22}^{\mathrm{b}} & \mathrm{k}_{23}^{\mathrm{b}} & \mathrm{k}_{24}^{\mathrm{b}} \\ \mathrm{k}_{31}^{\mathrm{b}} & \mathrm{k}_{32}^{\mathrm{b}} & \mathrm{k}_{33}^{\mathrm{b}} & \mathrm{k}_{34}^{\mathrm{b}} \\ \mathrm{k}_{41}^{\mathrm{b}} & \mathrm{k}_{42}^{\mathrm{b}} & \mathrm{k}_{43}^{\mathrm{b}} & \mathrm{k}_{44}^{\mathrm{b}} \end{bmatrix} \tag{100}$$

where the superscript b stands for the bending matrix. Each sub-matrix has a dimension

of 3×3, corresponding to three DOFs, i.e. w, θ_x and θ_y.

The stiffness matrix of a rectangular shell element in the local coordinate system is then formulated by combining equation (99) and (100):

$$\mathrm{k}_e = \begin{bmatrix}
\mathrm{k}^{\mathrm{m}}_{11} & 0 & 0 & \mathrm{k}^{\mathrm{m}}_{12} & 0 & 0 & \mathrm{k}^{\mathrm{m}}_{13} & 0 & 0 & \mathrm{k}^{\mathrm{m}}_{14} & 0 & 0 \\
0 & \mathrm{k}^{\mathrm{b}}_{11} & 0 & 0 & \mathrm{k}^{\mathrm{b}}_{12} & 0 & 0 & \mathrm{k}^{\mathrm{b}}_{13} & 0 & 0 & \mathrm{k}^{\mathrm{b}}_{14} & 0 \\
0 & 0 & 0 & 0 & 0 & 0 & 0 & 0 & 0 & 0 & 0 & 0 \\
\mathrm{k}^{\mathrm{m}}_{21} & 0 & 0 & \mathrm{k}^{\mathrm{m}}_{22} & 0 & 0 & \mathrm{k}^{\mathrm{m}}_{23} & 0 & 0 & \mathrm{k}^{\mathrm{m}}_{24} & 0 & 0 \\
0 & \mathrm{k}^{\mathrm{b}}_{21} & 0 & 0 & \mathrm{k}^{\mathrm{b}}_{22} & 0 & 0 & \mathrm{k}^{\mathrm{b}}_{23} & 0 & 0 & \mathrm{k}^{\mathrm{b}}_{24} & 0 \\
0 & 0 & 0 & 0 & 0 & 0 & 0 & 0 & 0 & 0 & 0 & 0 \\
\mathrm{k}^{\mathrm{m}}_{31} & 0 & 0 & \mathrm{k}^{\mathrm{m}}_{32} & 0 & 0 & \mathrm{k}^{\mathrm{m}}_{33} & 0 & 0 & \mathrm{k}^{\mathrm{m}}_{34} & 0 & 0 \\
0 & \mathrm{k}^{\mathrm{b}}_{31} & 0 & 0 & \mathrm{k}^{\mathrm{b}}_{32} & 0 & 0 & \mathrm{k}^{\mathrm{b}}_{33} & 0 & 0 & \mathrm{k}^{\mathrm{b}}_{34} & 0 \\
0 & 0 & 0 & 0 & 0 & 0 & 0 & 0 & 0 & 0 & 0 & 0 \\
\mathrm{k}^{\mathrm{m}}_{41} & 0 & 0 & \mathrm{k}^{\mathrm{m}}_{42} & 0 & 0 & \mathrm{k}^{\mathrm{m}}_{43} & 0 & 0 & \mathrm{k}^{\mathrm{m}}_{44} & 0 & 0 \\
0 & \mathrm{k}^{\mathrm{b}}_{41} & 0 & 0 & \mathrm{k}^{\mathrm{b}}_{42} & 0 & 0 & \mathrm{k}^{\mathrm{b}}_{43} & 0 & 0 & \mathrm{k}^{\mathrm{b}}_{44} & 0 \\
0 & 0 & 0 & 0 & 0 & 0 & 0 & 0 & 0 & 0 & 0 & 0
\end{bmatrix} \tag{101}$$

Similarly, the mass matrix of a rectangular shell element can be obtained by combining the mass matrices of a 2-D rectangular solid element and a rectangular plate element.

3.4 Non-linear Solution Method

In this section, two non-linear FE solution method, i.e. static implicit method and dynamic explicit method are summarised.

3.4.1 Implicit Method

Newton-Raphson method is one of the most commonly used solution procedures in non-linear implicit analysis (Harewood and McHugh, 2007). Unlike solving a linear problem, the solution cannot be obtained by solving a single system of equations for the non-linear problem. Hence, in the non-linear implicit analysis, the loading is applied gradually and incrementally. Normally, the simulation breaks into a number of load increments and finds the approximate equilibrium at the end of the each increment. It

often takes several iterations to determine an acceptable solution for a given increment.

The equilibrium equation in an iteration of the implicit method is defined as (Abaqus analysis user's manual, 2008):

$$\mathrm{F} - \mathrm{I} = \mathrm{K}c \tag{102}$$

where F is the external force vector, I is the internal force vector, K is the stiffness matrix of the structure, and c is the displacement correction vector.

Figure 3.7 shows the non-linear response of a structure to a load increment $\Delta\mathrm{F}$. Based on structure's configuration at the initial displacement of U_0, the initial stiffness matrix of the structure K_0, is determined. A displacement correction c_a, is calculated from

$$c_\mathrm{a} = \mathrm{K}_0^{-1}\Delta\mathrm{F} \tag{103}$$

The configuration of the structure is now updated to a new displacement of U_a and a new stiffness of the structure K_a, is formed based on U_a. Internal force I_a is also calculated at this stage, where

$$\mathrm{I}_\mathrm{a} = \mathrm{K}_\mathrm{a}\mathrm{U}_\mathrm{a} \tag{104}$$

The force residual of this iteration, R_a, can be calculated as:

$$\mathrm{R}_\mathrm{a} = \mathrm{F} - \mathrm{I}_\mathrm{a} \tag{105}$$

In order to ensure the accuracy of the solution, certain convergence criterion is applied. If both R_a and c_a are smaller than the defined tolerance values, it means that the solution has converged. If any of the convergence check does not satisfy the criterion, further iterations will be performed in order to bring the external force and internal force into balance.

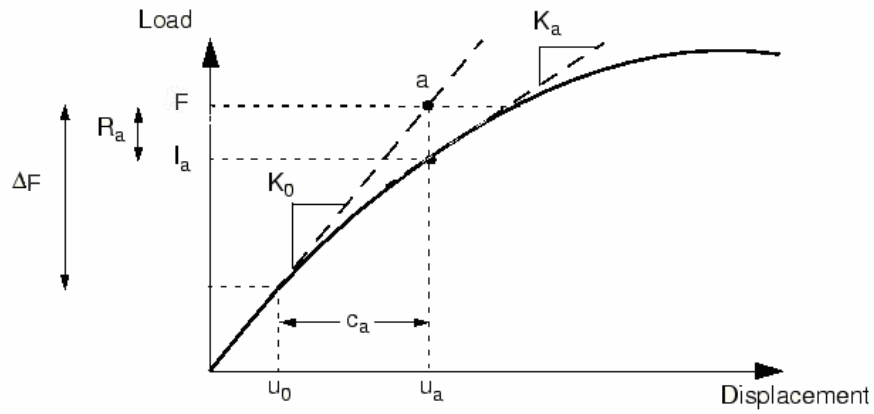

Figure 3.7 First iteration in an increment (Abaqus analysis user's manual, 2008)

Assuming the first iteration does not achieve convergence, the second iteration uses the stiffness K_a and force residual R_a to determine another displacement correction c_b, which brings the system closer to equilibrium, as shown in Figure 3.8. Using the internal force calculated from structure's new configuration, the force residual of the second iteration, R_b, is calculated. Both R_b and c_b are compared against the tolerance of force residual and displacement increment (U_b-U_0) at this iteration. If necessary, further iterations will be performed.

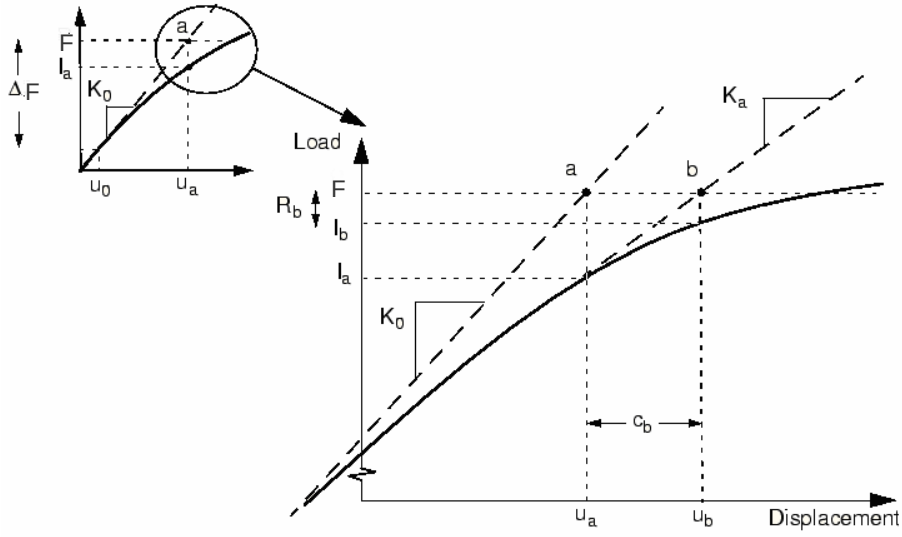

Figure 3.8 Second iteration in an increment (Abaqus analysis user's manual, 2008)

3.4.2 Explicit Method

Similar to the implicit method, the non-linear response in the explicit method is also obtained incrementally. At the beginning of an increment (t) in the explicit analysis, based on the dynamic equilibrium equation:

$$\mathrm{F} - \mathrm{I} = \mathrm{M}\ddot{u} \tag{106}$$

The nodal accelerations ($\ddot{u}$) can be calculated by:

$$\ddot{u}\,|_{(t)} = \mathrm{M}^{-1}(\mathrm{F} - \mathrm{I})\,|_{(t)} \tag{107}$$

where M is the nodal mass matrix. The acceleration of any node is completely determined by the mass and the net force acting on it.

The accelerations are integrated through time using the central difference rule, whereby the change of velocity is calculated from equation (108), assuming that the acceleration is constant over the time increment:

$$\dot{u}\,|_{(t+\Delta t/2)} = \dot{u}\,|_{(t-\Delta t/2)} + \frac{\Delta t\big|_{(t+\Delta t)} + \Delta t\big|_{(\Delta t)}}{2}\ddot{u}\,|_{(t)} \tag{108}$$

The velocities are integrated through time and added to the displacement (u) at the beginning of the increment to calculate the displacements at the end of the increment:

$$u\,|_{(t+\Delta t)} = u\,|_{(t)} + \Delta t\,|_{(t+\Delta t)}\dot{u}\,|_{(t+\Delta t/2)} \tag{109}$$

In order to obtain accurate results from the explicit method, the time increment has to be extremely small which ensures that the acceleration through the time increment is nearly constant. Therefore an explicit analysis typically requires many thousands of increments. The size of the increment is determined by the stability limit:

$$\Delta t = \min(\frac{L^e}{\mathrm{c}^d}) \tag{110}$$

where L^e is the characteristic element length, c^d is the wave speed of the material:

$$c^d = \sqrt{\frac{\lambda + 2\mu}{\rho}} \tag{111}$$

where λ and μ are Lamé's elastic constants. If T is the actual time of the analysed process, the number of time increments required n can be obtained by:

$$n = \frac{T}{\Delta t} = \frac{T}{\min(L^e \times \sqrt{\frac{\rho}{\lambda + 2\mu}})} \tag{112}$$

Normally it is unfeasible to run a quasi-static analysis with its real time scale, as the computing time is extremely long (Harewood and McHugh, 2007). Two techniques have been used to speed up the analysis: the first method is by artificially increasing the loading or deformation rate, known as load rate scaling; the second method is to increase the density of the material, known as mass scaling. According to equations (110) - (112), mass scaling by a factor of q^2 should have the same speeding up effects as load rate scaling by a factor of q. Mass scaling is preferable as it does not affect the mechanical response of rate-dependent material (Tekkaya, 2000). Nevertheless, if a very large speed-up factor is applied, the corresponding inertial forces will affect the mechanical response and produce unrealistic dynamic results. The general rule to control the inertial effects resulting from mass scaling is to ensure that the kinetic energy of the material should not exceed a small portion (typically 5%-10%) of its internal energy during the majority of the duration of the process (Abaqus analysis user's manual, 2008).

3.5 Material Constitutive Model

3.5.1 von Mises Yield Criterion

Figure 3.9 shows a idealised bi-linear stress-strain curve, where the material behaves elastically until the initial yielding stress σ_y is reached (Dunne and Petrinic, 2005). If at a strain of ε the load is reversed (unloading), the stress-strain response is assumed to follow the elastic law, i.e. the gradient of the unloading stress-strain curve is again the Young's modulus E, as it is in the elastic loading process. Once a stress of zero is obtained, the remaining strain is the plastic strain ε^p and the recovered strain is the

elastic strain ε^{e}. Therefore, the total strain ε can be decomposed into elastic and plastic parts (Belytschko et al., 2000)

$$\varepsilon = \varepsilon^{\mathrm{e}} + \varepsilon^{\mathrm{p}} \tag{113}$$

which is known as the classical additive decomposition of strain.

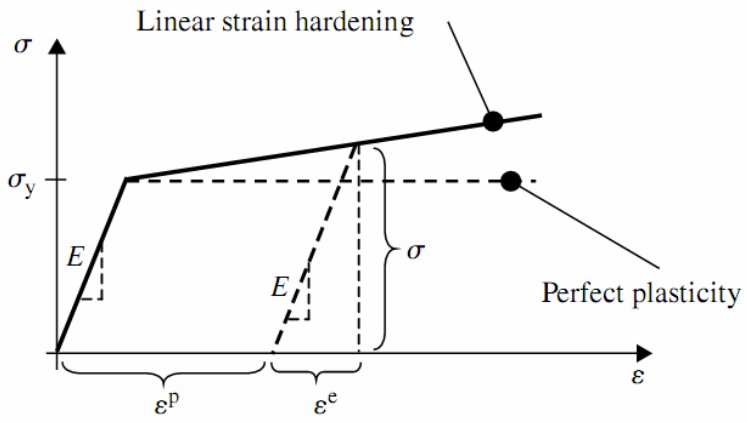

Figure 3.9 Bi-linear stress-strain curve (Dunne and Petrinic, 2005)

As shown in Figure 3.9, for a bilinear stress-strain relationship, the stress achieved at a strain of ε can be calculated by

$$\sigma = E\varepsilon^{\mathrm{e}} = E(\varepsilon - \varepsilon^{\mathrm{p}}) \tag{114}$$

As a commonly used yield criterion for isotropic, non-porous metal materials, the von Mises yield function is defined as (Dunne and Petrinic, 2005)

$$f = \sigma_{\mathrm{e}} - \sigma_{\mathrm{y}} \tag{115}$$

where σ_{y} is the yield stress measured from the uni-axial material tensile test, while σ_{e} is known as the effective stress or von Mises equivalent stress. The effective stress in terms of principal stresses is defined as,

$$\sigma_{\mathrm{e}} = \frac{1}{\sqrt{2}}\left[(\sigma_1 - \sigma_2)^2 + (\sigma_2 - \sigma_3)^2 + (\sigma_3 - \sigma_1)^2\right]^{\frac{1}{2}} \tag{116}$$

or in terms of direct and shear stresses,

$$\sigma_{\mathrm{e}} = \left[\frac{3}{2}\left(\sigma_{11}{}^2 + \sigma_{22}{}^2 + \sigma_{33}{}^2 + 2\sigma_{12}{}^2 + 2\sigma_{23}{}^2 + 2\sigma_{31}{}^2\right)\right]^{\frac{1}{2}} \tag{117}$$

where the subscripts 1, 2, and 3 represent the X, Y, and Z directions.

The yield criterion shown in equation (115) is given by

$$f < 0: \text{ Elastic deformation} \tag{118}$$

$$f = 0: \text{ Plastic deformation} \tag{119}$$

3.5.2 Strain Hardening

Figure 3.10 shows the isotropic strain hardening under a uni-axial stress σ_2, as discussed in Section 2.1.3.2. In order to ensure the hardening to take place and the load point to stay on the yield surface, the yield surface must expand as the stress increases. The amount of the expansion can be expressed as a function of accumulated plastic strain p, which is given as

$$p = \int \mathrm{d}p = \int \dot{p}\mathrm{d}t \tag{120}$$

where $\dot{p}$ is the effective plastic strain rate

$$\dot{p} = \frac{\sqrt{2}}{3}\left[\left(\dot{\varepsilon}_1^{\,\mathrm{p}} - \dot{\varepsilon}_2^{\,\mathrm{p}}\right)^2 + \left(\dot{\varepsilon}_2^{\,\mathrm{p}} - \dot{\varepsilon}_3^{\,\mathrm{p}}\right)^2 + \left(\dot{\varepsilon}_3^{\,\mathrm{p}} - \dot{\varepsilon}_1^{\,\mathrm{p}}\right)^2\right]^{\frac{1}{2}} \tag{121}$$

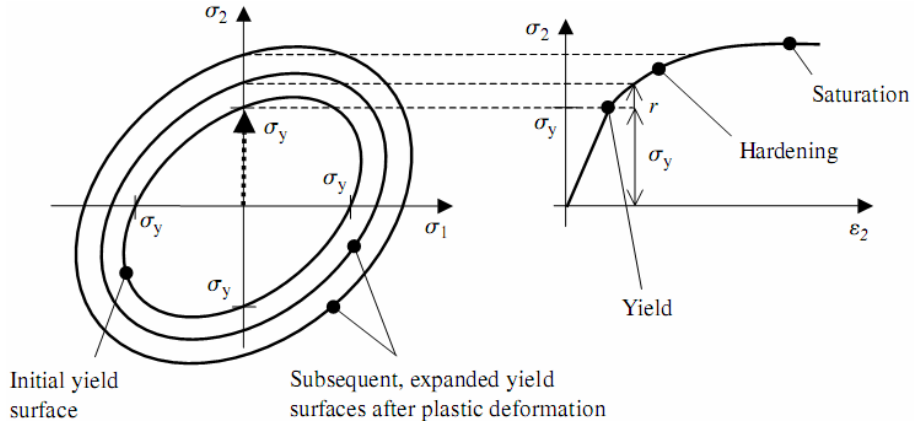

Figure 3.10 Isotropic strain hardening (Dunne and Petrinic, 2005)

The yield function becomes

$$f(\sigma, p) = \sigma_{\mathrm{e}} - \sigma_{\mathrm{y}}(p) = 0 \tag{122}$$

As shown in Figure 3.10,

$$\sigma_y(p) = \sigma_{y0} + r(p) \tag{123}$$

in which σ_{y0} is the initial yield stress and $r(p)$ is called isotropic hardening function.

Figure 3.11 shows a stress-strain curve of linear strain hardening and the linear isotropic hardening function can be written as

$$\mathrm{d}r(p) = h\mathrm{d}p \tag{124}$$

where h is known as the plastic hardening modulus.

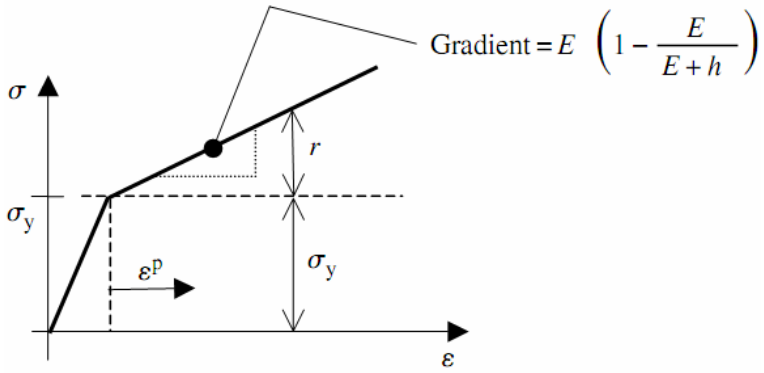

Figure 3.11 Stress-strain curve of linear strain hardening (Dunne and Petrinic, 2005)

For uni-axial conditions, $\mathrm{d}p = \mathrm{d}\varepsilon^p$ and the stress increase due to isotropic hardening is just $\mathrm{d}r$, therefore

$$\mathrm{d}\varepsilon^p = \frac{\mathrm{d}\sigma}{h} \tag{125}$$

The increment in elastic strain

$$\mathrm{d}\varepsilon^e = \frac{\mathrm{d}\sigma}{E} \tag{126}$$

The total strain can be expressed as

$$\mathrm{d}\varepsilon = \frac{\mathrm{d}\sigma}{E} + \frac{\mathrm{d}\sigma}{h} = \mathrm{d}\sigma\left(\frac{E+h}{Eh}\right) \tag{127}$$

Thus

$$\mathrm{d}\sigma = E\left(1-\frac{E}{E+h}\right)\mathrm{d}\varepsilon \tag{128}$$

3.6 Contact algorithms

Contact simulation, which is among the most difficult aspects for non-linear FE problems, is also implemented in an incremental manner (Belytschko et al., 2000). In each time increment of a metal forming problem simulation, there are three main aspects of the contact modellling: identifying the area on the surfaces that are in contact; calculating the contact force in the normal direction of the surfaces due to penetrations; thereafter calculating the tangential force caused by friction. Four corresponding contact formulations, i.e. contact surface weighting, tracking approach, constraint enforcement method, and friction models, are discussed in this section.

3.6.1 Contact Surface Weighting

To analyse the contact problem, master and slave surfaces have to be defined. The master surface is the surface with “hard” material, for instance, the tools in the metal forming simulation; whereas the slave surface is the surface with relatively “soft” material such as the deformable blank. In general, there are two kinds of contact weighting methods, i.e. a pure master-slave surface weighting and a balanced master-slave surface weighting. In the pure master-slave surface weighting method, only the penetrations of slave nodes into master surface will be resisted. There is no restriction for the master surface to penetrate into the slave surface. Conversely, the balanced master-surface weighting applies the pure master-slave weighting twice, reversing the surfaces on the second pass, which minimises the penetrations of the contact bodies. Therefore it provides more accurate results than the pure master-slave surface in most cases and should be used whenever possible. The pure master-slave surface weighting is used in the case such as when a rigid surface contacts a deformable surface.

3.6.2 Tracking Approach

In the simulation of the contact / impact problem, a node on a contact surface is possible to contact any facet on the opposite contact surface. There are two commonly used

contact tracking approaches, i.e. global search and local search (ABAQUS analysis user's manual, 2008). At the beginning of the simulation, an exhaustive global search is carried out to determine the closet master surface facet for each slave node of each contact pair. As the computing cost of global search is relatively high, a global search is only conducted every few hundred time increments in a contact / impact model. Conversely, a less expensive local search is performed in most time increments, where a given slave node only searches the facets which are attached to the previous tracked master surface node to determine the closest facet. Because the time increments are small in most situations, the movement amongst contacting bodies is very limited from one increment to the next and the local search is adequate to track the motion of the contact surfaces.

3.6.3 Constraint Enforcement Method

In the simulation of contact problem, two methods to enforce contact conditions have been commonly used, i.e. a kinematic predictor/corrector method and a penalty method (ABAQUS analysis user's manual, 2008). By using the kinematic contact method, the kinematic state of the model is first advanced without considering the contact conditions in each increment of the analysis. If the slave nodes penetrate into the master surface, the time increment, the depth of the penetration of each node, the mass associated with it will be used to calculate the resisting force to oppose the penetration. This resisting force will make the slave nodes to exactly contact with the master surface. In other words, no penetration of slave nodes into the master surface is allowed in the kinematic contact method. The penalty contact applies less stringent enforcement of contact constraints than the kinematic contact method. It searches for the slave node penetration in the current configuration. Contact forces, which calculated as the penetration distance times the penalty stiffness, are applied to the slave nodes to oppose the penetration. At the same time, opposite forces act on the master surface at the penetration point.

3.6.4 Frictional Model

Apart from the normal forces, when surfaces are in contact, they normally transmit shear forces across their interface as well. Coulomb friction is a common friction model used to describe the interaction between two contacting surfaces. The tangential motion will not start until the frictional shear stress reaches a critical value (τ_{crit}), which is defined by:

$$\tau_{crit} = \mu \cdot p \tag{129}$$

where μ is the coefficient of friction and p is the normal contact pressure. If the shear stress is below τ_{crit}, there will no relative motion between the contact surfaces (sticking). While when the frictional shear stress reaches its critical value relative motion (slipping) occurs.

3.7 Summary

In this chapter, the fundamental theory of Finite Element Method, such as Hamilton's Principle and basic analysis procedure of FEM, has been discussed. The formulations of four different types of finite elements, i.e. 3-D solid element, 2-D plane stress/strain element, plate element and shell element, are presented. Two commonly used non-linear FE solution methods, implicit method and explicit method, are compared. Additionally, the elastic-plastic material constitutive model and contact algorithms of FE simulation have been briefly outlined. Furthermore, the application of FEM to the metal spinning simulation, e.g. development and verification of the metal spinning FE models, are given in Section 4.2, 5.3 and 6.3 of the following chapters.

4. Effects of Roller Path Profiles on Material Deformation

Until recently, the limited research work on the roller path profiles have been mainly carried out by means of experimental investigation alone (Hayama et al., 1970) or by simplified 2-D FE simulation (Liu et al., 2002). Possible causes of wall thinning in the workpiece during conventional spinning are still not fully understood. For this reason, four representative roller path profiles, i.e. combined concave and convex, convex, linear, and concave curves, have been designed and used to carry out experimental investigation in this study. 3-D elastic-plastic FE models of metal spinning have been developed by using commercial FE software - Abaqus. The FE models have been verified by conducting mesh convergence study, evaluating scaling techniques, and comparing dimensional results. Finally, effects of these roller path profiles on the variations of tool force, stress, wall thickness, and strain in the conventional spinning have been analysed numerically. The results show that using a concave path produces relatively high tool forces, stresses and reduction in wall thickness, comparing with the corresponding results obtained from other roller paths. Conversely, low tool forces, stresses and wall thinning are obtained in the FE model using a convex roller path.

4.1 Experimental Investigation

4.1.1 Experimental Setup

By using the commercial spinning Computer-Aided Manufacturing (CAM) software - OPUS, CNC programs of various roller passes have been developed. Figure 4.1 illustrates the setup and the schematic diagram of the spinning experiment, where the angle between the roller axis and the mandrel axis is 45°. The blank is made of mild steel (DC01) and its diameter and thickness are 240 *mm* and 2 *mm*, respectively. A feed rate of 800 *mm/min* and a spindle speed of 400 *rpm* are chosen for all the experimental

runs, as these parameters are commonly used in the production of Metal Spinners Group Ltd and have been verified by FE simulation before conducting the experiments.

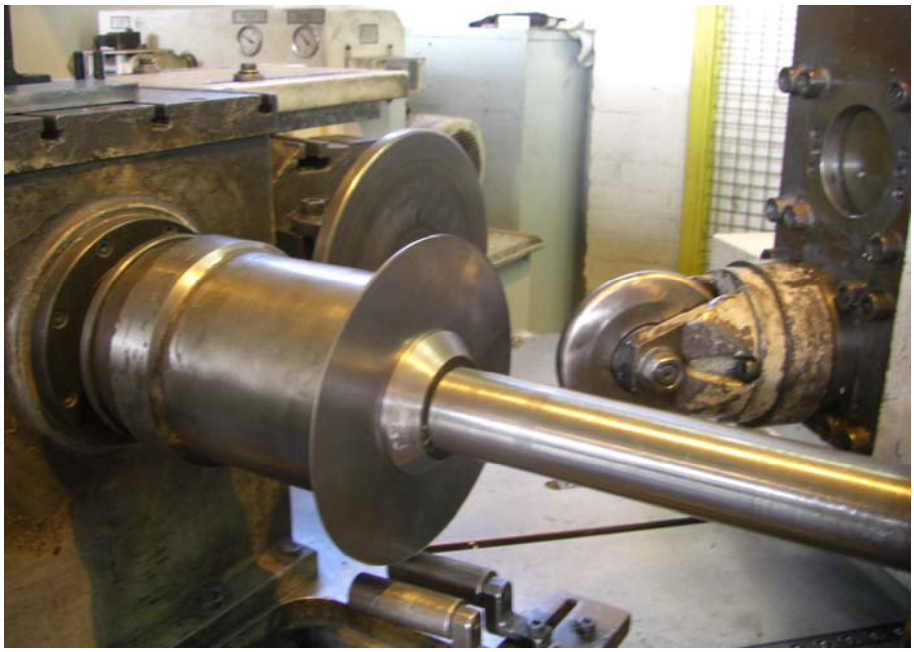

(a) Experimental setup

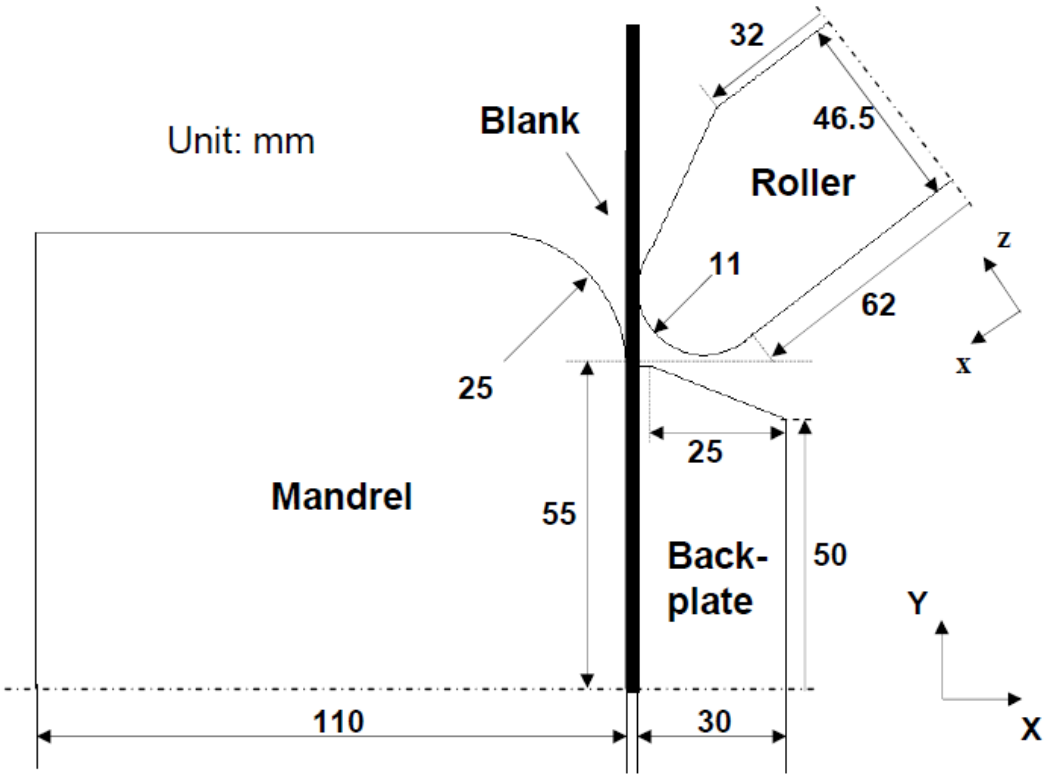

(b) Schematic diagram

Figure 4.1 Spinning experiment

4.1.2 Design of Various Roller Path Profiles

Based on the results of FE simulations and corresponding verifying experiments using a range of CNC roller path designs, four representative roller path profiles have been selected for analysing their effects on the material deformation of the conventional spinning process. As shown in Figure 4.2, these roller path profiles include combined concave and convex roller path (Trial 1), convex roller path (Trial 2), linear roller path (Trial 3) and concave roller path (Trial 4). It is clear that all roller path designs consist of two forward passes and one backward pass between them. The equations of trendlines of the first forward pass of each path design have been given in Figure 4.2. The positions of the final points of the corresponding roller passes in these path designs are approximately the same, where the coordinates of the final points are also shown in Figure 4.2.

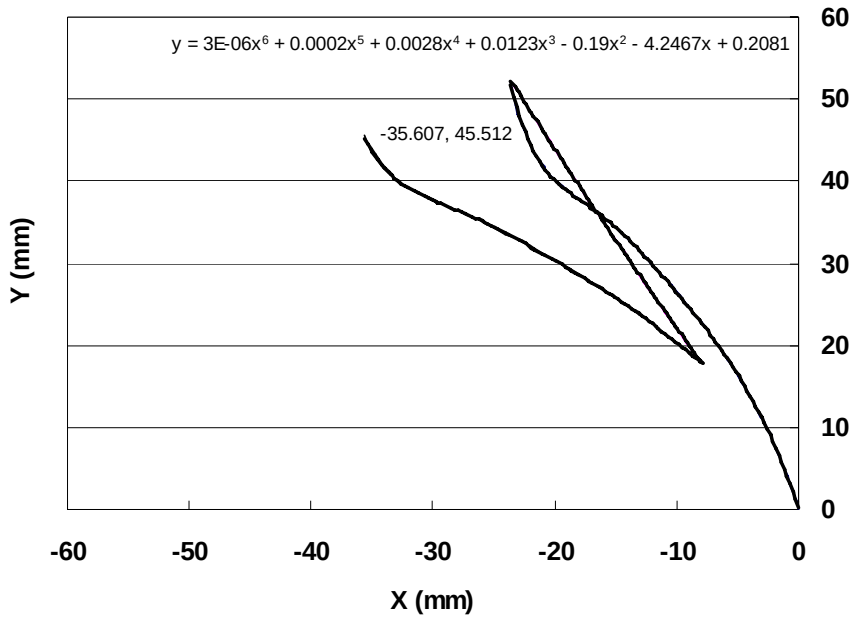

(a) Roller path - Trial 1

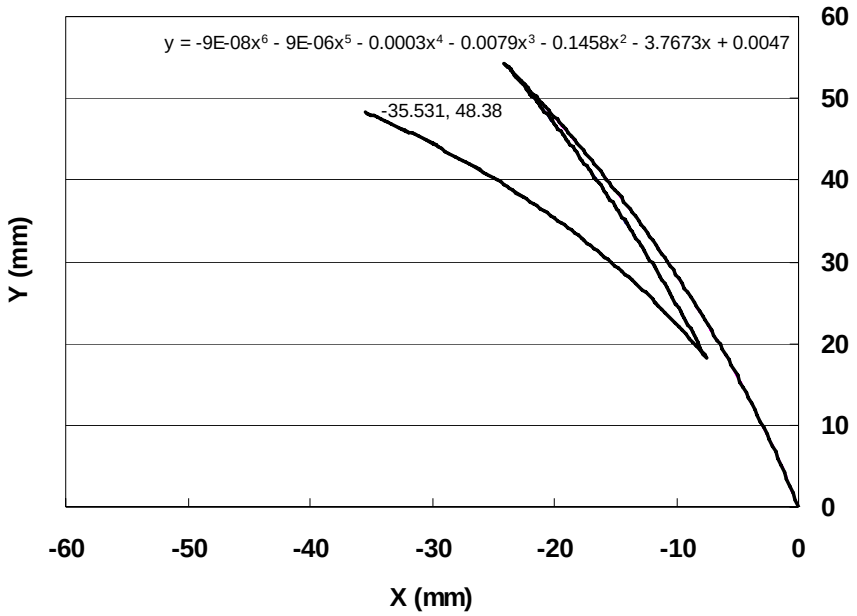

(b) Roller path - Trial 2

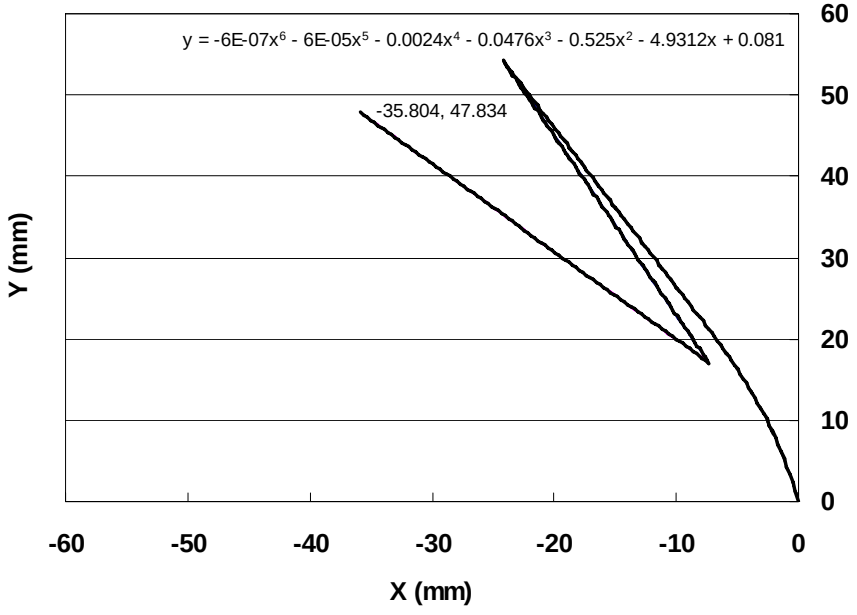

(c) Roller path - Trial 3

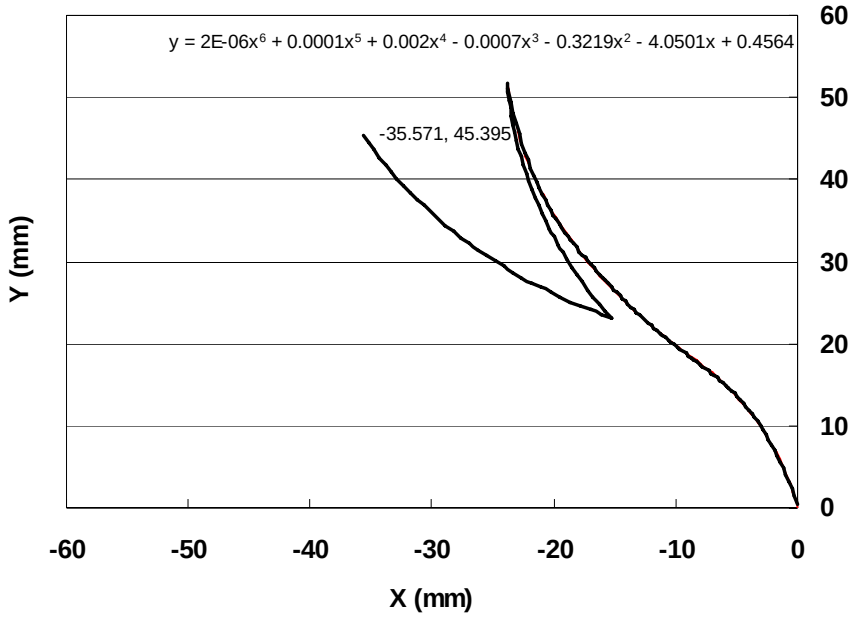

(d) Roller path - Trial 4

Figure 4.2 Roller path profile design

Verifying experiments have been carried out by using roller path Trials 1, 2 and 3. Figure 4.3 illustrates the experimentally spun samples; their wall thickness variations have been measured and used to evaluate the FE analysis results. In addition, the roller path Trials 5 and 6, shown in Figure 4.4, are developed to study the effects of roller path curvature on the wall thickness variation. Clearly, both of the roller path designs use concave curves, but a greater curvature is used in roller path Trial 6.

(a) Trial 1 (b) Trial 2 (c) Trial 3

Figure 4.3 Experimentally spun samples by using different CNC roller paths

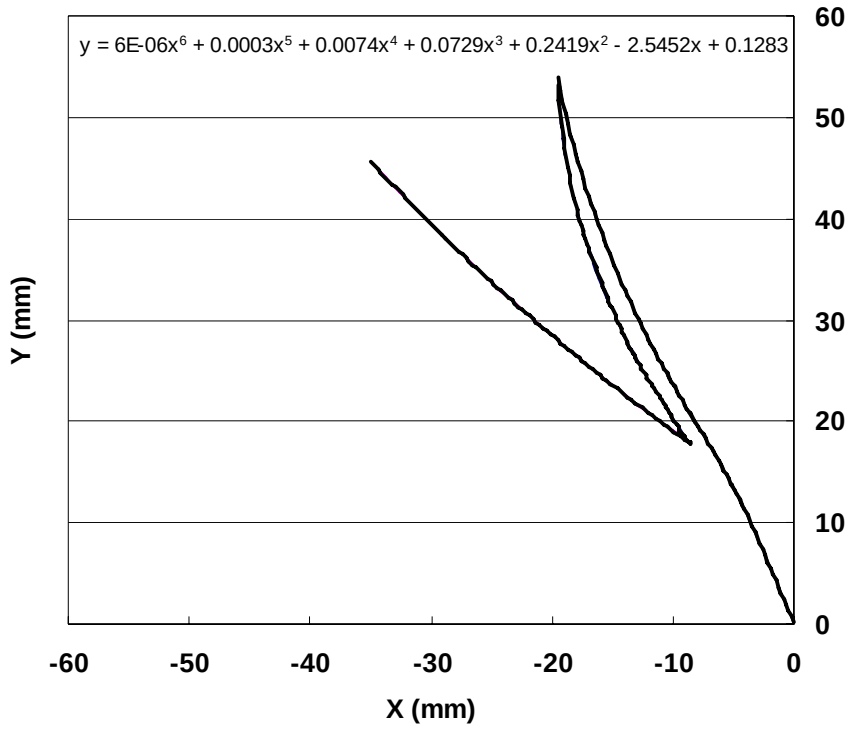

(a) Roller path – Trial 5

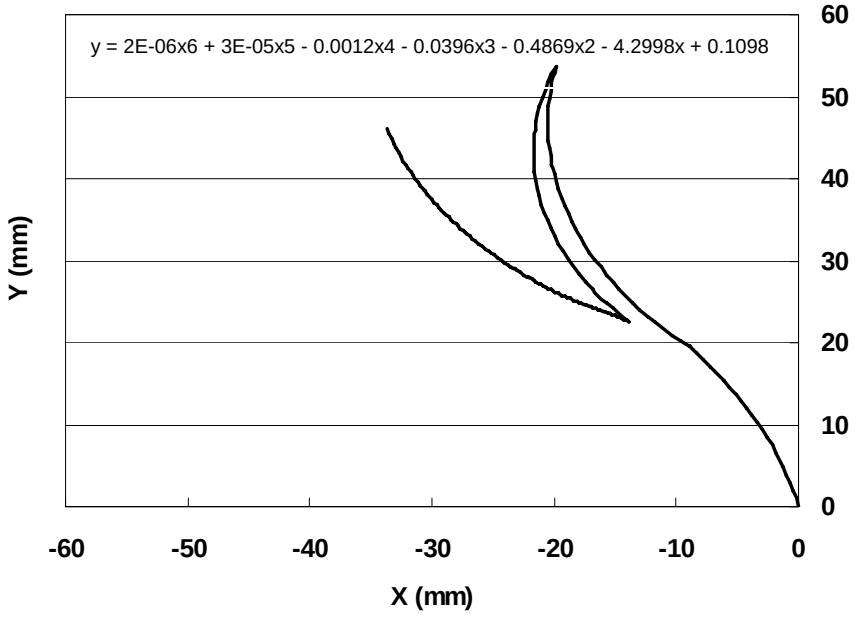

(b) Roller path – Trial 6

Figure 4.4 Concave roller path profiles using different curvatures

4.2 Finite Element Simulation

4.2.1 Development of Finite Element Models

The explicit FE solution method has been chosen to analyse the spinning process. Comparing with the implicit FE method, the explicit FE method determines a solution by advancing the kinematic state from one time increment to the next, without iteration. It is more robust and efficient for analysing the metal spinning process, which can be considered as a quasi-static problem including large membrane deformation and complex contact conditions.

In order to improve the computational efficiency, the spinning tools – roller, mandrel, and backplate, are modeled as 3-D analytical rigid bodies, leaving the blank as the only deformable body. 3-D eight noded reduced integration linear continuum shell elements (SC8R), which provide a better capability to model two–side contact behaviour and transverse shear deformation than 2-D conventional shell elements, are used to mesh the blank. Moreover, it has been observed that the SC8R element can produce accurate numerical results, based on a force measurement experiment and the corresponding FE simulation (Long et al., 2011).

In this study, nine integration points along the element thickness direction have been used in order to accurately compute the state of stress through the blank thickness, as also suggested by Klimmek et al. (2002). Enhanced hourglass control, which provides an increased resistance to the hourglassing problem and more accurate displacement solutions than the default hourglass control (Abaqus analysis user's manual, 2008), is used in the FE analysis models. A central area (radius of 50 *mm*) of the blank is neglected, since it is clamped between the mandrel and the backplate and almost no deformation takes place. The sweep meshing technique is employed to mesh the blank, in which 4320 elements and 9000 nodes are generated.

The material of the blank is assumed to be homogeneous and isotropic. The elastic behaviour of the material is defined by Young's modulus of 198.2 GPa, Poisson's ratio

of 0.3, and mass density of 7861 kg/m3. The von Mises yielding criterion and isotropic hardening have been used to model the material plastic response. Figure 4.5 shows the true stress-strain curve of the material obtained from a uni-axial tensile test, where a flat sample was tested at room temperature under ASTM E8M (Standard Test Methods for Tension Testing of Metallic Materials) by Westmoreland Mechanical Testing & Research, Ltd.

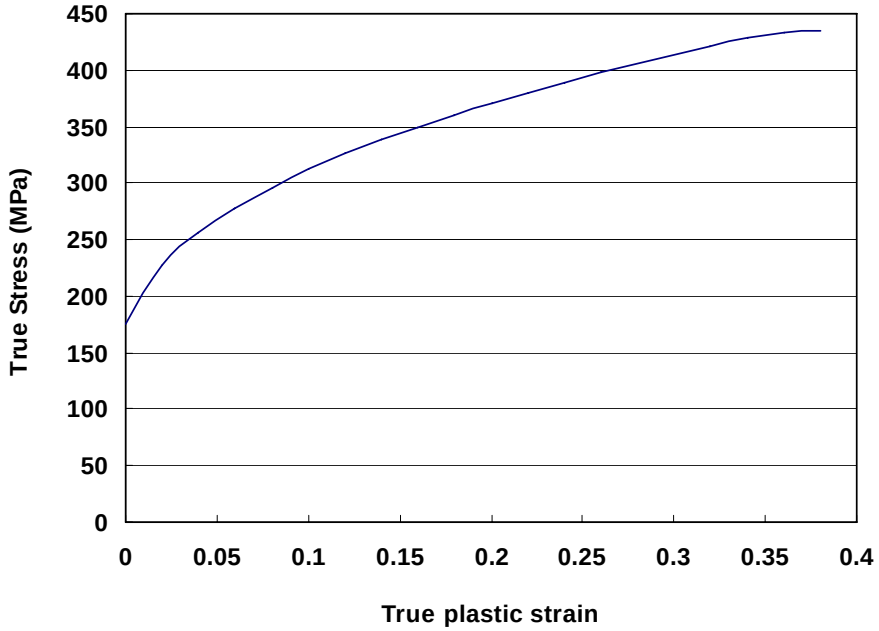

Figure 4.5 True stress-strain curves of Mild steel (DC01)

The penalty enforcement method and Coulomb's friction law have been used to simulate the normal and sliding contact behaviors between the tools and blank, respectively. The frictional coefficient between the roller and the blank is set to be low, since the roller rotates along its own axis during the spinning process. Three Coulomb frictional coefficients have been assigned to three contact pairs of tools and blank: mandrel-blank 0.2, backplate-blank 0.5, and roller-blank 0.02 (Razavi et al., 2005).

Three steps have been applied in the spinning simulation. At the first step, a compressive force of 150 *kN* is applied on the backplate, which accounts for the blank being clamped between the backplate and mandrel. The second step involves applying

a rotational boundary condition to the backplate and mandrel, in order to model the synchronous rotation of the blank, backplate and mandrel. Finally, to realise the complex nonlinear roller path (passes), two displacement boundary conditions in the local x and z directions, as shown in Figure 4.1(b), are applied to the roller.

These two displacement boundary conditions are calculated by transferring the CNC programs, which are initially developed in the global coordinate system (X-Y), into the local coordinates (x-z). The following equations have been used to calculate the local coordinates from the global coordinates:

$$x = -X\sin\theta - Y\cos\theta \tag{130}$$

$$z = X\cos\theta - Y\sin\theta \tag{131}$$

where (x, z) is the local coordinates, (X, Y) represents the global coordinates, and θ is the angle between axis X and axis z, which is 45° in this experimental setup.

Additionally, to speed-up the FE solution time, the mass scaling method with a scaling factor of 25 has been used in all of the models. Parallel FE analyses which can effectively reduce the computing time in the simulation of spinning process (Quigley and Monaghan, 2002b) have been performed using a workstation of Quad-Core AMD Opteron^{TM} CPU 2.2GHz and RAM of 6GB.

4.2.2 Verification of Finite Element Models

In this section, FE models are verified not only by evaluating mesh convergence and assessing scaling methods, but also by comparing the FE analysis dimensional results with experimental measurements.

4.2.2.1 Mesh Convergence Study

A mesh convergence study has been carried out on the FE model using roller path Trial 1. Table 4.1 gives details of the meshes used in the three FE models and the

corresponding numerical results of maximum tool forces and minimum wall thicknesses. The mesh density used in FE model 2 and FE model 3 is about two and three times of that used in FE model 1, respectively.

Comparing with the axial force obtained from model 3, both model 1 and model 2 produce similar axial force results, where the relative errors are 2%. However, significant differences in the radial force and tangential force have been observed between model 1 and model 3, where the relative errors are 48% and 9%, respectively. By increasing the number of elements from 1920 to 4320, the relative errors of the radial force and tangential force between model 2 and model 3 have been decreased to 7% and 1%, respectively. On the other hand, a minimum wall thickness of 1.945 *mm* is obtained by model 1, while model 2 produces a wall thickness of 1.908 *mm*, which is much closer to the corresponding value of model 3, i.e. 1.909 *mm*.

Table 4.1 Mesh convergence study

Model	Number of elements	Radial nodes	Circumferential nodes	Average aspect ratio	CPU time* (*h:m:s*)	F_a (*N*)	F_r (*N*)	F_t (*N*)	Thickness (*mm*)
1	1920	17	120	2.46	112:42:55	4182	1833	265	1.945
2	4320	25	180	1.65	223:51:37	4177	1327	289	1.908
3	6380	30	220	1.41	338:39:50	4104	1239	292	1.909

Furthermore, the sensitivity of stress to the mesh density of the FE models has also been analysed. As illustrated in Figure 4.6(a) – (c), similar von Mises stress distributions of the three FE models listed in Table 4.1 have been observed during the 1st forward pass. As shown in Figure 4.6(d), which compares the variations of von Mises stress along a radial node path under the local forming zone, a good agreement between model 2 and model 3 has been observed and the maximum difference of stresses in the local forming zone is only 2%. Nevertheless, there is a considerable difference of stresses in the local forming zone between model 1 and model 3, where the maximum

error is 9%. Therefore, by analysing the variations of tool forces, wall thickness and stress of these three FE models with different mesh density, it is believed that sufficient convergence has been achieved by using the meshing of FE model 2, which has been used in all the FE models of this study.

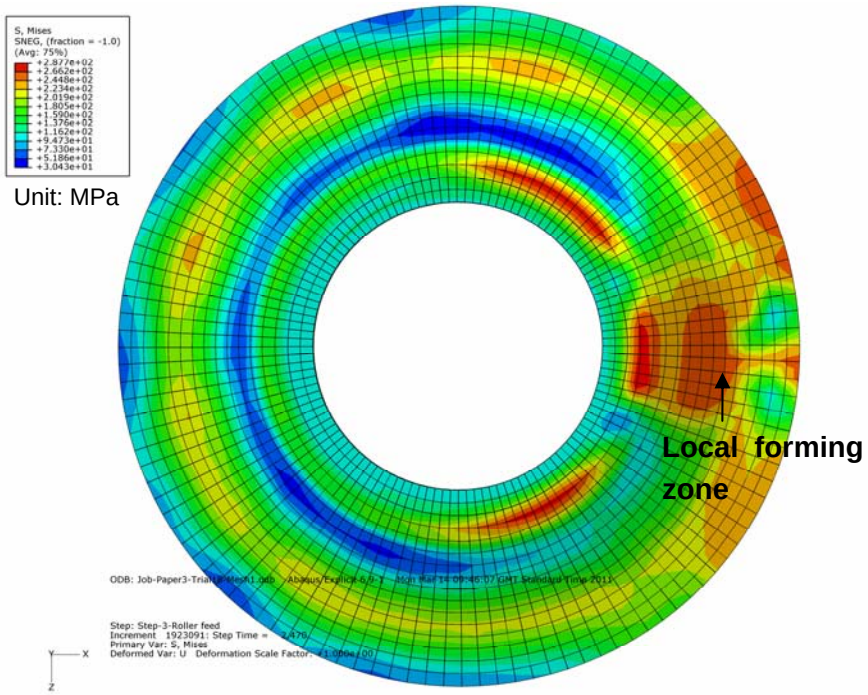

(a) Model 1

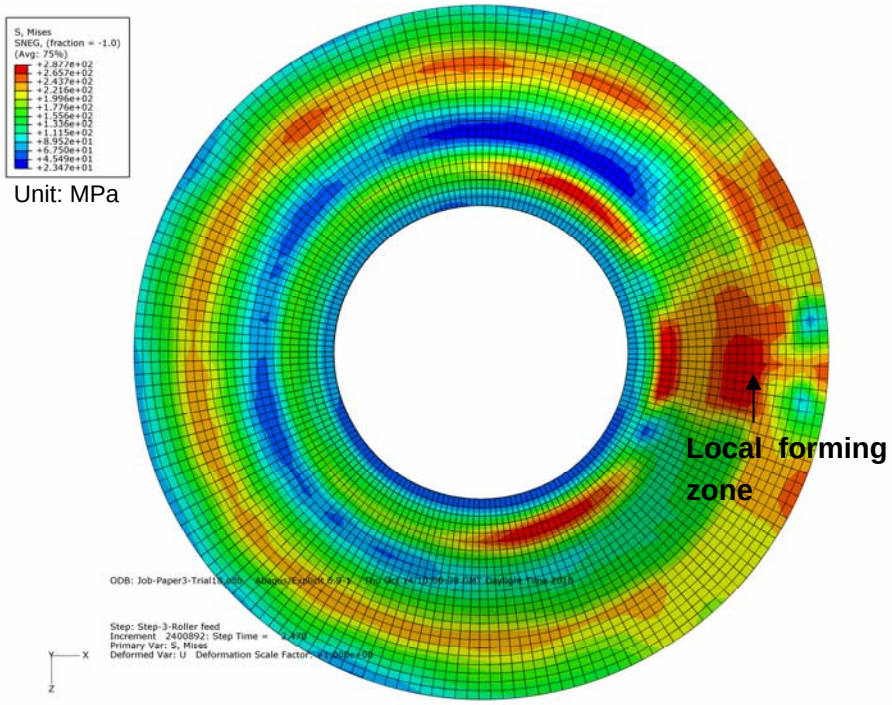

(b) Model 2

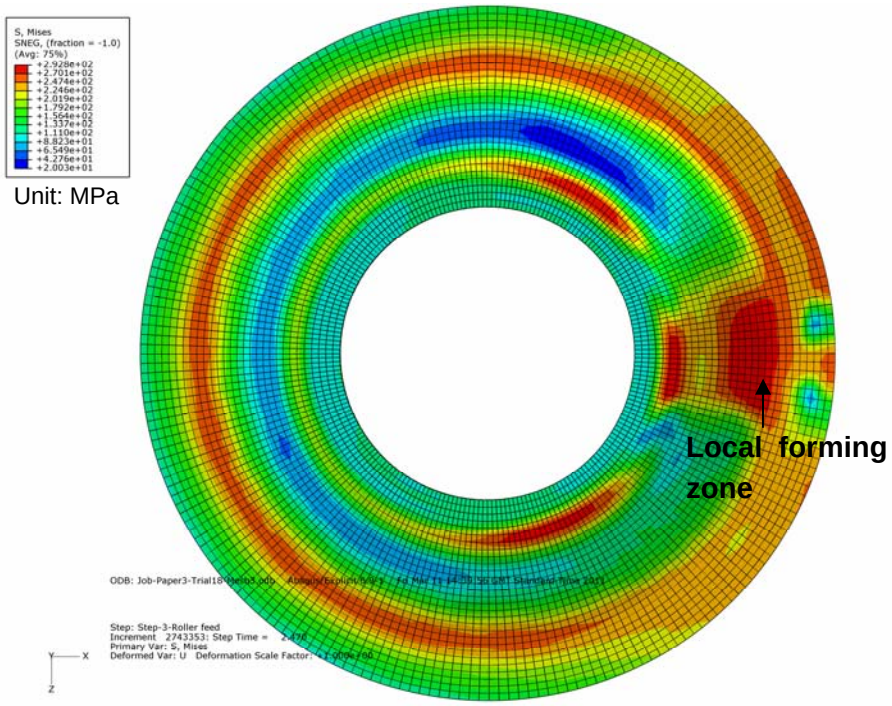

(c) Model 3

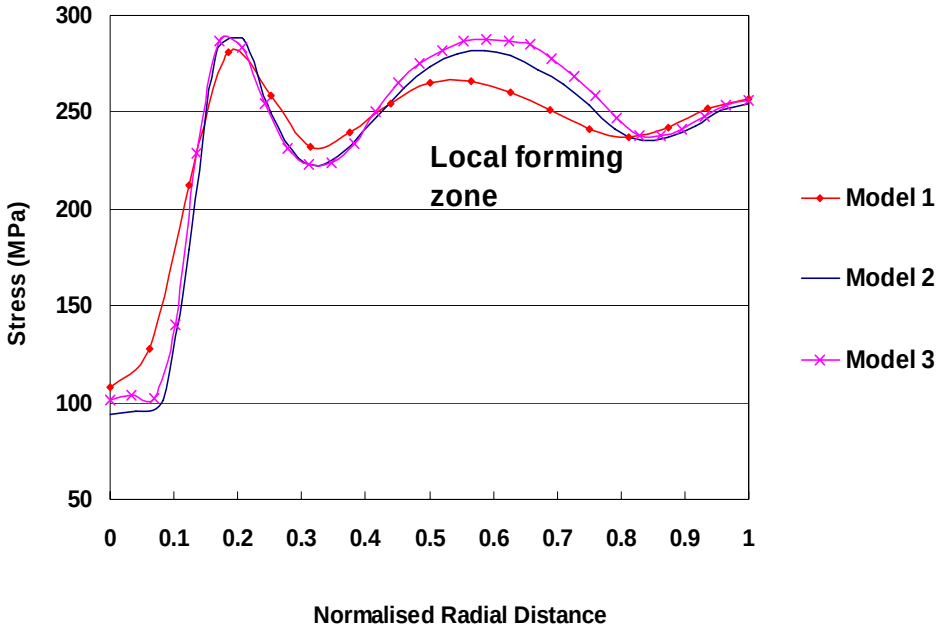

(d) Stress distribution along radial path

Figure 4.6 Variations of von Mises stress in 1st forward pass of FE model

4.2.2.2 Assessment of Scaling Methods

The simulation accuracy and computing efficiency of two scaling methods, i.e. load rate scaling and mass scaling, have been evaluated in this section. As shown in Table 4.2, CPU time and FE analysis results of two models, which use mass scaling by a factor of 25 (Model 2) and load rate scaling by an equivalent factor of 5 (Model 4), are compared with a model which does not use any scaling (Model 5). In terms of result accuracy, both the scaling models agree well with none scaling model. The maximum errors of radial forces in both scaling models are below 1%. The corresponding errors of axial and tangential forces are less than 6%. There is almost no difference of wall thickness among these models. As for the computing efficiency, both scaling methods speed up the simulation process by a factor of 5, indicating that using a mass scaling factor of q^2 or a load rate scaling factor of q would speed up the spinning FE simulation by a factor of q, in agreement with equation (110)-(112).

Table 4.2 Scaling method study – Trial 1

Model	**Scaling method**	**Scaling factor**	**Stable increment** (*s*)	**Processing time** (*s*)	**CPU time** (*h:m:s*)	F_a (*N*)	F_r (*N*)	F_t (*N*)	**Thickness** (*mm*)
2	Mass scaling	25	1.029e-6	10.29	223:51:37	4177	1327	289	1.908
4	Rate scaling	5	2.058e-7	2.06	222:56:03	4180	1357	292	1.908
5	No scaling	1	2.058e-7	10.29	1119:04:40	3927	1345	278	1.914

4.2.2.3 Comparison of Dimensional Results

Figure 4.7 compares the wall thickness variations of three experimentally spun samples using different roller path profiles with the corresponding FE analysis results. The maximum errors between experimental and FE analysis results of thickness for Trial 1, Trial 2 and Trial 3 are 4.5%, 2.5% and 3%, respectively. Therefore it is considered that the FE simulation shows good correlation with the experiment.

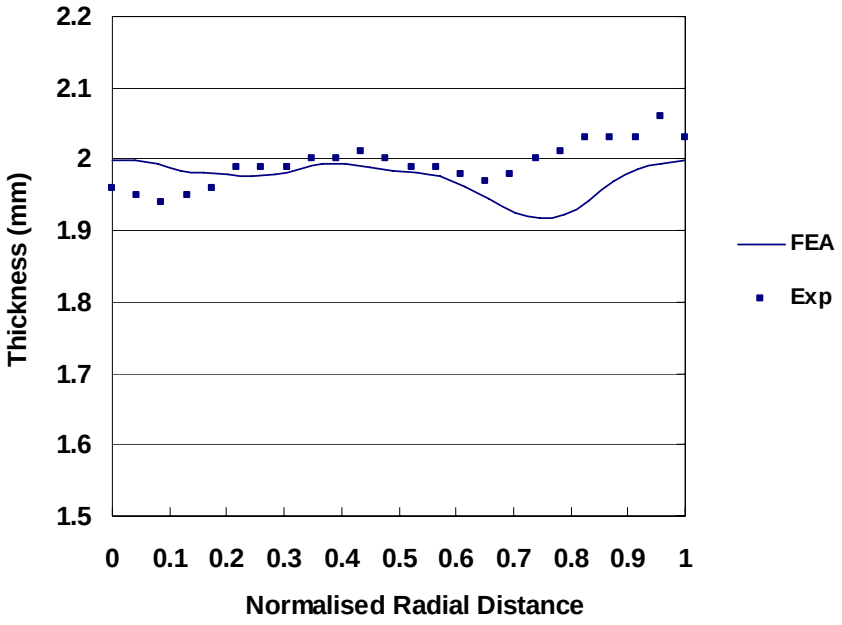

(a) Trial 1

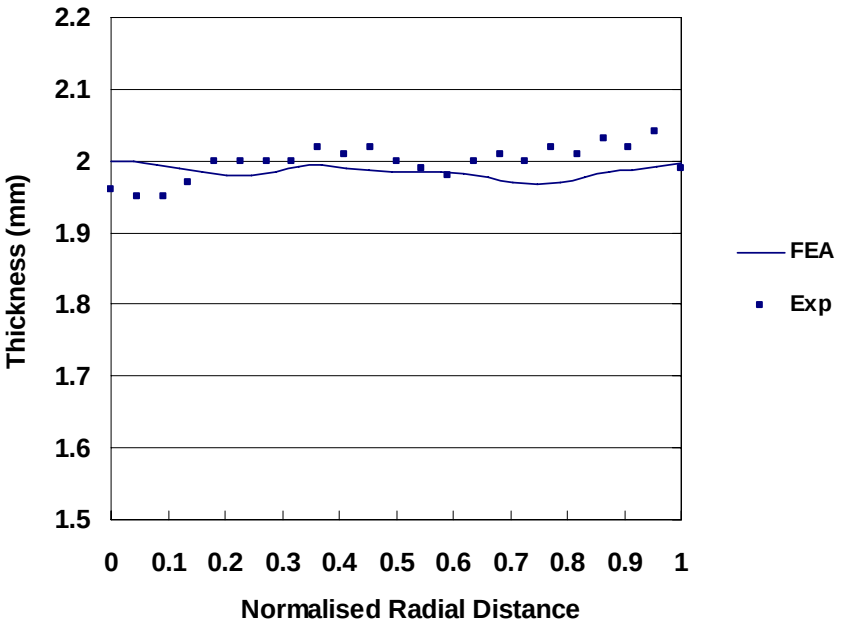

(b) Trial 2

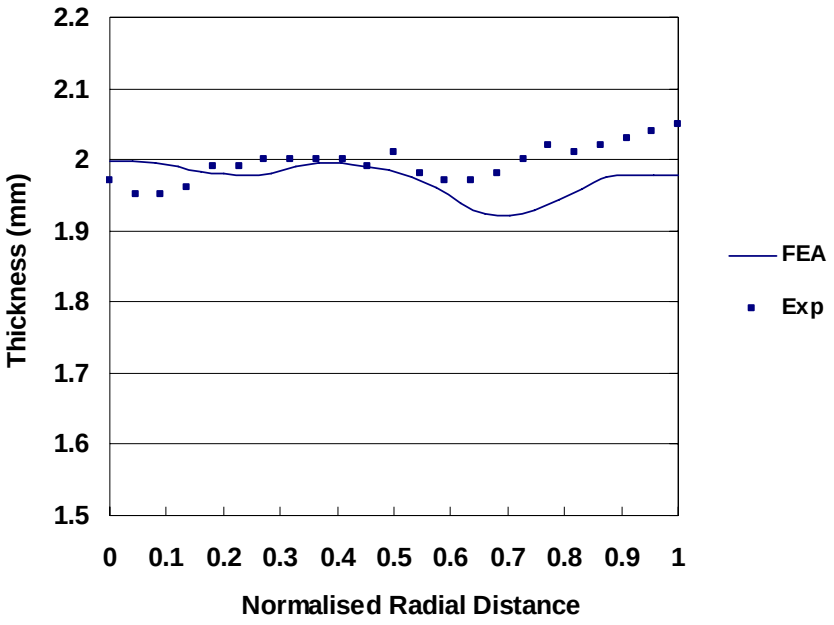

(c) Trial 3

Figure 4.7 Comparison of wall thickness between FE analysis and experimental results

4.3 Results and Discussion

In this section, the effects of various roller path profiles on the tool forces, stresses, wall thickness, and strains have been analysed numerically.

4.3.1 Tool Forces

In this study, the definition of tool force components is shown in Figure 2.1(b), where the radial tool force – F_r and axial tool force – F_a are defined in line with the radial direction and the axial direction of the mandrel, respectively; and the tangential tool force – F_t is perpendicular to both the axial and radial forces. Figure 4.8 compares the maximum radial, axial and tangential tool forces using the four roller path designs over three passes as given in Figure 4.2. Clearly, the axial forces are the highest among three force components, while the tangential force is the lowest. In addition, the concave path produces the highest radial, axial and tangential forces amongst these four roller path profiles. As shown in Figure 4.8(a), in the first forward pass, there is not much difference

amongst the four roller paths in terms of their effects on radial forces; while the convex roller path produces the lowest force in the second forward roller pass. As illustrated in Figure 4.8(b) and 4.8(c), in the forward passes, the lowest axial and tangential forces are observed in the FE models which use the convex roller path. Therefore, it is clear that a convex roller path generally produces the lowest tool forces.

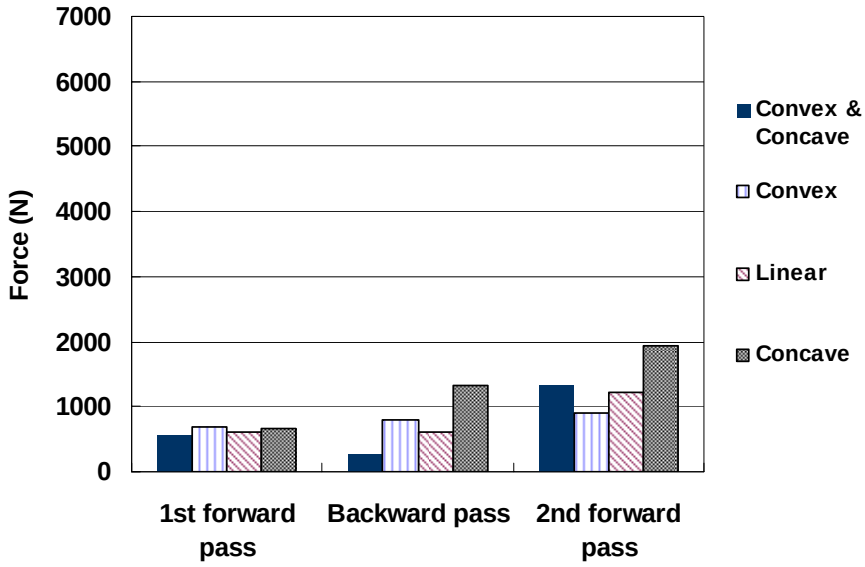

(a) Maximum radial force

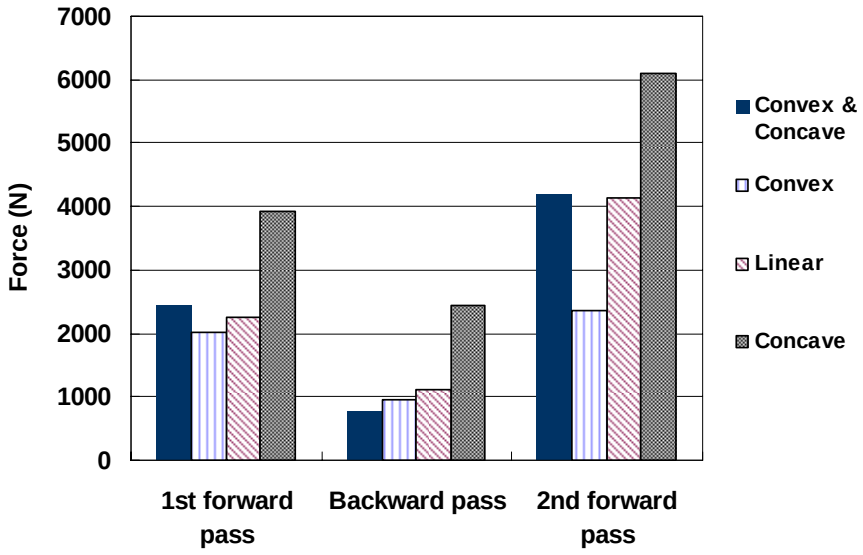

(b) Maximum axial force

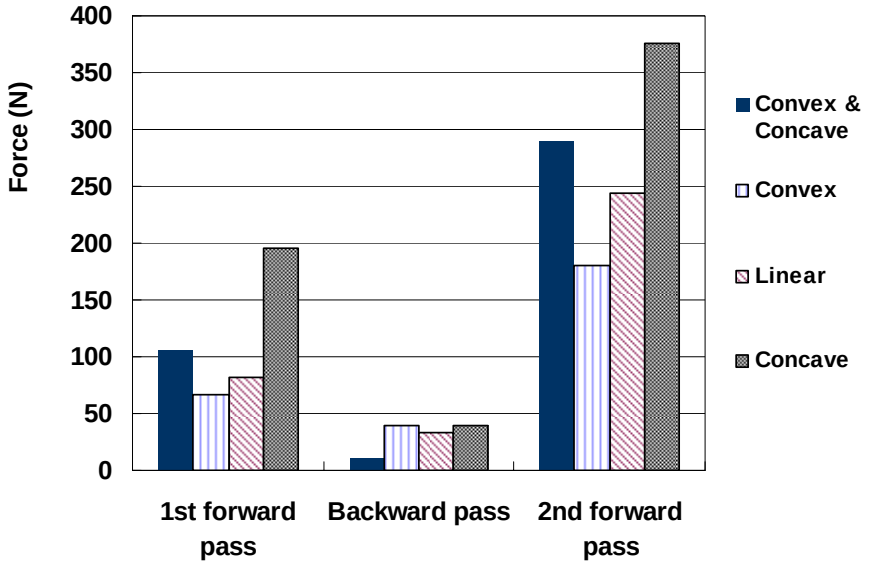

(c) Maximum tangential force

Figure 4.8 Comparison of tool forces using various roller path profiles

Table 4.3 shows the ratios of maximum force components using the four roller path profiles. It is noticeable that the ratios between maximum radial forces to maximum tangential forces of all the four roller path profiles remain unchanged as 5:1. However, the ratios of maximum axial force to maximum tangential force vary between 13:1 for the convex roller path and 17:1 for the linear roller path.

Table 4.3 Ratios of maximum force components using various roller path profiles

Roller Path Profiles	Ratios of Maximum Forces
Trial 1 - Combined convex and concave path	$F_a : F_r : F_t$ = 14: 5: 1
Trial 2 - Convex path	$F_a : F_r : F_t$ = 13: 5: 1
Trial 3 - Linear path	$F_a : F_r : F_t$ = 17: 5: 1
Trial 4 - Concave path	$F_a : F_r : F_t$ = 16: 5: 1

4.3.2 Wall Thickness

Figure 4.9 illustrates the effects of the four roller path profiles on wall thickness variations. It is clear that the wall thickness reduces significantly in two regions: Region A and B. Region A is located between the backplate's clamped area and the workpiece's last point of contact with the mandrel. Region B is located between the workpiece's last contact point with the mandrel and its contact point with the roller.

As illustrated in Figure 4.9(a), after the 1st forward pass, a dramatic wall thickness reduction is observed in Region B, especially in the FE model which uses the concave roller path (Trial 4), where the wall thickness is reduced by 4%. On the other hand, only 0.8% of wall thinning is seen when using the convex roller path (Trial 2); while the wall thicknesses decrease by 1% in the FE analysis models which apply combined convex and concave roller path (Trial 1) and linear roller path (Trial 3).

According to the FE analysis results, there are almost no thickness changes during the backward passes for all of these four roller path trials, thus the thickness variation diagram of the backward pass is not shown here. As shown in Figure 4.9(b), after the second forward roller pass, there is almost no thickness change for the Region A, due to the fact that in the second forward pass the roller does not deform this region, which has already been formed in the first forward pass.

However, at Region B, the wall thickness of the model which uses the concave roller path further decreases by 4% and reaches a thickness of 1.84 *mm*, while the wall thickness of the model using the convex roller path profile only further decreases by 0.5% and remains at 1.97 *mm*. It is thus clear that using the concave roller path in spinning tends to cause the highest reduction of the wall thickness and using the convex roller path helps to minimise wall thickness variations, as also reported by Auer et al. (2004).

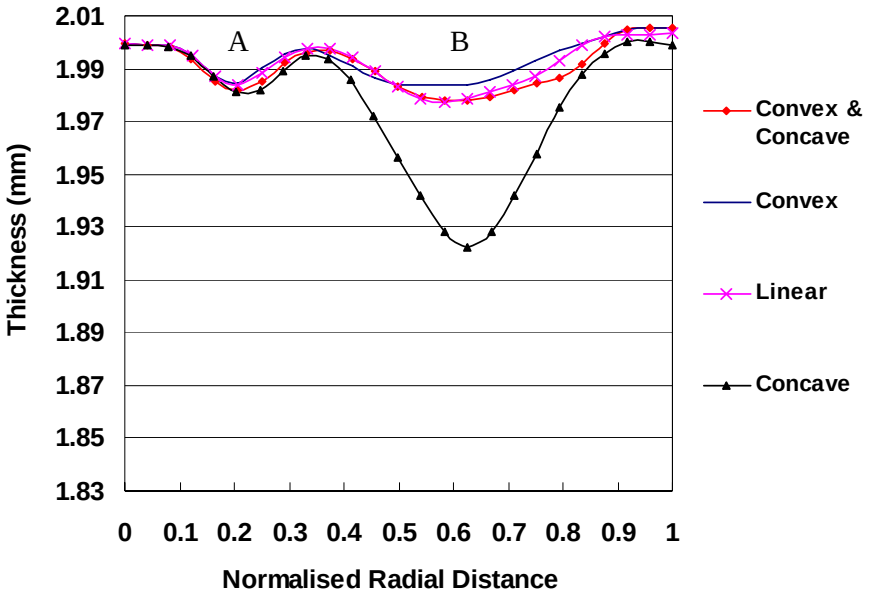

(a) After 1st forward pass

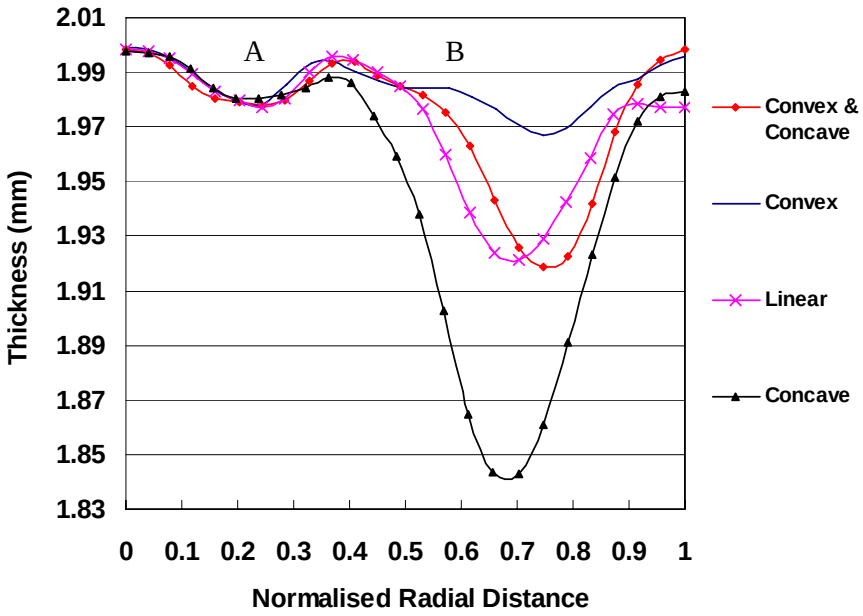

(b) After 2nd forward pass

Figure 4.9 Wall thickness variations using various roller path profiles

Figure 4.10 illustrates the wall thickness variations of FE models using concave roller path profiles with different curvatures - Trial 5 and 6, as shown in Figure 4.4. Clearly, the model using roller path Trial 6, which has a greater curvature of the concave curve than

that of Trial 5, produces a greater wall thickness reduction. Thus it is believed that a greater curvature used in the concave path would result in a greater thinning in wall thickness of a spun part formed by the conventional spinning process.

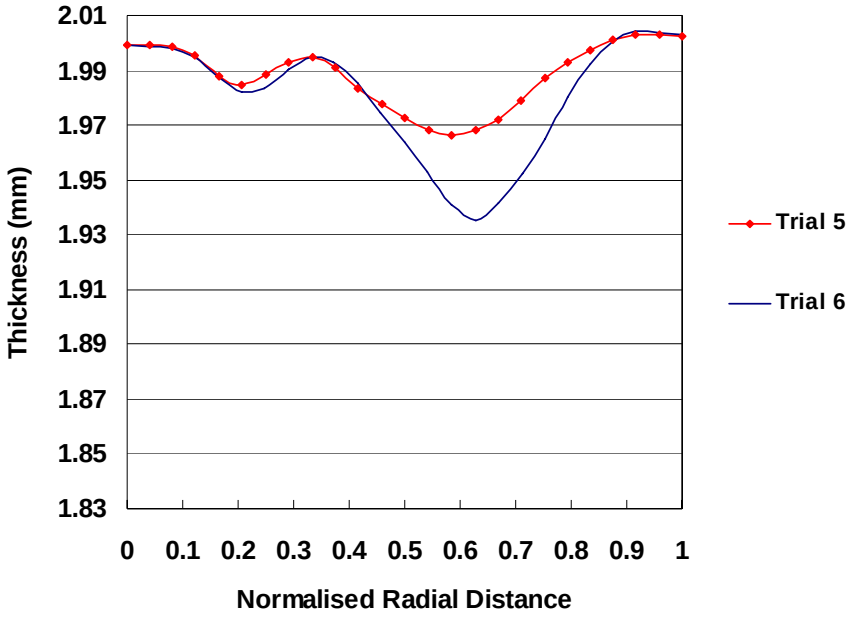

(a) After 1st forward pass

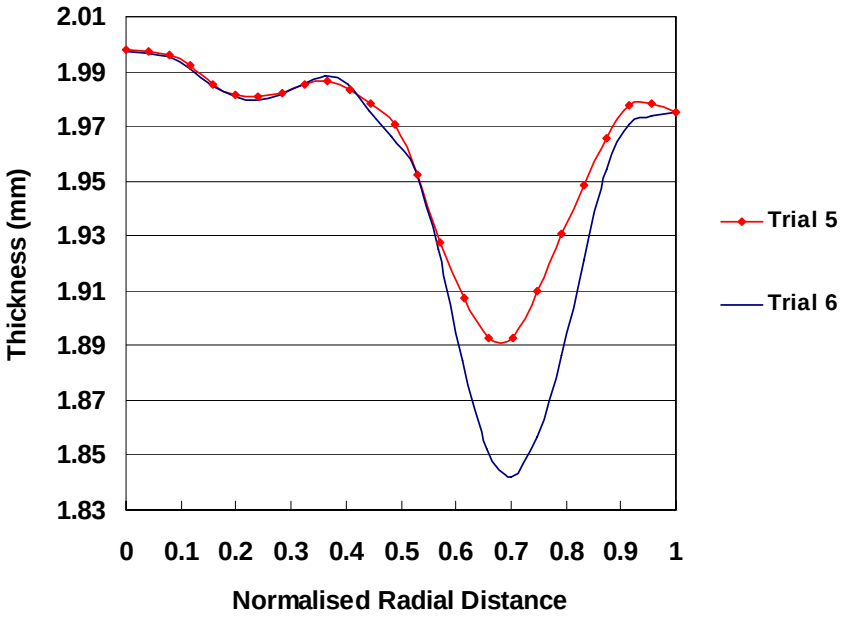

(b) After 2nd forward pass

Figure 4.10 Wall thickness variations using concave path with different curvatures

4.3.3 Stresses

A global cylindrical coordinate system has been used to output the stress values. The radial stress is defined in line with the radial-axis of the mandrel; while the tangential normal stress is in the direction perpendicular to the radial-axis and axial-axis of the mandrel. Figure 4.11 illustrates radial stress (σ_r) variations on both the outer (roller facing) and inner surface (mandrel facing) of a cross-section away from the roller contact position after the first forward pass in the FE models using the four roller path profiles.

As shown in Figure 4.11(a) and (b), the distributions of these radial stresses by using the four roller path profiles are similar. However, much higher radial stresses are induced using the concave roller path in comparison with the corresponding stresses of FE models generated using other roller paths. Furthermore, it is clear that the outer surface of Region A is subjected to high compressive radial stresses; while its inner surface is under tensile radial stresses. Conversely, around Region B, higher tensile and compressive radial stresses are observed on its outer and inner surfaces, respectively. Therefore, Region A and B are subjected to radial bending effects in opposite directions.

Tangential stress (σ_t) variations on both the outer and inner surface of a cross-section away from the roller contact position after the first roller pass have been plotted in Figure 4.12. It is noticeable that the outer surface of Region A is under compressive tangential stresses, as shown in Figure 4.12(a). Moreover, tensile and compressive tangential stresses are observed on the outer and inner surfaces of Region B, respectively. Much higher tangential stresses are shown on the inner surface of workpiece when the concave roller path is applied.

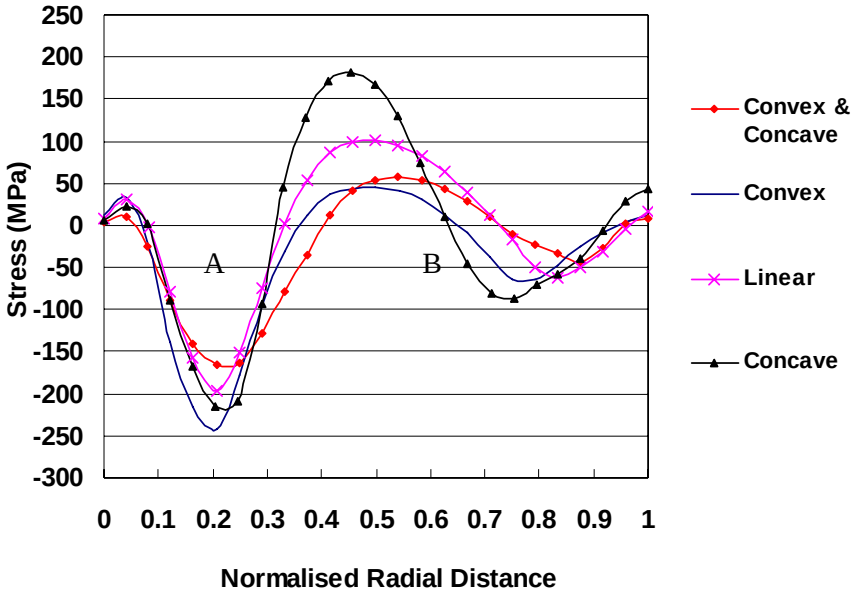

(a) Outer surface of workpiece

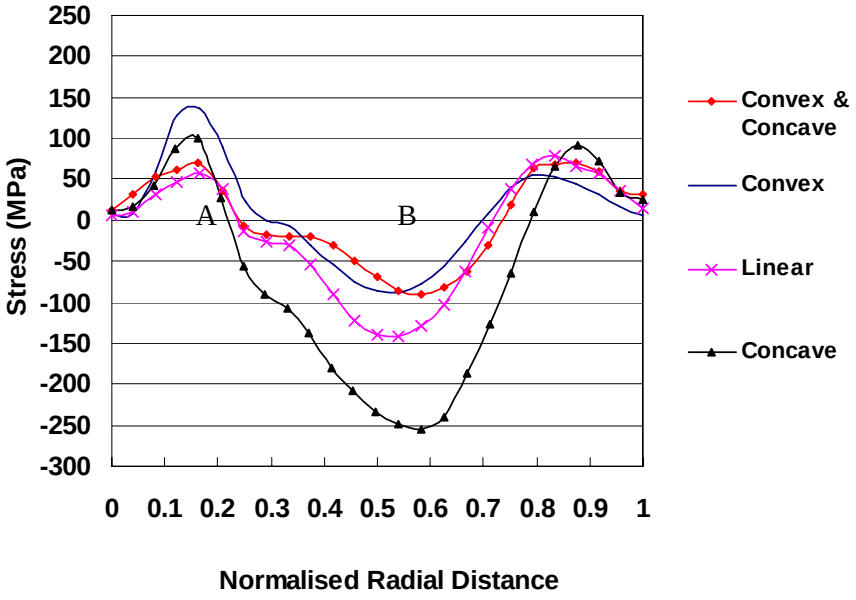

(b) Inner surface of workpiece

Figure 4.11 Radial stress variations after 1st forward pass

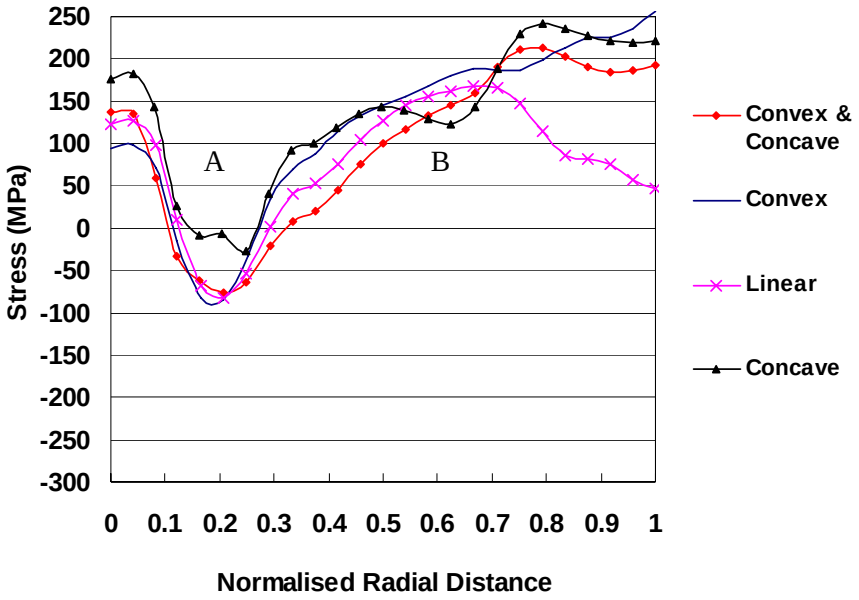

(a) Outer surface of workpiece

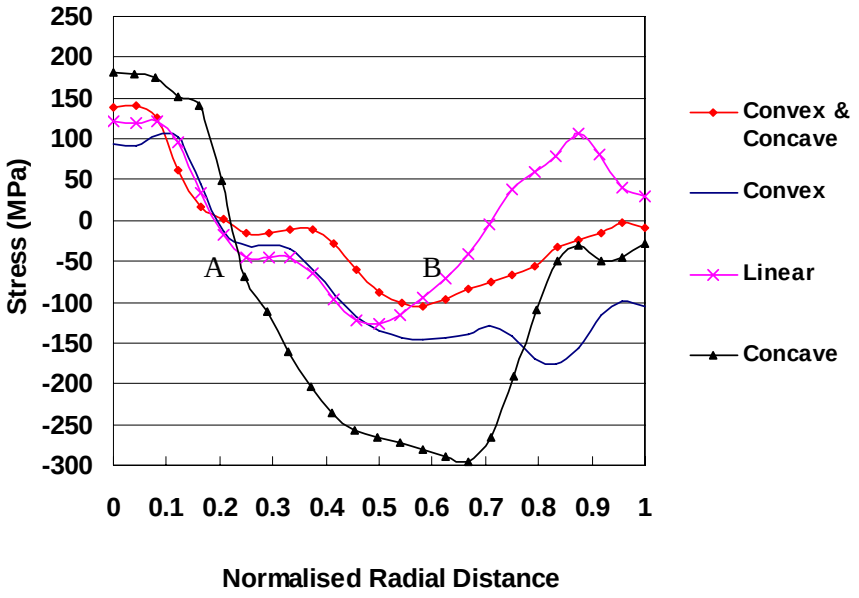

(b) Inner surface of workpiece

Figure 4.12 Tangential stress variations after 1st forward pass

4.3.4 Strains

In order to analyse the cause of wall thinning in the conventional spinning process, variations of the maximum in-plane principal strain (radial strain) and minimum in-plane principal strain (tangential strain) after the first forward pass have been plotted in Figure 4.13 and 4.14, respectively. As shown in Figure 4.13(a), high tensile radial strains are observed in both Region A and B in the outer surface of workpiece; whilst in the inner surface high tensile radial strains take place mainly around Region B, as demonstrated in Figure 4.13(b). These high in-plane tensile radial strains are believed to be the reason of the significant wall thinning in Regions A and B shown in Figure 4.9. In addition, the FE model which uses a concave roller path profile produces much higher tensile radial strains in Region B than FE models which use other roller path profiles, resulting in a higher amount of wall thinning when the concave roller path is applied.

As shown in Figure 4.14, except for Region A in the outer surface of the workpece, both the inner and outer surfaces are subjected to in-plane compressive tangential strains, which would lead to a certain degree of compensation to the wall thinning. However, the dominant high in-plane tensile radial strains shown in Figure 4.13 play a decisive role in wall thinning. It is also noticeable that unlike the variations of in-plane radial strains amongst the models using various roller path profiles, there is not much difference of in-plane tangential strains.

Figure 4.15(a) illustrates the variations of out-of-plane principal strain (thickness strain) in the outer surface of the workpiece. It is clear that both Region A and B of the outer surface are subjected to high compressive thickness strains, indicating the decreasing of wall thickness in those regions. The variations of the thickness strain in the inner surface of the workpiece have been plotted in Figure 4.15(b). In Region A of the inner surface, the low tensile thickness strain is cancelled out by the relatively high compressive thickness strain of the outer surface. Conversely, the compressive thickness strain in the inner surface of Region B is enhanced by the compressive thickness strain of its outer surface. These combined effects of the strains result in less wall thinning in Region A than Region B, as shown in Figure 4.9.

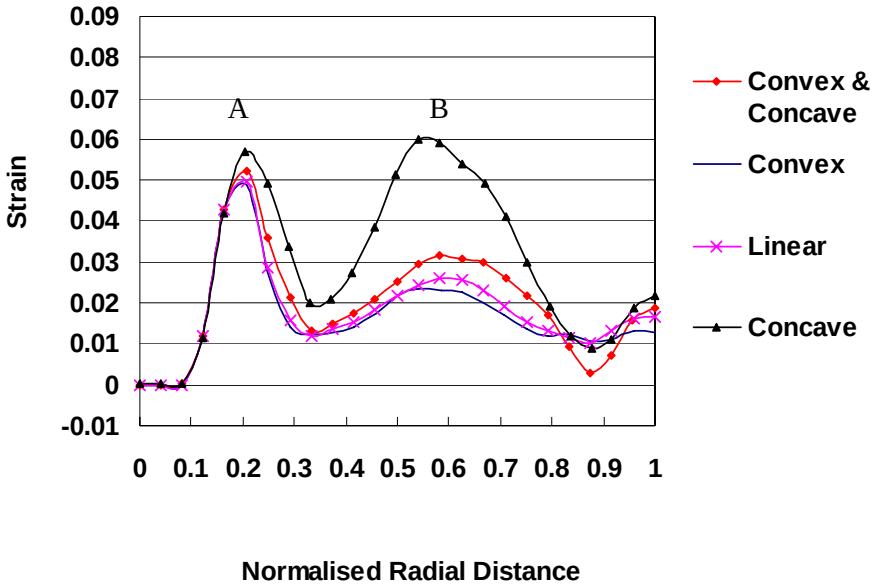

(a) Outer surface of workpiece

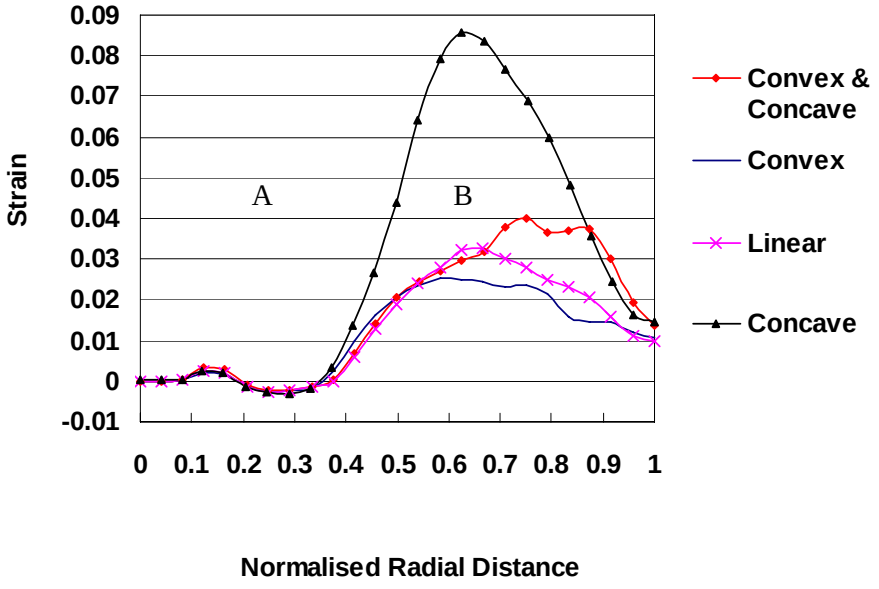

(b) Inner surface of workpiece

Figure 4.13 Maximum in-plane principal strain (radial strain) after 1st forward pass

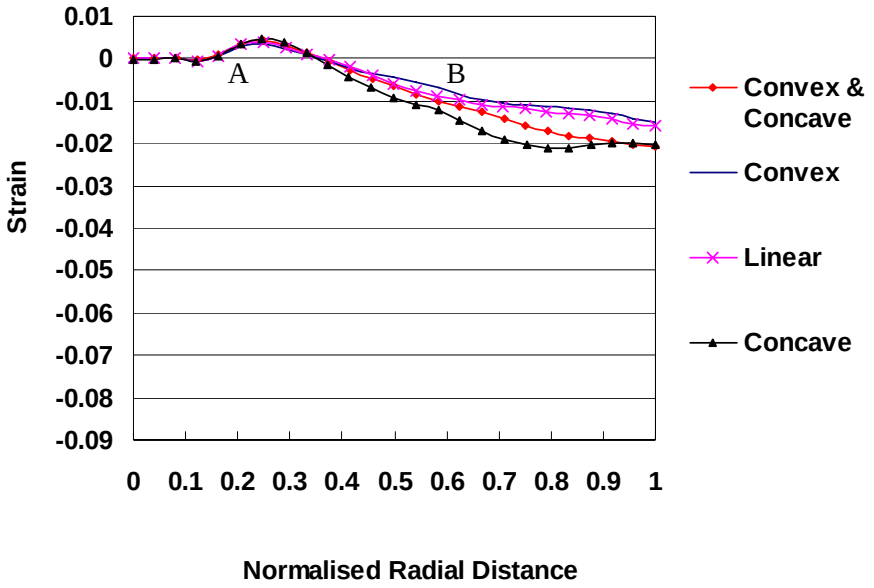

(a) Outer surface of workpiece

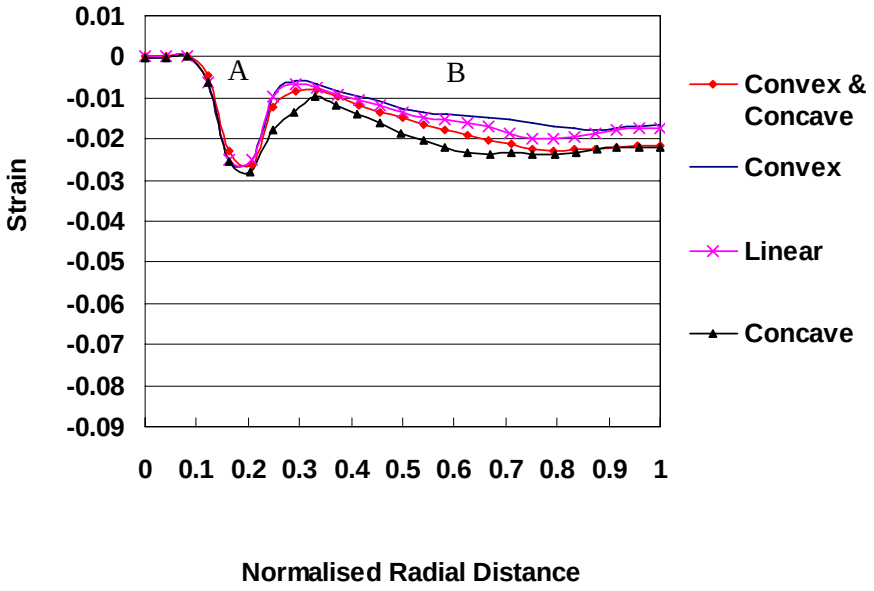

(b) Inner surface of workpiece

Figure 4.14 Minimum in-plane principal strain (tangential strain) after 1st forward pass

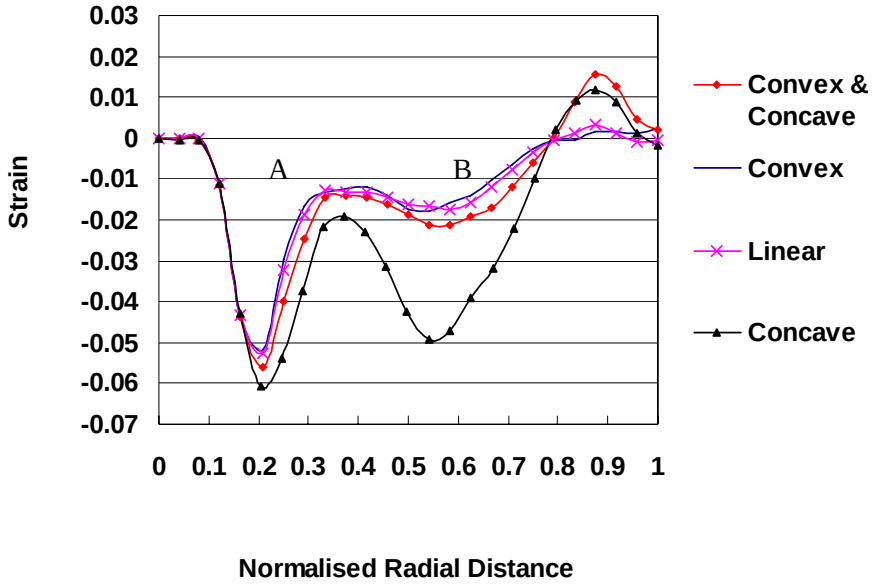

(a) Outer surface of workpiece

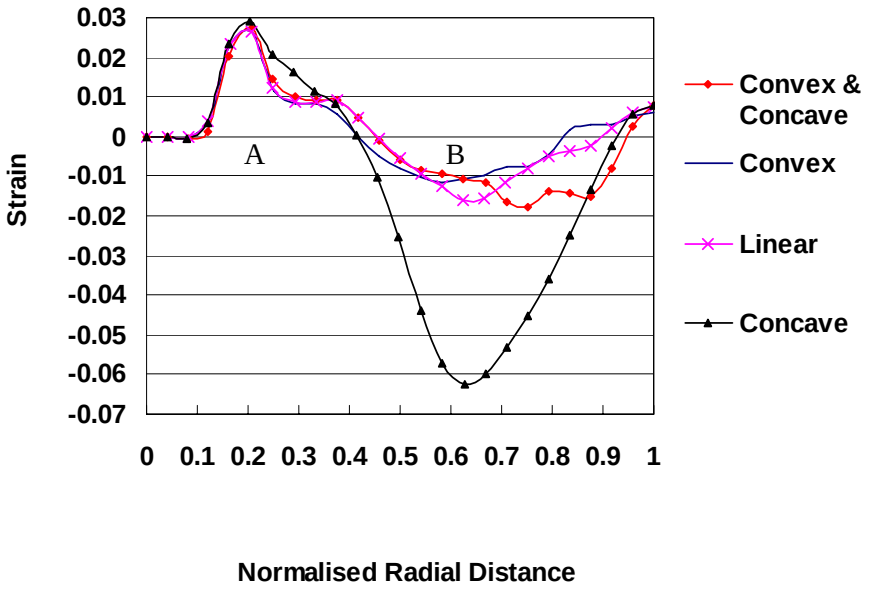

(b) Inner surface of workpiece

Figure 4.15 Out-of-plane principal strain (thickness strain) after 1st forward pass

4.4 Summary and Conclusion

In this chapter, four different roller path profiles, i.e. combined concave and convex, convex, linear and concave curves, have been designed by using spinning CAM software - OPUS. The 3-D elastic-plastic FE models of metal spinning are developed by using FE software - Abaqus. The FE models have been verified by carrying out mesh convergence study, assessing scaling methods, and also by comparing the dimensional results. Based on the experimental investigation and FE analysis of the conventional spinning process using the various roller path profiles, the following conclusions may be drawn:

a) Both mass scaling and load scaling methods are able to significantly speed up the FE simulation of a conventional spinning process. Using a mass scaling factor of f^2 or a load rate scaling factor of f would speed up the spinning FE simulation by a factor of f.
b) FE analysis results indicate that the concave roller path produces the highest tool forces amongst the four different roller path designs. The lowest tool forces are generally observed when the convex roller path is used.
c) Using the concave roller path tends to cause the highest reduction of the wall thickness of the spun part, while the convex roller path helps to maintain the original wall thickness. A greater curvature of the concave path would result in a higher amount of wall thinning of the spun part.
d) High tensile radial strains and low compressive tangential strains have been observed in the FE models. In addition, if a concave roller path is applied, much higher tensile radial strains would be obtained, resulting in greater wall thinning.
e) Two pairs of oppositely directed radial bending effects have been observed in the workpiece during the conventional spinning process.

5. Analysis of Material Deformation in Multi-pass Conventional Spinning

In the current academic research, most published papers on conventional spinning are based on mandrels with a simple linear profile, e.g. conical and cylindrical shapes. Investigations on spinning are mainly limited to no more than three passes (mainly a linear path). Nevertheless, in the industry application, a considerable amount of roller passes have to be used in order to successfully spin a complicated product. Therefore, it is essential to develop a method of generating multiple roller passes for a mandrel with a nonlinear profile and to investigate the material deformation in the multi-pass spinning process. In this chapter, to make the workpiece conform to the non-linear profile of a mandrel, the tool compensation technique has been proposed and employed in the CNC multiple roller passes design. The Taguchi method is used to design the experimental runs and analyse the effects of three process parameters on the dimensional variations of the spun parts. Furthermore, FE simulation is conducted to investigate the variations of tool forces, stresses, wall thickness and strains in this multi-pass spinning process.

5.1 Experimental Investigation

Based on the same experimental setup of Chapter 4, i.e. Figure 4.1, multiple roller passes which can successfully complete the spun part are developed and used to conduct the experiment. The blanks are again made of mild steel (DC01) with diameter of 240 *mm* and thickness of 2 *mm*. In this section, the methodologies of tool compensation and Taguchi experimental design are discussed.

5.1.1 Tool Compensation in CNC Programming

To make the workpiece conform to the nonlinear profile of the mandrel, tool compensation has to be taken into account in the process of designing multiple roller

passes. By studying the case that the roller traces the contour of the mandrel, how to set the tool compensation in the multi-pass design is investigated. As shown in Figure 5.1, Point A, i.e. the intersection point of tangential lines of the roller nose, represents the point on the roller path generated by CNC programming. R is the radius of the round part of the mandrel; r is the roller nose radius. Point *o* is the center of the round part of the mandrel, which is also assigned to be the origin of the coordinate system. Assuming that the coordinate of point A is (x, y), certain geometrical relationships among r, R, x and y, can be obtained by analysing the right-angled triangle (oBC), where

$$oC = oF + FC = x + r \tag{132}$$

$$CB = CE + EB = y + r \tag{133}$$

$$oB = oD + DB = R + r \tag{134}$$

Thus, according to the Pythagoras Theorem, we have

$$(x + r)^2 + (y + r)^2 = (R + r)^2 \quad (x>0,\ y>0) \tag{135}$$

which is the CNC roller path when the roller traces the contour of mandrel. Therefore the design of roller passes should be based on the modified mandrel geometry given in equation (135) as shown in the blue dotted curve of Figure 5.1. This tool compensation technique can also be extended to the design of roller passes for other mandrel profiles, such as linear and concave curve, etc.

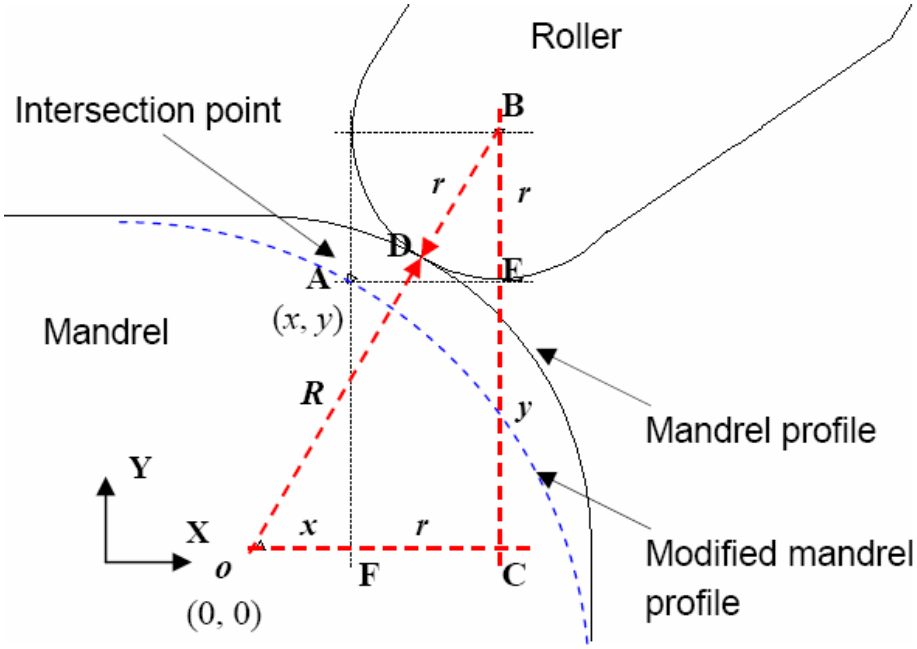

Figure 5.1 Tool compensation

By contrast, if the roller passes are developed based on the mandrel profile, rather than the modified mandrel profile as shown in Figure 5.1, the workpiece cannot fully contact with the mandrel, resulting in wrinkling failures due to unsupported flange. Figure 5.2 illustrates a multi-pass design which does not take the tool compensation into account; and a severe wrinkling failure is observed on the corresponding experimental spun part.

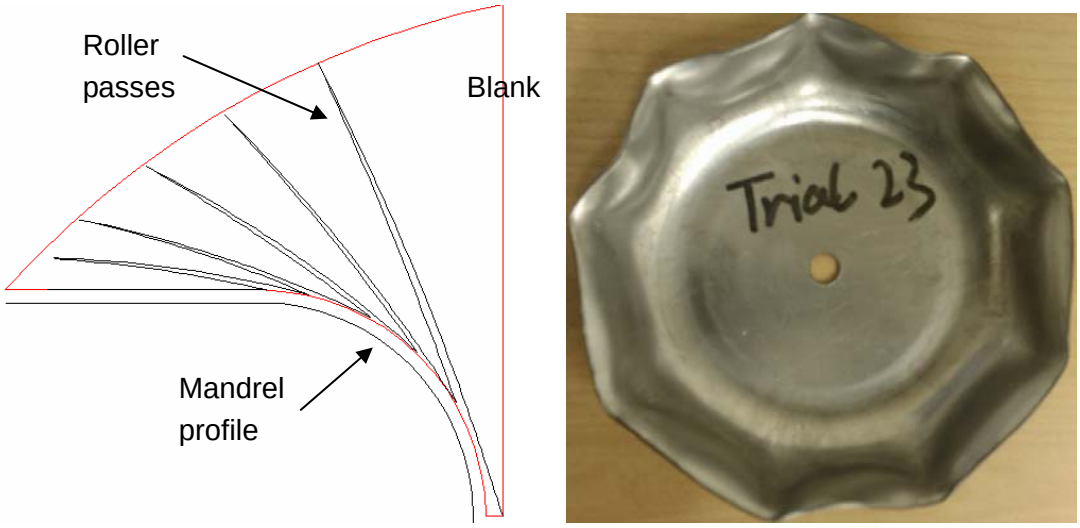

Figure 5.2 Multi-pass design and spun sample without tool compensation

As shown in Figure 5.3, by offsetting a desired clearance on the modified mandrel profile, multiple CNC roller passes are designed, where six pairs of roller passes have been used. Since the roller is not a perfect rigid body, to make the workpiece fully conform to the mandrel, a clearance of 1.5 *mm*, which is slightly lower than the blank thickness (2 *mm*), has been used in this study. The detailed information (coordinates, time) of the roller passes is given in Appendix 1. Figure 5.4 shows four different stages of this multi-pass spinning experiment in progress. Clearly, the roller progressively forms the workpiece onto the mandrel.

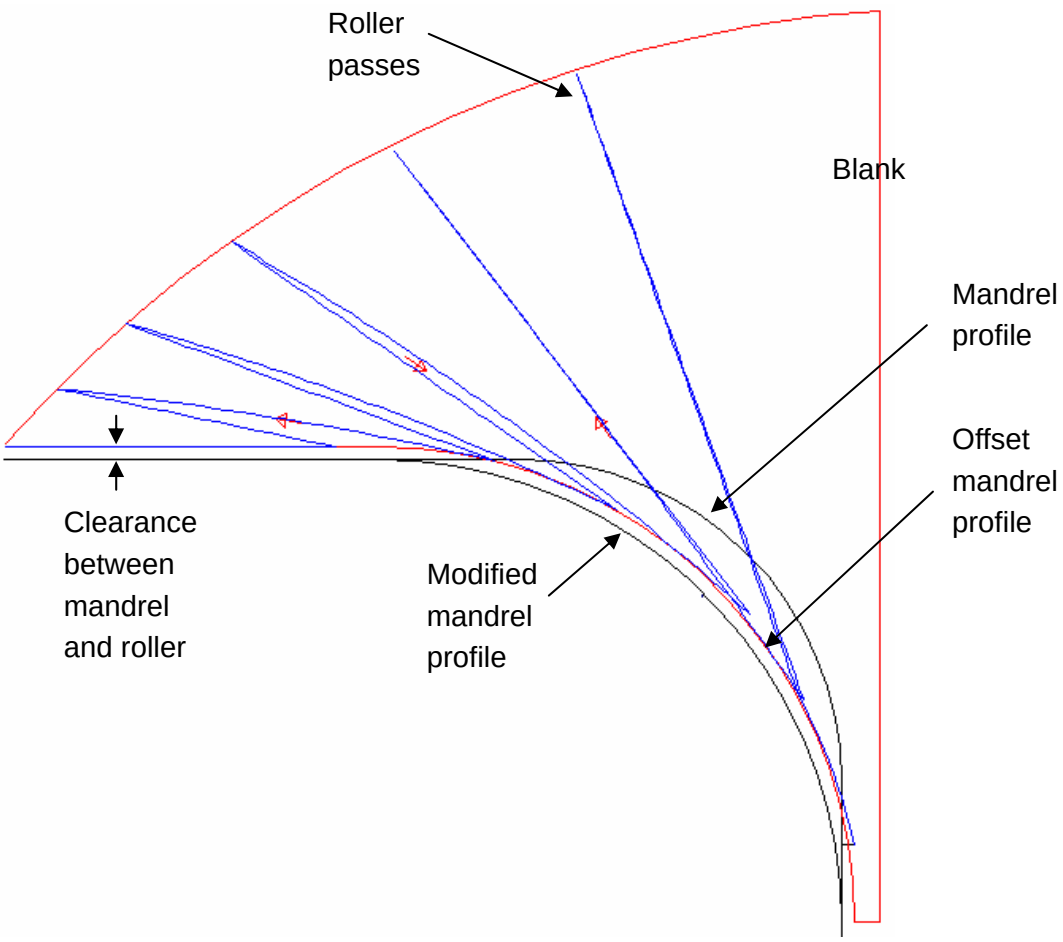

Figure 5.3 Roller passes design using tool compensation

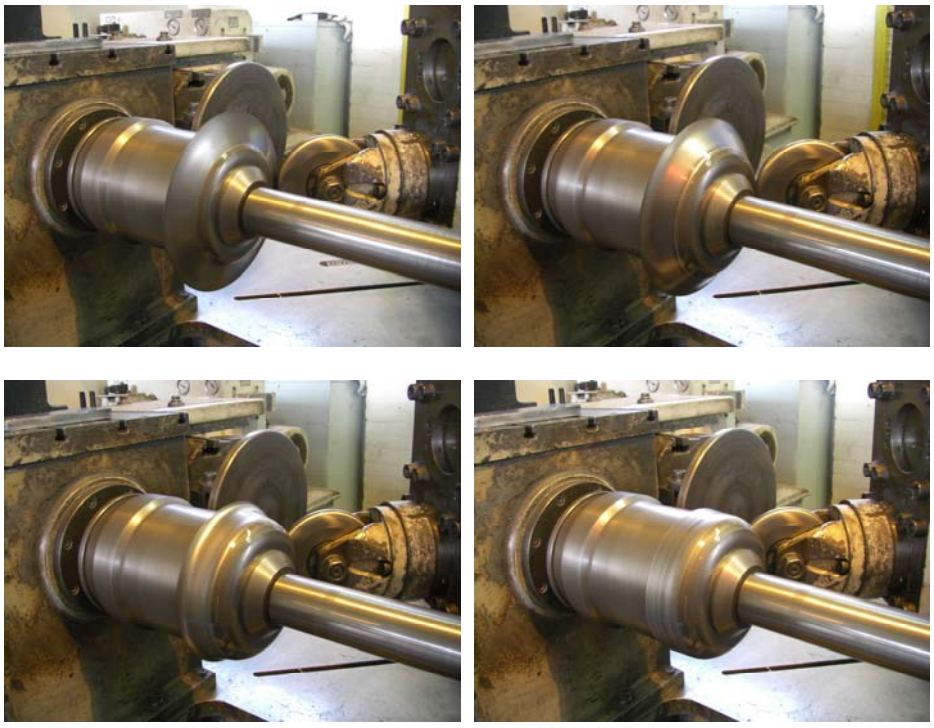

Figure 5.4 Spinning experiment in progress

5.1.2 Experimental Design by Taguchi Method

An L4 (2^3) orthogonal array of the Taguchi method has been used to generate the experimental runs. The orthogonal array is a technique that only requires a fraction of the full factorial experiment and provides sufficient information to determine the effects of input factors by using Analysis of Means (ANOM). ANOM is an analytical process which quantifies the mean response for each level of the input factor (Fowlkes and Creveling, 1995). The term “orthogonal” refers to the balance of various combinations of input factors so that no one factor contributes more or less weight in the experiment than other factors.

The Taguchi method concerns the variation as well as the ability of a system to meet a target. A term called Signal to Noise ratio (S/N) is used to measure the variability. In the case where the aim is to achieve the larger the better value but with minimum variability, the Signal to Noise ratio is defined as (Fowlkes and Creveling, 1995):

$$S/N = -10\log(\frac{1}{n}\sum_{i=1}^{n}\frac{1}{y_i^2}) \tag{136}$$

Similarly when the aim is to achieve the smaller the better values but with minimum variability, the ratio is defined as:

$$S/N = -10\log(\frac{1}{n}\sum_{i=1}^{n}y_i^2) \tag{137}$$

where n is the sample number used in the experiment and y_i are the outputs from different samples.

Three variables, i.e. spindle speed, feed rate and type of material, are considered as the experimental input factors. Each input factor has two levels, as shown in Table 5.1. The values of input factors are chosen based on the process design experience in Metal Spinners Group Ltd. Two samples have been used for each experimental run, to minimise the experimental errors. The depths, inside diameters and wall thickness

variations of the spun parts have been measured as the output factors. Figure 5.5 shows the measurement of the thickness and depth variations by using a probe indicator and a depth gauge, respectively.

Table 5.1 Experimental input factors and levels

Factor	Code	Level	
		1	2
Feed Rate (*mm/min*)	F	300	900
Spindle Speed (*rpm*)	S	500	1000
Material	M	Aluminum (1050H14)	Mild Steel (DC01)

Figure 5.5 Experimental measurements

5.2 Experimental Results and Discussion

Table 5.2 illustrates the experimental runs and the corresponding dimensional results, i.e. the average values of the depths, inside diameters and the minimum wall thickness of the experimental spun parts. Figure 5.6 illustrates one spun part from each experimental run, where crackling failure is observed near the opening of the cup in experimental run 4. By comparing the experimental run 1 and 4, in which the blanks are made of aluminum, it is clear that higher feed ratio (ratio of feed rate to spindle speed) results in crackling failures, as the feed ratio in run 1 and run 4 are 0.6 *mm/rev* and 0.9 *mm/rev*, respectively. In addition, mild steel has much stronger ability to stand cracking failures in metal spinning, since the feed ratio applied on mild steel (run 3) is as twice as

that used on aluminum (run 4), and yet no cracks take place in experimental run 3. Software Minitab has been used to analyse the effects of input factors on the dimensional output factors in this experiment.

Table 5.2 Experimental runs and dimensional results

Run	F	S	M	Feed Ratio (*mm/rev*)	Sample Number	Diameter (*mm*)	Wall Thickness (*mm*)	Depth (*mm*)	Material Failure
1	1	1	1	0.6	1.1	173.7	1.47	66.90	None
					1.2	173.6	1.45	67.13	
2	1	2	2	0.3	2.1	173.6	1.50	63.32	None
					2.2	173.7	1.55	63.24	
3	2	1	2	1.8	3.1	173.3	1.60	61.08	None
					3.2	173.4	1.65	61.28	
4	2	2	1	0.9	4.1	173.9	0.60	75.69	Cracking
					4.2	173.9	0.98	73.79	

(a) Run 1 (b) Run 2 (c) Run 3 (d) Run 4

Figure 5.6 Experimental spun parts

5.2.1 Diameter of Spun Part

Figure 5.7 shows the main effects plot for diameter means and S/N ratios, respectively. It has shown that in this experiment both the spindle speed (S) and material type (M) have relatively strong impacts on the diameter means and variability of spun part, while only minor effects have been found from the feed rate (F). Nevertheless, it is noticeable that the maximum differences of the diameter values at different input levels are only 0.3 *mm*, indicating none of these three input factors have significant effects on the diameter

of the spun part in this experiment.

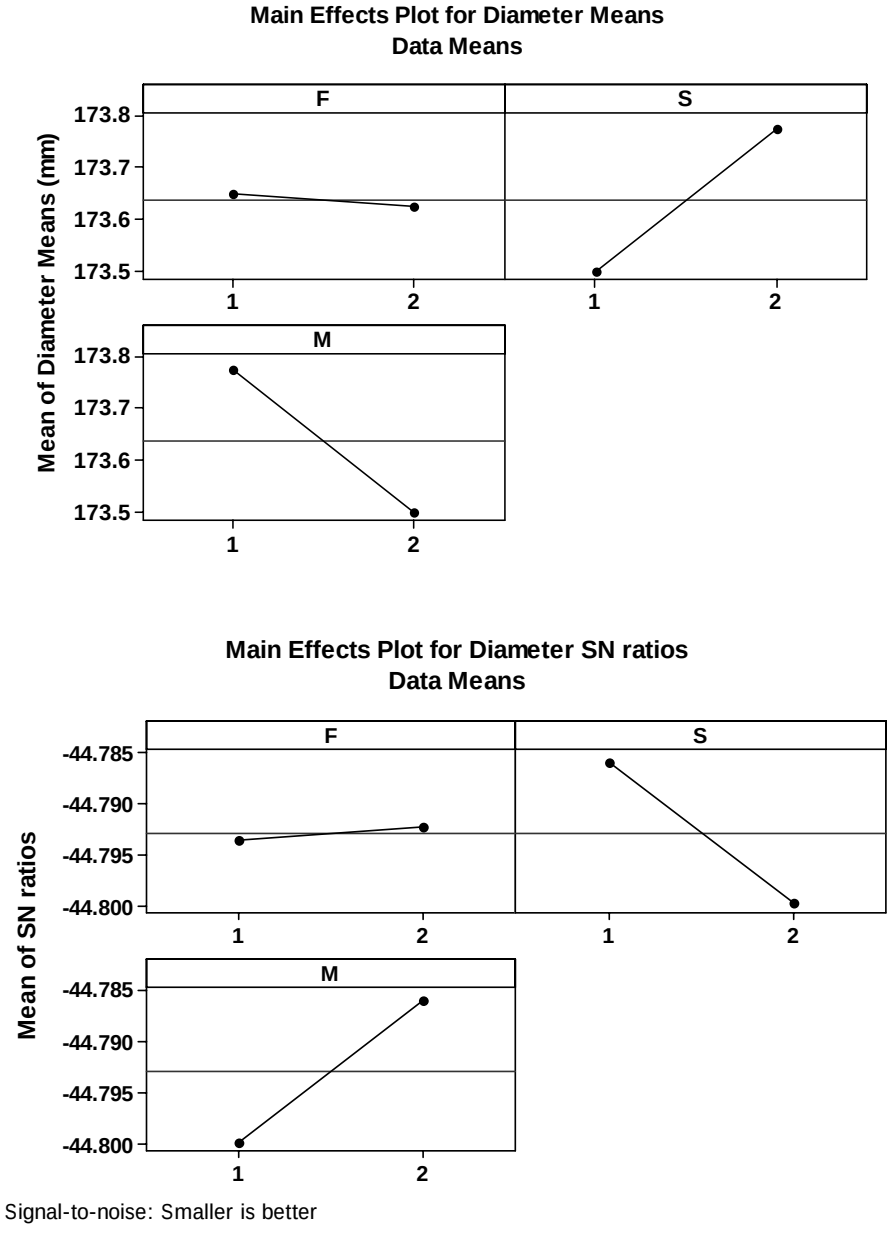

Figure 5.7 Main effects plot for diameter

5.2.2 Thickness of Spun Part

As can be seen from Figure 5.8, the type of material (M) has slightly higher effects on the mean value and variability of wall thickness than the effects from spindle speed (S) and feed rate (F). It is clear that using a relatively “soft” material, i.e. aluminum, produces a lower wall thickness value. In addition, a thinner workpiece is also obtained when a high spindle speed is used, as agreed with Wang et al. (2010). Nevertheless, it

has been shown that in this experiment a higher level of feed rate leads to a thinner workpiece according to the response table of the mean thickness. This may be explained by the fact that severe thinning take places near the crack of sample 4, resulting in a low mean value of thickness. However, it has been reported that in the case of crack-free spinning process, using a higher feed ratio can help to maintain the original wall thickness (Pell, 2009). This conclusion is also confirmed by comparing the thickness results of experimental run 2 and 3 shown in Table 5.2, where a greater wall thickness is achieved when a higher feed ratio is used on the mild steel samples.

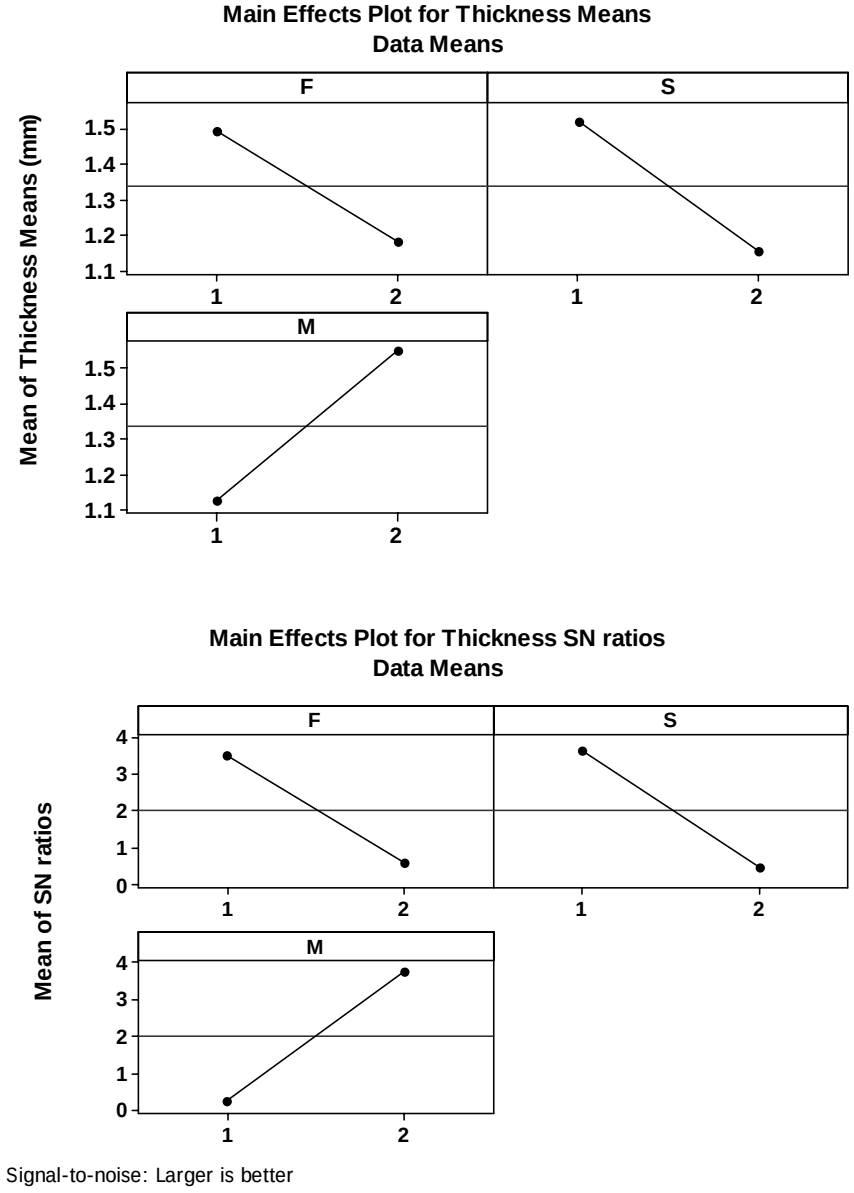

Figure 5.8 Main effects plot for thickness

5.2.3 Depth of Spun Part

As illustrated in Figure 5.9, the type of the material (M) has the most significant effects on the mean value as well as the variability of the depth of the spun part, followed by the spindle speed (S), and the feed rate (F). Due to the volume constancy of the material during the spinning process, the depth has a converse change in relation to the thickness change. Hence, the input factors have the opposite effects on the depth than the thickness.

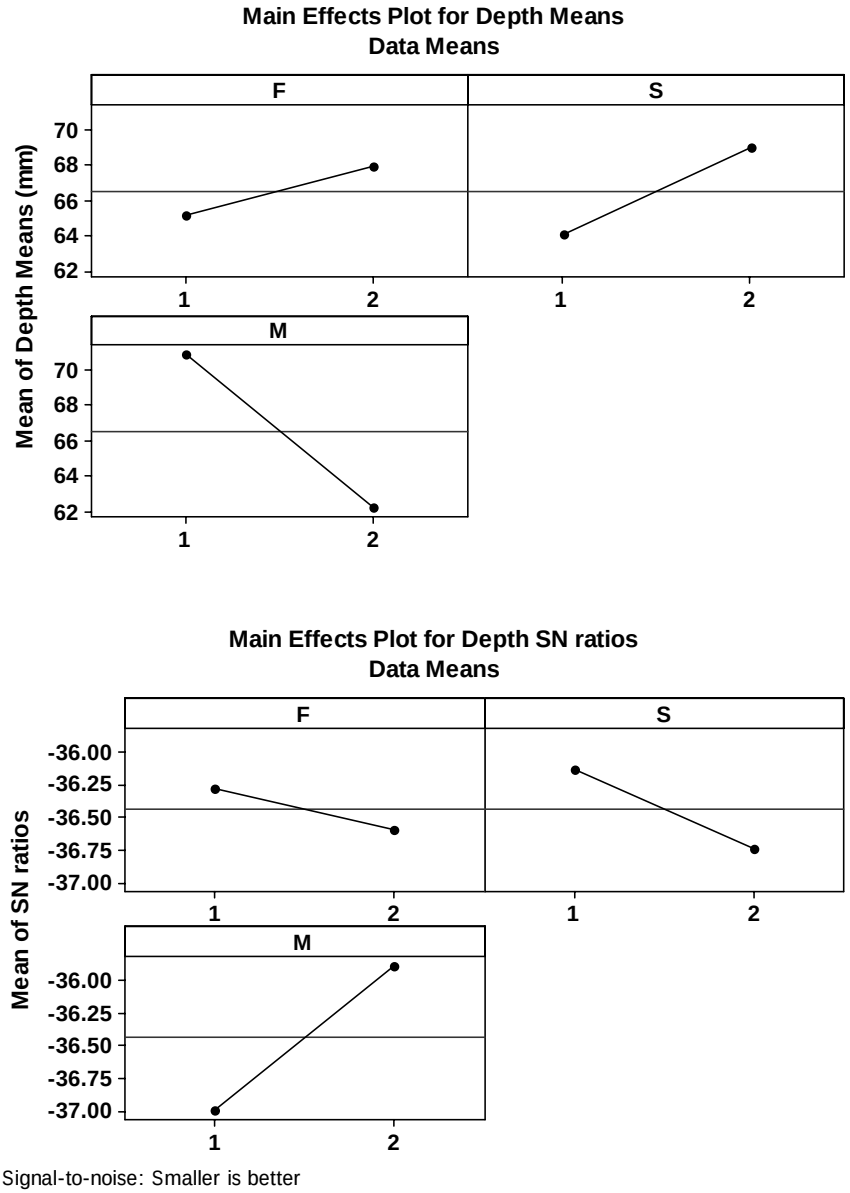

Figure 5.9 Main effects plot for depth

5.3 Finite Element Simulation

5.3.1 Development of Finite Element Models

By using the same techniques of FE simulation discussed in Section 4.2, a FE model of the experimental run 3 has been developed and used to analyse the material deformation in multi-pass conventional spinning. Figure 5.10 shows eight stages of the spinning process in FE simulation. Clearly, the roller forms the workpiece progressively onto the mandrel by six pairs of roller passes.

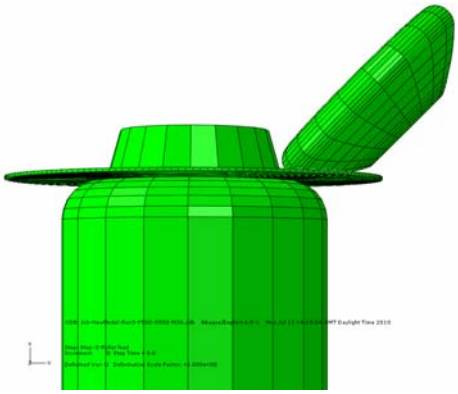

(a) Beginning of the spinning process

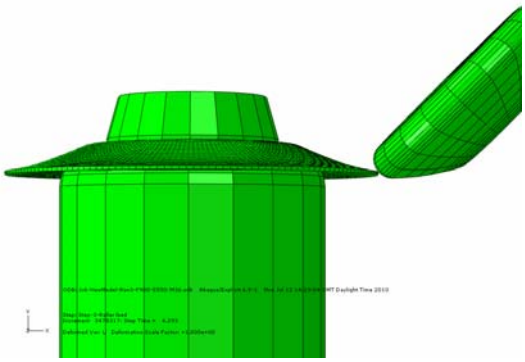

(b) End of the 1st forward pass

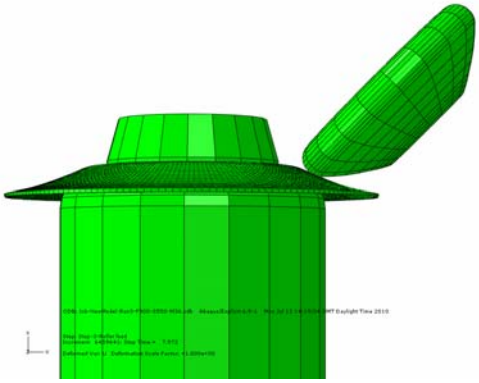

(c) Beginning of 2nd forward pass

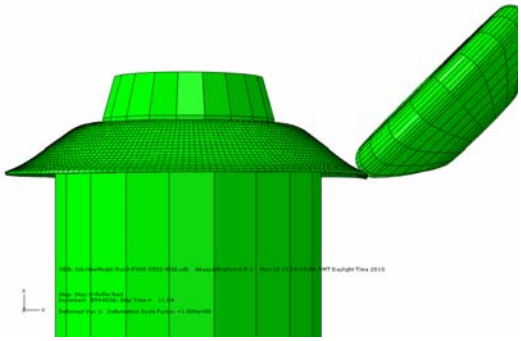

(d) End of the 2nd forward pass

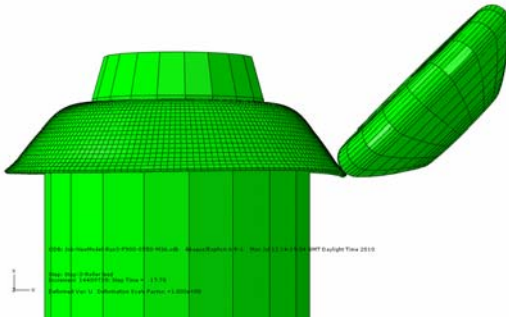

(e) End of 3rd forward pass

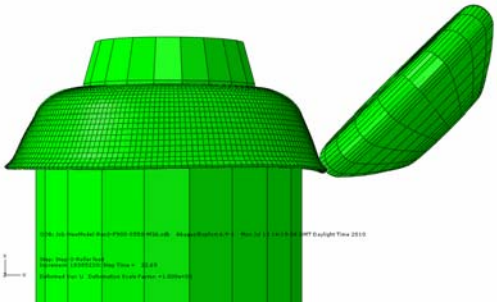

(f) End of the 4th forward pass

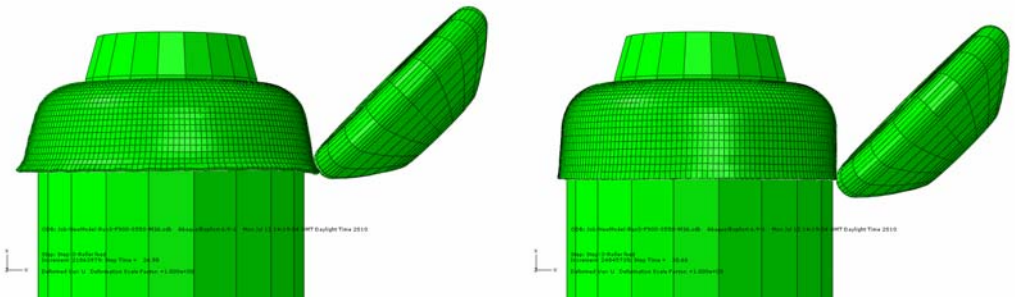

(g) End of 5th forward pass (h) End of the 6th forward pass

Figure 5.10 Spinning process using off-line designed roller passes

5.3.2 Verification of Finite Element Models

In this chapter, FE models have been verified by three approaches: at first, the dimensional results of the FE model have been compared with the corresponding experimental measurements. As shown in Table 5.3, the errors of the depth and diameter are 3.41% and 0.38%, respectively, indicating that the FE analysis results are in agreement with the experimental results. According to Figure 5.11, the maximum difference in thickness between the FE simulation and experimental results is 0.3 *mm* (15%). The relatively high error in thickness may be the result of: 1) thickness variations of the raw metal blank; 2) errors in measurement of the thin workpiece; 3) wear of the roller nose causing errors in the tool compensation of the CNC roller passes design; 4) in the current FE simulation it is assumed that the coefficient of friction between roller and workpiece is constant, while in reality the coefficient of friction may decay from the assumed constant value after “sliding” takes place (Abaqus analysis user’s manual, 2008), resulting in errors accumulating through the FE simulation of the multi-pass spinning process.

Table 5.3 Comparison of depth and diameter FEA vs. experimental results

	Mean experimental results	**FEA results**	**Errors**
Depth (*mm*)	61.18	59.09	3.41%
Diameter (*mm*)	173.35	174.01	0.38%

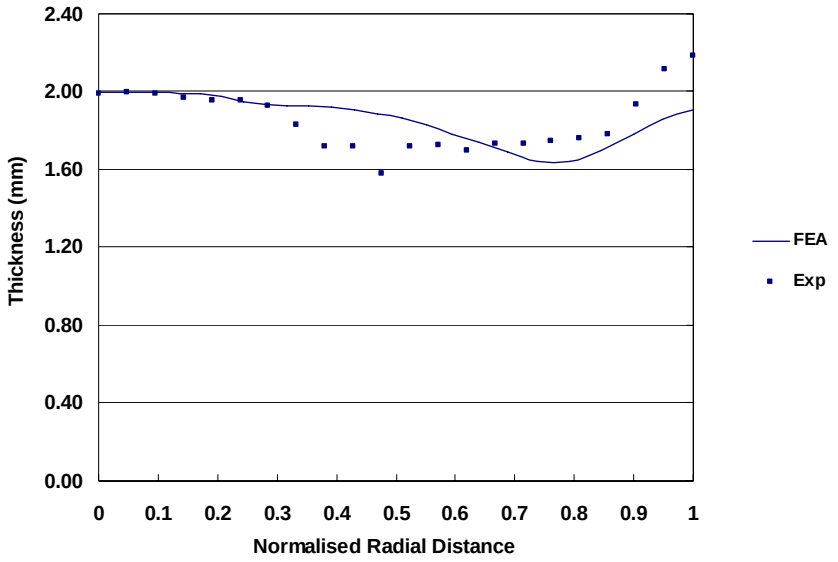

Figure 5.11 Comparison of experimental and FE analysis results of wall thickness

Secondly, FE models have also been verified by investigating the energy ratios of the spinning process (Abaqus analysis user's manual, 2008). As shown in Figure 5.12, at the beginning of the spinning process, the rotation of the workpiece dominates, thus the ratio of the kinetic energy to the internal energy of the workpiece is extremely high. However, this ratio decreases gradually throughout the spinning process, resulting from the increasing degree of the plastic deformation of the workpiece. Clearly, during more than 2/3 time period of the spinning process, the ratio of the kinetic energy to the internal energy of the workpiece is below 10%, indicating that the inertia effects due to mass scaling do not significantly affect the simulation results. In addition, the ratio of the artificial strain energy to the internal energy of the workpiece is below 1% throughout the spinning process. Thus it is believed that the "hourglassing" problem is well controlled and would not affect the simulation accuracy.

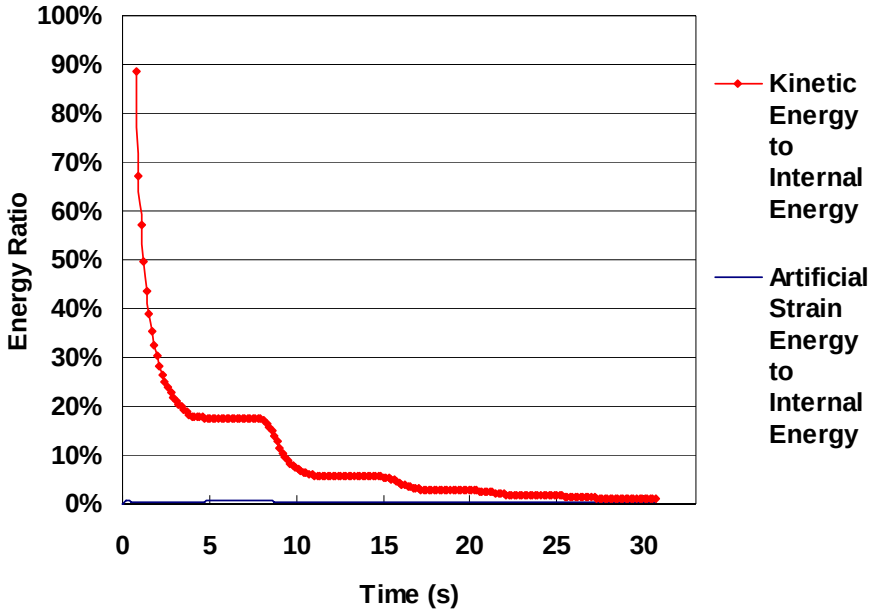

Figure 5.12 Evaluation of energy ratios in FE model

Thirdly, it has been shown that the FE simulation technique used in this study is able to produce accurate results of tool forces (Long et al., 2011), by comparing the tool forces from the FE analysis with the corresponding tool forces measured in a 3-pass spinning experiment. As shown in Figure 5.13, a good agreement of axial forces is achieved between the experiment and FE simulation.

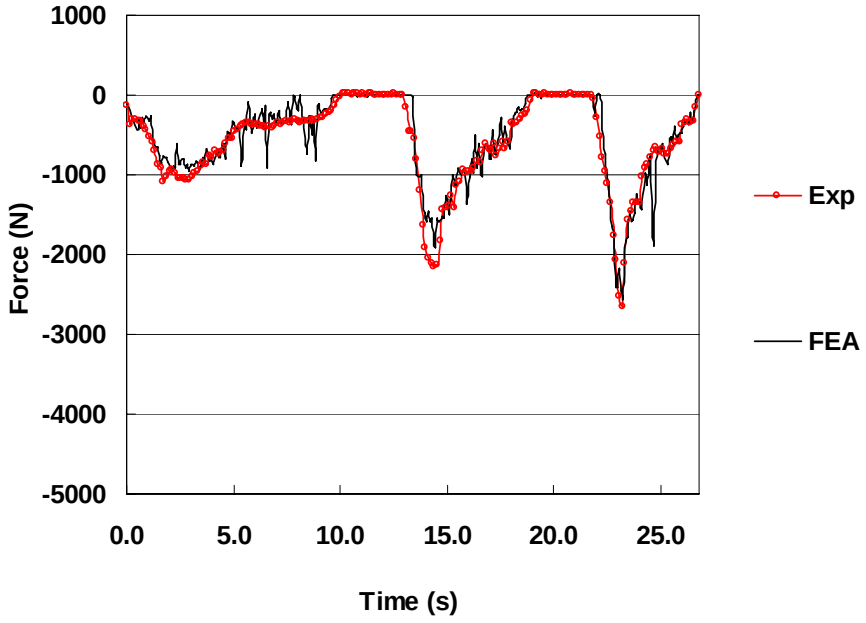

Figure 5.13 Comparison of experimental and FE analysis results of axial forces (Long et al., 2011)

5.4 Finite Element Analysis Results and Discussion

In this section, to gain insight into the material deformation of the multi-pass conventional spinning process, the variations of tool forces, stresses, wall thickness and strains in the FE model of experimental run 3 have been analysed.

5.4.1 Tool Forces

The history of three tool force components has been plotted in Figure 5.14, which clearly demonstrates six stages, representing the six pairs of roller passes in the spinning process. Figure 5.14 shows that the axial force dominates and increases gradually in the first 3 forward passes, since at the beginning of the spinning process the workpiece is mainly subjected to bending effects, as demonstrated in Figure 5.10(a)-(e). By contrast, the radial force increases dramatically over the six roller passes, as a result of that the roller gradually compresses the workpiece onto the mandrel, especially during the last 3 passes shown in Figure 5.10(f)-(h). Furthermore, the tangential force is much lower than the axial and radial forces during the spinning process, as also reported in the experimental investigations of multi-pass spinning (Jagger, 2010, Wang et al., 1989).

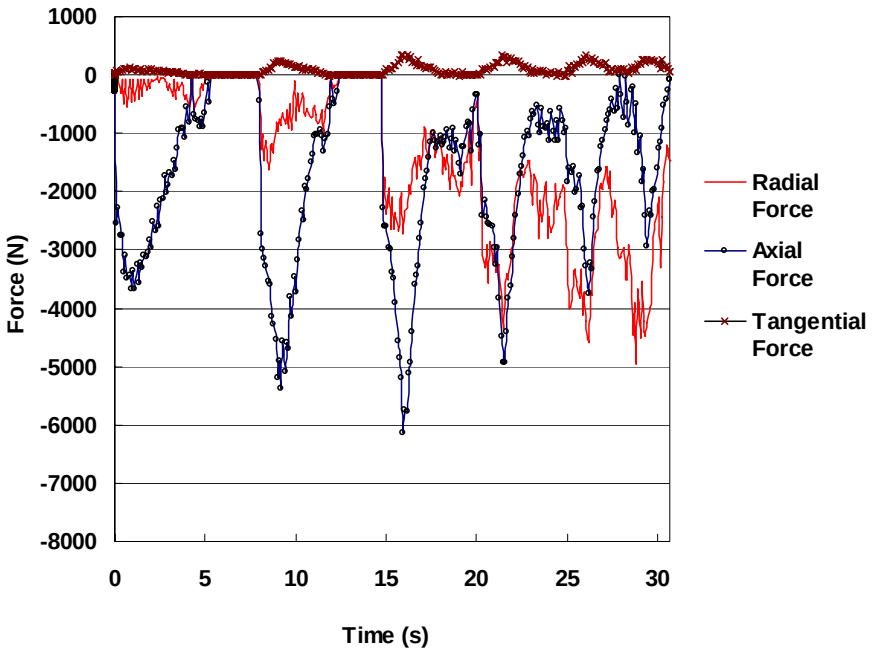

Figure 5.14 History of tool forces of FE simulation

Table 5.4 shows the maximum tool forces and their ratios of this FE model over six roller passes. It is noticeable that the ratios of the maximum axial force to the maximum tangential force decrease from 25 to 11 through this multi-pass spinning process. By contrast, the ratios of the maximum radial force to the maximum tangential force increase from 4 to 18 from the first to the sixth roller pass.

Table 5.4 Ratios of maximum tool forces of FE model

Pass Number	F_a (*N*)	F_r (*N*)	F_t (*N*)	Ratios of Force
1	3661.7	559.0	146.1	$F_a : F_r : F_t$ = 25: 4: 1
2	5369.1	1635.4	249.6	$F_a : F_r : F_t$ = 22: 7: 1
3	6133.2	2727.7	339.7	$F_a : F_r : F_t$ = 18: 8: 1
4	4918.5	4359.2	334.0	$F_a : F_r : F_t$ = 15: 13: 1
5	3757.5	4571.5	355.8	$F_a : F_r : F_t$ = 11: 13: 1
6	2940.6	4954.3	277.2	$F_a : F_r : F_t$ = 11: 18: 1

5.4.2 Stresses

The contours of radial and tangential stresses of the workpiece at the beginning of the first forward roller pass have been plotted in Figure 5.15. Apparently, the stress distribution is much more complicated than the theoretical stress distribution shown in Figure 1.4.

As illustrated in Figure 5.15(a), Region A, the area between the roller contact and the backplate clamped area, is under high tensile radial stress. Conversely, Region B, which is between the roller contact point and the rim of the workpiece, is under compressive radial stress. In addition, a ring zone of high compressive radial stresses has been observed at Region C of the workpiece. It indicates that when Region A rotates away from the local forming zone and enters Region C, the high tensile radial

stresses turn into high compressive radial stresses.

Figure 5.15(b) shows the distribution of tangential stress of workpiece at the beginning of the first forward roller pass. Although the roller does not contact Region D yet, it has been subjected to high compressive tangential stresses. As soon as Region D rotates away from the local forming zone, the high compressive tangential stresses “recover” to low tensile tangential stresses, as shown in the Region E of Figure 5.15(b). Moreover, the areas close to the roller contact point along the circumferential direction of workpiece, i.e. Region F, are under high tensile tangential stresses.

The distribution of radial and tangential stresses in the workpiece at the beginning of the first backward roller pass is shown in Figure 5.16. It is clear that the area under roller contact is subjected to compressive stresses in both radial and tangential directions, as agreed with theoretical stress pattern shown in Figure 1.4. Region G, which is located between the backplate clamped region and roller contact zone, as shown in Figure 5.16(a), is under high tensile radial stress.

As shown in Figure 5.16(b), a toothed pattern of tangential stresses is observed along flange area of the workpiece, as also reported by Sebastiani et al. (2007), who claimed that the toothed pattern may be a pre-state to wrinkling. However, in this study no correlations have been observed between this toothed stress pattern and the wrinkling failure. It may be explained by two reasons: at first, this toothed stress pattern is originated from the high tensile tangential stresses. No high compressive tangential stresses, which normally result in wrinkling failures, are observed except at the roller contact area. Secondly, wrinkling generally occurs in forward passes when there is no support to the flange and it is thus rare to have wrinkles in backward passes (Runge, 1994).

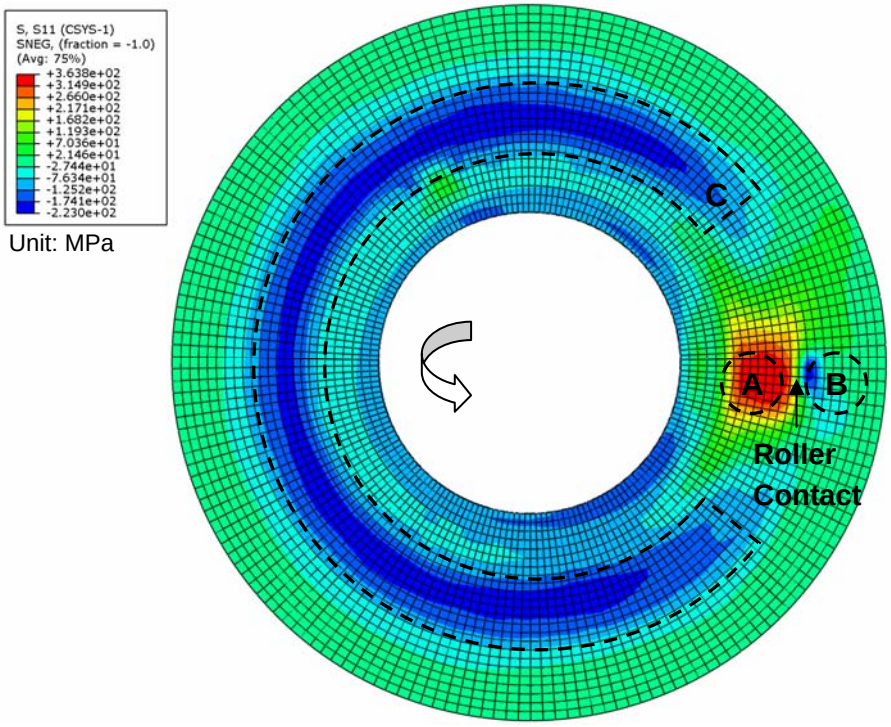

(a) Radial stress

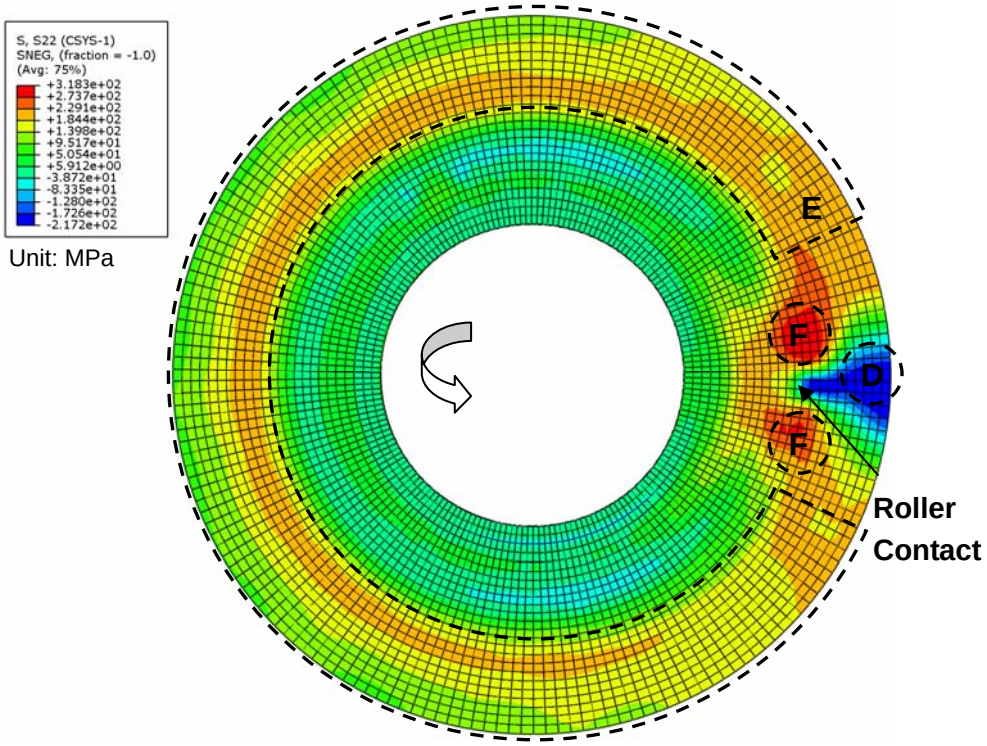

(b) Tangential stress

Figure 5.15 Variations of stresses at the beginning of 1st forward pass

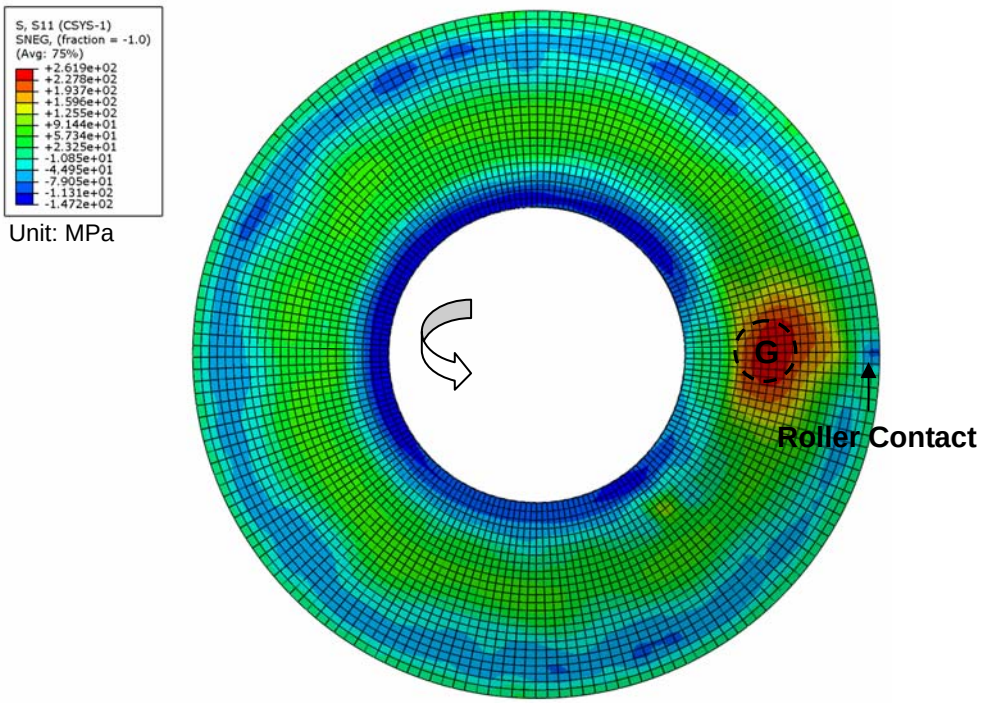

(a) Radial stress

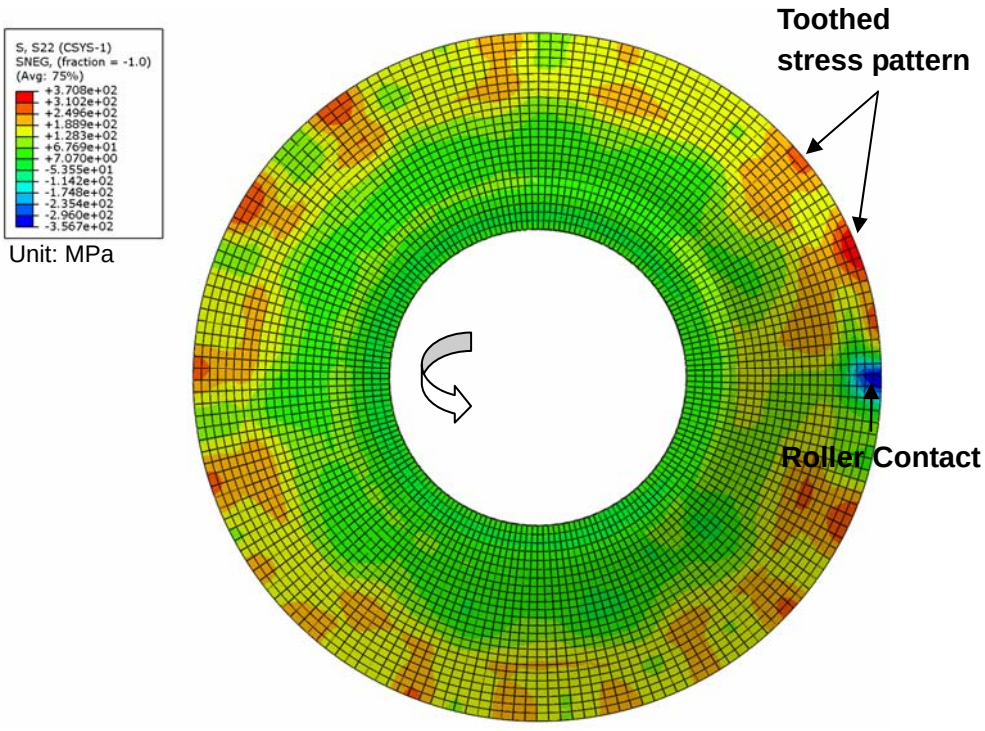

(b) Tangential stress

Figure 5.16 Variations of stresses at the beginning of 1st backward pass

5.4.3 Wall Thickness

According to the FE analysis results, there is almost no thickness change after the backward pass in the multi-pass conventional spinning. Figure 5.17(a) illustrates the wall thickness variations after each forward roller pass of the FE model. Clearly, in this conventional spinning process, the workpiece has been thinned gradually over these six roller passes. From the first roller pass to the fifth roller pass, the workpiece is thinned by approximately 3% after each pass, while in the last pass the wall thickness is reduced by 4%. The total reduction of the wall thickness after six roller passes of this spinning process is 19%. In addition, it has been observed that the highest thinning zone of the workpiece has been shifted from the bottom of the cup to the cup opening during this spinning process, as shown in Region R, S, and T of Figure 5.17(b), (c) and (d), which are the wall thickness contours after the first, third and sixth roller pass, respectively. This may indicate that materials flow towards the rim of blank through the forward passes in the conventional spinning process.

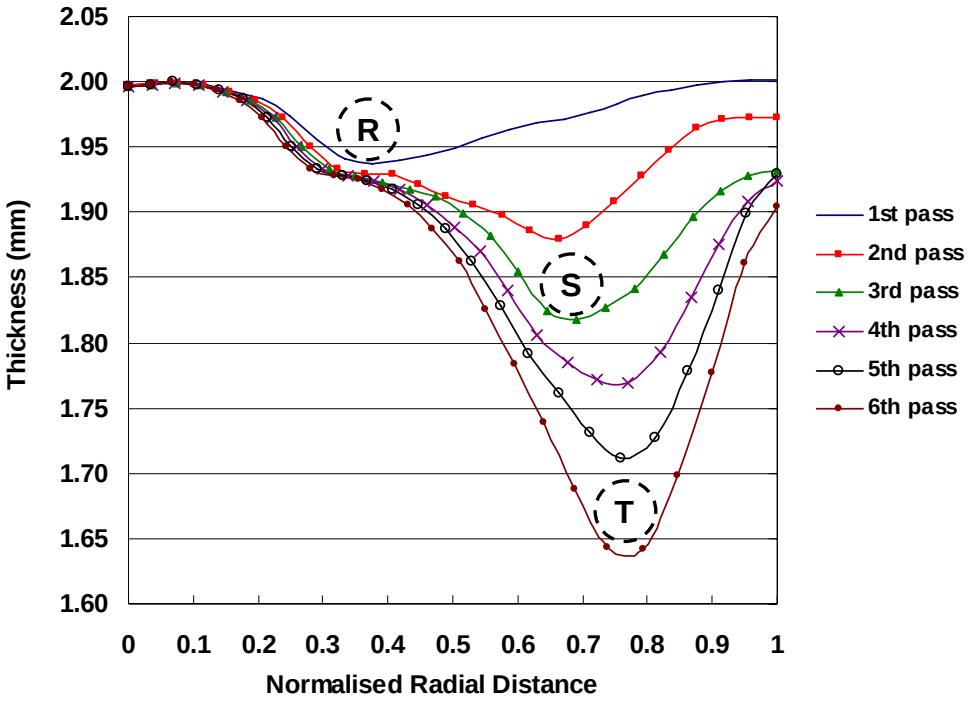

(a) Wall thickness variations after each pass

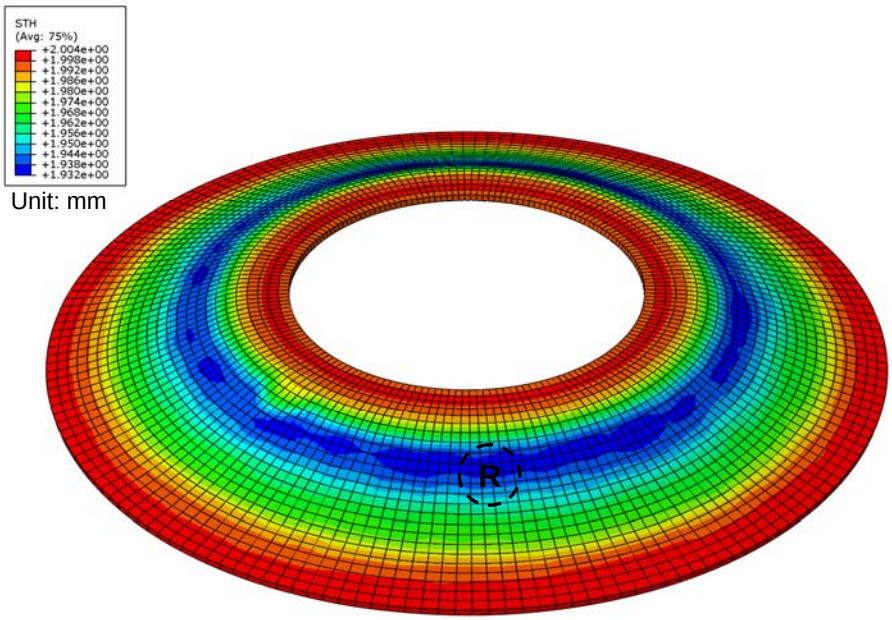

(b) Contour of wall thickness after 1st pass

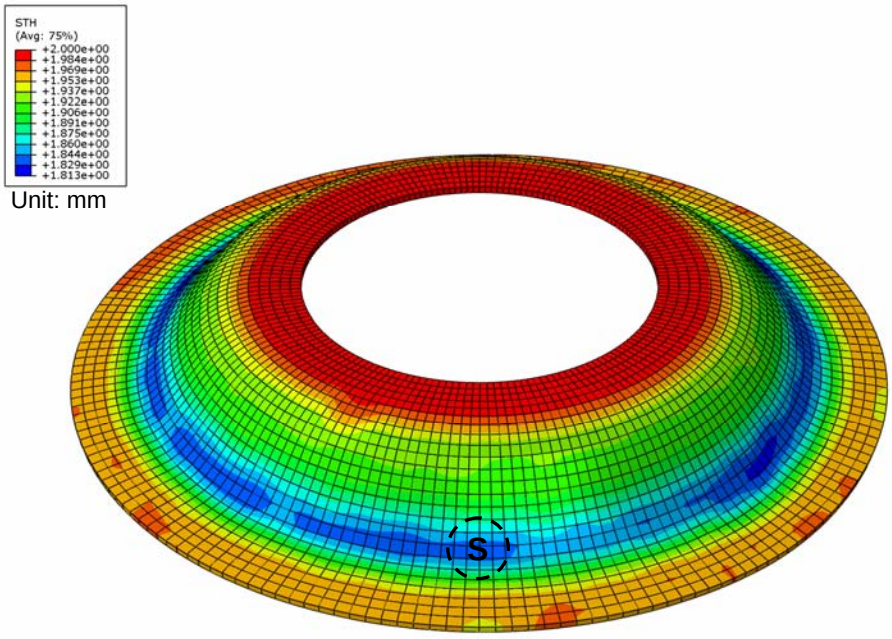

(c) Contour of wall thickness after 3rd pass

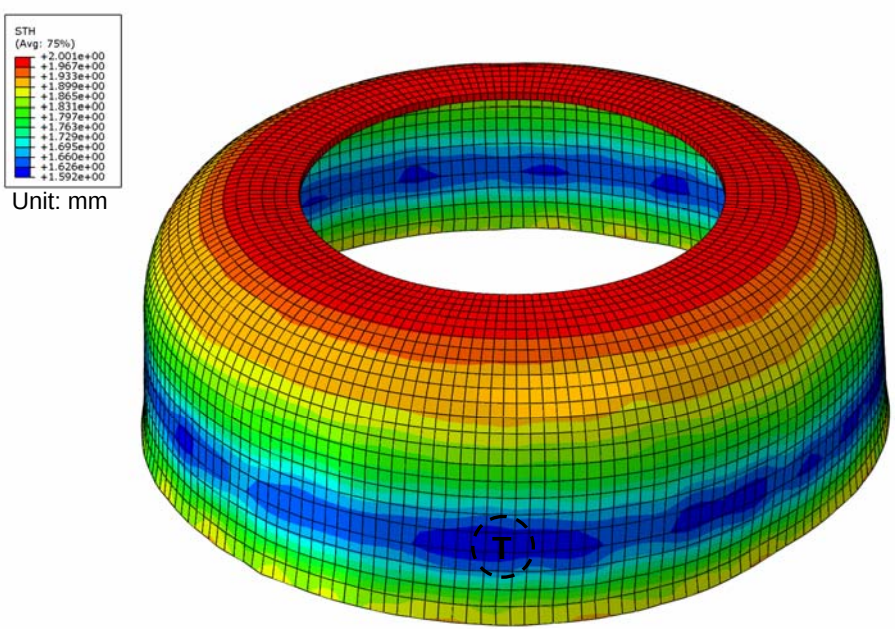

(d) Contour of final wall thickness

Figure 5.17 Variations of wall thickness

5.4.4 Strains

Figure 5.18 shows the radial, tangential and thickness strains of the workpiece at beginning of the first roller pass. It is noticeable that these strains distribute almost uniformly in the circumferential direction but vary along the radial direction of the workpiece. As shown in the Region J of Figure 5.18(a) and (b), a ring zone of compressive radial and tangential strains has been observed between the roller contact and the rim of the workpiece. Those compressive strains result in tensile thickness strains in the corresponding ring zone, as shown in the Region J of Figure 5.18(c). This slight thickening of the workpiece may result from the fact that material builds up in front of the roller at the beginning of the first forward pass.

Conversely, tensile radial and tangential strains take place in a ring zone between the backplate clamped area and roller contact area, as illustrated in the Region K of Figure 5.18(a) and (b). These tensile strains lead to compressive thickness strains in the corresponding zone shown in Figure 5.18(c). Thus, it is clear that wall thickness

increases in Region J, while decreases in Region K. Nevertheless, according to the thickness strain contour shown in Figure 5.18(c), the thickness strain of the thinning in Region K is 3.6 times as the thickening in Region J.

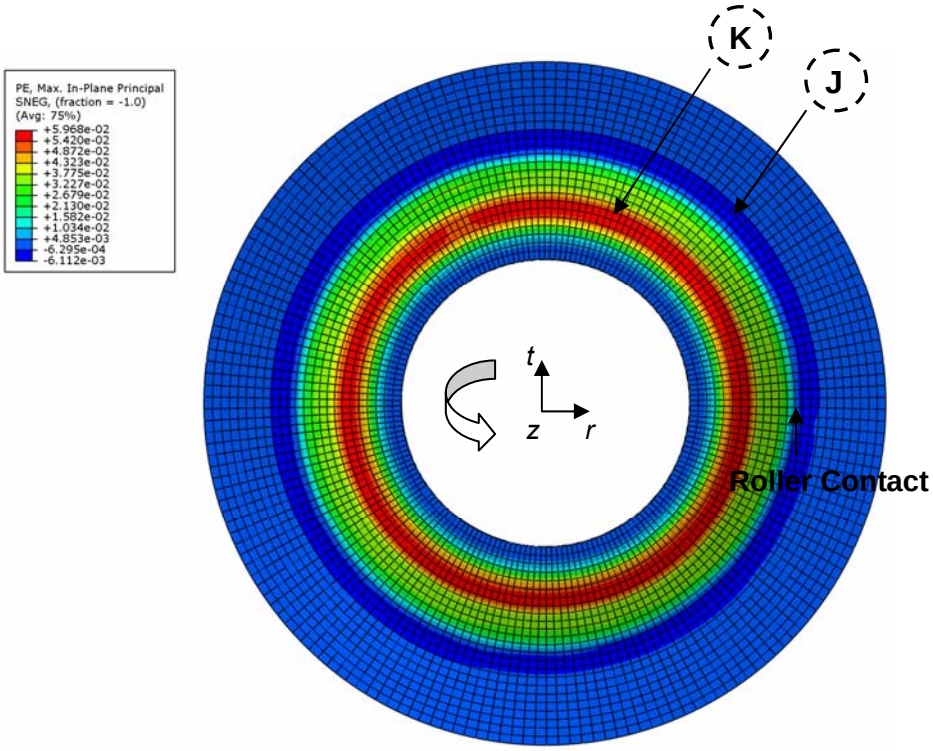

(a) Radial strain

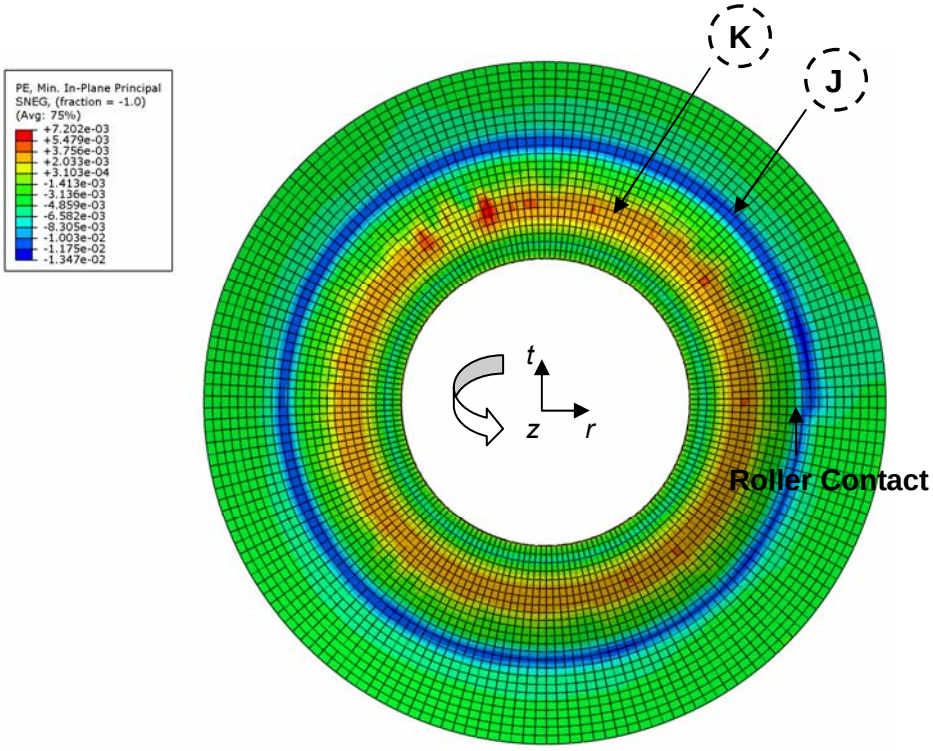

(b) Tangential strain

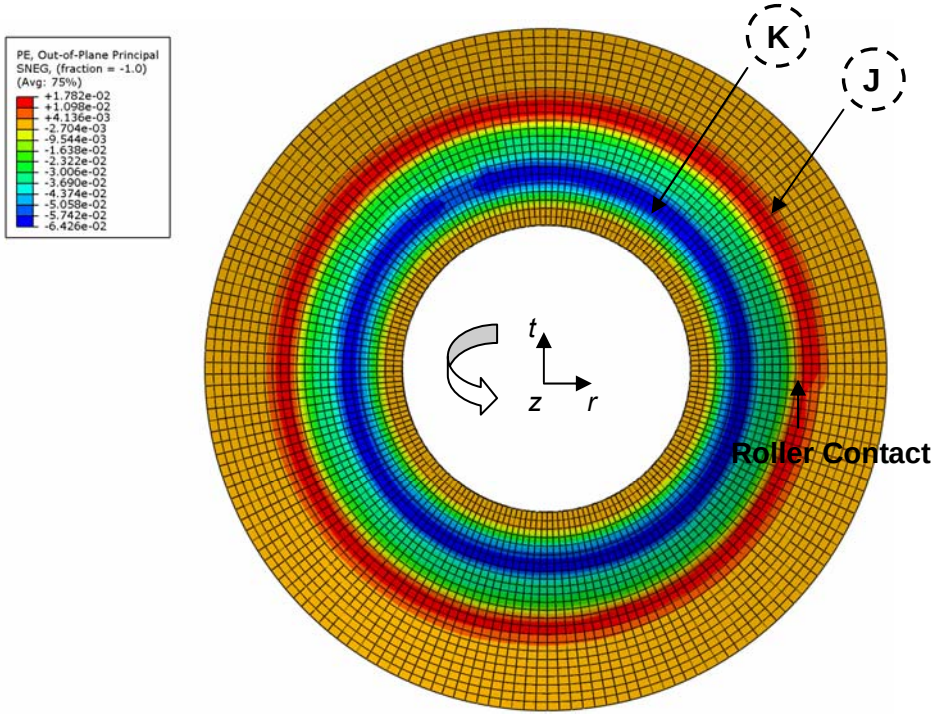

(c) Thickness strain

Figure 5.18 Variations of strains at the beginning of 1st pass

5.5 Summary and Conclusion

In this chapter, to make the workpiece conform to the non-linear profile of the mandrel, the tool compensation technique is proposed and used in the CNC multiple roller passes design. The Taguchi method has been employed to analyse the effects of process parameters on the dimensional variations of the experimental samples. In order to gain insight into the material deformation of the multi-pass conventional spinning process, history of tool forces, distributions of stress and strains, and wall thickness variations of a FE model have been analysed numerically. According to the results of the experiment investigation and FE simulation, within the range of the process parameters used in this chapter, the following conclusions may be drawn:

a) Experimental results indicate that the type of material has the most significant effects on the variations of thickness and depth of the spun parts, followed by the

spindle speed and the feed rate. However, none of these input factors show significant effects on the diameter variations of spun parts in this experiment.

b) A high feed ratio can help to maintain the original wall thickness but cracking failures may take place if a large feed ratio is used. Comparing with aluminum, mild steel is much “stronger” to withstand cracking failures in the conventional spinning process, since a feed ratio of 1.8 *mm*/*rev* is applied on mild steel blanks while a feed ratio of 0.9 *mm*/*rev* is used on aluminum blanks, and yet no cracks take place on the mild steel blanks.

c) According to the FE analysis results of this spinning process, the axial force is the highest and the tangential force is the lowest. The axial force increases in the first three passes and decreases gradually in the last three passes. Conversely, the radial force continues to increase throughout the six roller passes.

d) Stress analysis by FE simulations shows that in the forward roller pass, high tensile and compressive radial stresses take place behind and in front of the roller contact. In the backward pass, a toothed tangential stress pattern has been noticed in the flange area.

e) FE analysis results show that the wall thickness of the workpiece decreases gradually after each forward roller pass. The thinnest zone on the workpiece has been shifted from the bottom to the opening of the cup, while the spinning process progresses.

f) Strains distribute almost uniformly in the circumferential direction but vary along the radial direction of the workpiece. At the beginning of a forward pass, a ring zone of tensile radial and tangential strains has been observed between the backplate clamped area and the roller contact zone, resulting in compressive thickness strains, i.e. wall thinning.

6. Study on Wrinkling Failures

In this chapter, wrinkling failure in conventional spinning has been studied by theoretical analysis, experimental investigation and Finite Element simulation. The energy method and two-directional plate buckling theory have been used to predict the critical condition of wrinkling failure in conventional spinning. The severity of wrinkles is quantified by calculating the standard deviation of the radial coordinates of element nodes on the edge of the workpiece obtained from the FE models. A forming limit study for wrinkling has been carried out and it shows there is a feed ratio limit beyond which wrinkling failures will take place. It is believed that if the high compressive tangential stresses in the local forming zone do not “recover” to tensile tangential stresses after roller contact, wrinkling failure will occur. Furthermore, the computational performance of the solid and shell elements in simulating the spinning process is examined.

6.1 Theoretical Analysis

It is believed that wrinkling in sheet metal forming is a local phenomenon, which depends on the local curvatures and stress states (Hutchinson and Neale, 1985). Hence, the region being investigated for flange wrinkling may be simplified as a rectangular plate (Wang and Cao, 2000), as shown in Figure 6.1. The length of a half-wave wrinkled flange in the tangential direction (x axis) is a; the width of the wrinkled flange in the radial direction (y axis) is b. The following assumptions have been made in order to simplify the theoretical analysis:

1) Shear stresses are neglected;
2) No dynamic effects are considered;
3) Wall thickness remains constant throughout the spinning process;
4) The loading of roller is simplified as a lateral concentrated load P, perpendicular to the plate.

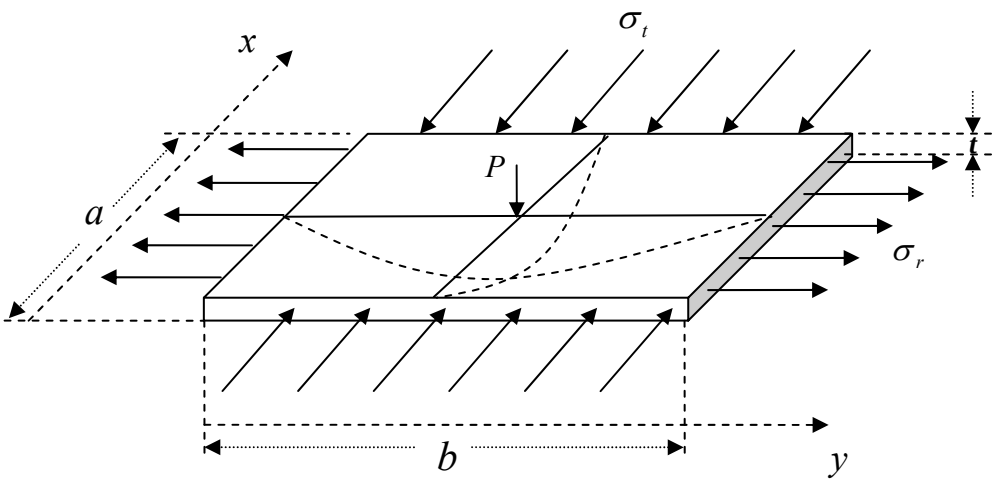

Figure 6.1 Schematic of a buckled plate in flange region

6.1.1 Energy Method

According to the theoretical stress pattern in a metal spinning process under a forward roller pass, it is assumed that the rectangular plate of the flange region is subjected to compressive tangential stresses and tensile radial stresses. To determine the critical condition of wrinkling failures in the spinning process, an energy method has been employed. In the wrinkling of metal spinning due to lateral collapse, four main energies generated in the plate of the flange region have been taken into account:

E_b, the energy due to bending in the wrinkled flange;

E_t, the energy due to circumferential shortening of the flange under compressive tangential stresses;

E_r, the energy due to radial elongation of the flange under tensile radial stresses;

E_l, the energy due to displacement caused by lateral concentrated load from the roller.

The critical condition reaches when

$$E_r + E_b = E_t + E_l \tag{138}$$

where E_r and E_b are the energies which tend to restore the equilibrium, while E_t, and E_l are the energies that lead to wrinkling failures.

6.1.2 Theoretical Model

Assuming that the buckled deflection surface, as illustrated by the dotted curves in Figure 6.1, is given by the equation (Timoshenko, 1936):

$$w = \gamma \sin\frac{\pi x}{a}\sin\frac{\pi y}{b} \tag{139}$$

where γ is the maximum deflection of the buckling surface.

The energy due to bending can be calculated by (Timoshenko, 1936):

$$E_b = \frac{1}{2}D\int_0^b\int_0^a\left\{\left(\frac{\partial^2 w}{\partial x^2}+\frac{\partial^2 w}{\partial y^2}\right)^2 - 2(1-\nu)\left[\frac{\partial^2 w}{\partial x^2}\frac{\partial^2 w}{\partial y^2}-\left(\frac{\partial^2 w}{\partial x \partial y}\right)^2\right]\right\}dxdy \tag{140}$$

Substituting (139) into (140),

$$E_b = \frac{ab}{8}D\gamma^2\left(\frac{\pi^2}{a^2}+\frac{\pi^2}{b^2}\right)^2 \tag{141}$$

where D is the flexural rigidity of plate

$$D = \frac{Et^3}{12(1-\nu^2)} \tag{142}$$

where E is the Young's Modulus, t is the wall thickness, v is the Poisson's ratio. It has been shown that the elastic bending theory can be extended to cover plastic bending by replacing E with the reduced modulus E_0 (Gere, 2001):

$$E_0 = \frac{4EE_p}{\left(\sqrt{E}+\sqrt{E_p}\right)^2} \tag{143}$$

where E_p is the slope of the stress-strain curve at a particular value of strain in the plastic region.

The energy due to tangential stress σ_t can be calculated by

$$E_t = \frac{1}{2}\int_0^a\int_0^b \sigma_t t\left(\frac{\partial w}{\partial x}\right)^2 dxdy \tag{144}$$

Substituting (139) into (144), we obtain

$$E_t = \frac{b\gamma^2\pi^2 t\sigma_t}{8a} \tag{145}$$

The energy due to radial stress σ_r can be calculated by

$$E_r = \frac{1}{2}\int_0^b \int_0^a \sigma_r t \left(\frac{\partial w}{\partial y}\right)^2 dydx \tag{146}$$

Substituting (139) into (146), we obtain

$$E_r = \frac{a\gamma^2\pi^2 t\sigma_r}{8b} \tag{147}$$

According to Timoshenko and Woinowsky-Krieger (1959), the deflection resulting from a concentrated load P can be expressed as

$$w = \alpha \frac{Pb^2}{D} \tag{148}$$

where α is a numerical factor, the value of which depends on the ratio of a/b and is given in Table 6.1.

Table 6.1 Factor α for deflection equation (Timoshenko and Woinowsky-Krieger, 1959)

a/b	1.0	1.1	1.2	1.4	1.6	1.8	2.0	3	∞
α	0.01160	0.01265	0.01353	0.01484	0.01570	0.01620	0.01651	0.01690	0.01695

The lateral energy E_l due to the concentrated loading P can be calculated as:

$$E_l = \int_0^{\gamma} P dw = \frac{D\gamma^2}{2\alpha b^2} \tag{149}$$

Substituting (141), (145), (147) and (149) into (138), we have

$$D\left(\frac{\pi^2}{a^2}+\frac{\pi^2}{b^2}\right)^2 + \frac{\pi^2 t}{b^2}\sigma_r = \frac{\pi^2 t}{a^2}\sigma_t + \frac{4D}{\alpha a b^3} \tag{150}$$

Dividing Equation (150) by $\frac{\pi^2 t}{a^2}$ and introducing notations σ_e and λ, where

$$\sigma_e = \frac{\pi^2 D}{a^2 t} \tag{151}$$

$$\lambda = \frac{a}{b} \tag{152}$$

The critical condition of wrinkling can be expressed as:

$$\sigma_e\left[\left(1+\lambda^2\right)^2-\frac{4\lambda^3}{\alpha\pi^4}\right]=\sigma_t-\sigma_r\lambda^2 \tag{153}$$

It is clear that in this theoretical model, the critical tangential stress and radial stress of wrinkling depend on the geometry of the half-wave wrinkled plate and material properties of the blank.

6.2 Experimental Investigation

6.2.1 Experimental Setup

An experiment has been carried out to study the wrinkling failures in the conventional spinning process. Figure 6.2 shows the setup of the spinning experiment and its schematic diagram, where the angle between the roller axis and the mandrel axis is 45°. The blank is made of mild steel (DC01). The thickness and diameter of the blank are 1.2 *mm* and 120 *mm*, respectively.

a) Experimental setup

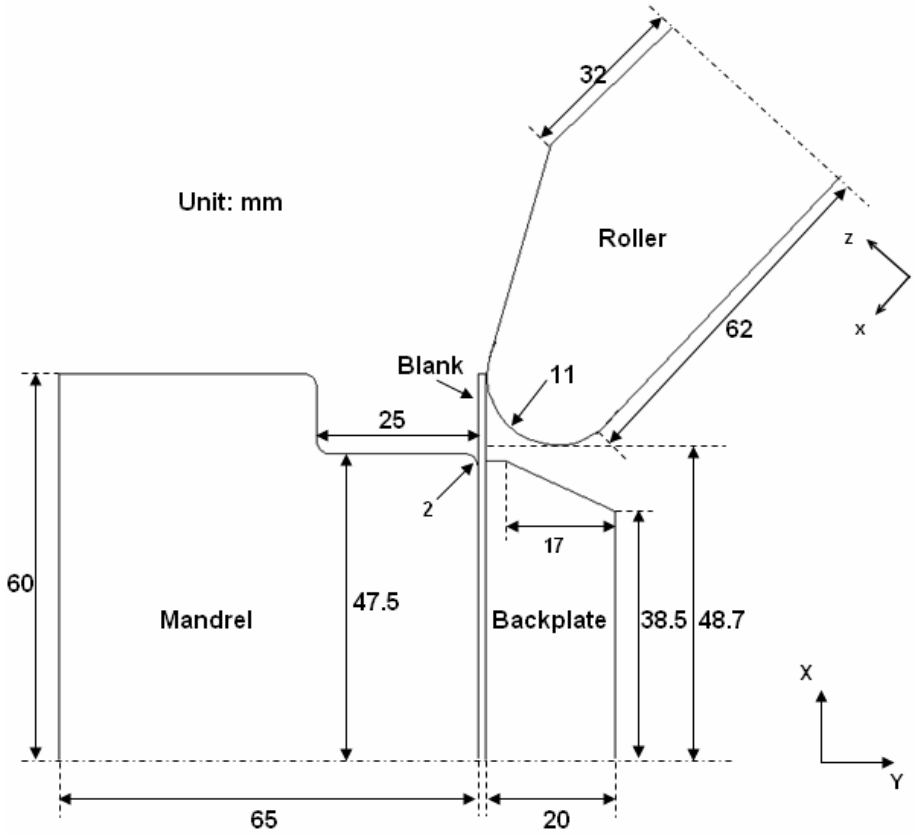

b) Schematic diagram

Figure 6.2 Spinning experiment of wrinkling investigation

6.2.2 Process Parameters

Figure 6.3 illustrates the roller passes used in the experiment, clearly only the two forward passes are effective as the backward pass does not deform the blank. Table 6.2 shows the process parameters used in four experimental runs. In an experimental run, the feed rate in the axial direction of the roller (z-axis in Figure 6.2b) is almost constant, while the feed rate in the radial direction of the roller (x-axis in Figure 6.2b) changes with time. 300% and 600% of the initial feed rate used in experimental run E1 are applied to experimental run E2 and E3, respectively. Only the first pass of experimental run E3 is used in experimental run E4.

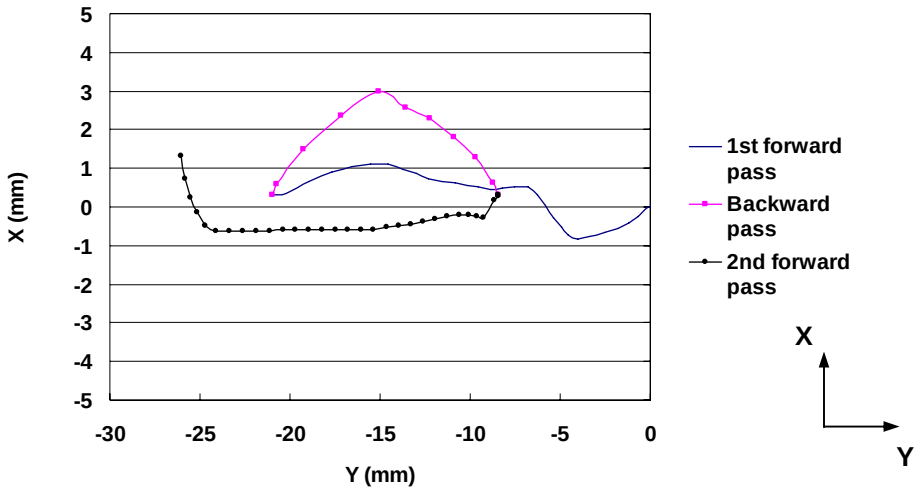

Figure 6.3 Roller passes used in the experiment

Table 6.2 Process parameters of experimental runs

Sample Number	**Spindle Speed** (*rpm*)	**Longitudinal Feed Rate** (z-axis) (*mm/min*)
E1	400	212 (Initial feed rate)
E2	400	300% of Initial feed rate
E3	400	600% of Initial feed rate
E4	400	600% of Initial feed rate (only the first roller pass is applied)

As shown in Figure 6.4(a), sample E1 has no wrinkles with relatively smooth surface. Increasing the initial feed rate by 300% and 600%, the surface of the sample E2 and E3 become rough accordingly, as shown in Figure 6.4(b) and 6.4(c). In addition, by comparing the experimental spun part E3 and E4 of Figure 6.4(c) and 6.4(d), it is clear that wrinkling occurs in the first pass, and then smoothed out during the second pass. However, the high feed rate of the roller pass leads to extremely rough surface finish, which also reported by Chen et al. (2001).

Figure 6.4 Experimental samples

6.3 Finite Element Simulation

Since the wrinkling failures only take place in the first forward roller pass of this experiment, the backward pass and the second forward pass are neglected in the FE simulation. The information of the roller pass has been given in the Appendix 2. Table 6.3 presents the process parameters of some of the FE models and the corresponding flange states. The mass scaling technique is used in these FE models to speed up the computation. A mass scaling factor of 25 has been used in Model 1 - 6, in which the spindle speed varies between 400 *rpm* to 800 *rpm*. Conversely, no mass scaling is used in Model 7, which applies a significantly high spindle speed – 1800 *rpm*, in order to prevent the inertial effects due to mass scaling. The first three models (Model 1 - Model 3) use the same setting as experimental sample E1, E2 and E4.

Table 6.3 FE analysis process parameters and flange state of spun part

Model	Replay feed rate	Feed rate (*mm/min*)	Spindle speed (*rpm*)	Mass scaling factor	Feed ratio (*mm/r*)	Process duration (*s*)	Flange state
Model 1	100%	212	400	25	0.53	5.44	No wrinkles
Model 2	300%	636	400	25	1.59	1.81	Wrinkling
Model 3	600%	1272	400	25	3.18	0.91	Wrinkling
Model 4	800%	1696	800	25	2.12	0.68	Wrinkling
Model 5	200%	424	600	25	0.71	2.72	No wrinkles
Model 6	600%	1272	800	25	1.59	0.91	Wrinkling
Model 7	600%	1272	1800	1	0.71	0.91	No wrinkles

6.3.1 Element Selection

To evaluate the performance of the 8 noded reduced integration linear solid element (C3D8R) and the 8 noded reduced integration linear continuum shell element (SC8R) for the wrinkling simulation of the spinning process, three FE models have been compared using the experimental setting of sample E4. Detailed meshing information is shown in Table 6.4, where Model 3a and 3b applied the same process parameters as Model 3 defined in Table 6.3, but with different element types and number of elements through thickness direction of the blank.

Table 6.4 FE models using different types and numbers of elements

Model		Type of element	Elements through thickness	Number of element	Stable increment (*s*)	CPU time (*h:m:s*)	Flange state
Wrinkling Model	Model 3a	C3D8R	1	5200	4.71e-7	08:51:12	No wrinkles
	Model 3b	C3D8R	4	20800	1.37e-7	48:09:38	Minor wrinkles
	Model 3	SC8R	1	5200	5.66e-7	14:18:07	Severe wrinkles
Wrinkle -free Model	Model 5a	C3D8R	1	5200	5.12e-7	13:14:48	No wrinkles
	Model 5b	C3D8R	4	20800	2.12e-7	62:55:34	No wrinkles
	Model 5	SC8R	1	5200	5.66e-7	21:44:38	No wrinkles

Figure 6.5 compares the deformed workpieces of these FE models with the corresponding experimental sample. As shown in Figure 6.5(a), although an extremely fine mesh has been used, Model 3a, which uses one single layer of solid elements in the thickness direction, cannot capture the wrinkling failure occurred in the experiment. Using four layers of elements through the thickness direction slightly improves the results, where minor wrinkling is observed on the deformed FE workpiece, as shown in Figure 6.5(b). However, it is still unable to represent the real severe wrinkles of the experiment sample as shown in Figure 6.5(d).

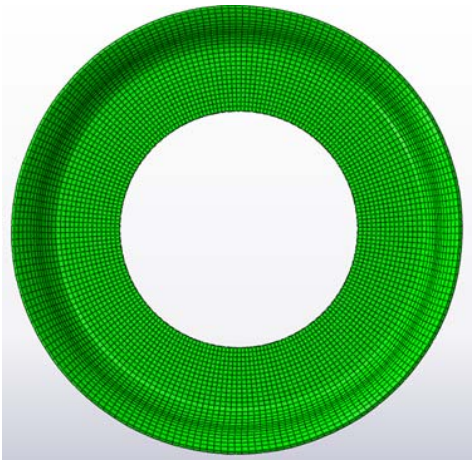

(a) Model 3a

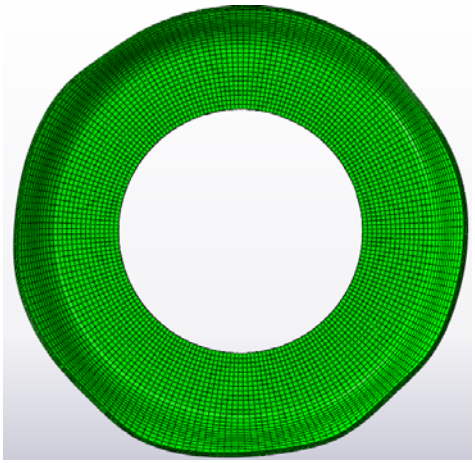

(b) Model 3b

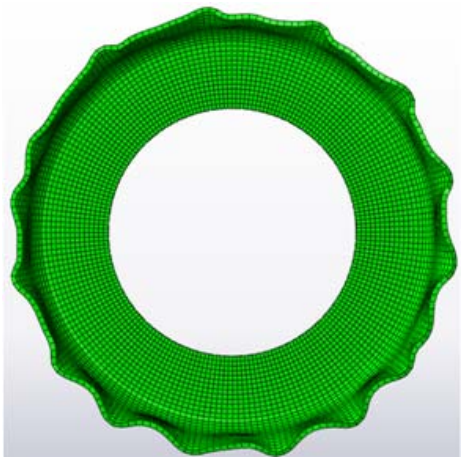

(c) Model 3

(d) Experimental sample (E4)

Figure 6.5 Comparison of deformed workpiece using different types and numbers of elements

On the other hand, Model 3, which uses a single layer of continuum shell elements in the thickness direction with nine integration points, produces much better results, as

shown in Figure 6.5(c). By increasing the number of the solid element layers through the thickness direction could improve FE results, but it is computationally unfeasible to carry out a spinning process simulation using a FE model with several element layers in the thickness direction. Significantly long computing time is required not only due to a large number of elements but also an extremely small element length which significantly decreases the stability limit value of the explicit solution, according to equation (110). In this study, it has shown that the computing time of Model 3b is almost four times of that of Model 3, as details given in Table 6.3.

To further investigate the computing performance of the two element types on spinning simulation not involving wrinkling, axial and radial forces obtained from wrinkle-free models – Model 5a, 5b and 5 have been compared. As can be seen from Figure 6.6, the tool forces of Model 5a, which uses one layer of solid elements, is about three times higher than the corresponding values of Model 5 where one layer of continuum shell elements is used. This has been confirmed by Long et al. (2011) that the axial force of FE model using one layer solid elements is approximately 2.3 times of the experimentally measured value. Long et al. (2011) also report that using one layer continuum shell elements can produce accurate force results.

Additionally, by using four layers of the solid element in Model 5b, the force values are significantly decreased, as a result of using four integration points through the thickness direction. However, the forces are still higher than the corresponding values obtained from Model 5, where the maximum difference is approximately 50%. The overestimation of the tool forces by Model 5a and 5b may be resulted from the artificially introduced hourglass control stiffness to limit the propagation of the “hourglassing” deformation mode. It is therefore evident that the reduced integration linear solid element is not suitable for the metal spinning simulation. Conversely, the reduced integration linear continuum shell element is able to produce accurate FE analysis results such as wrinkling and tool forces.

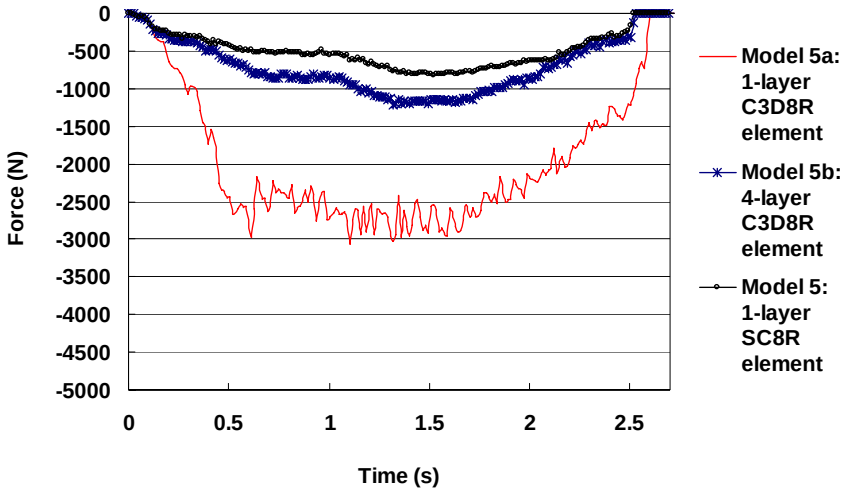

(a) Axial forces

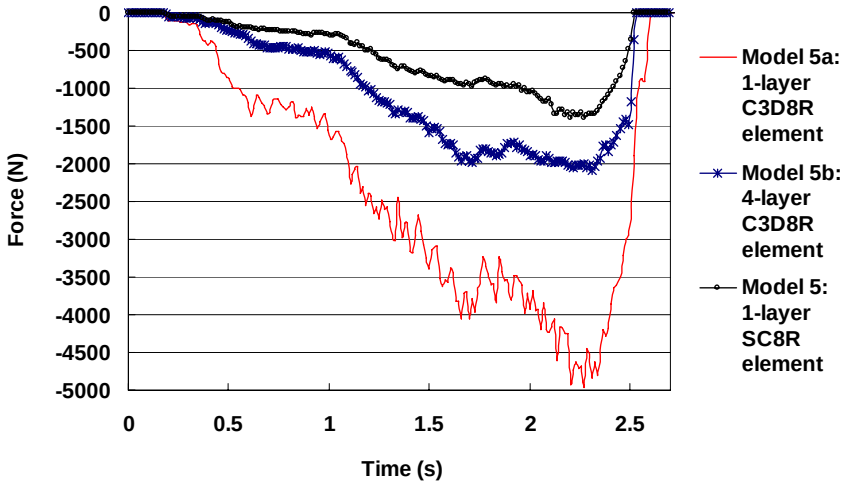

(b) Radial forces

Figure 6.6 Force comparisons of wrinkle-free models using different types and numbers of elements

6.3.2 Verification of FE Models

The number of wrinkles and the height of the experimental spun cup have been measured to verify the FE models. By comparing Figure 6.5(c) and Figure 6.5(d), there are 20 wrinkles according to the FE results, whereas 24 wrinkles are observed in the experimental sample. The difference may result from the fact that some of the minor wrinkles on the experimental sample are difficult to be captured in the FE model. The average height of the FE sample is about 13.8 *mm*, while approximately 14 *mm* has

been measured from the experimental sample. Therefore it is believed that the FE analysis results are in agreement with the experimental results.

Figure 6.7 compares the ratios of the artificial strain energies to the internal energies from the three wrinkle-free models – Model 5a, 5b and 5. It is clear that the energy ratio is around 1% throughout the whole spinning process in Model 5 which uses one layer continuum shell elements, demonstrating that "hourglassing" is not an issue in this model. However, the energy ratio is extremely high in Model 5a with one layer of solid elements. It shows that "hourglassing" is a major problem which could significantly affect the results. By using 4 layers of solid elements in Model 5b, this energy ratio has decreased dramatically but is still much higher than the energy ratio obtained from Model 5.

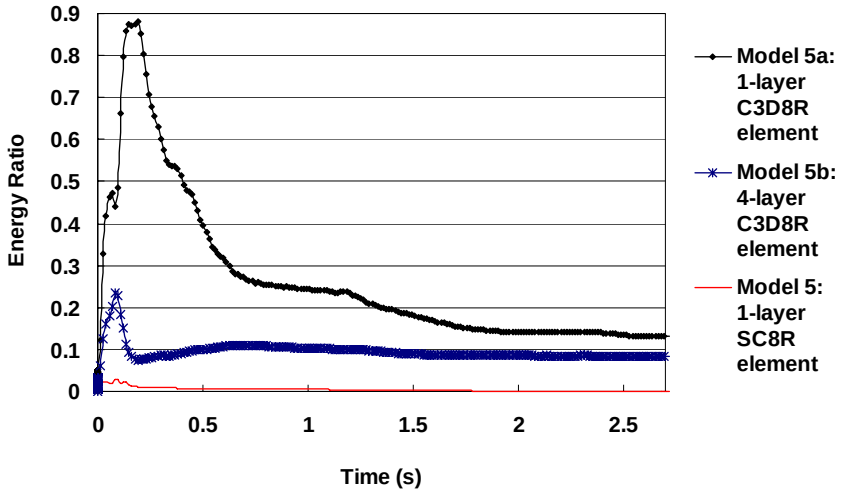

Figure 6.7 Ratio of artificial strain energy to internal energy of the wrinkle-free models

6.4 Results and Discussion

In this section, an approach to quantify the severity of wrinkles is proposed. A forming limit diagram is drawn based on results of a number of FE models using various feed rates and spindle speeds. Furthermore, the variations of tool forces, stresses and wall thickness have been studied numerically. The theoretical analysis model of wrinkling is verified by comparing the theoretical stress state with the FE analysis stress results.

6.4.1 Severity of Wrinkle

Deformed workpieces obtained from Model 2, 4 and 5 defined in Table 6.2 are shown in Figure 6.8, which suggests that with an increasing of feed ratio, wrinkling failure tends to take place. Moreover, the severity of wrinkles increases accordingly when applying higher feed ratios. In order to quantify the severity of wrinkles, the radial coordinates of element nodes located on the edge of the deformed workpiece along the circumferential direction are plotted in Figure 6.9.

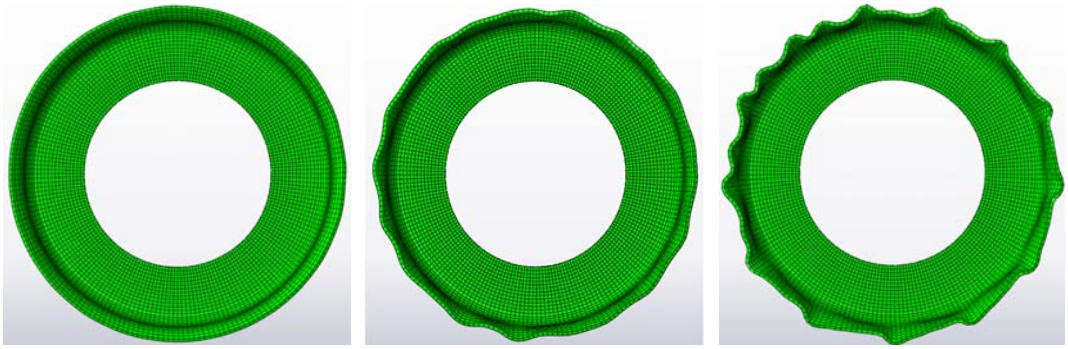

(a) Model 5 (0.71 *mm/rev*) (b) Model 2 (1.59 *mm/rev*) (c) Model 4 (2.12 *mm/rev*)

Figure 6.8 Effects of roller feed ratio on wrinkling

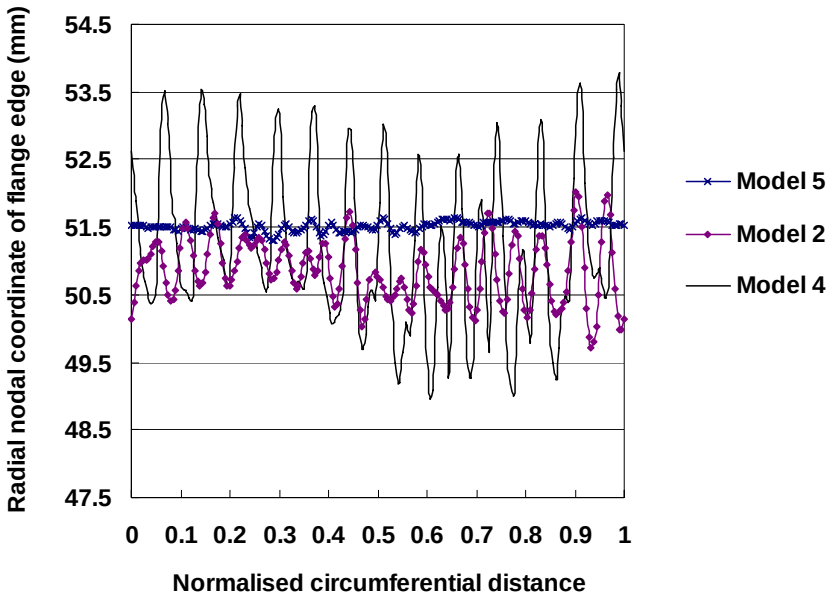

Figure 6.9 Severity of wrinkles of FE models

The mean, maximum, minimum and standard deviations of these radial coordinate values, which illustrate various degrees of the wrinkles, are calculated by equation (154) and (155) and shown in Table 6.5.

$$\overline{U} = \frac{\sum_{i=1}^{N} U_i}{N} \tag{154}$$

$$\mathrm{s} = \sqrt{\frac{1}{N-1}\sum_{i=1}^{N}(U_{\mathrm{i}} - \overline{U})^2} \tag{155}$$

Where $\overline{U}$ is the mean value of these radial coordinate, U_i is the radial coordinate of node i and N is the number of the nodes along the edge of workpiece in the FE model.

Table 6.5 Standard deviations of wrinkle amplitudes

Model	**Feed ratio** (*mm/rev*)	**Maximum radial coordinate** (*mm*)	**Minimum radial coordinate** (*mm*)	**Mean radial coordinate** (*mm*)	**Standard deviation** (*mm*)
Model 5	0.71	51.645	51.304	51.515	0.068
Model 2	1.59	52.020	49.721	50.842	0.467
Model 4	2.12	53.791	48.965	51.132	1.179

As shown in Table 6.5, it is clear that when the feed ratio is 0.71 *mm/rev*, the standard deviation of the radial coordinates of the element nodes on the edge of the deformed workpiece is 0.068 *mm*, indicating no wrinkling takes place in Model 5, as confirmed in Figure 6.8(a). However, by increasing the feed ratios to 1.59 *mm/rev* and 2.12 *mm/rev*, the standard deviation of the radial coordinates increase to 0.467 *mm* and 1.179 *mm*, respectively. It shows that the severity of the wrinkles increases exponentially when increasing the feed ratio.

6.4.2 Forming Limit of Wrinkling

A formability study has been carried out by applying different combinations of the feed rate and spindle speed in the FE models. A feed ratio of 0.71 *mm/rev* has been found to be the forming limit of wrinkling for the spinning process considered, beyond which

wrinkling failures will take place. A forming limit diagram for wrinkling is illustrated in Figure 6.10, which also indicates that the wrinkling tends to occur when using high feed rates or low spindle speeds. In other words, using high feed ratio increases the possibility of the wrinkling failure. This finding has also been confirmed by the experimental investigations of both shear forming (Hayama et al., 1966) and one-pass deep drawing spinning (Xia et al., 2005). The wrinkling zone and wrinkling-free zone is approximately separated by a straight line, as shown in Figure 6.10. It suggests that as long as keeping the feed ratio below the feed ratio limit, increasing the feed rate and spindle speed proportionally, the wrinkling failure can be prevented, as agreed with Hayama et al. (1966).

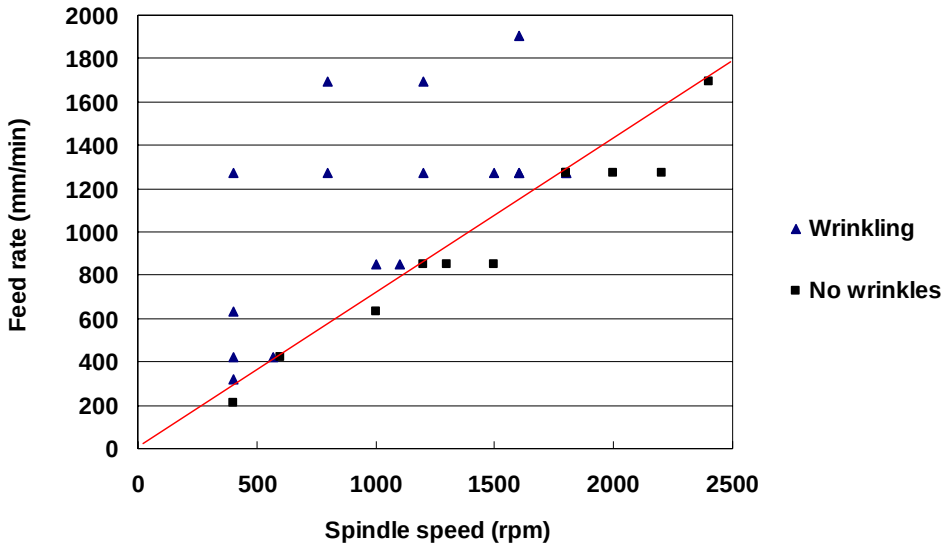

Figure 6.10 Forming limit diagram for wrinkling

However, the feed ratio limit obtained in Figure 6.10 is only valid for this specific experimental setting. The feed ratio limit depends on a number of key parameters of the spinning process, such as the blank material, blank thickness, blank diameter and roller path etc. In this study, the effects of blank thickness have also been investigated. As shown in Table 6.6, the feed ratio limit increases when using thicker blanks. It suggests that the thicker the blank, the higher capability to stand the wrinkling failure, as also reported by Kleiner et al. (2002).

Table 6.6 Feed ratio limits of various thicknesses of blanks

Thickness of blank (*mm*)	**Feed ratio limit of wrinkling** (*mm/rev*)
1.2	0.71
1.6	1.06
2.0	1.88

6.4.3 Tool Forces

Figure 6.11 compares the tool force components of the two wrinkle-free models, i.e. Model 5 and Model 7 as defined in Table 6.3, which use same feed ratio but with different spindle speeds and feed rates. Clearly, the corresponding tool force components of these two models are almost exactly the same. This supports the assertion that as long as keeping the feed ratio constant, by changing the feed rate and the spindle speed proportionally, there would be no significant effects on the final spun product. Furthermore, during the spinning process the tangential force is the smallest among three force components. In the initial stage of spinning, because the workpiece is mainly subjected to bending effects, the axial force is greater than the radial force. At the middle stage of the process, the axial force begins to decrease due to the remaining flange decreases gradually; while the radial force continues to increase and peaks at the end of the process. This may be a result of the roller forcing the blank towards the mandrel at the final stage, as corresponding to the roller passes shown in Figure 6.3.

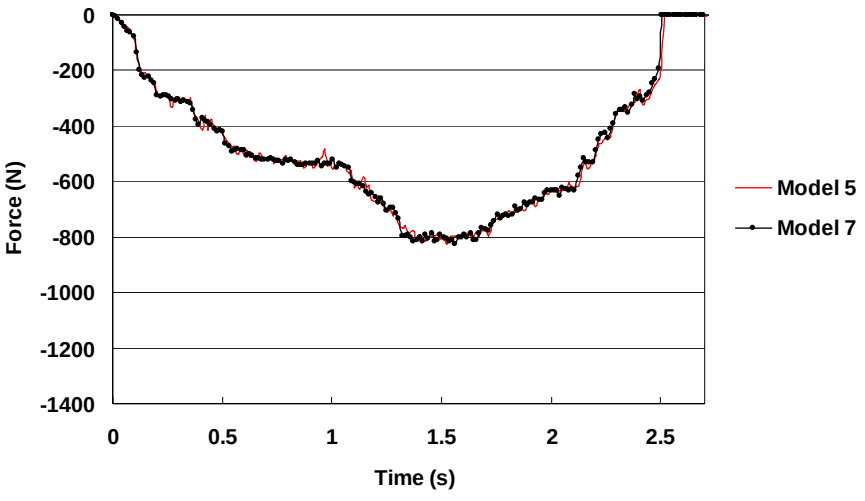

(a) Axial force

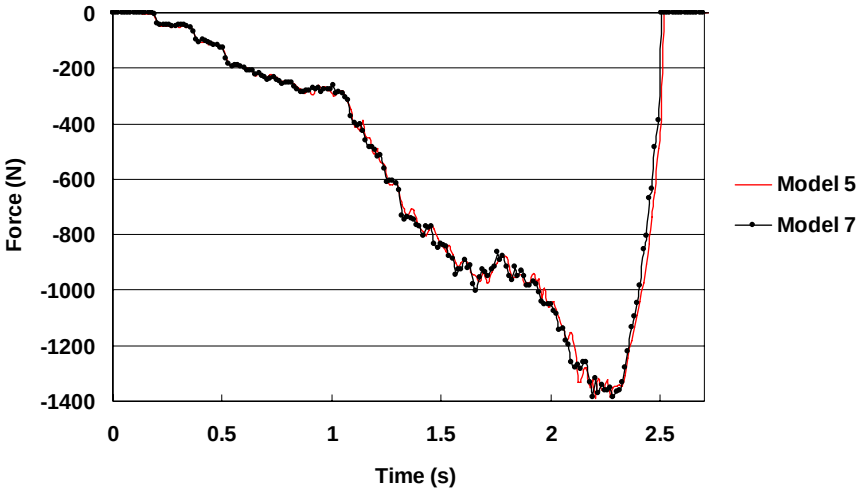

(b) Radial force

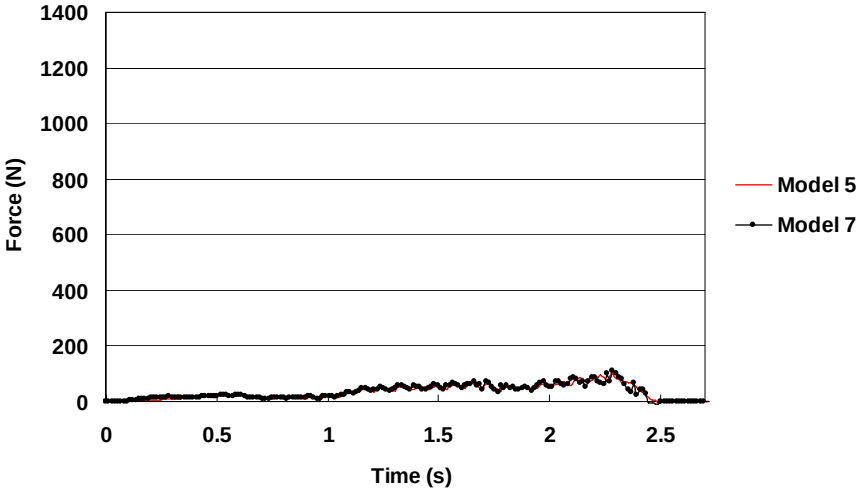

(c) Tangential force

Figure 6.11 Force histories of wrinkle-free models (Model 5 and 7)

Figure 6.12 illustrates the force history of a wrinkling model – Model 4. Comparing with the corresponding forces of wrinkle-free model shown in Figure 6.11, the magnitudes of the forces are much higher at the second half stage of the spinning process, when severe deformation takes place due to wrinkles appearing on the flange. In addition, according to Figure 6.12, sudden changes and fluctuations of forces are clearly shown around 0.4*s*. These sudden changes and fluctuations of tool forces may be resulted from the existing wrinkles on the workpiece interacting with the roller. As shown in

Figure 6.13, wrinkling failure initiates at 0.34*s* and is extending to the whole flange around 0.36*s*. Consequently, it is considered that these sudden changes and fluctuations in tool forces may be used to determine the moment when wrinkling occurs, as also reported by Arai (2003) and Hayama (1981).

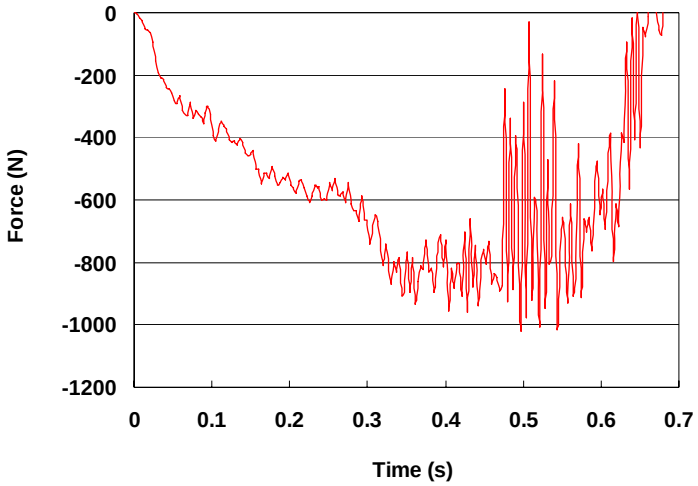

(a) Axial force

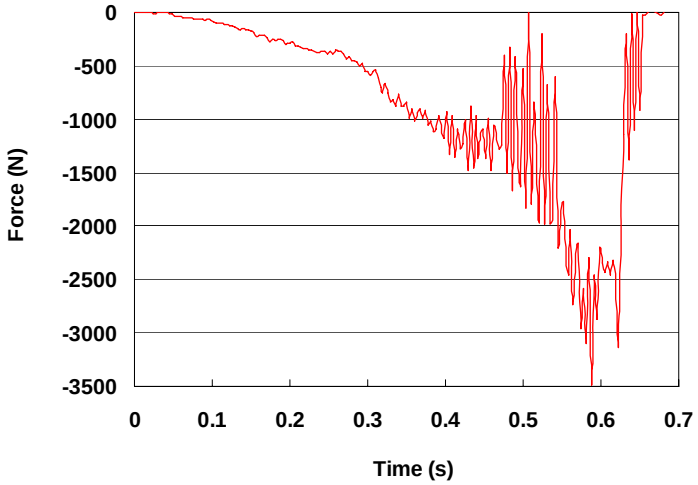

(b) Radial force

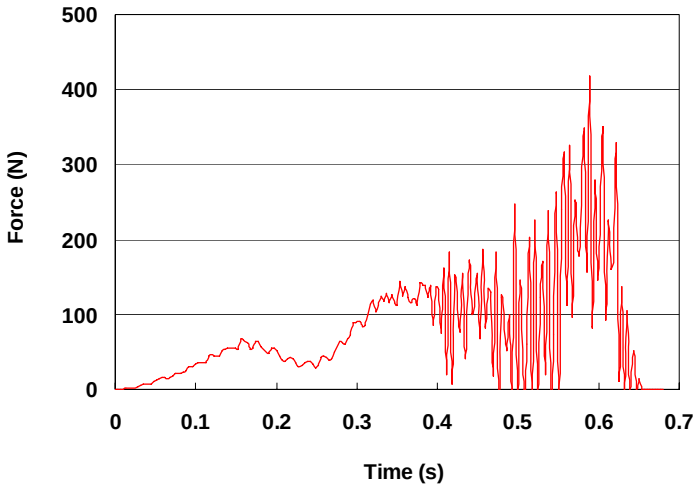

(c) Tangential force

Figure 6.12 Force histories of wrinkling model (Model 4)

6.4.4 Stresses

A distinct difference of the tangential stress distributions has been found between the wrinkling model (Model 4) and the wrinkle-free model (Model 5). Figure 6.13 shows the tangential stress variations through the wrinkling developing process in Model 4. Figure 6.14 shows the tangential stress contours of the wrinkle-free model – Model 5 at the corresponding stages. According to Figure 6.13(a) and 6.14(a), at Stage 1 there is no apparent difference of the tangential stress distributions between these two models. As can be seen from Figure 6.13(b), wrinkles take place around processing time of 0.34*s*. The compressive tangential stresses distribute not only in the roller contact zone but also in other areas of the flange. At stage 3 shown in Figure 6.13(c), the compressive tangential stresses locate regularly along the circumferential direction of workpiece and more wrinkles are generated. Conversely, at the corresponding stages of the wrinkling-free model illustrated in Figure 6.14(b) and 6.14(c), there are no compressive tangential stresses observed on the flange area, except at the roller contact zone.

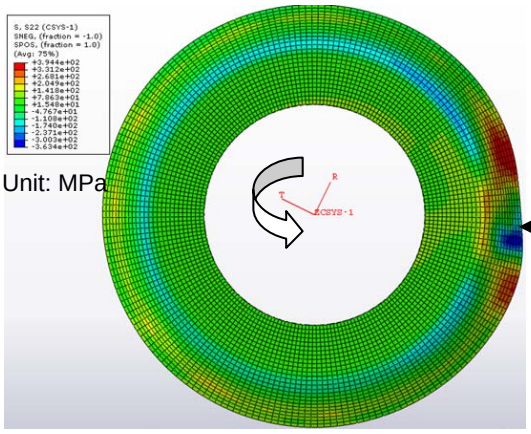

(a) Stage 1, time = 0.295 s

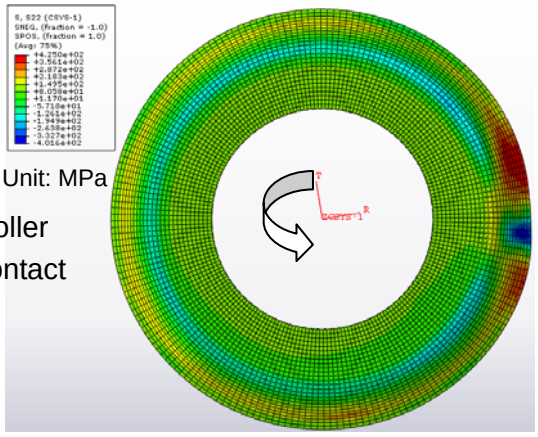

(a) Stage 1 time=1.179s

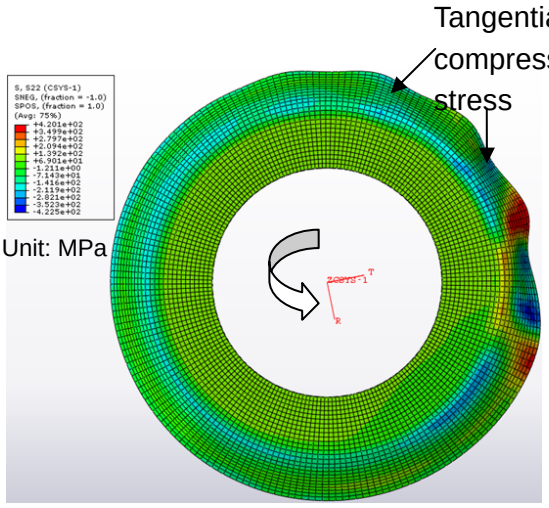

(b) Stage 2, time = 0.34s

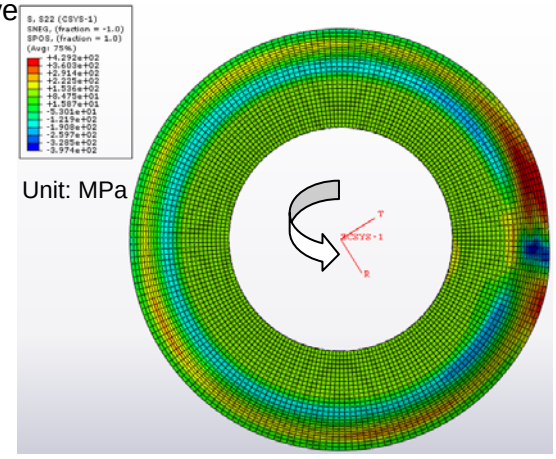

(b) Stage 2, time = 1.360s

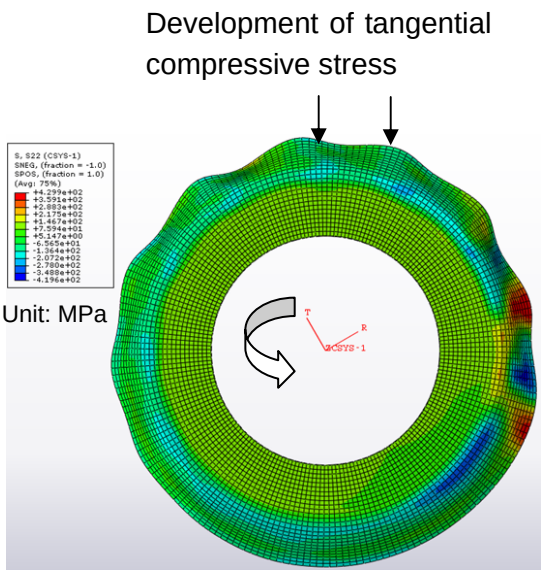

(c) Stage 3, time = 0.363s

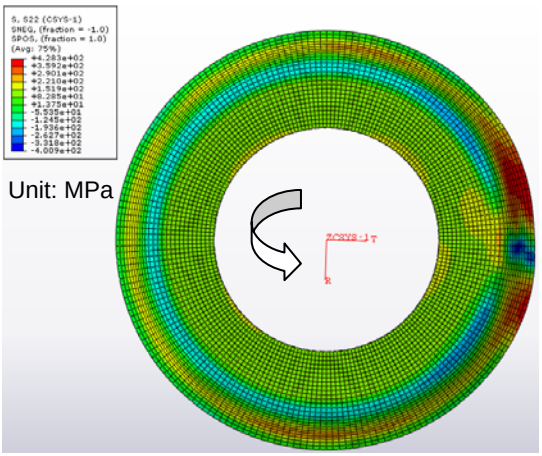

(c) Stage 3, time = 1.451s

Figure 6.13 Tangential stress distribution of wrinkling model (Model 4)

Figure 6.14 Tangential stress distribution of wrinkle-free model (Model 5)

It is believed that in the wrinkle-free model, the compressive tangential stresses “recover” to tensile tangential stresses when the current contact area moves away from the roller, as also observed in Figure 5.15(b). Conversely, in the wrinkling model the compressive tangential stresses induced at the roller contact zone do not fully “recover” to tensile tangential stresses after being deformed. This may be because the compressive stresses at the roller contact zone are beyond the buckling stability limit, resulting in some compressive tangential stresses remaining in the previous contact zone thus leading to the wrinkling failure.

In order to verify the critical condition of wrinkling by theoretical analysis as given in equation (153), stress distributions of a flange area where wrinkling initiates at have been plotted in Figure 6.15, where the length in the tangential direction of flange area, a=11.3 *mm*, while the width in the radial direction of flange area, b=10.4 *mm*, which give λ =1.1 and α =0.01265 according to Table 6.1. Substituting the material and dimensional parameters into Equations (142), (151), and (152), the left side in equation (153) can be calculated as:

$$\sigma_e\left[\left(1+\lambda^2\right)^2-\frac{4\lambda^3}{\alpha\pi^4}\right]=47.2\text{MPa} \tag{156}$$

By using the query function of Abaqus, radial and tangential stresses in the elements at the edges of this flange area have been output. It has been observed that the value of tangential stress at the edge along the radial direction of the flange area varies between 72 MPa and 225 MPa, while the value of radial stress at the edge along the tangential direction of the flange area ranges from 134 MPa to 161 MPa. Thus the maximum value of the right side in equation (153) obtained by substituting the highest tangential stress and the lowest radial stress:

$$\sigma_t-\sigma_r\lambda^2=54.2\text{MPa} \tag{157}$$

Clearly, the result of theoretical analysis obtained in (156) is in agreement with the result of FE simulation given by (157). However, this theoretical analysis model has its limitations: At first, since the theoretical model in (153) use the tangential and radial stresses to predict the critical condition of wrinkling failure, it would be quite difficult to

use the model in the spinning industry, where the stress state of a blank cannot be determined without conducting numerical analysis such as FE simulation. Secondly, in the theoretical analysis the radial and tangential stresses are assumed to be uniform along the edges of the flange area, while FE simulation indicates that the distributions of stresses on the edges of the flange region are much more complicated as shown in Figure 6.15.

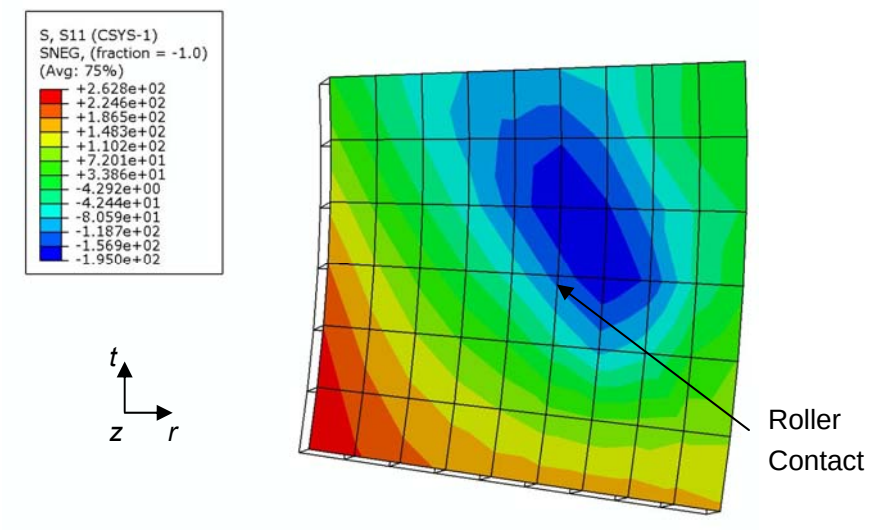

(a) Radial stress

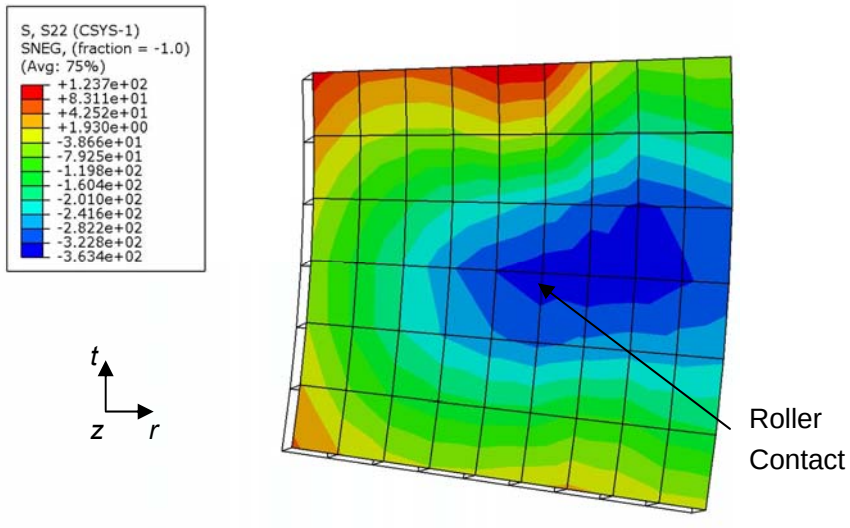

(b) Tangential stress

Figure 6.15 Stress distributions in flange at wrinkling zone (Model 4)

6.4.5 Thickness

Figure 6.16 illustrates the effects of feed ratio on the wall thickness distribution of the spun cylindrical cup. Clearly, less thinning of the wall thickness takes place if a high feed ratio is applied. This finding agrees with Runge (1994) who suggests that lower feed ratios produce excessive material flow to the edge of the workpiece and unduly thin the wall thickness. Shearing between the roller and workpiece due to frictional effects may be one of the main reasons of the material thinning. Considering the roller feeds the same distance during the spinning process, when using a lower feed ratio, the roller will scan the workpiece with more revolutions, thus leading to higher shearing effects than spinning at a high feed ratio.

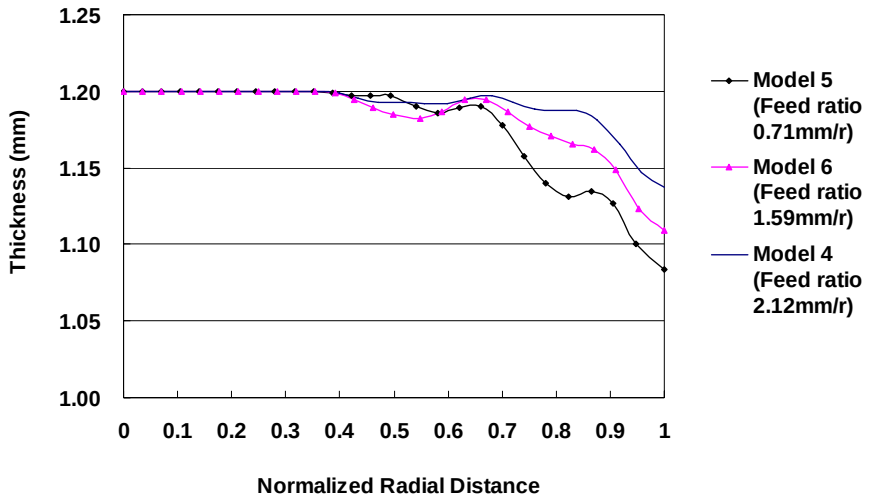

Figure 6.16 Wall thickness distributions at different feed ratios

It is clear that in order to maintain the original blank thickness unchanged, high feed ratios should be used. However, high feed ratios could also lead to rough surface finish and material failures. Figure 6.17 shows the effects of feed ratio on the quality of spun part. It may be necessary to find a “trade-off” feed ratio, which not only can help to maintain the original blank thickness unchanged but also prevent the material failures and produce good surface finish.

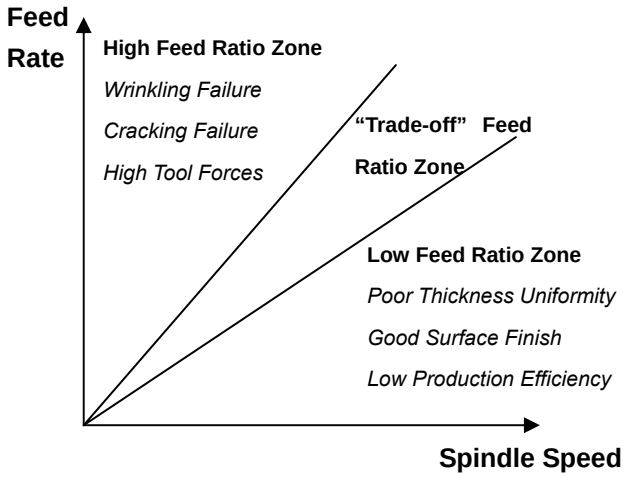

Figure 6.17 Effects of feed ratio in blank metal spinning

6.5 Summary and Conclusion

In this chapter, wrinkling failure in conventional spinning has been studied by theoretical analysis, experimental investigation and Finite Element simulation. The following conclusions may be drawn:

a) The energy method and two-directional plate buckling theory have been used to predict the critical condition of wrinkling failure in the conventional spinning. However, theoretical analysis has shown considerable limitations in comparing with FE simulation as the stress state of the blank during spinning is far more complicated than the simplified assumptions made in the theoretical analysis.

b) This study has shown that the reduced integration linear solid element is not suitable for sheet metal spinning simulation, due to the "hourglassing" problem it suffered from. Conversely, the reduced integration linear continuum shell element, which can produce accurate FE analysis results such as wrinkling and tool forces, should be used to simulate the spinning process.

c) The severity of the wrinkles is quantified by calculating the standard deviation of the radial coordinates of element nodes on the edge of the spun cup in the FE models. The results have shown that the severity of the wrinkles increases exponentially when increasing the feed ratio.

d) A forming limit study of wrinkling indicates that there is a feed ratio limit beyond which wrinkling failures will occur. Increasing the feed rate and spindle speed proportionally, there won't be much effect on the conventional spinning process.

e) If the high compressive tangential stresses in the local forming zone do not "recover" to tensile tangential stresses after roller contact, wrinkling failure will occur.

f) Sudden changes and fluctuations of the tool forces, resulted from existing wrinkles on the workpiece interacting with the roller, could be used to determine the approximate moment of wrinkling occurrence.

g) High feed ratios help to maintain the original blank thickness unchanged. However, high feed ratios also lead to material failures and rough surface finish. It may be necessary to find a "trade-off" feed ratio zone in the spinning process design.

7. Conclusion and Future Work

This chapter summarises the key conclusions on material deformation and wrinkling failures of conventional spinning drawn from this study. Future research trends of sheet metal spinning process are also outlined.

7.1 Conclusion

In this study, numerical analysis and experimental investigation have been carried out to study the material deformation and wrinkling failures in the conventional spinning process. Key conclusions on six main aspects of this research work are summarised in the following:

1) Finite Element Simulation

3D elastic-plastic FE simulation of conventional spinning has been carried out under FE software platform – Abaqus. The computing performances of scaling methods and element types in the simulation of spinning have been evaluated, respectively. FE analysis results indicate that both mass scaling and load rate scaling methods with a suitable scaling factor can produce accurate numerical results, by comparing with a FE model that does not employ any scaling method. Using a mass scaling factor of f^2 or a load rate scaling factor of f would speed up the spinning FE simulation by a factor of f. In addition, FE analysis results also illustrate that the reduced integration linear solid element is not suitable for the metal spinning simulation, due to the “hourglassing” problem it suffered from. Conversely, it is believed that the reduced integration linear continuum shell element, which can produce accurate FE analysis results such as wrinkling and tool forces, should be used to simulate the sheet metal spinning process.

2) Experiment Investigation

In order to make the workpiece conform to the nonlinear profile of the mandrel, the tool compensation technique has been investigated and applied in the process of designing

multiple roller passes. The tool compensation method is developed based on the geometry relationship between the roller and the round part of mandrel, when using a roller to trace the mandrel contour. It has been reported that without taking tool compensation into account, wrinkling failures may take place on the workpiece due to unsupported flange. In addition, The Taguchi method has been used to design the experiment and to study the effects of process parameters on the dimensional variations of experimental samples. Experimental investigation is also employed in the analysis of wrinkling failures in the conventional spinning process.

3) Theoretical Analysis of Wrinkling

By using the energy method and two-dimensional plate buckling theory, a theoretical analysis model to predict the critical condition of wrinkling in the conventional spinning process has been developed. It shows that the radial and tangential stresses at the critical condition of wrinkling depend on the geometry of the half-wave wrinkled flange and the material properties of the blank. Nevertheless, theoretical analysis has shown considerable limitations in comparing with FE simulation as the stress state of the blank during spinning is far more complicated than the simplified assumptions on the stresses of the theoretical model.

4) Material Deformation

To gain insight into the material deformation of conventional spinning, variations of tool forces, stresses, and strains have been analysed numerically. Axial force dominates at the beginning of the conventional spinning when the workpiece is mainly subjected to bending. Radial force increases gradually as roller forms workpeice onto mandrel. Tangential force keeps almost constant during the conventional spinning process and is the smallest forces among three force components. Stress analysis shows that in the forward roller pass, high tensile and compressive radial stresses take place behind and in front of the roller contact. Two pairs of oppositely directed radial bending effects have been observed in the workpiece. High tensile radial strains and low compressive tangential strains are also noticed in the FE models.

5) Wrinkling Failures

Wrinkling failure in the conventional spinning process has been studied by using both numerical and experimental approaches. Compressive tangential stresses are observed at the flange area near the local forming zone but these will change into tensile tangential stresses after roller contact in the wrinkle-free models. However, if the compressive tangential stresses do not fully “recover” to tensile tangential stresses, wrinkling failure will take place. The severity of the wrinkles is quantified by calculating the standard deviation of the radial coordinates of element nodes on the edge of spun cup in the FE models. A forming limit study of wrinkling indicates that there is a feed ratio limit beyond which wrinkling failures will occur. Increasing the feed rate and spindle speed proportionally, there will not be much effect on the conventional spinning process. Sudden changes and fluctuations of the tool forces, resulted from existing wrinkles on the workpiece interacting with the roller, could be used to determine the approximate moment of wrinkling occurrence.

6) Process Parameters

According to the experimental results analysis by the Taguchi method, the type of material has the most significant effects on the thickness and depth variations of spun parts, followed by the spindle speed and the feed rate. Nevertheless, none of these input factors show significant effects on the diameter variations. Among four different roller path designs, i.e. combined concave and convex, convex, linear, and concave curves, the concave roller path produces the highest tool forces, stresses and deduction of wall thickness. A greater curvature of the concave path, a higher amount of wall thinning would take place. On the other hand, lowest tool forces, stresses and wall thinning are obtained when using the convex roller path. Furthermore, it has been shown that high feed ratios help to maintain the original blank thickness. However, high feed ratios also lead to material failures and rough surface finish. It is thus necessary to find a “trade-off” feed ratio zone in the spinning process design.

7.2 Future Work

In this section, four future areas of investigation on the sheet metal spinning process are identified:

a) FE Simulation of Cracking Failures in Spinning

Up to now, there is no research being conducted on the FE simulation of cracking failures in the conventional spinning process, although cracking failures also significantly affects the production efficiency and product quality. Hence, it is believed that applying FE analysis method to predict and prevent cracking failures in the conventional spinning is beneficial to the industrial spinning process design. Developing a suitable material damage model, e.g. defining damage initiation criteria and damage evolution law, may be one of the key aspects in the FE simulation of cracking failures in the sheet metal spinning process.

b) Experimental Design and Optimisation

To further analyse the effects of process parameters and their interactions on the quality of spun part, future experimental design of metal spinning should attempt to take more input factors at various levels into account, such as the tooling parameters shown in Figure 1.6. In addition, future work by employing the regression modelling or response surface methods may be essential to predict the relationships amongst process parameters and optimise the outputs of metal spinning process.

c) Innovation of Sheet Metal Spinning

Metal spinning process is constrained by two features (Music and Allwood, 2011): it can only produce axially symmetric parts; a dedicated mandrel is required for each part. In order to break through these limitations, further research works on asymmetric spinning and spinning using a general purpose mandrel may be essential. This may require to design spinning machines with new control systems, such as, force feedback control (Sekiguchi and Arai, 2010) and synchronous control (Shimizu, 2010).

d) Theoretical Analysis of Wrinkling Involving Process Parameters

In this study, the tangential and radial stresses in the local forming zone of workpiece have been used to predict the critical condition of wrinkling failure. However, this theoretical model is quite difficult to be directly used in the spinning industry, where the stress state of workpiece cannot be analysed without carrying out numerical analysis such as FE simulation. Thus, it is of practical importance to develop a theoretical analysis approach to relate process parameters, for instance, feed rate, spindle speed and roller path etc, to the critical stress state in the workpiece and thereby to the wrinkling failure.

Reference

ABAQUS ANALYSIS USER'S MANUAL 2008. *ver 6.8*.

ALBERTI, N., CANNIZZARO, L., LO VALVO, E. & MICARI, F. 1989. Analysis of metal spinning processes by the ADINA code. *Computers & Structures,* 32**,** 517-525.

ALBERTI, N. & FRATINI, L. 2004. Innovative sheet metal forming processes: numerical simulations and experimental tests. *Journal of Materials Processing Technology,* 150**,** 2-9.

ARAI, H. 2003. Robotic metal spinning-shear spinning using force feedback control. *2003 IEEE International Conference on Robotics and Automation.* Taipei, Taiwan.

ARAI, H. 2006. Force-controlled metal spinning machine using linear motors. *2006 IEEE International Conference on Robotics and Automation.* Orlando, Florida.

AUER, C., ERDBR GGE, M. & G BEL, R. 2004. Comparison of multivariate methods for robust parameter design in sheet metal spinning. *Applied Stochastic Models in Business and Industry,* 20**,** 201-218.

AVITZUR, B., FLOREEN, S., HUCKE, H. H. & RAGONE, D. V. 1959. *An investigation of metal spinning: progress report*, College of Engineering, Department of Chemical and Metallurgical Engineering, The University of Michigan.

AVITZUR, B. & YANG, C. T. 1960. Analysis of power spinning of cones. *Journal of Engineering for Industry - Transactions of ASME,* 82**,** 231–245.

AWISZUS, B. & H RTEL, S. 2011. Numerical simulation of non-circular spinning: a rotationally non-symmetric spinning process. *Production Engineering***,** 1-8.

BAI, Q., YANG, H. & ZHAN, M. 2008. Finite Element modeling of power spinning of thin-walled shell with hoop inner rib. *Transactions of Nonferrous Metals Society of China,* 18**,** 6-13.

BELYTSCHKO, T., LIU, W. K., & MORAN B. 2000. *Nonlinear Finite Elements for continua and structures*, Chichester, John Wiley & Sons Ltd.

BENI, H. R., BENI, Y. T. & BIGLARI, F. R. 2011. An experimental–numerical investigation of a metal spinning process. *Proceedings of the Institution of Mechanical Engineers, Part C: Journal of Mechanical Engineering Science,* 225**,** 509-519.

CHEN, M.-D., HSU, R.-Q. & FUH, K.-H. 2005a. An analysis of force distribution in shear spinning of cone. *International Journal of Mechanical Sciences,* 47**,** 902-921.

CHEN, M.-D., HSU, R.-Q. & FUH, K.-H. 2005b. Effects of over-roll thickness on cone surface roughness in shear spinning. *Journal of Materials Processing Technology,* 159**,** 1-8.

CHEN, M. D., HSU, R. Q. & FUH, K. H. 2001. Forecast of shear spinning force and surface roughness of spun cones by employing regression analysis. *International Journal of Machine Tools and Manufacture,* 41**,** 1721-1734.

CHU, E. & XU, Y. 2001. An elastoplastic analysis of flange wrinkling in deep drawing process. *International Journal of Mechanical Sciences,* 43**,** 1421-1440.

DUNNE, F. & PETRINIC, N. 2005. *Introduction to computational plasticity*, Oxford University Press.

EL-KHABEERY, M. M., FATTOUH, M., EL-SHEIKH, M. N. & HAMED, O. A. 1991. On the conventional simple spinning of cylindrical aluminium cups. *International Journal of Machine Tools and Manufacture,* 31**,** 203-219.

ESSA, K. & HARTLEY, P. 2009. Numerical simulation of single and dual pass conventional spinning processes. *International Journal of Material Forming,* 2**,** 271-281.

ESSA, K. & HARTLEY, P. 2010. Optimization of conventional spinning process parameters by means of numerical simulation and statistical analysis. *Proceedings of the Institution of Mechanical Engineers, Part B: Journal of Engineering Manufacture,* 224**,** 1691-1705.

FILIP, A. C. & NEAGO, I. 2010. Simulation of the metal spinning process by multi-pass path using AutoCAD/VisualLISP. *Proc. of 3rd WSEAS International Conference on Engineering Mechanics, Structures, Engineering Geology (EMESEG '10).* Corfu Island, Greece.

FOWLKES, W. Y. & CREVELING, C. M. 1995. *Engineering methods for robust product design: using Taguchi methods in technology and product development*, Addison-Wesley.

GERE, J. M. 2001. *Mechanics of materials,* Pacific Grove, CA, Brooks/Cole.

HAGAN, E. & JESWIET, J. 2003. A review of conventional and modern single-point sheet metal forming methods. *Proceedings of the Institution of Mechanical Engineers, Part B: Journal of Engineering Manufacture,* 217**,** 213-225.

HAMILTON, S. & LONG, H. 2008. Analysis of conventional spinning process of a cylindrical part using finite element method. *Steel Research International, Verlag Stahleisen GmbH,* 79**,** 632-639.

HAREWOOD, F. J. & MCHUGH, P. E. 2007. Comparison of the implicit and explicit finite element methods using crystal plasticity. *Computational Materials Science,* 39**,** 481-494.

HAYAMA, M. 1981. Study on spinnability of aluminium and its alloys. *Bulletin of Faculty of Engineering, Yokohama National University,* 30**,** 63-72.

HAYAMA, M., KUDO, H. & SHINOKURA, T. 1970. Study of the pass schedule in conventional simple spinning. *Bulletin of JSME,* 13**,** 1358-1365.

HAYAMA, M. & MUROTA, T. 1963. On the study of metal spinning. *Bulletin of Faculty of Engineering, Yokohama National University,* 12**,** 53–88.

HAYAMA, M., MUROTA, T. & KUDO, H. 1965. Experimental study of shear spinning. *Bulletin of JSME,* 8**,** 453-460.

HAYAMA, M., MUROTA, T. & KUDO, H. 1966. Deformation modes and wrinkling of flange on shear spinning. *Bulletin of JSME,* 9**,** 423-433.

HAYAMA, M. & TAGO, A. 1968. The fracture of walls on shear spinning - study on the spinnability of aluminium plates. *Bulletin of Faculty of Engineering, Yokohama National University,* 17**,** 93-103.

HUTCHINSON, J. W. & NEALE, K. W. 1985. Wrinkling of curved thin sheet metal. *Plastic Instability***,** 71-78.

JACKSON, K. & ALLWOOD, J. 2009. The mechanics of incremental sheet forming. *Journal of Materials Processing Technology,* 209**,** 1158-1174.

JAGGER, P. 2010. Tool force measurements in the metal spinning process *MEng Dissertation, School of Engineering and Computing Sciences, Durham*

University.

JOSHI, A. M. 2002. *Strain studies in sheet metal stampings* [Online]. Available: http://www.metalwebnews.com/howto/sheet-metal/sheetmetal-study.pdf[Accessed February 2011].

JURKOVIC, M., JURKOVIC, Z. & MAHMIC, M. 2006. An analysis and modelling of spinning process without wall-thickness reduction. *METABK,* 45**,** 307-312.

KALPAKCIOGLU, S. 1961a. On the mechanics of shear spinning. *Journal of Engineering for Industry - Transactions of ASME,* 83**,** 125–130.

KALPAKCIOGLU, S. 1961b. A study of shear-spinability of metals. *Journal of Engineering for Industry - Transactions of ASME,* 83**,** 478-484.

KALPAKJIAN, S. & SCHMID, S. 2001. *Manufacturing, engineering & technology,* London, Prentice Hall.

KANG, D.-C., GAO, X.-C., MENG, X.-F. & WANG, Z.-H. 1999. Study on the deformation mode of conventional spinning of plates. *Journal of Materials Processing Technology,* 91**,** 226-230.

KAWAI, K. & HAYAMA, M. 1987. Roller pass programming in conventional spinning by NC spinning machine. *Advanced Technology of Plasticity,* 11**,** 711-718.

KAWAI, K., YANG, L. N. & KUDO, H. 2007. A flexible shear spinning of axi-symmetrical shells with a general-purpose mandrel. *Journal of Materials Processing Technology,* 192-193**,** 13-17.

KEGG, R. 1961. A new test method for determination of spinnability of metals. *Journal of Engineering for Industry - Transactions of ASME,* 83**,** 118-125.

KIM, J., PARK, J. & KIM, C. 2006. A study on the mechanics of shear spinning of cones. *Journal of Mechanical Science and Technology,* 20**,** 806-818.

KLEINER, M., EWERS, R., KUNERT, J., HENKENJOHANN, N. & AUER, C. 2005. *Optimisation of the shear forming process by means of multivariate statistical methods*[Online].Available:http://www.statistik.tu-dortmund.de/fileadmin/user_upload/Lehrstuehle/MSind/SFB_475/2005/tr23-05.pdf [Accessed February 2011].

KLEINER, M., G BEL, R., KANTZ, H., KLIMMEK, C. & HOMBERG, W. 2002. Combined methods for the prediction of dynamic instabilities in sheet metal spinning. *CIRP Annals - Manufacturing Technology,* 51**,** 209-214.

KLIMMEK, C., GOBEL, R., HOMBERG, W., KANTZ, H. & KLEINER, M. 2002. Finite element analysis of sheet metal forming by spinning. *Proc. of 7th International Conference on Technology of Plasticity.* Yokohama, Japan.

KOBAYASHI, S. 1963. Instability in conventional spinning of cones. *Journal of Engineering for Industry - Transactions of ASME,* 85**,** 44-48.

KOBAYASHI, S., HALL, I. K. & THOMSEN, E. G. 1961. A theory of shear spinning of cones. *Journal of Engineering for Industry,* 83**,** 485-495.

LEE, K. S. & NOBLE, C. F. 1982. The effect of relative angle between work and roller axes on forces and material characteristics in flow turning of aluminium cones. *Proc. of 2nd International Conference on Rotary Metal-Working Processes.* Stratford upon Avon, UK.

LIU, C.-H. 2007. The simulation of the multi-pass and die-less spinning process. *Journal of Materials Processing Technology,* 192-193**,** 518-524.

LIU, J. H., YANG, H. & LI, Y. Q. 2002. A study of the stress and strain distributions of first-pass conventional spinning under different roller-traces. *Journal of Materials*

Processing Technology, 129**,** 326-329.

LIU, G. R. & QUEK, S. S. 2003. *The Finite Element method: a practical course*, Oxford, Butterworth-Heinemann.

LONG, H. & HAMILTON, S. 2008. Simulation of effects of material deformation on thickness variation in conventional spinning. *Proc. of 9th International Conference on Technology of Plasticity.* Kyeongju, South Korea.

LONG, H., WANG, L. & JAGGER, P. 2011. Roller force analysis in multi-pass conventional spinning by finite element simulation and experimental measurement. *The 10th International Conference on Technology of Plasticity.* Aachen, Germany.

LU, X., ZHANG, S., HOU, H., LI, J., ZHOU, L. & LI, Z. 2006. Three dimensional FE analysis on flange bending for TC4 alloy during shear spinning. *Journal of Materials Science and Technology,* 22**,** 855-859.

MA, F., YANG, H. & ZHAN, M. 2010. Plastic deformation behaviors and their application in power spinning process of conical parts with transverse inner rib. *Journal of Materials Processing Technology,* 210**,** 180-189.

MONTGOMERY, D. C. 2009. *Design and analysis of experiments*, John Wiley & Sons (Asia)

MORI, K.-I. & NONAKA, T. 2005. Simplified three-dimensional finite element simulation of shear spinning process based on axisymmetric modeling. *Journal of Manufacturing Processes,* 7**,** 51-56.

MUSIC, O. & ALLWOOD, J. M. 2011. Flexible asymmetric spinning. *CIRP Annals - Manufacturing Technology,* In Press, Corrected Proof.

MUSIC, O., ALLWOOD, J. M. & KAWAI, K. 2010. A review of the mechanics of metal spinning. *Journal of Materials Processing Technology,* 210**,** 3-23.

OZER, A. & ARAI, H. 2009. Robotic metal spinning-experimental implementation using an industrial robot arm. *2009 IEEE International Conference on Robotics and Automation.* Kobe, Japan.

PELL, S. 2009. Simulation of the metal spinning process. *MEng Dissertation, School of Engineering and Computing Sciences, Durham University*

PEREZ, A., GARC A, J. & FRANCISCO, P. 1984. A study about parameters influence in shear spinning. *Proc. of 3rd International Conference on Rotary Metal-Working Processes.* Kyoto, Japan.

POLLITT, D. H. 1982. The development of a new playback or skill recording control system for metal spinning *Proc. of 2nd International Conference on Rotary Metal-Working Processes.* Stratford upon Avon, UK.

QUIGLEY, E. & MONAGHAN, J. 1999. An analysis of conventional spinning of light sheet metal. *International Conference on Sheet Metal.* Erlangen, Germany.

QUIGLEY, E. & MONAGHAN, J. 2000. Metal forming: an analysis of spinning processes. *Journal of Materials Processing Technology,* 103**,** 114-119.

QUIGLEY, E. & MONAGHAN, J. 2002a. Enhanced finite element models of metal spinning. *Journal of Materials Processing Technology,* 121**,** 43-49.

QUIGLEY, E. & MONAGHAN, J. 2002b. The finite element modelling of conventional spinning using multi-domain models. *Journal of Materials Processing Technology,* 124**,** 360-365.

RAO, S. S. 2005. *The Finite Element method in engineering*. Burlington,

Butterworth-Heinemann.

RAZAVI, H., BIGLARI, F. R. & TORABKHANI, A. 2005. Study of strains distribution in spinning process using FE simulation and experimental work. *Tehran International Congress on Manufacturing Engineering (TICME2005).* Tehran, Iran.

REITMANN, V. & KANTZ, H. 2001. *Plastic wrinkling and flutter in sheet metal spinning* [Online]. Available: http://www.vreitmann.de/reitmann/wrinkling.html [Accessed 15 February 2011].

RUNGE, M. 1994. *Spinning and flow forming (Pollitt, D. H. Trans)*, Leifield GmbH.

SATOH, T. & YANAGIMOTO, S. 1982. On the spinnability of steel sheets. *Proc. of 2nd International Conference on Rotary Metal-Working Processes.* Stratford upon Avon, UK.

SEBASTIANI, G., BROSIUS, A., EWERS, R., KLEINER, M. & KLIMMEK, C. 2006. Numerical investigation on dynamic effects during sheet metal spinning by explicit finite-element-analysis. *Journal of Materials Processing Technology,* 177**,** 401-403.

SEBASTIANI, G., BROSIUS, A., HOMBERG, W. & KLEINER, M. 2007. Process characterization of sheet metal spinning by means of Finite Elements. *Key Engineering Materials,* 334**,** 637-644.

SEKIGUCHI, A. & ARAI, H. 2010. Synchronous die-less spinning of curved products. *Steel Research International,* 81**,** 1010-1013.

SENIOR, B. W. 1956. Flange wrinkling in deep-drawing operations. *Journal of Mechanics and Physics of Solids,* 4**,** 235-246.

SHIMIZU, I. 2010. Asymmetric forming of aluminum sheets by synchronous spinning. *Journal of Materials Processing Technology,* 210**,** 585-592.

SLATER, R. A. C. 1979a. The effects of mandrel speed and roller feed rate on the external surface finish during the spin-forging of 70/30 brass sheet metal cones *Proc. of 1st International Conference on Rotary Metal-Working Processes.* London, UK.

SLATER, R. A. C. 1979b. A review of analytical and experimental investigations of the spin-forging of sheet metal cones. *Proc. of 1st International Conference on Rotary Metal-Working Processes.* London, UK.

SORTAIS, H. C., KOBAYASHI, S. & THOMSEN, E. G. 1963. Mechanics of conventional spinning. *Journal of Engineering for Industry - Transactions of ASME,* 85**,** 346–350.

TEKKAYA, A. E. 2000. State-of-the-art of simulation of sheet metal forming. *Journal of Materials Processing Technology,* 103**,** 14-22.

TIMOSHENKO, S. 1936. *Theory of elastic stability,* New York ; London, McGraw-Hill Book Company, inc.

TIMOSHENKO, S. & WOINOWSKY-KRIEGER, S. 1959. *Theory of plates and shells,* New York, McGraw-Hill book company.

WANG, L. 2005. *Finite Element Analysis of C_{64} Railway Vehicle*. BEng Thesis, Dalian Jiaotong University.

WANG, L. & LONG, H. 2010. Stress analysis of multi-pass conventional spinning. *Proc. of 8th International Conference on Manufacturing Research.* Durham, UK.

WANG, L. & LONG, H. 2011a. Investigation of effects of roller path profiles on wrinkling

in conventional spinning. *The 10th International Conference on Technology of Plasticity.* Aachen, Germany.

WANG, L. & LONG, H. 2011b. Investigation of material deformation in multi-pass conventional metal spinning. *Materials & Design,* 32**,** 2891-2899.

WANG, L. & LONG, H. 2011c. A study of effects of roller path profiles on tool forces and part wall thickness variation in conventional metal spinning. *Journal of Materials Processing Technology,* 211**,** 2140-2151.

WANG, L., LONG, H., ASHLEY, D., ROBERTS, M. & WHITE, P. 2010. Analysis of single-pass conventional spinning by Taguchi and finite element methods. *Steel Research International,* 81**,** 974-977.

WANG, L., LONG, H., ASHLEY, D., ROBERTS, M. & WHITE, P. 2011. Effects of roller feed ratio on wrinkling failure in conventional spinning of a cylindrical cup. *Proceedings of the Institution of Mechanical Engineers, Part B, Journal of Engineering Manufacture,* 225, 1991-2006.

WANG, Q., WANG, T. & WANG, Z. R. 1989. A study of the working force in conventional spinning. *Proc. of 4th International Conference on Rotary Forming.* Beijing, China.

WANG, X. & CAO, J. 2000. An Analytical Prediction of Flange Wrinkling in Sheet Metal Forming. *Journal of Manufacturing Processes,* 2**,** 100-107.

WICK, C., BENEDICT, J. T. & VEILLEUX, R. F. 1984. *Tool and Manufacturing Engineers Handbook,* Michigan, USA, Society of Manufacturing Engineers.

WILSON, J. S. 2005. *Sensor technology handbook* Oxford, Newnes.

WONG, C. C., DEAN, T. A. & LIN, J. 2003. A review of spinning, shear forming and flow forming processes. *International Journal of Machine Tools and Manufacture,* 43**,** 1419-1435.

XIA, Q., SHIMA, S., KOTERA, H. & YASUHUKU, D. 2005. A study of the one-path deep drawing spinning of cups. *Journal of Materials Processing Technology,* 159**,** 397-400.

YOUNGER, A. 1979. The effect of roller tool profile on the tool forces in hydraulic metal spinning. *Proc. of 1st International Conference on Rotary Metal-Working Processes.* London, UK.

ZHAN, M., YANG, H., JIANG, Z. Q. & ZHANG, J. H. 2008. 3D FEM analysis of forming parameters on cone spinning based on orthogonal experimental design method. *Proc. of 9th International Conference on Technology of Plasticity.* Kyeongju, South Korea

ZHAN, M., YANG, H., ZHANG, J. H., XU, Y. L. & MA, F. 2007. 3D FEM analysis of influence of roller feed rate on forming force and quality of cone spinning. *Journal of Materials Processing Technology,* 187-188**,** 486-491.

ZHANG, S.-H., LU, X.-Y., LIU, H., HOU, H.-L., LI, Z.-Q. & ZENG, Y.-S. 2010. Effects of feeding ratio on flange bending in shear spinning. *International Journal of Material Forming***,** 1-7.

ZHAO, J.-H., CHAMPLIAUD, H. & DAO, T.-M. 2007. Simulation of shear spinning process using finite element method. *Proc. of 18th IASTED International Conference: Modelling and Simulation.* Montreal, Canada.

Appendix

Appendix 1 Roller Path information of Multiple Pass Spinning Study

Global coordinate (calculated from CNC program)		**Local coordinate**		**Time***	**Amplitude of local displacement boundary conditions**	
X	Y	x	z	T	Amp x	Amp z
0	0	0	0	0	0	0
0.943	-0.224	-0.50841	0.825194	0.072693	-0.01755	0.011344
1.881	-0.467	-0.99985	1.660287	0.145365	-0.03451	0.022823
2.813	-0.73	-1.4729	2.505279	0.217995	-0.05084	0.034439
3.74	-1.013	-1.92828	3.360879	0.290688	-0.06656	0.046201
4.661	-1.314	-2.36669	4.224963	0.363358	-0.08169	0.058079
5.576	-1.635	-2.78671	5.098947	0.436084	-0.09619	0.070093
6.483	-1.974	-3.18834	5.980002	0.508705	-0.11005	0.082205
7.383	-2.332	-3.5716	6.869542	0.581349	-0.12328	0.094433
8.276	-2.709	-3.93646	7.767568	0.654048	-0.13587	0.106778
9.161	-3.105	-4.28224	8.673372	0.726765	-0.1478	0.11923
10.037	-3.518	-4.60963	9.584832	0.7994	-0.1591	0.131759
10.904	-3.95	-4.91722	10.50336	0.87205	-0.16972	0.144386
11.763	-4.4	-5.20643	11.42897	0.94478	-0.1797	0.15711
11.662	-4.3	-5.20572	11.28684	0.95544	-0.17968	0.155156
12.61	-4.637	-5.63776	12.19547	1.030899	-0.19459	0.167647
13.559	-4.974	-6.07051	13.10481	1.106428	-0.20953	0.180147
14.507	-5.311	-6.50255	14.01344	1.181887	-0.22444	0.192638
15.456	-5.649	-6.9346	14.92349	1.257442	-0.23935	0.205148
16.404	-5.986	-7.36664	15.83212	1.332901	-0.25427	0.217639
17.353	-6.323	-7.79939	16.74146	1.40843	-0.2692	0.230139
18.301	-6.66	-8.23143	17.65009	1.483889	-0.28411	0.24263
19.249	-6.997	-8.66347	18.55872	1.559348	-0.29903	0.25512
20.198	-7.334	-9.09622	19.46806	1.634877	-0.31396	0.267621
21.146	-7.671	-9.52826	20.3767	1.710336	-0.32888	0.280111
22.095	-8.008	-9.96101	21.28604	1.785866	-0.34381	0.292612
23.043	-8.345	-10.3931	22.19467	1.861324	-0.35872	0.305102
23.992	-8.682	-10.8258	23.10401	1.936854	-0.37366	0.317603
24.94	-9.019	-11.2578	24.01264	2.012313	-0.38857	0.330093
25.889	-9.356	-11.6906	24.92198	2.087842	-0.40351	0.342594
26.837	-9.693	-12.1226	25.83061	2.163301	-0.41842	0.355084
27.785	-10.03	-12.5547	26.73924	2.23876	-0.43333	0.367575
28.734	-10.367	-12.9874	27.64858	2.314289	-0.44827	0.380075
29.682	-10.704	-13.4195	28.55721	2.389748	-0.46318	0.392566
30.631	-11.042	-13.8515	29.46726	2.465303	-0.4781	0.405076

31.579	-11.379	-14.2836	30.37589	2.540762	-0.49301	0.417567
32.528	-11.716	-14.7163	31.28523	2.616291	-0.50794	0.430067
33.476	-12.053	-15.1483	32.19386	2.69175	-0.52286	0.442558
34.424	-12.39	-15.5804	33.1025	2.767209	-0.53777	0.455048
35.373	-12.727	-16.0131	34.01184	2.842738	-0.55271	0.467549
36.321	-13.064	-16.4452	34.92047	2.918197	-0.56762	0.480039
37.27	-13.401	-16.8779	35.82981	2.993727	-0.58255	0.49254
38.218	-13.738	-17.31	36.73844	3.069186	-0.59747	0.50503
39.167	-14.075	-17.7427	37.64778	3.144715	-0.6124	0.517531
40.115	-14.412	-18.1748	38.55641	3.220174	-0.62732	0.530021
41.063	-14.749	-18.6068	39.46504	3.295633	-0.64223	0.542512
42.012	-15.086	-19.0396	40.37438	3.371162	-0.65716	0.555012
42.96	-15.423	-19.4716	41.28302	3.446621	-0.67208	0.567503
43.909	-15.76	-19.9043	42.19235	3.522151	-0.68701	0.580003
44.857	-16.097	-20.3364	43.10099	3.597609	-0.70193	0.592494
45.8	-16.435	-20.7642	44.00679	3.67274	-0.71669	0.604946
46.705	-16.772	-21.1658	44.88502	3.745168	-0.73055	0.617019
47.7	-17.109	-21.6311	45.82688	3.823958	-0.74661	0.629966
48.605	-17.446	-22.0327	46.70511	3.896386	-0.76048	0.642039
49.509	-17.783	-22.4337	47.58263	3.968744	-0.77431	0.654102
50.504	-18.12	-22.8989	48.5245	4.047533	-0.79037	0.667049
51.409	-18.457	-23.3006	49.40272	4.119961	-0.80424	0.679122
52.404	-18.794	-23.7659	50.34459	4.19875	-0.8203	0.692069
53.309	-19.131	-24.1675	51.22282	4.271178	-0.83416	0.704142
54.304	-19.468	-24.6328	52.16468	4.349967	-0.85022	0.717089
55.209	-19.805	-25.0344	53.04291	4.422395	-0.86408	0.729162
56.203	-20.142	-25.499	53.98407	4.501113	-0.88012	0.7421
57.108	-20.479	-25.9006	54.86229	4.573542	-0.89398	0.754173
58.103	-20.816	-26.3659	55.80416	4.652331	-0.91004	0.76712
59.008	-21.153	-26.7675	56.68239	4.724759	-0.9239	0.779193
60.003	-21.49	-27.2328	57.62425	4.803548	-0.93996	0.79214
59.007	-21.146	-26.7718	56.67673	4.882578	-0.92405	0.779115
58.102	-20.801	-26.3758	55.79285	4.955218	-0.91038	0.766965
57.106	-20.456	-25.9155	54.84462	5.034272	-0.89449	0.75393
56.2	-20.111	-25.5188	53.96003	5.106982	-0.8808	0.741769
55.205	-19.766	-25.0592	53.0125	5.185965	-0.86494	0.728744
54.209	-19.421	-24.5988	52.06427	5.26502	-0.84905	0.715709
53.303	-19.076	-24.2021	51.17968	5.33773	-0.83535	0.703549
52.308	-18.731	-23.7425	50.23216	5.416713	-0.81949	0.690524
51.402	-18.387	-23.3451	49.34828	5.489396	-0.80577	0.678373
50.407	-18.042	-22.8855	48.40075	5.56838	-0.78991	0.665348
49.501	-17.697	-22.4888	47.51616	5.64109	-0.77622	0.653188
48.505	-17.352	-22.0285	46.56793	5.720144	-0.76033	0.640153
47.6	-17.007	-21.6325	45.68405	5.792784	-0.74666	0.628002
46.604	-16.662	-21.1722	44.73582	5.871838	-0.73077	0.614968
45.608	-16.317	-20.7119	43.78759	5.950893	-0.71489	0.601933

44.732	-15.972	-20.3364	42.92421	6.021505	-0.70193	0.590064
43.776	-15.628	-19.9036	42.00497	6.097705	-0.68699	0.577428
42.82	-15.283	-19.4716	41.08503	6.173931	-0.67208	0.564781
41.863	-14.938	-19.0389	40.16437	6.250228	-0.65714	0.552125
40.907	-14.593	-18.6068	39.24443	6.326454	-0.64223	0.539479
39.951	-14.248	-18.1748	38.32448	6.40268	-0.62732	0.526833
38.995	-13.903	-17.7427	37.40453	6.478906	-0.6124	0.514187
38.038	-13.558	-17.31	36.48388	6.555202	-0.59747	0.501531
37.082	-13.213	-16.8779	35.56394	6.631428	-0.58255	0.488885
36.126	-12.869	-16.4452	34.6447	6.707629	-0.56762	0.476248
35.17	-12.524	-16.0131	33.72475	6.783855	-0.55271	0.463602
34.213	-12.179	-15.5804	32.8041	6.860152	-0.53777	0.450946
33.257	-11.834	-15.1483	31.88415	6.936378	-0.52286	0.4383
32.301	-11.489	-14.7163	30.96421	7.012604	-0.50794	0.425654
31.345	-11.144	-14.2843	30.04426	7.08883	-0.49303	0.413008
30.388	-10.799	-13.8515	29.12361	7.165126	-0.4781	0.400352
29.432	-10.454	-13.4195	28.20366	7.241352	-0.46318	0.387706
28.476	-10.11	-12.9867	27.28442	7.317553	-0.44825	0.375069
27.52	-9.765	-12.5547	26.36448	7.393779	-0.43333	0.362423
26.564	-9.42	-12.1226	25.44453	7.470005	-0.41842	0.349777
25.607	-9.075	-11.6899	24.52388	7.546301	-0.40349	0.337121
24.651	-8.73	-11.2578	23.60393	7.622527	-0.38857	0.324475
23.695	-8.385	-10.8258	22.68399	7.698753	-0.37366	0.311829
22.739	-8.04	-10.3938	21.76404	7.774979	-0.35875	0.299183
21.782	-7.695	-9.96101	20.84339	7.851276	-0.34381	0.286527
20.826	-7.351	-9.52826	19.92415	7.927477	-0.32888	0.27389
19.87	-7.006	-9.09622	19.0042	8.003703	-0.31396	0.261244
18.914	-6.661	-8.66418	18.08426	8.079929	-0.29905	0.248598
17.957	-6.316	-8.23143	17.1636	8.156225	-0.28411	0.235942
17.001	-5.971	-7.79939	16.24366	8.232451	-0.2692	0.223296
16.045	-5.626	-7.36735	15.32371	8.308677	-0.25429	0.21065
15.089	-5.281	-6.9353	14.40377	8.384903	-0.23938	0.198003
14.132	-4.936	-6.50255	13.48311	8.4612	-0.22444	0.185348
13.176	-4.592	-6.0698	12.56387	8.5374	-0.2095	0.172711
12.22	-4.247	-5.63776	11.64393	8.613626	-0.19459	0.160065
11.264	-3.902	-5.20572	10.72398	8.689852	-0.17968	0.147419
12.086	-4.482	-5.37684	11.71535	8.765304	-0.18559	0.161047
12.907	-5.062	-5.54725	12.706	8.840695	-0.19147	0.174665
13.728	-5.643	-5.71696	13.69737	8.916129	-0.19733	0.188293
14.548	-6.225	-5.88525	14.68873	8.991545	-0.20313	0.201921
15.368	-6.808	-6.05283	15.6808	9.067004	-0.20892	0.215558
16.188	-7.392	-6.21971	16.67358	9.142507	-0.21468	0.229206
17.006	-7.976	-6.38517	17.66494	9.217888	-0.22039	0.242834
17.824	-8.561	-6.54993	18.65701	9.293312	-0.22608	0.256471
18.642	-9.147	-6.71398	19.64979	9.36878	-0.23174	0.270119
19.459	-9.734	-6.87661	20.64257	9.444231	-0.23735	0.283766

20.276	-10.321	-7.03925	21.63535	9.519682	-0.24296	0.297413
21.092	-10.909	-7.20047	22.62812	9.595115	-0.24853	0.311061
21.907	-11.498	-7.36027	23.6209	9.670532	-0.25405	0.324708
22.722	-12.088	-7.51937	24.61439	9.745993	-0.25954	0.338365
23.536	-12.679	-7.67706	25.60787	9.821437	-0.26498	0.352022
24.35	-13.27	-7.83474	26.60136	9.896881	-0.27042	0.365679
25.163	-13.862	-7.99101	27.59484	9.972309	-0.27582	0.379337
25.975	-14.455	-8.14587	28.58833	10.04772	-0.28116	0.392994
26.787	-15.049	-8.30002	29.58252	10.12318	-0.28648	0.40666
27.599	-15.643	-8.45417	30.57671	10.19863	-0.2918	0.420327
28.41	-16.238	-8.6069	31.5709	10.27407	-0.29707	0.433994
29.22	-16.834	-8.75822	32.5651	10.34949	-0.3023	0.447661
30.03	-17.431	-8.90884	33.55999	10.42496	-0.3075	0.461337
30.839	-18.029	-9.05804	34.55489	10.50041	-0.31264	0.475014
31.647	-18.627	-9.20653	35.54909	10.5758	-0.31777	0.488681
32.455	-19.226	-9.35432	36.54399	10.65124	-0.32287	0.502357
33.263	-19.826	-9.50139	37.53959	10.72672	-0.32795	0.516044
34.07	-20.427	-9.64706	38.5352	10.80219	-0.33298	0.52973
34.876	-21.028	-9.79201	39.5301	10.87759	-0.33798	0.543406
35.682	-21.63	-9.93626	40.5257	10.95304	-0.34296	0.557093
36.487	-22.233	-10.0791	41.52131	11.02848	-0.34789	0.570779
37.291	-22.837	-10.2205	42.51692	11.1039	-0.35277	0.584465
38.095	-23.441	-10.3619	43.51252	11.17932	-0.35765	0.598151
38.899	-24.046	-10.5027	44.50884	11.25478	-0.36251	0.611847
39.702	-24.652	-10.642	45.50515	11.33023	-0.36732	0.625543
40.504	-25.259	-10.7798	46.50146	11.40567	-0.37207	0.639239
41.306	-25.867	-10.917	47.49848	11.48115	-0.37681	0.652945
42.107	-26.475	-11.0535	48.4948	11.55657	-0.38152	0.666641
42.907	-27.084	-11.1886	49.49111	11.63198	-0.38618	0.680337
43.707	-27.694	-11.3229	50.48813	11.70743	-0.39082	0.694043
44.507	-28.304	-11.4573	51.48515	11.78288	-0.39546	0.707748
45.305	-28.916	-11.5888	52.48217	11.85831	-0.4	0.721454
46.104	-29.528	-11.721	53.4799	11.93379	-0.40456	0.735169
46.901	-30.14	-11.8518	54.47621	12.00916	-0.40907	0.748865
47.698	-30.754	-11.9812	55.47394	12.08461	-0.41354	0.762581
48.495	-31.368	-12.1106	56.47167	12.16007	-0.41801	0.776296
49.29	-31.984	-12.2372	57.4694	12.2355	-0.42238	0.790012
50.086	-32.599	-12.3652	58.46712	12.31094	-0.42679	0.803727
50.88	-33.216	-12.4903	59.46485	12.38636	-0.43111	0.817442
51.675	-33.833	-12.6162	60.46329	12.46183	-0.43546	0.831167
52.468	-34.452	-12.7392	61.46172	12.53728	-0.4397	0.844893
53.261	-35.07	-12.863	62.45945	12.61268	-0.44398	0.858608
54.053	-35.69	-12.9846	63.45788	12.68812	-0.44817	0.872333
53.251	-35.076	-12.8517	62.45662	12.76387	-0.44358	0.858569
52.449	-34.462	-12.7187	61.45536	12.83963	-0.439	0.844805
51.647	-33.848	-12.5858	60.45409	12.91538	-0.43441	0.831041

50.845	-33.234	-12.4529	59.45283	12.99113	-0.42982	0.817277
50.043	-32.62	-12.3199	58.45157	13.06689	-0.42523	0.803513
49.241	-32.007	-12.1863	57.45101	13.1426	-0.42062	0.789759
48.439	-31.393	-12.0533	56.44975	13.21835	-0.41603	0.775995
47.637	-30.779	-11.9204	55.44849	13.2941	-0.41144	0.762231
46.835	-30.165	-11.7875	54.44722	13.36986	-0.40685	0.748467
46.033	-29.551	-11.6545	53.44596	13.44561	-0.40226	0.734703
45.231	-28.937	-11.5216	52.4447	13.52136	-0.39768	0.720939
44.43	-28.323	-11.3894	51.44414	13.59706	-0.39311	0.707184
43.628	-27.709	-11.2564	50.44288	13.67281	-0.38852	0.69342
42.826	-27.095	-11.1235	49.44161	13.74857	-0.38394	0.679656
42.024	-26.481	-10.9906	48.44035	13.82432	-0.37935	0.665892
41.222	-25.867	-10.8576	47.43909	13.90007	-0.37476	0.652128
40.42	-25.253	-10.7247	46.43782	13.97583	-0.37017	0.638364
39.618	-24.639	-10.5918	45.43656	14.05158	-0.36558	0.6246
38.816	-24.025	-10.4588	44.4353	14.12733	-0.36099	0.610836
38.014	-23.411	-10.3259	43.43403	14.20309	-0.35641	0.597072
37.212	-22.798	-10.1922	42.43348	14.2788	-0.35179	0.583318
36.41	-22.184	-10.0593	41.43221	14.35455	-0.3472	0.569554
35.608	-21.57	-9.92636	40.43095	14.4303	-0.34262	0.55579
34.806	-20.956	-9.79343	39.42969	14.50606	-0.33803	0.542026
34.004	-20.342	-9.66049	38.42843	14.58181	-0.33344	0.528262
33.202	-19.728	-9.52756	37.42716	14.65756	-0.32885	0.514498
32.4	-19.114	-9.39462	36.4259	14.73332	-0.32426	0.500734
31.598	-18.5	-9.26168	35.42464	14.80907	-0.31967	0.48697
30.796	-17.886	-9.12875	34.42337	14.88483	-0.31509	0.473206
29.994	-17.272	-8.99581	33.42211	14.96058	-0.3105	0.459442
29.192	-16.658	-8.86288	32.42085	15.03633	-0.30591	0.445678
28.39	-16.044	-8.72994	31.41958	15.11209	-0.30132	0.431914
27.588	-15.43	-8.597	30.41832	15.18784	-0.29673	0.41815
26.786	-14.816	-8.46407	29.41706	15.26359	-0.29214	0.404386
25.984	-14.202	-8.33113	28.41579	15.33935	-0.28756	0.390622
25.182	-13.589	-8.19749	27.41524	15.41506	-0.28294	0.376868
24.38	-12.975	-8.06455	26.41397	15.49081	-0.27835	0.363104
23.578	-12.361	-7.93162	25.41271	15.56656	-0.27377	0.34934
22.776	-11.747	-7.79868	24.41145	15.64232	-0.26918	0.335576
21.974	-11.133	-7.66574	23.41018	15.71807	-0.26459	0.321812
21.172	-10.519	-7.53281	22.40892	15.79383	-0.26	0.308048
20.37	-9.905	-7.39987	21.40766	15.86958	-0.25541	0.294284
19.568	-9.291	-7.26694	20.40639	15.94533	-0.25082	0.28052
18.766	-8.677	-7.134	19.40513	16.02109	-0.24624	0.266755
17.964	-8.063	-7.00106	18.40387	16.09684	-0.24165	0.252991
18.624	-8.805	-6.94308	19.39523	16.17132	-0.23965	0.266619
19.282	-9.549	-6.88227	20.3866	16.24581	-0.23755	0.280247
19.936	-10.297	-6.8158	21.37796	16.32033	-0.23525	0.293875
20.587	-11.047	-6.7458	22.36862	16.39481	-0.23284	0.307493

21.234	-11.8	-6.67085	23.35857	16.46927	-0.23025	0.321102
21.879	-12.555	-6.59306	24.34851	16.54375	-0.22756	0.33471
22.52	-13.313	-6.51033	25.33776	16.6182	-0.22471	0.348309
23.159	-14.074	-6.42407	26.32771	16.69273	-0.22173	0.361918
23.794	-14.838	-6.33285	27.31695	16.76724	-0.21858	0.375516
24.426	-15.604	-6.2381	28.30548	16.84172	-0.21531	0.389106
25.054	-16.373	-6.13839	29.29331	16.91618	-0.21187	0.402685
25.68	-17.144	-6.03586	30.28114	16.99067	-0.20833	0.416264
26.302	-17.918	-5.92838	31.26826	17.06514	-0.20462	0.429834
26.921	-18.695	-5.81666	32.25538	17.13964	-0.20077	0.443403
27.537	-19.474	-5.7014	33.2418	17.21413	-0.19679	0.456963
28.149	-20.256	-5.58119	34.2275	17.2886	-0.19264	0.470513
28.758	-21.04	-5.45745	35.2125	17.36306	-0.18837	0.484054
29.364	-21.827	-5.32946	36.1975	17.43756	-0.18395	0.497594
29.967	-22.616	-5.19794	37.1818	17.51203	-0.17941	0.511125
30.566	-23.408	-5.06147	38.16538	17.58651	-0.1747	0.524646
31.162	-24.203	-4.92076	39.14897	17.66103	-0.16984	0.538167
31.754	-25	-4.7758	40.13114	17.73549	-0.16484	0.551669
32.343	-25.799	-4.62731	41.1126	17.80994	-0.15971	0.56516
32.929	-26.601	-4.47457	42.09407	17.88443	-0.15444	0.578652
33.512	-27.406	-4.31759	43.07553	17.95898	-0.14902	0.592144
34.091	-28.212	-4.15708	44.05487	18.03341	-0.14348	0.605607
34.667	-29.022	-3.99162	45.03492	18.10795	-0.13777	0.619079
35.239	-29.833	-3.82262	46.01285	18.18238	-0.13194	0.632522
35.808	-30.647	-3.64938	46.99078	18.25687	-0.12596	0.645966
36.373	-31.464	-3.47119	47.968	18.33137	-0.11981	0.659399
36.935	-32.282	-3.29017	48.94381	18.40581	-0.11356	0.672813
37.494	-33.103	-3.10491	49.91962	18.4803	-0.10717	0.686227
38.049	-33.927	-2.91469	50.89472	18.55481	-0.1006	0.699632
38.601	-34.753	-2.72095	51.86911	18.62932	-0.09392	0.713026
39.149	-35.581	-2.52296	52.84209	18.70379	-0.08708	0.726402
39.694	-36.411	-2.32143	53.81436	18.77826	-0.08013	0.739767
40.235	-37.244	-2.11496	54.78593	18.85275	-0.073	0.753123
40.773	-38.079	-1.90495	55.75678	18.92725	-0.06575	0.766469
41.308	-38.916	-1.6914	56.72693	19.00176	-0.05838	0.779805
41.838	-39.755	-1.4729	57.69496	19.07618	-0.05084	0.793112
42.366	-40.597	-1.25087	58.6637	19.15072	-0.04317	0.806429
42.889	-41.44	-1.0246	59.62961	19.22513	-0.03536	0.819707
43.41	-42.286	-0.79479	60.59622	19.29964	-0.02743	0.832995
43.926	-43.134	-0.56003	61.56072	19.37409	-0.01933	0.846253
44.439	-43.985	-0.32103	62.52521	19.44862	-0.01108	0.859512
44.949	-44.837	-0.0792	63.48829	19.52309	-0.00273	0.872751
45.455	-45.692	0.167584	64.45066	19.5976	0.005784	0.885981
45.957	-46.548	0.4179	65.41091	19.67203	0.014424	0.899181
46.456	-47.407	0.672459	66.37116	19.74654	0.02321	0.912381
46.951	-48.268	0.93126	67.33	19.82102	0.032143	0.925562

46.372	-47.44	0.75519	66.3351	19.8968	0.026066	0.911885
45.793	-46.611	0.578413	65.3395	19.97264	0.019964	0.898199
45.214	-45.783	0.402344	64.3446	20.04841	0.013887	0.884522
44.635	-44.954	0.225567	63.34899	20.12425	0.007786	0.870836
44.056	-44.126	0.049497	62.35409	20.20003	0.001708	0.85716
43.477	-43.297	-0.12728	61.35848	20.27587	-0.00439	0.843473
42.898	-42.469	-0.30335	60.36358	20.35165	-0.01047	0.829797
42.319	-41.641	-0.47942	59.36869	20.42742	-0.01655	0.81612
41.74	-40.812	-0.6562	58.37308	20.50326	-0.02265	0.802434
41.16	-39.984	-0.83156	57.37747	20.57908	-0.0287	0.788748
40.581	-39.155	-1.00833	56.38187	20.65492	-0.0348	0.775062
40.002	-38.327	-1.1844	55.38697	20.7307	-0.04088	0.761385
39.423	-37.498	-1.36118	54.39136	20.80653	-0.04698	0.747699
38.844	-36.67	-1.53725	53.39646	20.88231	-0.05306	0.734022
38.265	-35.841	-1.71403	52.40086	20.95815	-0.05916	0.720336
37.686	-35.013	-1.8901	51.40596	21.03393	-0.06524	0.70666
37.107	-34.185	-2.06617	50.41106	21.1097	-0.07132	0.692983
36.528	-33.356	-2.24294	49.41545	21.18554	-0.07742	0.679297
35.949	-32.528	-2.41901	48.42055	21.26132	-0.08349	0.66562
35.37	-31.699	-2.59579	47.42494	21.33716	-0.0896	0.651934
34.791	-30.871	-2.77186	46.43005	21.41293	-0.09567	0.638257
34.212	-30.042	-2.94864	45.43444	21.48877	-0.10177	0.624571
33.633	-29.214	-3.1247	44.43954	21.56455	-0.10785	0.610895
33.054	-28.385	-3.30148	43.44393	21.64039	-0.11395	0.597208
32.474	-27.557	-3.47684	42.44833	21.71621	-0.12001	0.583522
31.895	-26.729	-3.65291	41.45343	21.79198	-0.12608	0.569846
31.316	-25.9	-3.82969	40.45782	21.86782	-0.13218	0.556159
30.737	-25.072	-4.00576	39.46292	21.9436	-0.13826	0.542483
30.158	-24.243	-4.18254	38.46732	22.01944	-0.14436	0.528797
29.579	-23.415	-4.35861	37.47242	22.09522	-0.15044	0.51512
29	-22.586	-4.53538	36.47681	22.17105	-0.15654	0.501434
28.421	-21.758	-4.71145	35.48191	22.24683	-0.16262	0.487757
27.842	-20.93	-4.88752	34.48701	22.32261	-0.1687	0.474081
27.263	-20.101	-5.0643	33.49141	22.39845	-0.1748	0.460395
26.684	-19.273	-5.24037	32.49651	22.47422	-0.18088	0.446718
26.105	-18.444	-5.41715	31.5009	22.55006	-0.18698	0.433032
26.538	-19.339	-5.09046	32.43994	22.62463	-0.1757	0.44594
26.967	-20.236	-4.75954	33.37756	22.6992	-0.16428	0.45883
27.392	-21.135	-4.42437	34.31377	22.77378	-0.15271	0.471699
27.813	-22.036	-4.08496	35.24857	22.84837	-0.141	0.48455
28.231	-22.938	-3.74272	36.18195	22.92293	-0.12918	0.49738
28.644	-23.843	-3.39482	37.11391	22.99754	-0.11717	0.510192
29.054	-24.749	-3.04409	38.04447	23.07212	-0.10507	0.522984
29.46	-25.657	-2.68913	38.9736	23.14672	-0.09282	0.535756
29.861	-26.566	-2.32992	39.89991	23.22124	-0.08042	0.54849
30.259	-27.477	-1.96717	40.82552	23.2958	-0.0679	0.561214

30.653	-28.39	-1.60018	41.74971	23.37038	-0.05523	0.573918
31.043	-29.305	-1.22895	42.67248	23.44497	-0.04242	0.586604
31.429	-30.222	-0.85348	43.59384	23.51959	-0.02946	0.599269
31.811	-31.14	-0.47447	44.51308	23.59417	-0.01638	0.611906
32.189	-32.059	-0.09192	45.4302	23.66869	-0.00317	0.624513
32.563	-32.981	0.295571	46.34661	23.74332	0.010202	0.63711
32.933	-33.904	0.686601	47.2609	23.8179	0.023699	0.649679
33.299	-34.828	1.081166	48.17306	23.89244	0.037317	0.662218
33.661	-35.754	1.479974	49.08382	23.967	0.051082	0.674738
34.019	-36.682	1.883025	49.99316	24.0416	0.064994	0.687238
34.373	-37.611	2.289612	50.90037	24.11617	0.079028	0.699709
34.723	-38.542	2.700441	51.80618	24.19076	0.093208	0.712161
35.069	-39.474	3.114805	52.70986	24.26532	0.10751	0.724584
35.411	-40.408	3.533413	53.61213	24.33992	0.121958	0.736987
35.749	-41.343	3.955555	54.51228	24.41449	0.136529	0.749361
36.083	-42.279	4.381234	55.4103	24.48902	0.151222	0.761706
36.413	-43.218	4.811862	56.30762	24.56367	0.166085	0.774041
36.739	-44.157	5.245318	57.20211	24.63822	0.181046	0.786337
37.06	-45.098	5.683724	58.09448	24.71279	0.196178	0.798604
37.378	-46.04	6.124959	58.98543	24.78735	0.211408	0.810852
37.691	-46.984	6.571143	59.87427	24.86194	0.226808	0.82307
38.001	-47.929	7.020156	60.76169	24.93654	0.242306	0.835269
38.306	-48.875	7.473412	61.64628	25.01108	0.25795	0.84743
38.607	-49.823	7.93091	62.52945	25.08568	0.273741	0.85957
38.905	-50.772	8.391236	63.41121	25.16028	0.28963	0.871692
39.198	-51.722	8.855805	64.29015	25.23484	0.305665	0.883774
39.487	-52.673	9.32391	65.16696	25.30939	0.321822	0.895827
39.771	-53.626	9.796964	66.04165	25.38397	0.33815	0.907851
40.052	-54.58	10.27285	66.91493	25.45856	0.354575	0.919856
40.329	-55.535	10.75227	67.78608	25.53314	0.371122	0.931831
40.601	-56.491	11.23593	68.65441	25.60768	0.387816	0.943768
40.244	-55.537	10.81378	67.72739	25.68408	0.373246	0.931025
39.887	-54.583	10.39164	66.80038	25.76047	0.358675	0.918281
39.529	-53.629	9.970206	65.87265	25.8369	0.344129	0.905528
39.172	-52.675	9.548063	64.94564	25.91329	0.329558	0.892785
38.815	-51.721	9.12592	64.01862	25.98969	0.314988	0.880041
38.458	-50.767	8.703777	63.0916	26.06608	0.300417	0.867298
38.1	-49.812	8.281635	62.16317	26.14258	0.285847	0.854535
37.743	-48.858	7.859492	61.23615	26.21897	0.271276	0.841792
37.386	-47.904	7.437349	60.30914	26.29537	0.256706	0.829048
37.029	-46.95	7.015206	59.38212	26.37176	0.242135	0.816305
36.672	-45.996	6.593064	58.4551	26.44816	0.227564	0.803562
36.314	-45.042	6.171628	57.52738	26.52458	0.213018	0.790809
35.957	-44.088	5.749485	56.60036	26.60098	0.198448	0.778065
35.6	-43.134	5.327342	55.67335	26.67737	0.183877	0.765322
35.243	-42.179	4.904493	54.74562	26.75384	0.169282	0.752569

34.885	-41.225	4.483057	53.8179	26.83026	0.154736	0.739816
34.528	-40.271	4.060914	52.89088	26.90666	0.140165	0.727072
34.171	-39.317	3.638771	51.96386	26.98305	0.125595	0.714329
33.814	-38.363	3.216629	51.03685	27.05945	0.111024	0.701586
33.456	-37.409	2.795193	50.10912	27.13587	0.096478	0.688832
33.099	-36.455	2.37305	49.18211	27.21226	0.081908	0.676089
32.742	-35.5	1.950201	48.25438	27.28873	0.067313	0.663336
32.385	-34.546	1.528058	47.32736	27.36513	0.052742	0.650593
32.028	-33.592	1.105915	46.40035	27.44152	0.038171	0.637849
31.67	-32.638	0.684479	45.47262	27.51794	0.023625	0.625096
31.313	-31.684	0.262337	44.54561	27.59434	0.009055	0.612353
30.956	-30.73	-0.15981	43.61859	27.67074	-0.00552	0.599609
30.599	-29.776	-0.58195	42.69157	27.74713	-0.02009	0.586866
30.241	-28.822	-1.00338	41.76385	27.82355	-0.03463	0.574113
29.884	-27.867	-1.42623	40.83612	27.90002	-0.04923	0.56136
30.111	-28.852	-0.89025	41.69314	27.97583	-0.03073	0.573141
30.334	-29.837	-0.35143	42.54732	28.05157	-0.01213	0.584883
30.554	-30.823	0.190212	43.40009	28.12734	0.006565	0.596606
30.769	-31.809	0.735391	44.24933	28.20303	0.025383	0.60828
30.981	-32.797	1.284106	45.09786	28.27882	0.044322	0.619944
31.19	-33.785	1.834942	45.94426	28.35456	0.063334	0.63158
31.394	-34.774	2.390021	46.78784	28.43029	0.082493	0.643176
31.595	-35.764	2.947928	47.63001	28.50606	0.10175	0.654753
31.792	-36.755	3.509371	48.47005	28.58184	0.121129	0.666301
31.985	-37.746	4.073642	49.30726	28.65756	0.140605	0.67781
32.175	-38.738	4.640742	50.14306	28.73331	0.160179	0.689299
32.361	-39.731	5.211377	50.97674	28.80908	0.179875	0.700759
32.543	-40.724	5.784841	51.80759	28.8848	0.199668	0.712181
32.721	-41.719	6.362547	52.63703	28.96061	0.219608	0.723583
32.896	-42.713	6.941667	53.46364	29.0363	0.239597	0.734946
33.066	-43.709	7.525737	54.28812	29.11208	0.259756	0.74628
33.233	-44.705	8.111929	55.11049	29.18783	0.279989	0.757584
33.397	-45.702	8.700949	55.93144	29.26361	0.30032	0.76887
33.556	-46.699	9.293504	56.74885	29.33933	0.320772	0.780106
33.712	-47.697	9.888888	57.56486	29.41509	0.341322	0.791324
33.864	-48.696	10.48781	58.37874	29.49087	0.361994	0.802512
34.012	-49.695	11.08956	59.18979	29.56662	0.382764	0.813661
34.156	-50.694	11.69413	59.99801	29.64232	0.403632	0.824771
34.297	-51.694	12.30154	60.80482	29.71806	0.424597	0.835862
34.433	-52.695	12.91318	61.6088	29.79382	0.445708	0.846914
34.566	-53.696	13.52695	62.41066	29.86956	0.466893	0.857937
34.696	-54.698	14.14355	63.2111	29.94534	0.488175	0.868941
34.821	-55.7	14.76368	64.00801	30.02107	0.509579	0.879896
34.943	-56.703	15.38664	64.80351	30.09685	0.531081	0.890831
35.061	-57.706	16.01243	65.59617	30.17259	0.552681	0.901727
35.175	-58.71	16.64176	66.38672	30.24838	0.574403	0.912595

35.285	-59.714	17.27391	67.17444	30.32413	0.596222	0.923423
35.391	-60.718	17.90889	67.95933	30.39985	0.618139	0.934213
35.494	-61.723	18.5467	68.7428	30.47561	0.640153	0.944983
35.279	-60.701	17.97607	67.86811	30.55394	0.620457	0.932959
35.065	-59.678	17.40402	66.99342	30.63233	0.600713	0.920935
34.85	-58.656	16.83338	66.11873	30.71066	0.581017	0.908911
34.635	-57.634	16.26275	65.24404	30.78898	0.561321	0.896887
34.421	-56.612	15.69141	64.37005	30.8673	0.541601	0.884872
34.206	-55.59	15.12077	63.49536	30.94562	0.521905	0.872848
33.991	-54.568	14.55014	62.62067	31.02395	0.502209	0.860824
33.777	-53.546	13.97879	61.74669	31.10226	0.482488	0.84881
33.562	-52.523	13.40745	60.87129	31.18067	0.462768	0.836776
33.347	-51.501	12.83682	59.9966	31.25899	0.443072	0.824752
33.132	-50.479	12.26618	59.12191	31.33732	0.423376	0.812728
32.918	-49.457	11.69484	58.24792	31.41563	0.403656	0.800714
32.703	-48.435	11.1242	57.37323	31.49396	0.38396	0.78869
32.488	-47.413	10.55357	56.49854	31.57229	0.364264	0.776665
32.274	-46.391	9.982226	55.62455	31.6506	0.344544	0.764651
32.059	-45.368	9.410884	54.74916	31.729	0.324824	0.752617
31.844	-44.346	8.840249	53.87447	31.80733	0.305128	0.740593
31.629	-43.324	8.269614	52.99977	31.88566	0.285432	0.728569
31.415	-42.302	7.698272	52.12579	31.96397	0.265712	0.716555
31.2	-41.28	7.127636	51.2511	32.0423	0.246016	0.704531
30.985	-40.258	6.557001	50.37641	32.12063	0.22632	0.692507
30.984	-41.279	7.279664	51.09766	32.1972	0.251263	0.702421
30.983	-42.301	8.003035	51.81961	32.27385	0.276231	0.712346
30.982	-43.322	8.725698	52.54086	32.35043	0.301174	0.722261
30.981	-44.344	9.449068	53.26282	32.42708	0.326142	0.732185
30.98	-45.365	10.17173	53.98407	32.50365	0.351085	0.7421
30.979	-46.387	10.8951	54.70602	32.5803	0.376053	0.752024
30.978	-47.408	11.61776	55.42727	32.65688	0.400996	0.761939
30.977	-48.43	12.34113	56.14923	32.73353	0.425963	0.771864
30.976	-49.452	13.0645	56.87118	32.81018	0.450931	0.781788
30.975	-50.473	13.78717	57.59243	32.88675	0.475874	0.791703
30.973	-51.495	14.51125	58.31368	32.9634	0.500866	0.801618
30.972	-52.516	15.23391	59.03493	33.03998	0.52581	0.811532
30.971	-53.538	15.95728	59.75689	33.11663	0.550777	0.821457
30.97	-54.559	16.67994	60.47814	33.1932	0.575721	0.831372
30.969	-55.581	17.40331	61.20009	33.26985	0.600688	0.841296
30.968	-56.602	18.12598	61.92134	33.34643	0.625632	0.851211
30.967	-57.624	18.84935	62.6433	33.42308	0.650599	0.861135
30.966	-58.645	19.57201	63.36455	33.49965	0.675542	0.87105
30.965	-59.667	20.29538	64.0865	33.5763	0.70051	0.880975
30.964	-60.688	21.01804	64.80775	33.65288	0.725453	0.890889
30.963	-61.71	21.74141	65.52971	33.72953	0.750421	0.900814
30.962	-62.732	22.46478	66.25166	33.80618	0.775389	0.910738

30.961	-63.753	23.18745	66.97291	33.88275	0.800332	0.920653
30.959	-64.775	23.91152	67.69416	33.9594	0.825324	0.930568
30.958	-65.796	24.63419	68.41541	34.03598	0.850267	0.940483
30.957	-66.818	25.35756	69.13737	34.11263	0.875235	0.950407
30.956	-67.839	26.08022	69.85861	34.1892	0.900178	0.960322
30.955	-68.861	26.80359	70.58057	34.26585	0.925146	0.970246
30.954	-69.882	27.52625	71.30182	34.34243	0.950089	0.980161
30.953	-70.904	28.24962	72.02378	34.41908	0.975057	0.990085
30.952	-71.925	28.97229	72.74502	34.49565	1	1

* Run 3 & 4 (Feed rate = 900 *mm/min*)

Appendix 2 Roller Path information of Wrinkling Failure Study

Global coordinate (calculated from CNC program)		**Local coordinate**		**Time***	**Amplitude of local displacement boundary conditions**	
X	Y	x	z	T	Amp x	Amp z
0	0	0	0	0	0	0
-0.002	-0.106	0.076368	0.073539	0.16	0.008938	0.005768
-0.245	-0.645	0.629325	0.282843	0.32	0.073657	0.022184
-0.429	-1.227	1.170969	0.564271	0.48	0.137052	0.044257
-0.552	-1.794	1.658873	0.878227	0.64	0.194157	0.068881
-0.672	-2.542	2.272641	1.32229	0.8	0.265994	0.10371
-0.78	-3.335	2.909744	1.806658	0.96	0.340561	0.1417
-0.847	-4.036	3.452802	2.254964	1.12	0.404122	0.176862
-0.745	-4.538	3.735645	2.682056	1.28	0.437226	0.21036
-0.525	-4.952	3.872824	3.130362	1.44	0.453281	0.245522
-0.261	-5.377	3.986668	3.617558	1.6	0.466606	0.283734
0.027	-5.831	4.104048	4.142232	1.76	0.480344	0.324885
0.313	-6.298	4.232034	4.674683	1.92	0.495324	0.366646
0.53	-6.815	4.444166	5.193699	2.08	0.520152	0.407354
0.518	-7.505	4.940555	5.673118	2.24	0.57825	0.444956
0.471	-8.215	5.475835	6.14193	2.4	0.6409	0.481726
0.464	-8.896	5.962324	6.618519	2.56	0.69784	0.519106
0.511	-9.523	6.372446	7.095109	2.72	0.745841	0.556486
0.564	-10.149	6.777618	7.575235	2.88	0.793263	0.594144
0.62	-10.818	7.211075	8.087887	3.04	0.843996	0.634352
0.666	-11.546	7.693322	8.635188	3.2	0.900439	0.677278
0.731	-12.309	8.186882	9.220672	3.36	0.958206	0.723199
0.878	-12.998	8.570134	9.811814	3.52	1.003062	0.769564
0.982	-13.763	9.037532	10.42629	3.68	1.057767	0.817758
1.096	-14.561	9.521193	11.07117	3.84	1.114376	0.868338
1.109	-15.493	10.17102	11.73939	4	1.190433	0.920748
1.043	-16.534	10.95379	12.42882	4.16	1.282049	0.974821
0.91	-17.673	11.85323	13.14017	4.32	1.387321	1.030614
0.659	-18.923	12.9146	13.84656	4.48	1.511545	1.086019
0.346	-20.208	14.04455	14.53387	4.64	1.643797	1.139926
0.301	-20.933	14.58903	15.01471	4.8	1.707523	1.177639
0.602	-20.728	14.23123	15.08259	4.96	1.665646	1.182963
1.506	-19.289	12.57448	14.70429	5.12	1.471737	1.153292
2.357	-17.167	10.47225	13.80555	5.28	1.225689	1.082802
2.974	-15.057	8.543971	12.74984	5.44	1	1

* Model 1 of Table 6.2